Earthquake-Resisting Performance and Evaluation of Drift-hardening Concrete Walls

Wei, Chuxuan

(Degree)
博士（工学）

(Date of Degree)
2021-09-25

(Date of Publication)
2023-09-25

(Resource Type)
doctoral thesis

(Report Number)
甲第8163号

(URL)
https://hdl.handle.net/20.500.14094/D1008163

Earthquake-Resisting Performance and Evaluation of Drift-hardening Concrete Walls

ドリフト硬化型コンクリート壁の耐震性能および評価方法

Kobe University
Graduate School of Engineering

A Dissertation
Submitted to the Kobe University
for the Degree of Doctor of Philosophy

By

WEI CHUXUAN
（魏　楚軒）
Kobe, Hyogo, Japan

July, 2021

Acknowledgements

It is a genuine pleasure to express my deep sense of thanks and gratitude to my research supervisor Professor Yuping Sun, for providing me the precious opportunity to study in his laboratory throughout the period of my research work in Kobe University. This thesis would not have been successful without his patience guidance and support. During the three and half years, Professor Sun's timely and valuable suggestions, scholarly advice and scientific approach have helped me to a very great extent in both of my research work and life, which will always be my treasures in the future.

I would like to express my deepest appreciation to Professor Hideo Fujitani and Professor Shinichi Akutagawa from Department of Architecture and Civil Engineering at Kobe University, respectively, for their professional guidance, meticulous scrutiny, and precious advices.

I would also like to extend my deepest gratitude to Assistant Professor Takashi Takeuchi for his guidance for my dissertation, technical assistance for my experimental works and humors during my study and life in Japan.

I am also grateful to Associate Professor Takashi Fujinaga for his academic advice during the seminar, patient course guidance and test technical assistance during my three and half years in the laboratory.

All the experimental works of this research would not have been completed without the support of the technicians and staffs of the Department of Architecture. Many thanks to those who helped me, especially for the assistance of Mr. Masaru Kanao.

The financial support provided by the Teraura-Sayoko Memorial Scholarship Foundation (2020.4-2021.4) helped me cover the daily expenses, which is also kindly appreciated.

I also want to give sincere thanks to visiting Professor Hua Zhao from Chengdu University of Technology, Xiangcheng Zhang from Zhengzhou University, and numerous others, for their advice and guidance for my research.

To my fellow postgraduate students, I would like to acknowledge those who supported me extensively throughout my researches: Dr. A.X. Zhou, Dr. S.Y. Yuan, Dr. R. Han, Dr. C.J. Wei, Dr. F.Q. Shen, Dr. L.X. Zeng, Mr. Y. Feng, Ms. M. Jia, Mr. J.Y. Che, Mr. J. Luo, Ms. C. Zhang, Mr. T. Nakagawa, Mr. H. Yamada, Mr. T. Sakanaka, Mr. H. Mizoguchi and numerous others. Thank you all for providing insightful comments and suggestions on a range of topics.

Last but not the least, I am extremely grateful to my family, for their constant and unwavering support, nurturing and encouragements during my life.

Chuxuan Wei
2021.05.17

Contents

List of Tables

List of Figures

CHAPTER One

Introduction

1.1 Backgrounds

Earthquake has been considered as one of the most devastating natural hazards that cause great loss of life and property, and an average of 10,000 people killed by earthquakes each year, while annual economic losses are in the billions of dollars and often constitute a large percentage of the GDP of the affected country [1.1].

Reinforced concrete buildings represent one of the most prevalent construction types in regions of high seismic activity such as Japan [1.2]. In Japan, the history of seismic design in Japanese building code started in 1924 when the Urban Building Law was revised, as a consequence of the disaster of great Kanto earthquake of 1923 [1.3]. This initial seismic design method has aimed at the safety and serviceability of buildings during medium earthquake motions until 1981, when the building code of Japan experienced its largest revision. The new, second phase design for earthquakes is being added to give safety against severe earthquakes [1.4]. Besides, after numerous painful experiences of earthquakes, many countries and organizations had made great effort on estimation of earthquake consequences and the mitigation of these consequences [1.5]. Considering the balance between seismic performance and economy, based on considerable researches conducted all over the world, several modern representative building codes such as ISO 3010 [1.6], IBC code [1.7], Euro code [1.8], and ASCE code [1.9], introduced almost identical seismic design criteria for the structures located in earthquake-prone regions.

In current seismic design procedures, two limit states should be considered for building structures to protect the life and property of the occupants against earthquake motions, life safety and damage limitation [1.10]. To satisfy the life safety limit state, the engineer should design the building such that neither the entire building nor an individual story collapse. The damage limit state aims to prevent and control damage to the building, though some permanent deformation to energy dissipating devices is acceptable. Even if some damage occurs, the building must still satisfy the life-safety limit state during a subsequent earthquake.

Fig. 1.1-1 Damaged ductile concrete building in major earthquakes [1.16-1.19]

The above-mentioned limit states were simply summarized and applied as the performance objectives of seismic design code in China (GB 50011-2001) [1.11], which was “no damage at minor earthquakes, repairable damage under moderate earthquakes, and no collapse under severe earthquakes”. To achieve these objectives, the RC structures were required to remain elastic condition without any severe structural defects after minor earthquake, and even with serious damage under a major earthquake, the structures should not collapse and exhibit ductility during or/and after devastating earthquake [1.12]. Therefore, the ductile concrete structures had been concerned as the favorite seismic resistance solution in the last decades. However, recently, the earthquake engineering community has been reassessing the seismic design procedures, in the wake of devastating earthquakes which caused extensive damage, loss of life and property (Hyogo, Japan, 17 January 1995; $ 150 billion and 6,000 deaths; Sichuan province, China, May 12 2008; $ 150 billion and 69,000 deaths; Gorkha, Nepal, 25 April 2015; $ 20 billion and 9,000 death) [1.13-1.15]. Structural engineering community had to face a new challenge, as can be seen in Fig. 1.1-1, these ductile concrete buildings had to be demolished due to their large residual deformation even they did not collapse during major earthquake. To reduce the cost of recovery and reconstruction, and to make sure the buildings and infrastructures maintains sufficient resistance to intense aftershocks after a major earthquake, a new solution is urgently necessary.

Professor Sun has proposed an alternative, referred to as drift-hardening structure, with higher seismic performance than simple life safety [1.20], aiming at the improvement of the performance objectives for current seismic design codes, from the original one to “no damage at moderate earthquakes, repairable damage under severe earthquakes”. As shown in Fig. 1.1-

2, comparing with conventional ductile structures, this new solution exhibits two improved seismic performances:
(1) drift hardening capability, which implies stable response without degradation in lateral resistance up to large drift level. In other words, the structural system should have a positive secondary stiffness till large deformation.
(2) controlled residual deformation after having experienced large deformation induced by devastating earthquake, which is expressed by the so-called resilience in hysteresis and means high reparability and low repairing cost.

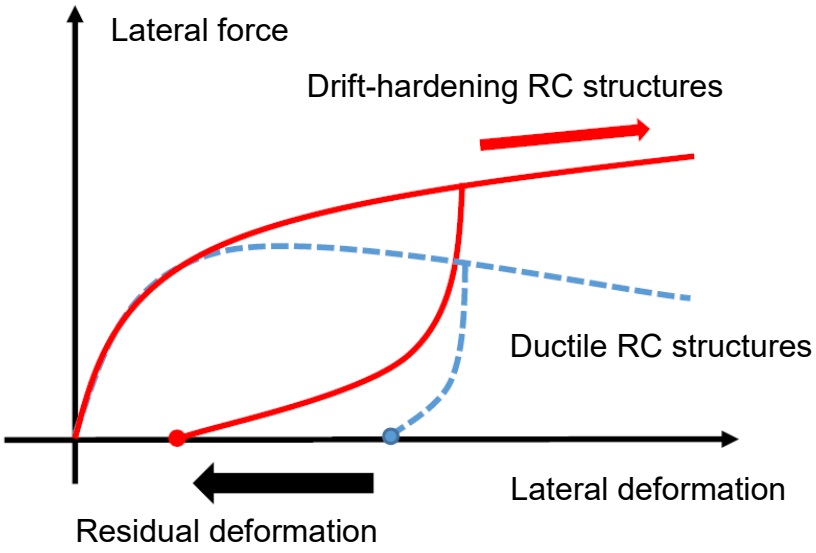

Fig. 1.1-2 Comparison between ductile structures and drift-hardening structures

In order to provide concrete members resilience and drift hardening capability, Sun and his research team have conducted experimental and theoretical works on seismic behavior and design of drift-hardening concrete structures since 2009 [1.21], obtaining several important results on the improved seismic behavior of drift hardening concrete columns. On the other hand, the study about drift hardening shear walls is still at the initial stage since 2018 [1.22], and pointing out several problems remained to be fixed. These results and problems will be reviewed in the next sections along with the previous works by other researchers.

1.2 Previous studies on resilient concrete shear walls

Reinforced concrete (RC) shear walls are a common and cost-effective way of providing lateral force resistance to buildings in seismic areas around the world. Conventional RC shear walls are properly designed to have a ductile response under design level earthquakes in order to absorb the input earthquake energy, which leads to significant residual drift and damage accumulated at the wall base plastic hinge region after the earthquake [1.23]. However, structures with large residual drifts were found to be difficult to repair after earthquakes, which inevitably leads to high repair cost and business downtime [1.24]. Hence, the cost of

consequences of structural damage after an earthquake is significant to the building's owners.

To reduce residual drift of concrete wall structural systems after sever earthquake, Priestley and Tao [1.25] first proposed the idea of utilizing unbonded post-tensioned (PT) tendons to enhance the beam-column joint, which provided RC frame structures improved resilience. This effective method had been widely applied to fabricate RC shear walls as illustrated in Fig. 1.2-1(1) [1.26]. Lu et al. introduced a new design form, in which the separating steel plates were used as bottom slits in the shear wall to weaken the connection at the wall-foundation joint so that the cracks could be easily formed at the joint by the guild of the steel plates. Because the inelastic deformation was primarily concentrated at the wall-foundation joint, the tension deformation and strain of the wall panel was significantly reduced to protect the wall from being damaged. The main measured results are shown in Fig. 1.2-1(2), comparing with conventional specimen SW0, since pre-stressed steel tendons were used to provide extra vertical restoring load to achieve self-centering capacity of specimen SW1-1, this method eliminated the residual strain of the reinforcements crossing the wall-foundation joint. However, as apparent in Fig. 1.2-1(2), the method by Lu et al. did not, if any, enhance the lateral resistance force of concrete shear wall.

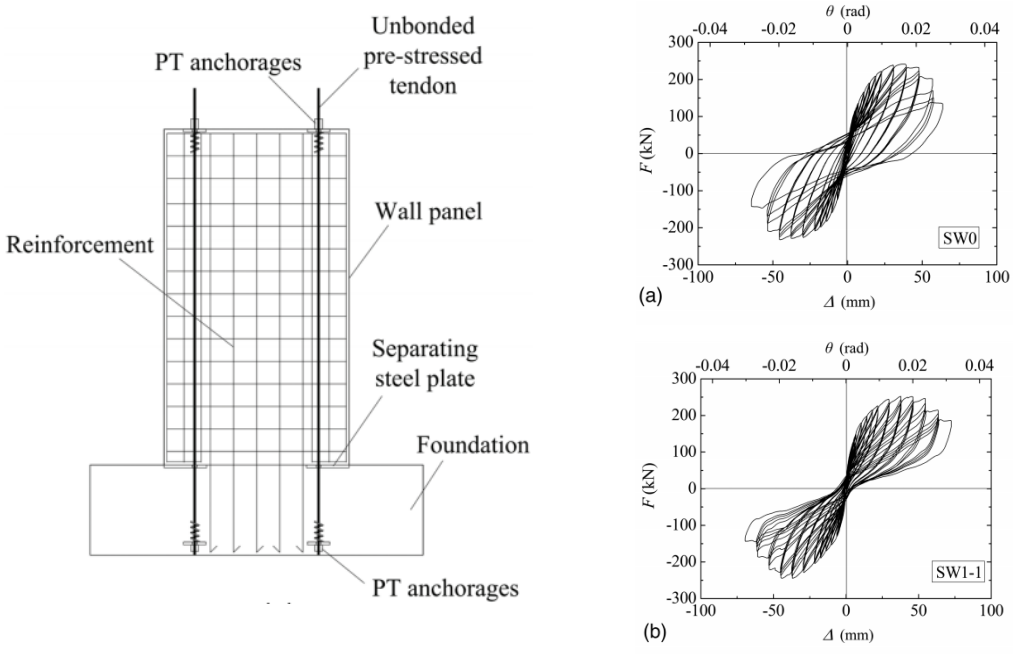

(1) Schematic of specimen (2) Comparison of test results

Fig. 1.2-1 Self-centering shear walls with post-tensioned (PT) tendons [1.26]

Instead of utilizing pre-stressed tendon at boundary zones of RC shear wall, José I et al. conducted experiments about specimen which was confined by unbonded pre-stressed strands with a high tensile strength of 1435Mpa, which located at the middle of wall panel [1.27]. The test result (see Fig. 1.2-2) indicated that the lateral response kept increasing along with drift ratio, and that the residual deformation was also controlled under an extreme low level. On the other hand, the hysteresis loop exhibited low energy dissipation characteristics, and severe damage of concrete was observed at the wall toe due to insufficient reinforcement.

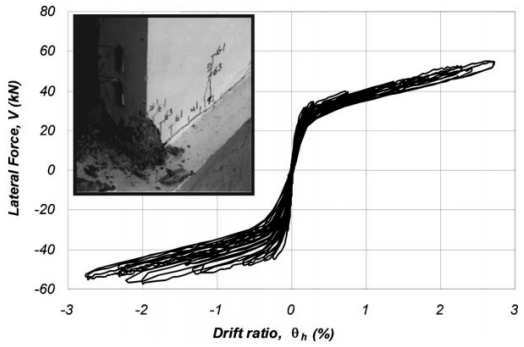

Fig. 1.2-2 Hysteresis response for self-centering specimen with photo of wall toe taken at end of testing [1.27]

Another technology of making resilient concrete members is to utilize non-bond high strength reinforcing bars. Nayera Mohamed et al. [1.28] conducted research about a concrete shear wall totally reinforced with V-ROD GFRP bars [1.29], which had an elastic modulus of 65.1 Gpa and guaranteed tensile strength of 1372 Mpa. Experimental results indicated that the FRP reinforced shear wall experienced less crack width than that experienced in steel reinforced shear wall due to the absence of yielding in the FRP bars. As shown in Fig. 1.2-3(a), The GFRP bar reinforced walls exhibited a reasonable stability of stiffness without strength degradation during reversed cyclic loading. However, the GFRP bar could not ensure a ductile behavior to the wall and is relatively weak to compression, and brittle failure mode with abrupt decrease of lateral resistance might occur due to compressive rupture of GFRP bars at large deformation as illustrated in Fig. 1.2-3(b), which should be completely avoid in a seismic resistance system.

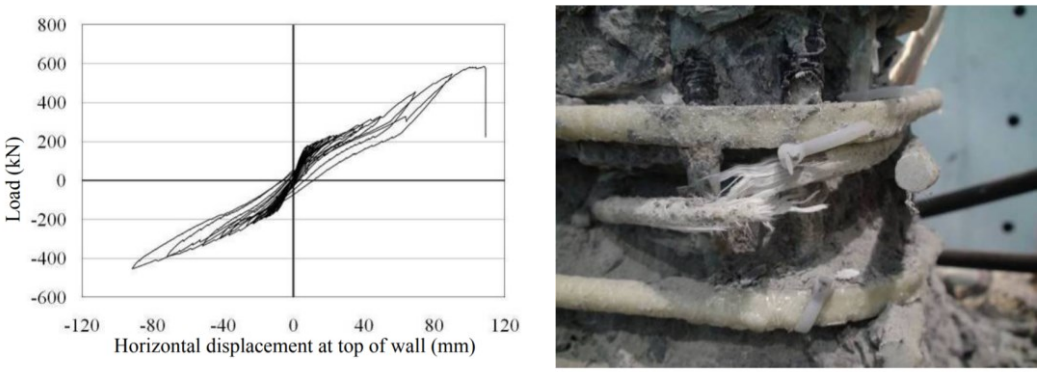

(a) Lateral load-displacement response (b) GFRP stirrups cut

Fig. 1.2-3 GFRP reinforced concrete shear wall [1.28].

Yuan W et al. [1.30] introduced another simple and effective method to provide concrete walls drift hardening capability, in which high strength PC strands were utilized as the longitudinal reinforcing bars placed in the edge zones of wall panel instead of general normal-strength deformed rebars. Measured results proved that the PC strands with high tensile strength but low bond strength could bring the shear wall positive secondary stiffness up to drift level of about 2.5% as shown in Fig. 1.2-4(a), and control the residual crack width of concrete walls under a relative low level. On the other hand, as shown in Fig. 1.2-4(b), insufficient transverse reinforcement in the wall panel may deteriorate the constraint of concrete to PC strands and

result in premature untwisting and buckling of them.

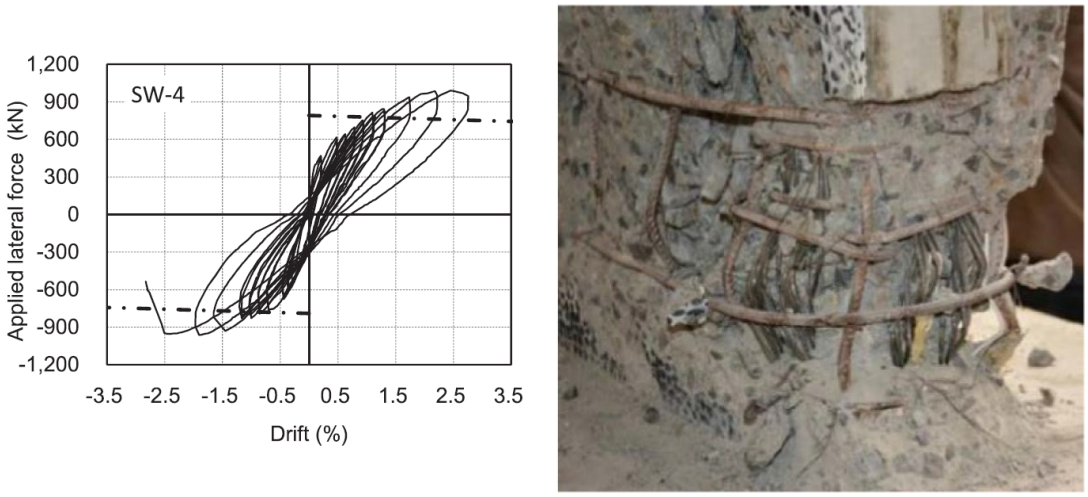

(a) Lateral force-drift responses (b) Photos of wall toe taken after testing

Fig. 1.2-4 PC strands reinforced concrete shear wall [1.30].

Sun et al. proposed an effective method to avoid the above-mentioned problems involved with the post-tensioned and un-bonded reinforcements, by simply replacing the conventional normal-strength rebars with ultra-high strength but low bond strength bars (SBPDN 1275/1420) as longitudinal reinforcing bars placed in the edge zones (referred as concentrated rebars) of shear wall. Previous research proved that due to the spiraled groove on the surface of SBPDN steel bar, its bond-strength is reduced to about one-fifth of that of deformed bar [1.31].

Based on their experimental results, Sun et al. have confirmed that utilizing SBPDN steel bars as the concentrated rebars of concrete shear walls, regardless of arrangement in Δ type or in parallel type [1.22, 1.32], could improve seismic response and reduce residual deformations after unloading from large displacements of RC shear wall in comparison with conventional reinforcement.

Fig. 1.2-5 shows comparison of lateral load versus drift ratio relationships of two concrete, shear walls, the only difference between them was that one was reinforced by normal-strength deformed rebars (SD345) and the other by SBPDN bars as their concentrated rebars. It is obvious in Fig. 1.2-5 that utilization of SBPDN rebar in concrete shear walls can significantly reduce residual deformation, meanwhile it can keep increasing lateral resistance force up to large drift [1.22]. However, because the flexure strength of the walls can be greatly enhanced by SBPDN rebars, here came along with a problem that brittle shear failure is more likely to occur if the shear reinforcement is not sufficient.

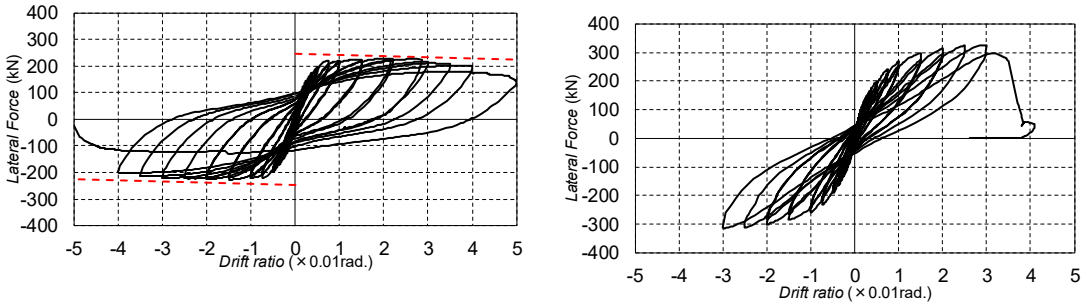

(a) Reinforced by ordinary bars (b) Reinforced by SBPDN bars.

Fig. 1.2-5 Comparison of lateral force versus drift ratio relationships [1.22]

1.3 Studies on precast RC walls

Construction industry had taken the responsibility of saving massive lives and properties from devastating disasters such as earthquakes, tsunamis, storms, and floods [1.33], and brought great massive wealth to developing countries. On the other hand, the construction industry caused serious environment problems tending to hinder sustainable development. Within the global development context, the environmental impact of construction activities is significant. Although the embodied greenhouse gas (GHG) emissions were limited by the Kyoto Protocol, the construction industry continues to generate 40–50% of all global GHG emissions [1.34]. According to the Environmental Protection Agency (EPA), the construction industry is responsible for 38% of the entire carbon dioxide (CO_2) emissions of the United States [1.35]. Furthermore, the cement industry produces 5% of world's GHG emissions [1.36]. Consequently, it is not enough to build efficiently and safely, construction should save non-renewable natural resources and respect the environment.

For concrete structures, savings in CO_2 emissions can be achieved not only by recycling and using novel materials, such as low-carbon cements and clinker substitutes, but also by decreasing the unit CO_2 emissions of each structural component in the design stage and construction processes, like the precast (PC) construction method [1.37]. PC engineering is defined as a process of transporting the manufactured concrete member to a construction and civil-engineering site and assembling it properly. It is widely used in construction sites, especially in counties developing rapidly like China due to its easy process management and great constructability. Moreover, PC structures are perceived as the future of construction engineering because of the shortening of the construction period, quality improvement, decrease in accidents, and eco-friendly concrete option that it provides to the construction industry [1.38].

However, in seismically active regions, the use of precast concrete structural systems has primarily been limited to low rise structures [1.39]. The main reason for their exclusion from use in medium and high-rise applications is the lack of knowledge of how this type of construction will perform under seismic loading conditions. Besides, at the horizontal connection of wall-base joint, both shear and vertical forces must be transferred, so the connector plays a dominant role in the seismic performance of precast shear wall.

Khaled A S. et al. [1.40] conducted an experiment to prove the effect of welded connector, which is shown in Fig. 1.3-1(a), on the seismic performance of precast RC shear wall, and the measured result is indicated in Fig. 1.3-1(a). It can be seen that this joint method provided precast concrete wall great ductility without decrease of shear resistance till large deformation. On the other hand, yielding of the steel connector led to large residual deformation, and the shear failure at the wall-base joint exhibited a brittle ultimate status.

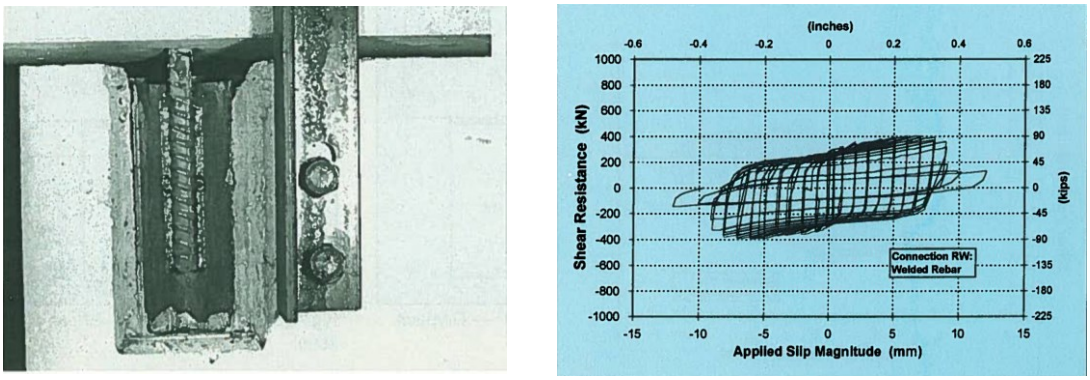

(a) Reinforcing bar with welded connection

(b) shear resistance vs. slip behavior

Fig. 1.3-1 Precast RC shear wall with horizontal welded connection [1.40]

Peng et al. [1.41] proposed a simply joint method as shown in Fig. 1.3-2 (a), in which the longitudinal steel bars in the precast concrete walls were connected by a steel sleeve using mortar, and test results indicated that the mortar–sleeve splicing effectively transferred the stresses on the vertical steel bars. Fig. 1.3-2 (b) displays the effect of the proposed method on the lateral force versus lateral deformation relationships, one can find that the precast specimen exhibited almost same lateral response till drift ratio of 0.013 rad. However, the connector significantly affected the wall response and caused a concentration of strains in the rebars just outside the splice, significantly affecting the deformation capacity of the wall. Due to the weak confinement effect in the region near the steel sleeve, the deformation capacity of the precast shear wall was significantly reduced, compared with the cast-in-place shear wall. Therefore, placing a rebar splice in the critical region of the wall should be avoided.

Xiao et al. introduced a disc spring (DS) device to improve the self-centering capability of precast RC shear wall, which is indicated in Fig. 1.3-3 (a). The experimental results shown in Fig. 1.3-3 (b), demonstrated that the friction material of this DS device exhibits stable and satisfactory energy dissipation, and all the designed DS devices provided precast shear walls good self-centering capability and stable energy dissipation. On the other hand, the lateral resistance force at large deformation became unstable, and the complicated construction procedure of the device involved considerably more time and economic costs.

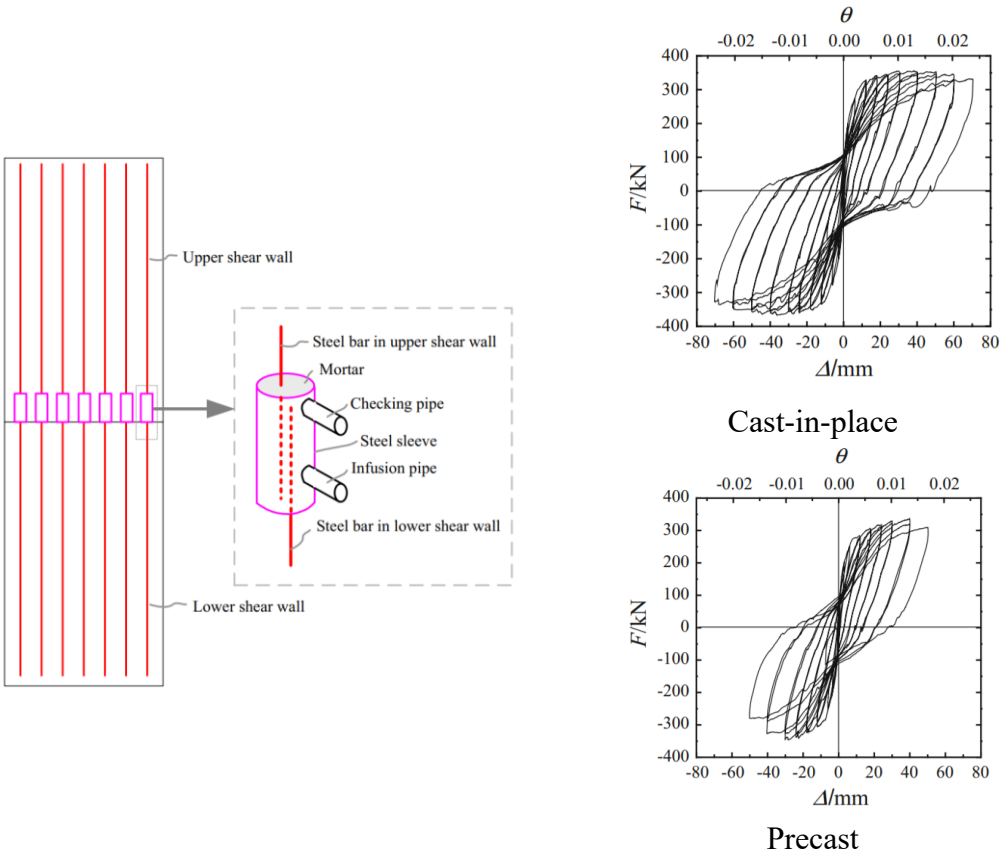

(a) Steel sleeve with mortar (b) Hysteretic curves

Fig. 1.3-2 Precast RC shear wall with steel sleeve connector [1.41].

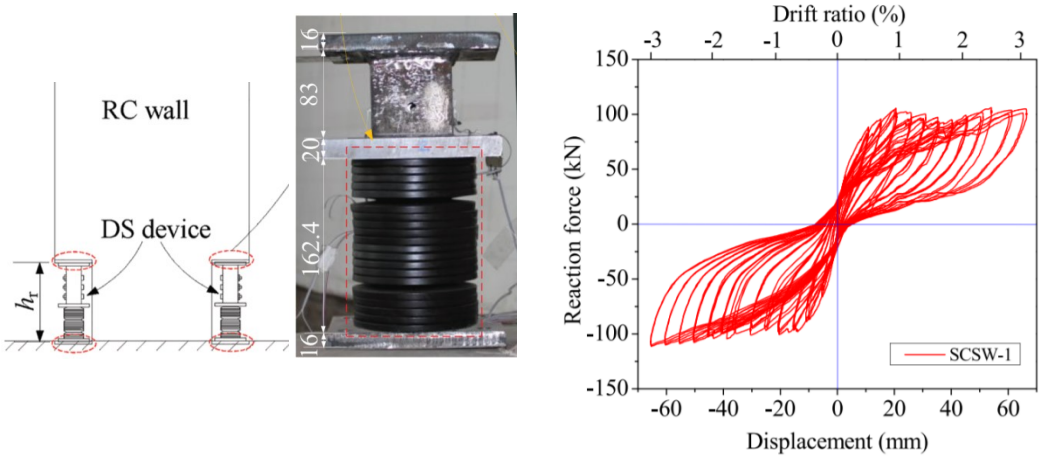

(a) Schematic of DC system (b) Hysteretic response

Fig. 1.3-3 Precast RC shear wall with steel sleeve connector [1.42].

To fully take the advantages of both the SBPDN rebars and the precast construction method, and for the purpose of providing potential solution for the above-mentioned problems. A simplified connection method at the wall-base joint is required, to ensure precast RC shear walls large resilience or drift hardening capability.

1.4 Studies on numerical modelling of concrete components

Along with development of innovative structures with new materials and new construction technologies, structural engineering community has also developed many analytical methods to predict seismic behavior and/or to evaluate ultimate capacities of the new concrete components [1.43]. Studies on new construction technology led to a better understanding of the cyclic behavior of self-centering concrete components. However, even with these enhanced methods, there is still limited information on the non-linear dynamic response of self-centering structure systems [1.44].

Christopoulos et al. [1.45] studied self-centering single-degree-of-freedom (SDOF) systems with various ranges of post-yielding stiffness and hysteretic energy dissipation capacity by introducing the concept of particular post-tensioned energy dissipating (PTED) system. The PTED system incorporates high strength post-tensioned (PT) bars to remain elastic during earthquakes, and confined energy-dissipating (ED) bars to yield both in tension and compression. Fig. 1.4-1 indicated an idealization of the flag-shaped hysteretic behavior of the PTED system, which is easily amenable to numerical modelling. The overall response, of the system can be decomposed into the non-linear elastic contribution from the PT-bars and the bilinear elasto-plastic hysteretic contribution from the ED-bars. However, compared with conventional RC shear walls, self-centering RC shear walls have a larger drift capacity, so inelastic deformations as well as residual drifts are expected to occur in such a system, the idealized model tends to underestimate the residual deformation.

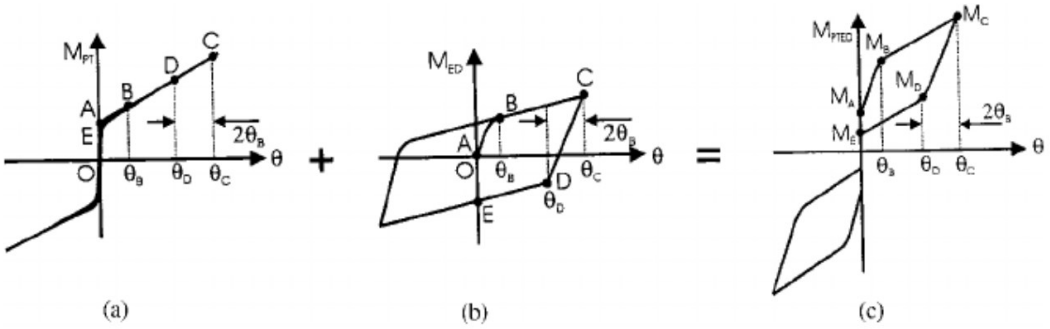

Fig. 1.4-1 Idealized hysteretic behavior of the PTED system [1.45].

Sina Basereh et al. [1.46] used three-dimensional (3D) finite element (FE) modeling to retrofit the analysis of self-centering RC shear walls under lateral cyclic loading. And as shown in Fig. 1.4-2, the improved analysis results predicted very well with the measured ones in the aspects of relative energy-dissipation ratio, lateral strength, residual displacement, and secant stiffness per cycle. Nevertheless, the FEM requires great efforts to prepare the input data and to analyze the output results, and may increase design cost significantly.

To promote reliable design and construction of buildings with innovative RC members, a reliable, accurate, and relatively simple design method is required. Sun and his research group [1.47] have developed an integrated method to evaluate seismic performance of RC components,

covering the effect of bond slippage of weakly bonded high-strength rebars and the confinement effect by transverse reinforcement, and providing the currently best option to study seismic behaviors of drift hardening RC shear walls.

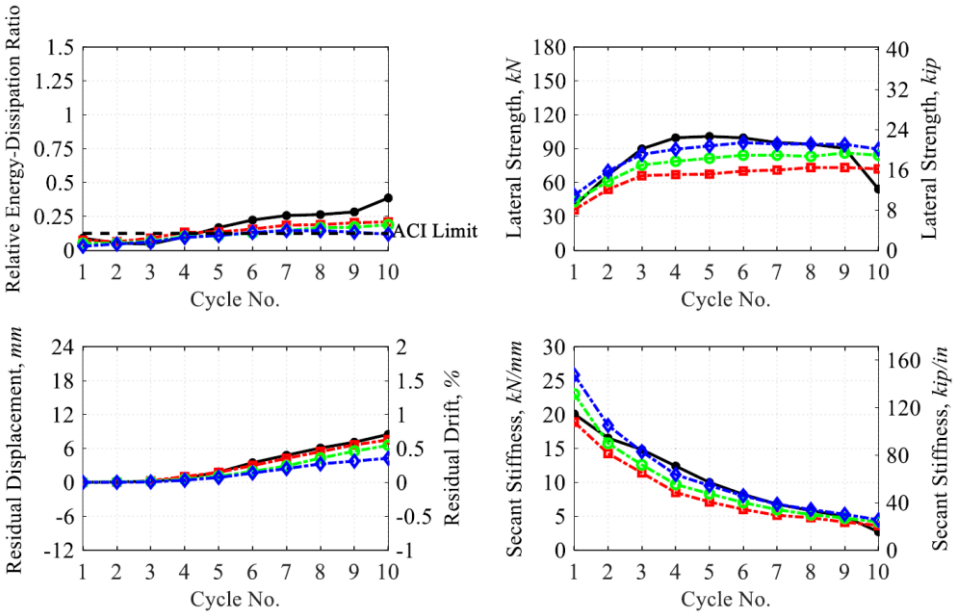

Fig. 1.4-2 Comparison of experimental results and analysis results of FEM [1.46]

1.5 Problems and research objectives

Based on the above-mentioned backgrounds and literature review, and comparing with previous researches, one can see that the utilizations of SBPDN steel bars as the longitudinal reinforcing bars at the edge zones of wall panel is an effective and simple way to make resilient or drift hardening concrete shear walls. However, in order to promote the application of drift hardening concrete (DHC) walls, there are still several important issues needed to be addressed as described below:

1) Effects of shear span ratio on seismic performance of DHC walls: The pilot study on seismic behavior of DHC walls by Sun et al. focused on verifying effectiveness of the use of SBPDN bars in shear walls with shear span ratio of 2.0. However, it is well known that seismic behaviors of concrete walls are strongly influenced by several structural factors, the most important one of which is the shear span ratio. To better understand seismic performance of DHC walls reinforced by SBPDN bars, therefore, it is necessary to clarify the effect of shear span ratio on the seismic performance of the walls.
2) Influence of placement detailing of distributed longitudinal reinforcement in wall panel on seismic properties of DHC walls: The previous study confirmed that because the flexure strength of DHC walls could be greatly enhanced by SBPDN rebars, brittle shear failure might occur at large drift if the shear reinforcement in wall panel is not sufficient. Furthermore, the buckling of distributed longitudinal bars in wall panels caused severe damage of concrete at the wall toe, which limited the drift-hardening capability. Hence, a

new placement method of the distributed longitudinal reinforcement in wall panel is desirable to avoid premature buckling of the longitudinal bars as well was shear failure of the DHC walls.

3) Feasibility of the precast DHC walls: With the demand of precast construction method increasing rapidly, the understanding of seismic behaviors for precast concrete walls reinforced with SBPDN bars is scarce. To fully take advantages of the combination of using SBPDN rebars and precast construction method, simple and reliable joint between the walls and foundations needs to be developed, and information on the seismic behavior of precast DHC walls is desirable.
4) Development of evaluation method for seismic capacities of DHC walls: Though numerous seismic evaluation methods have been proposed, it is not clear if these methods can be applied to DHC walls. In particular, for concrete walls, influence of shear deformation and plastic hinge length on overall cyclic behavior of the walls remains unclear.

Objectives of this doctor thesis are, 1) to obtain and present more experimental information on seismic performance of the rectangular concrete walls reinforced by SBPDN rebars, 2) to experimentally investigate the effect of shear span ratio on seismic performance of concrete walls reinforced by SBPDN rebars, 3) to verify the effectiveness of a new placement method of distributed longitudinal bars in the wall panel, 4) to propose a new type of anchorage for SBPDN rebars used in precast DHC walls and verify the effectiveness of the proposed anchorage, and 5) to propose an evaluation method for cyclic response of DHC walls by modifying the method proposed by Sun et al through taking the effects of shear deformation and placement detailing of the distributed longitudinal bars in the wall panel into consideration.

1.6 Format of this thesis

This dissertation consists of six chapters, and key points of each chapter are summarized as below:

The first chapter introduces backgrounds of this dissertation, reviews previous researches in the literature, and describes research objectives of this study.

In chapter two, a new arrangement of the distributed longitudinal (DL) normal-strength bars in the wall panel was proposed to avoid premature buckling of the DL bars as well as shear failure of concrete walls reinforced by SBPDN rebars. The primary objectives of this chapter are: 1) to obtain experimental information on seismic behaviors of the rectangular concrete walls reinforced by SBPDN rebars and/or normal-strength rebars as concentrated rebar, 2) to verify the effectiveness of the new arrangement method for DL bars, and 3) to investigate the influence of shear span ratio (a/D) and axial load ratio on the seismic behaviors of the concrete walls reinforced by SBPDN rebars. To achieve these goals, a total of six 1/3-scale cantilever rectangular concrete walls were designed, fabricated, and tested under reversed cyclic lateral loading while subjected to constant axial load. The experimental variables included, 1) steel type of the concentrated rebars (SBPDN bar and normal-strength bar), 2) the axial load ratio (0.15, 0.75), 3) the arrangement of longitudinal rebars, and 4) the shear span ratio (1.5, 2.0 and

2.5).

Chapter three presents experimental study on seismic performance of precast concrete walls with their SBPDN rebars being anchored into foundation beams through a simple connecting method. To verify if the use of SBPDN rebars can provide precast concrete walls the same drift-hardening capability as the cast-in-site concrete walls, five 1/3-scale cantilever rectangular concrete walls were fabricated by the proposed connecting method, and tested under reversed cyclic lateral loading while subjected to constant axial load. The experimental variables included, 1) the shear span ratio (1.5 and 2.0), 2) the axial load ratio (0.15, 0.075), and 3) the diameter of sheath ducts (120 mm and 100 mm) that accommodate the end anchorage portions of SBPDN rebars.

Chapter four is intended to experimentally verify effectiveness of a new anchorage method for SBPDN rebars of precast walls reinforced by SBPDN rebars. The new anchorage method differs from that adopted in the test walls described in chapter three. In the new method, the end portion with a certain length of SBPDN rebars have roll threaded screw instead of using nuts and bolts to prevent the slippage of SBPDN rebars. The experimental variables included the shear span ratio (1.5 and 2.0) and the length of threaded screw at the end portion of SBPDN rebars.

Chapter five deals with numerical analysis of seismic behavior of concrete walls reinforced with SBPDN rebars. A numerical analysis method is developed by modifying the method proposed by Sun et al, covering the effects of shear deformation, plastic hinge length, and placement of distributed longitudinal bars in wall panel. To verify validity and accuracy of the refined analytical method, the theoretical predictions by the refined method are compared with the measured results in terms of hysteresis loop, residual drift ratio, and the axial strain of concentrated rebars. Besides, it is also discussed whether the current code-prescribed design equations can be applied to predict the ultimate lateral capacities of the walls with SBPDN rebars.

Chapter Six summarizes the conclusions obtained through Chapter Two to Chapter Five, and presents several suggestions to deal with the problems remained to be solved.

References

[1.1] Elnashai Amr S., Luigi Di Sarno., “Fundamentals of earthquake engineering,” John Wiley & Sons, 2015, pp. 469.

[1.2] M. Baradaran Shoraka, “Seismic loss estimation of non-ductile reinforced concrete buildings”, Earthquake Engineering and Structural Dynamic, 2013, Vol. 42, pp. 297–310.

[1.3] Nakano K., Ishiyama Y., and Ohashi Y., “A Proposal of a New Aseismic Design Method for Buildings in Japan”, 7th WCEE Proc., Istanbul, Turkey, 1980, Vol. 4, pp. 41-48.

[1.4] Aoyama H., “Outline of earthquake provisions in the recently revised Japanese building code,” Bulletin of the New Zealand Society for Earthquake Engineering, 14(2), 1981, pp. 63-80.

[1.5] Melkumyan M., Mihul V., Gevorgyan E., "Retrofitting by base isolation of existing buildings in Armenia and in Romania and comparative analysis of innovative vs. conventional retrofitting," COMPDYN 2011, Corfu, Greece, 25–28 May, 2011, pp.1187-1210.
[1.6] International Organization for Standardization (ISO), "ISO 3010 Bases for design of structures – seismic actions on structures", 1988.
[1.7] IS 1893-2002, "Criteria for Earthquake resistant design structures, Part 1 General provisions and buildings," Bureau of Indian Standards, New Delhi, 2002, 45 pp.
[1.8] European Committee for Standardization (CEN), "Eurocode 8 - Design of structures for earthquake resistance - Part 1: General rules, seismic actions and rules for buildings", 2003
[1.9] American Society of Civil Engineering, "ASCE 7-05 Minimum Design Loads for Buildings and Other Structures", 2006
[1.10] Mistumasa M. et al., "Performance-Based Seismic Design Code for Buildings in Japan", Earthquake Engineering and Engineering Seismology, Vol. 4, No. 1, pp. 15- 25.
[1.11] Guqiang Li. et al., "Overview of Performance-Based Seismic Design of Building Structures in China", Seismic Structure Engineering, 2012, pp. 656-661.
[1.12] Hamada M, "Engineering for earthquake disaster mitigation," Springer, Japan, 2014, 328pp.
[1.13] Building Research Institute, "A Survey Report for Building Damage due to the 1995 Hyogoken-Nanbu Earthquake", 222p.
[1.14] "Special Interview about the Revision of Magnitude of the Wenchuan Earthquake" (in Chinese). CEA. May 20, 2008. Retrieved July 13, 2008. https://www.cea.gov.cn/news.asp?id=28352
[1.15] Katsuichiro G. et al., "The 2015 Gorkha Nepal earthquake: insights from earthquake damage survey",
[1.16] https://www.britannica.com/event/Sichuan-earthquake-of-2008
[1.17] https://phys.org/news/2016-06-afterslip-april-nepal-earthquake-buildup.html
[1.18] http://www.sxjz.org/Article.asp?id=4536
[1.19] https://www.britannica.com/event/Kobe-earthquake-of-1995
[1.20] Sun Y. et al. (2006): Analytical Study of Cyclic Response of Concrete Members Made of High-Strength Materials, The Eighth U.S. National Conference on Earthquake Engineering, Paper No. 1581.
[1.21] KITTAKA M. et al., "Experimental Study on RC Columns with Ultra High Strength Rebars (Part 1 Outline of Experiment)", Meeting of Architectural Institute of Japan, Aug. 2009, (In Japanese).
[1.22] Fujitani T. et al. (2018), "Effect of the type of concentrated rebars on seismic performance and evaluation of rectangular RC cantilever shear walls", Proceedings of the JCI, 40(2), pp. 313-318, (in Japanese).
[1.23] Wood S, Wright J, Moehle J. The 1985 Chile earthquake: observations on earth-quake-resistant construction in Vina del. Urbana: University of Illinois at Urbana-Champaign, 1987.
[1.24] Eguchi RT. Et al., "Direct economic losses in the northridge earthquake: a three-year post-event perspective", Earthquake Spectra, 1988, 14:2, pp. 45-64.

[1.25] MJN Priestley, JR Tao Seismic response of precast prestressed concrete frames with partially debonded tendons, PCI journal, 1993, 38(1), pp.58-69.
[1.26] Xilin L. et al., "Experimental Study of Self-Centering Shear Walls with Horizontal Bottom Slits", Journal of Structural Engineering, 2017, Vol. 143(3): 04016183.
[1.27] José I. et al., "Seismic Performance of Self-Centering Structural Walls Incorporating Energy Dissipators", J. Struct. Eng., 2007, 133(11), pp.1560-1570.
[1.28] Nayera M. et al., "Evaluation of a Shear Wall Reinforced with Glass FRP Bars Subjected to Lateral Cyclic Loading", 3rd Asia-Pacific Conference on FRP in Structures, 2012.
[1.29] Pultrall: V-ROD Reinforcing FRP Bars Data Sheet; www.pultrall.com
[1.30] Weiguang Yuan. et al., "Experimental study on seismic behavior of concrete walls reinforced by PC strands", Engineering Structures, 2018, Vol. 175, pp. 557-590
[1.31] Funato Y., Sun Y., Takeuchi T., and Cai G., "Modeling and Application of Bond Characteristic of High-strength Reinforcing Bar with Spiral Grooves," Proceedings of the Japan Concrete Institute, V.34, No.2, 2012, pp.157-162.
[1.32] Fukuhara Y. et al. (2018): Study on ductility of reinforced concrete rectangular shear wall with diagonal reinforcement, Proceedings of the JCI, 40(2), 325-330, (in Japanese).
[1.33] Hamada M, "Engineering for earthquake disaster mitigation," Springer, Japan, 2014, 328pp.
[1.34] CIWMB, Designing with Vision: A Technical Manual for Material Choices in Sustainable Construction, California Integrated Waste Management Board, Sacramento, 2000.
[1.35] J.S. Damtoft, J. Lukasik, D. Herfort, D. Sorrentino, E.M. Gartner, "Sustainable development and climate change initiatives", Cem. Concr. Res., 2008, 38 (2), pp. 115–127.
[1.36] E. Worrell, L. Price, N. Martin, C. Hendriks, L.O. Meida, "Carbon dioxide emissions from the global cement industry", Annu. Rev. Energy Environ, 2001, 26, pp. 303–329.
[1.37] J.K.W. Wong, H. Li, H. Wang, T. Huang, E. Luo, V. Li, "Toward low-carbon construction processes: the visualisation of predicted emission via virtual prototyping technology", Autom. Constr., 2013, 33, pp. 72–78.
[1.38] A. Hasanbeigi, L. Price, E. Lin, "Emerging energy-efficiency and CO2 emissionreduction technologies for cement and concrete production: a technical review", Renew. Sust. Energ. Rev., 2012, 16 (8), pp. 6220–6238.
[1.39] Connections for Precast and Pre stressed Concrete, 2nd Edition, Pre cast/Prestressed Concrete Institute, Chicago, IL, 1977.
[1.40] Khaled A S. et al., "Horizontal Connections for Precast Concrete Shear Wall Panels Under Cyclic Shear Loading", PCI journal, 1996, pp. 64-80.
[1.41] Yuan-Yuan Peng, Jia-Ru Qian, Yu-Hang Wang, "Cyclic performance of precast concrete shear walls with a mortar–sleeve connection for longitudinal steel bars", Materials and Structures, 2016, 49, pp.2455–2469.
[1.42] Shui-Jing Xiao, Long-He Xu, Zhong-Xian Li, "Design and experimental verification of disc spring devices in self-centering reinforced concrete shear walls", Structural Control and Health Monitoring, 2020, Vol. 27(7), e2549.
[1.43] Gulkan, P. and Sozen, M.A., "Inelastic responses of reinforced concrete structures to earthquake motions," ACI Journal, 1974, 71 (12), pp. 604 – 610.

[1.44] Ahmed Ghobarah, “Performance-based design in earthquake engineering: state of development”, Engineering Structures, 2001, Vol. 23, pp.878–884.
[1.45] Christopoulos C, Filiatrault A, Folz B., “Seismic response of self-centering hysteretic SDOF systems”, Earthq Eng Struct Dyn, 2002, Vol. 31(5), pp.1131–50.
[1.46] Sina Basereh. et al., “Reinforced-Concrete Shear Walls Retrofitted Using Weakening and Self-Centering: Numerical Modeling”, J. Struct. Eng., 2020, 146(7): 04020122.
[1.47] Sun YP, Fukuhara T, Kitajima H., “Analytical Study of Cyclic Response of Concrete Members Made of High-Strength Materials,” Proceedings of the 8th U.S. NCEE, San Francisco, USA, 2006; Paper No. 1581.

CHAPTER TWO

Seismic Behavior of Rectangular Concrete Walls Reinforced by Normal-Strength and SBPDN rebars

2.1 Introduction

Ductile reinforced concrete (RC) walls have been widely applied as the main lateral force resisting element for high-rise buildings located in earthquake-prone regions. According to the previous research by Wallace [2.1], sufficient ductility and energy dissipation of ductile RC walls can be achieved in earthquakes of Chile (2010), Japan (2011), and New Zealand (2011) where modern seismic design codes exist. However, due to their high lateral stiffness, ductile RC walls tend to attract large amount of seismic energy and hence to resist large earthquake-induced lateral loads, causing severe damage in potential plastic hinge regions of the walls, and leave large residual deformations that are generally very difficult to be repaired.

In order to meet the enhanced demand on seismic performance of RC structures, Sun et al. [2.2] proposed an alternative RC shear walls exhibit two improved seismic performance: (1) the lateral resistance kept increasing along with drift ratio till large deformation, which is referred as drift hardening capability, and (2) the so-called resilience in hysteresis, which implies the residual deformation is controlled under low level after large experienced drift level, in other words, high reparability and low repairing cost. Fig. 2.1-1 shows schematic lateral force versus drift response of ductile and drift-hardening RC walls.

Since 2010 the revised AIJ Standard for Structural Calculation of Reinforced Concrete Buildings [2.3] has permitted the use of concrete walls with rectangular cross section. Comparing with conventional concrete walls generally consisting of a thin wall web and one or two columns at the web wall edges, the lateral stiffness of rectangular RC walls is relatively low, but the utilization of longitudinal rebars concentrated at the edge zones (referred to as concentrated rebars hereafter) of shear walls can enhance the flexure resistance of shear walls without boundary columns. Fujitani et al. [2.4] have experimentally verified that using the weakly bonded ultra-high strength rebar (referred to as SBPDN rebar) as the concentrated rebars could assure the RC walls drift hardening capability and resilience until large drift level.

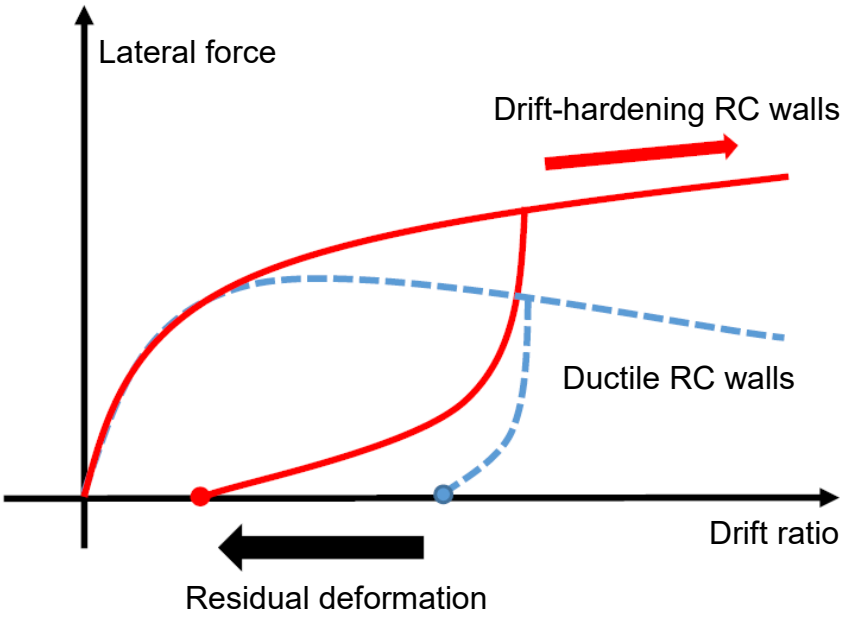

Fig. 2.1-1 Comparison between ductile walls and drift-hardening walls

However, the previous study by Fujitani et al also confirmed that because the flexure strength of the walls can be greatly enhanced by SBPDN rebars, brittle shear failure is more likely to occur at large drift if the shear reinforcement is not sufficient. To avoid premature shear failure of RC walls with SBPDN rebars, a new arrangement of distributed longitudinal (DL) bars in the wall panel. The DL bars were not anchored into the adjacent loading beams so that they do not directly resist the axial stress caused by bending moment and reduce the flexural strength of the wall section. This method is also expected to delay the local buckling of DL bars, to mitigate the damage of concrete near the wall toes, and to prevent shear failure of short walls reinforced with SBPDN rebars.

The primary objectives of this chapter are: 1) to obtain experimental information on seismic behaviors of the rectangular concrete walls reinforced by SBPDN rebars and/or normal-strength rebars as concentrated rebar, 2) to verify the effectiveness of the new arrangement method for DL bars in the wall panel, and 3) to investigate the influence of shear span ratio (a/D) and axial load ratio on the seismic behaviors of the concrete walls reinforced by SBPDN rebars.

2.2 Experimental program

2.2.1 Outlines of test specimens

To achieve the aforementioned goals of this chapter, a total of six 1/3-scale cantilever rectangular concrete shear walls were designed, fabricated, and tested under reversed cyclic lateral loading while subjected to constant axial load. The experimental variables included, 1) steel type of the concentrated rebars, 2) the applied axial load ratio, 3) the arrangement of longitudinal rebars 4) the shear span ratio.

Table 2.2-1 Primary experimental parameters and main test results

Year	Specimen	*a/D*	*n*	f'_c (N/mm^2)	Longitudinal rebars		Concentrated SBPDN rebars		Transverse rebars		Q_{exp}
					Type	ρ_{wv}(%)	Type	ρ_s(%)	Type	ρ_{wh}(%)	(kN)
2017	W20-FD-15	2.0	0.15	31.6	20-D6 Fixed	0.70	8-D13	0.58	D6@65 Height over 300mm	0.65	228
	W20-FU-15			31.8			8-U12.6		D6@45 Height less than 300mm	0.94	320
2019	W15-HU-15	1.5		34.0	20-D6 Not Fixed	0.70			D6@65	0.65	360
	W15-HU-073		0.073	33.9							329
	W20-HU-073	2.0		36.0							253
	W25-HU-073	2.5		35.8							191

a/D: shear span ratio; *n*: axial load ratio; f'_c: concrete cylinder strength; ρ_{wv} : reinforcement ratio of longitudinal rebars; ρ_s: reinforcement ratio of concentrated rebars; ρ_{wh}: volumetric ratio of transverse reinforcement. Q_{exp}: measured maximum lateral force (average);

Fig. 2.2-1 shows the dimensions and reinforcement details of the specimens, while Table 2.2-1 lists the primary experimental parameters along with the main test results. As obvious from Table 2.2-1 and Fig. 2.2-1, all specimens have identical cross section. Each specimen has a rectangular section of 150mm in thickness and 600mm in depth. The specimen of W15-Series had a shear span of 900 mm to give a shear span ratio of 1.5. As for specimens of W20-Series and W25-HU-073, their shear spans were 1200 mm and 1500 mm to give shear span ratios of 2.0 and 2.5, respectively.

The horizontal distributed (HD) bars were placed in a closed form to sustain shear force and provide effective confinement effect. For W20-F-Series, the HD bars were comprised of D6 deformed bars with a spacing of 45 mm for the wall panel with a height less than 300mm, and a spacing of 65 mm for the wall panel with a height over 300mm. As for HU-Series the HD bars with a spacing of 65 mm were applied for the wall panel.

Two kinds of reinforcements were used as the concentrated rebars of the test shear walls. They are SBPDN1275/1420 (U12.6) rebars with high yield strength and low bond strength, and SD345 (D13) deformed bars with normal yield strength and bond strength, both gave the same reinforcement ratio of concentrated rebars about 0.56% to the specimens. Eight SBPDN rebars with nominal diameter of 12.6mm were placed at the edge zones of wall panel for specimen W20-FU-15 and HU-Series, and each SBPDN rebar was anchored to a steel plate (having a thickness of 9mm) by bolts at both ends. While eight SD345 (D13) deformed bars were used as concentrated rebars for specimen

W20-FD-15, and each SD345 (D13) deformed bar was welded and fixed to the 9mm-thick end plate at both ends. In addition, D6 deformed bars with a space of 65mm (less than 6 times the diameter of the concentrated rebars) were applied as transverse confinement to prevent the

initial local buckling of concentrated rebars.

An axial load ratio (n) of 0.15 were applied for specimen W20-FD-15, W20-FU-15, and W15-HU-15, while n = 0.073 for the other specimens.

The longitudinal distributed (LD) bars consisted of twenty D6 deformed bars uniformly placed with a spacing of 59 mm to give a steel ratio of 0.70% for all specimens. While the DL bars of specimens of W20-FD-15 and W20-FU-15 were straightly fixed into both adjacent beams as shown in Fig. 2.2-1 (a) and (b). As for the other specimens of HU-series that is shown in in Fig. 2.2-1 (c), the DL bars were anchored at each end of wall panel with 180-degree hooks. Since the only difference between specimens of HU-Series is their shear span, only the details of W15-HU-15 were shown in Fig. 2.2-1 (c) as an example.

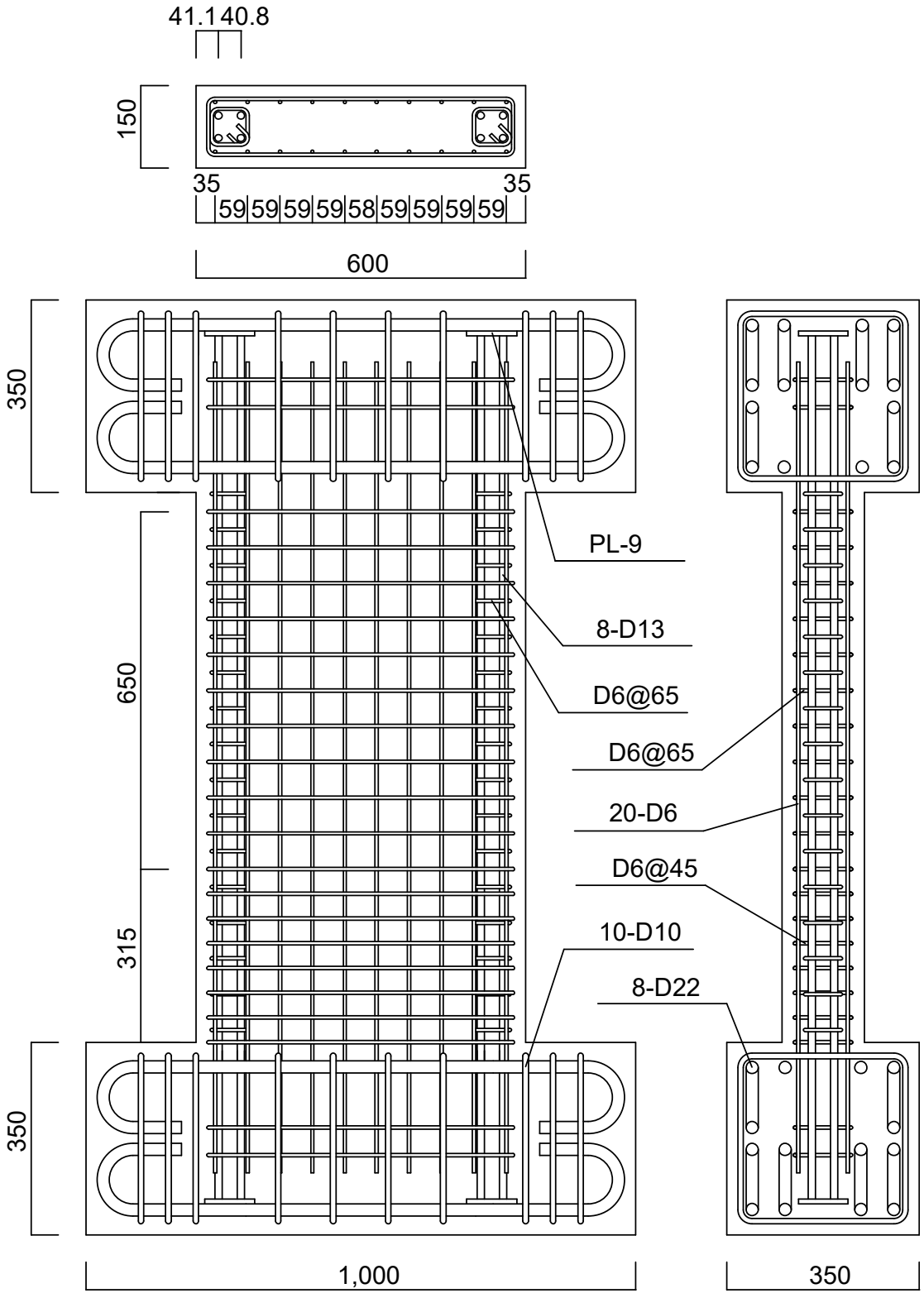

(a) W20-FD-15

Fig. 2.2-1 Reinforcement details of test shear walls (Unit: mm)

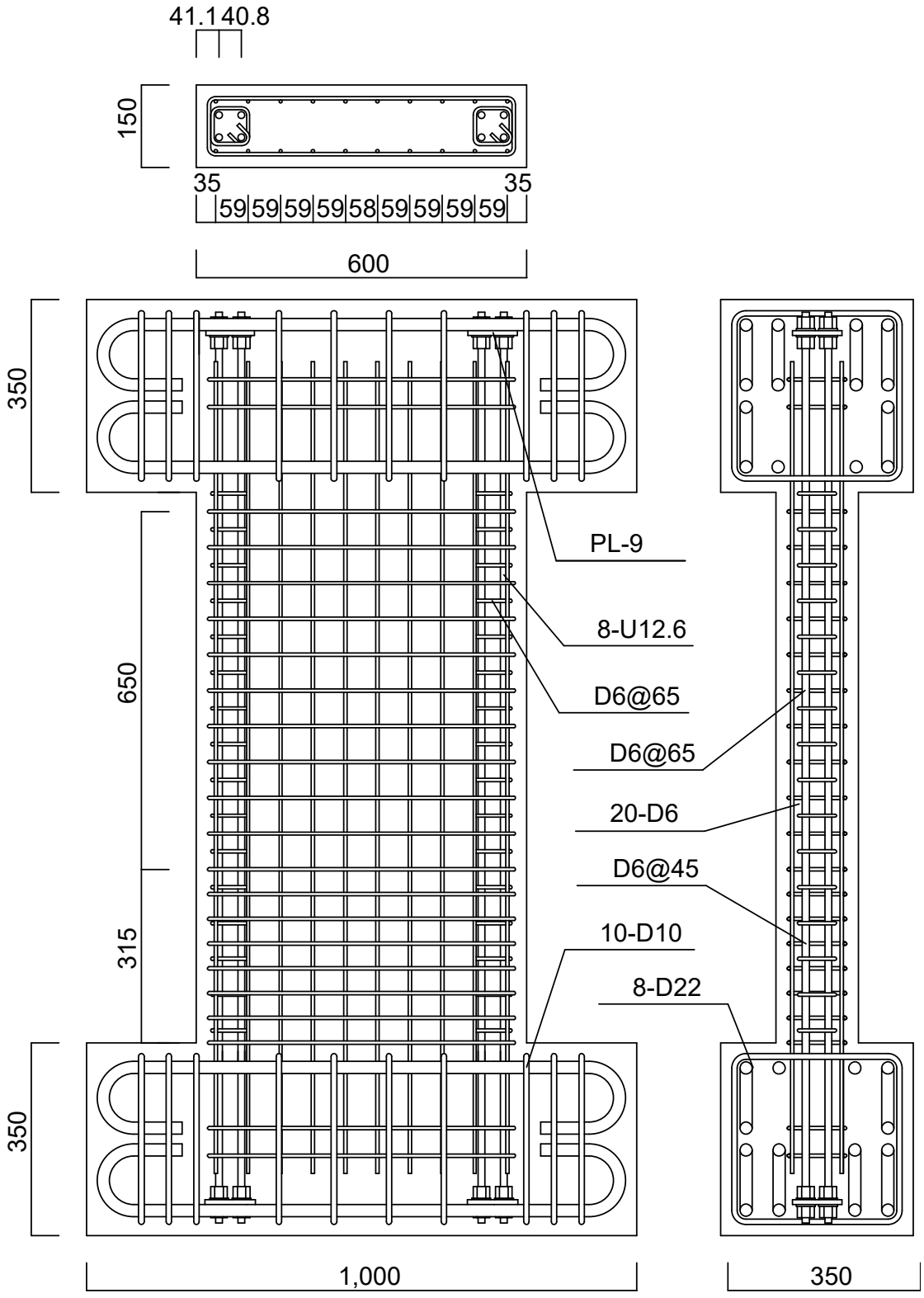

(b) W20-FU-15

Fig. 2.2-1 Continued

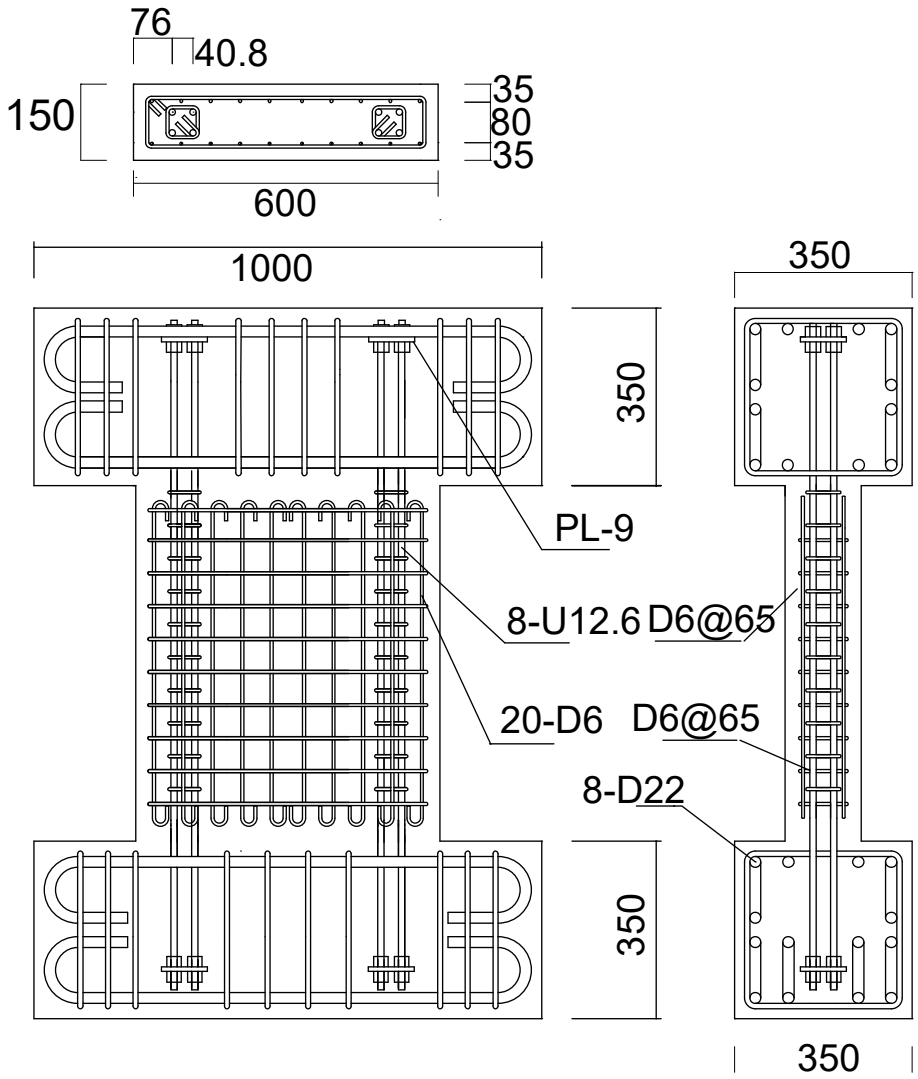

(c) W15-HU-15 and W-FU-Series

Fig. 2.2-1 Continued

2.2.2 Material properties

The ultra-high strength SBPDN 1275/1420 rebar with yield strength of about1380 MPa and spiral grooves on its surface as shown in Fig. 2.2-2 along with conventional SD345 (D13) deformed rebar whose yield strength was 393 MPa. According to previous research by Funato et al. [2.5], the SBPDN rebar has a low bond-strength about 3.0N/mm^2, which is about one-fifth of that of SD345 rebar.

Mechanical properties together with the tensile stress-strain curves of the used steels are summarized in Table 2.2-2 and Fig. 2.2-3 separately. For those who did not exhibit apparent yield plateau in their stress-strain relations, the yielding strengths of them were determined by the 0.2% offset yielding method.

(a) U12.6 (SBPDN1275/1420)

(b) D13 (SD345)

Fig. 2.2-2 Surface of the concentrated rebars

(a) D6 HD rebars (SD295A) 2017

No.	E_s (kN/mm^2)	f_y (N/mm^2)	ε_y (×0.01)	f_u (N/mm^2)	ε_f (×0.01)
No.1	186.51	436.53	0.234	542.63	16.69
No.2	187.16	436.85	0.233	542.31	14.57
No.3	188.22	432.59	0.230	542.63	15.85
Average	187.30	435.32	0.232	542.52	15.70

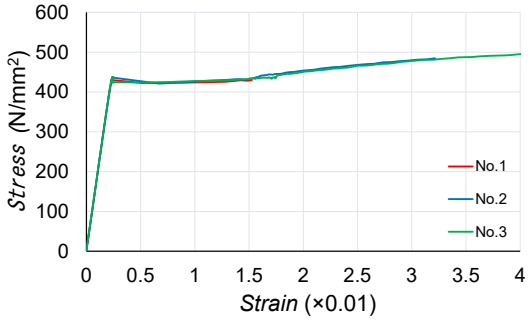

(b) D6 DL bars (SD295A) 2017

No.	E_s (kN/mm^2)	f_y (N/mm^2)	ε_y (×0.01)	f_u (N/mm^2)	ε_f (×0.01)
No.1	199.67	436.85	0.219	548.63	18.51
No.2	197.42	439.69	0.223	560.31	18.99
No.3	191.02	426.59	0.223	538.21	19.81
Average	196.04	434.38	0.222	549.05	19.11

※0.2% offset method was used for No.2 only.

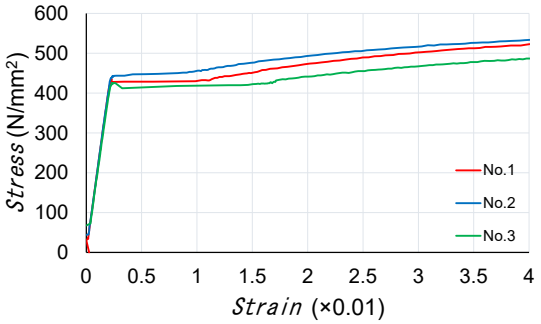

(c) D6 rebars (SD295A) 2019

No	E_s (kN/mm^2)	f_y (N/mm^2)	ε_y (×0.01)	f_u (N/mm^2)	ε_f (×0.01)
No.1	191.83	403.9	0.211	527.3	18.5
No.2	189.69	392.5	0.207	519.6	16.4
No.3	193.67	408.7	0.211	524.8	18.5
Average	191.73	401.69	0.209	523.89	17.8

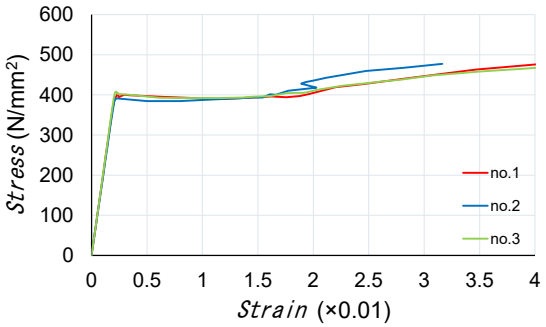

Table 2.2-2 Mechanical properties of the steels

Fig. 2.2-3 Stress-strain relationships of the steels

(d) D13 (SD345) 2017

No.	E_s (kN/mm^2)	f_y (N/mm^2)	ε_y (×0.01)	f_u (N/mm^2)	ε_f (×0.01)
No.1	184.19	387.69	0.210	573.16	17.66
No.2	164.93	398.58	0.242	570.32	15.44
No.3	167.11	391.32	0.234	568.90	15.60
Average	172.08	392.53	0.229	570.80	16.23

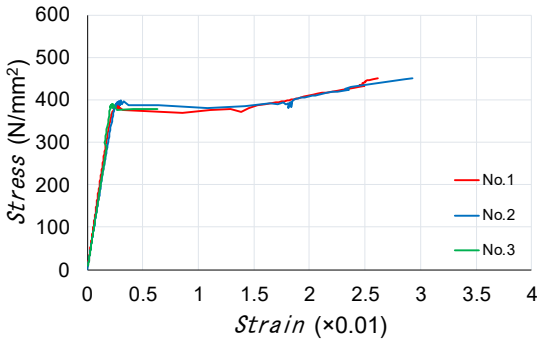

(e) U12.6 (SBPDN1275/1420) 2017

No.	E_s (kN/mm^2)	f_y (N/mm^2)	ε_y (×0.01)	f_u (N/mm^2)	ε_f (×0.01)
No.1	214.75	1380.85	0.843	1472.80	9.56
No.2	216.01	1382.86	0.840	1476.00	9.87
No.3	218.54	1378.04	0.831	1472.00	—
Average	216.44	1380.59	0.838	1473.60	9.71

※ 0.2% offset method were used.

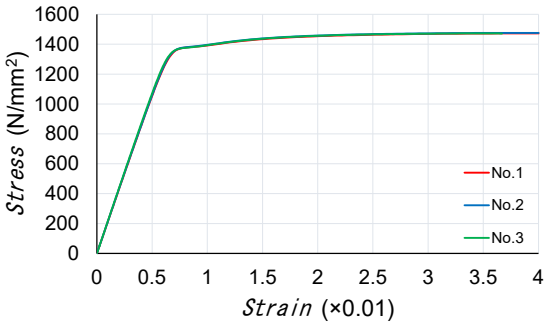

(f) U12.6 (SBPDN1275/1420) 2019

No	E_s (kN/mm^2)	f_y (N/mm^2)	ε_y (×0.01)	f_u (N/mm^2)	e_f (×0.01)
No.1	217.40	1398.07	0.843	1465.28	—
No.2	215.40	1391.17	0.846	1468.00	—
No.3	217.10	1391.70	0.841	1466.56	—
Average	216.63	1393.65	0.843	1466.61	—

※0.2% offset method were used.

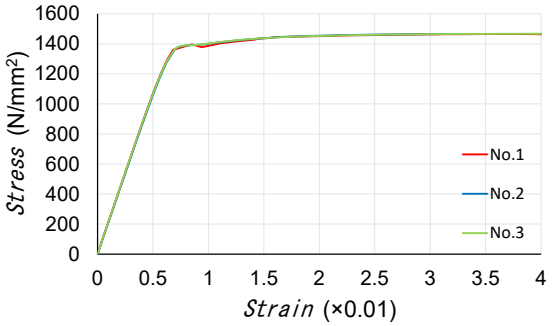

Table 2.2-2 Continued

Fig. 2.2-3 Continued

Note

E_s : Young's modulus
f_u : ultimate stress
f_y : yield stress
ε_f : coefficient of expansion
ε_y : yield strain

Ready-mixed concrete made of Portland cement and coarse aggregates with maximum particle size of 20mm was used to fabricate the specimens. Table 2.2-3 shows the mix proportions of concrete along with measured slumps and air contents. Concrete strengths were evaluated at the same day of loading by testing three standard cylinders (diameter: 100mm, height: 200mm), which were cured under the same condition to the shear walls, and test results are shown in

Table 2.2-1 for each specimen.

Table 2.2-3 Mix proportions for concrete

Year	W/C	Water (kg/m^3)	Cement (kg/m^3)	Fine aggregate (kg/m^3)	Coarse aggregate (kg/m^3)	Additives	Slump (mm)	Air content (%)
2017	0.57	188	330	858	886	3.3	212	3.8
2019	0.57	180	316	869	882	2.94	212	3.8

2.2.3 Test setup and loading program

The experiments were conducted using the setup shown in Fig. 2.2-4. The loading apparatus was designed to subject the shear wall to reversed cyclic lateral load and constant axial compression. A vertical hydraulic jack with a capacity of 1000 kN, which was connected to stiff loading frame via a roller, was used to apply constant axial compression. The reversed cyclic lateral load was applied by two 500 kN horizontal hydraulic jacks. The lateral loading was controlled by drift ratio (R), which is defined as the ratio of the lateral displacement at the loading point of lateral force (Δ) to the shear span (a) of each shear wall. Due to the limitation in the stroke length of the horizontal loading jacks, the west direction was applied as the initial tensile direction or the plus direction for specimen W20-FD-15, W20-FU-15, and W15-HU-073, while for specimen W20-HU-073, W25-HU-073, and W15-HU-15, the east direction was applied as the plus direction.

The loading program is shown in Fig. 2.2-5. To find out the first flexure or shear crack, the lateral loading was initially controlled by force before reaching drift ratio of 0.125%. After then, two complete loading cycles were applied at each specified level of targeted drifts (0.25%, 0.375%, 0.5%, 0.75%, 1%, 1.5%, and 2%), and one cycle was applied at each level of targeted drift after drift ratio was beyond 2%.

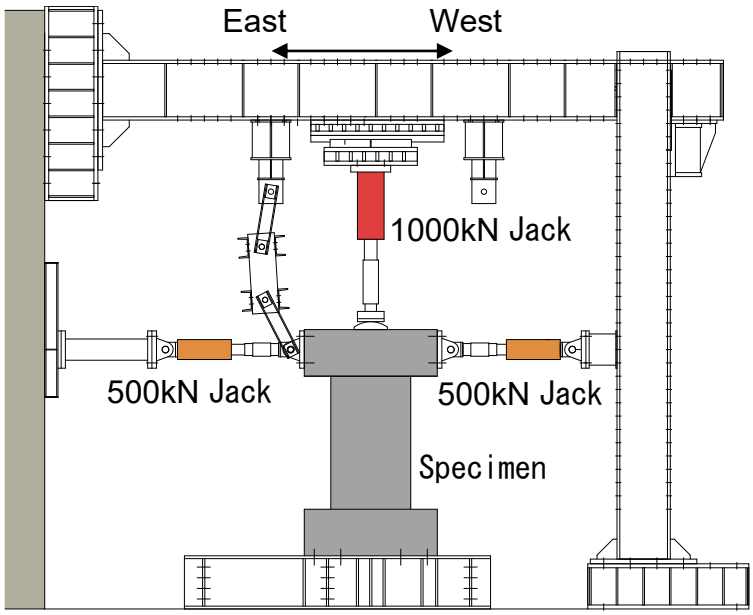

Fig. 2.2-4 Schematic view of test setup for shear walls

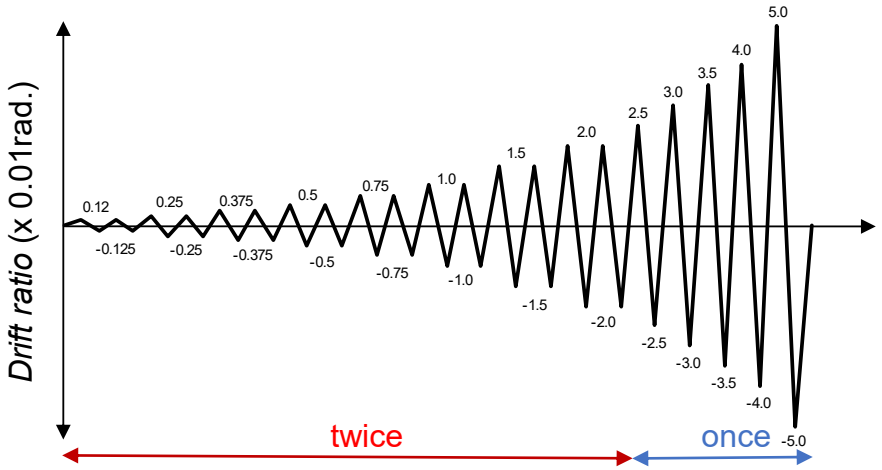

Fig. 2.2-5 Loading program

2.2.4 Instrumentation and measurement

Fig. 2.2-6 shows the locations of displacement transducers (DTs) for the tested specimens with the shear span ratio of 1.5(a) and 2.0(b) respectively. As shown in Fig. 2.2-6, two DTs were installed to measure the lateral displacement, and the average value measured by DTs No.1 and 2 were used as the lateral displacement of specimen. The other eight (four pairs of) DTs No.5 to 12, No.14 and 15were installed to measure the local vertical displacement at several targeted heights of specimens. Besides, DTs No.3 and 4 were applied to record the rotation while No.13 for recording the horizontal displacement of the rigid bottom stub. Overall view of testing is shown in Fig. 2.2-7. To measure the axial strain generated in the rebars of the walls, strain gauges were embedded for each specimen. Details of these measurements can be found in Fig. 2.2-8. Red, green, and blue marks represent the locations of embedded strain gauges for DL bars, HD rebars and concentrated rebars separately.

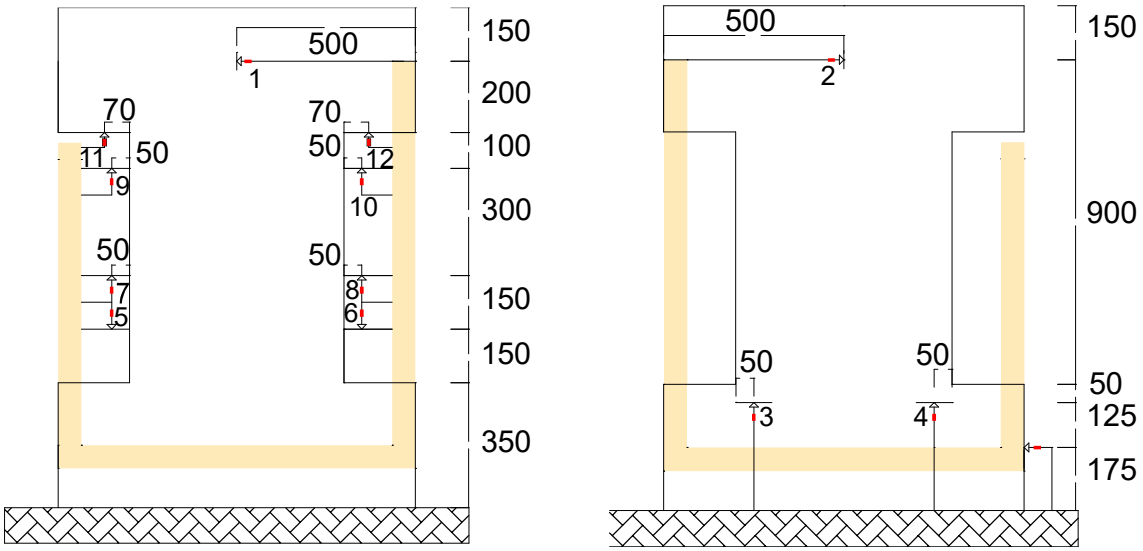

(1) North (2) South

(a) W15-Series

Fig. 2.2-6 Positions of displacement transducers (DTs) (Unit: mm)

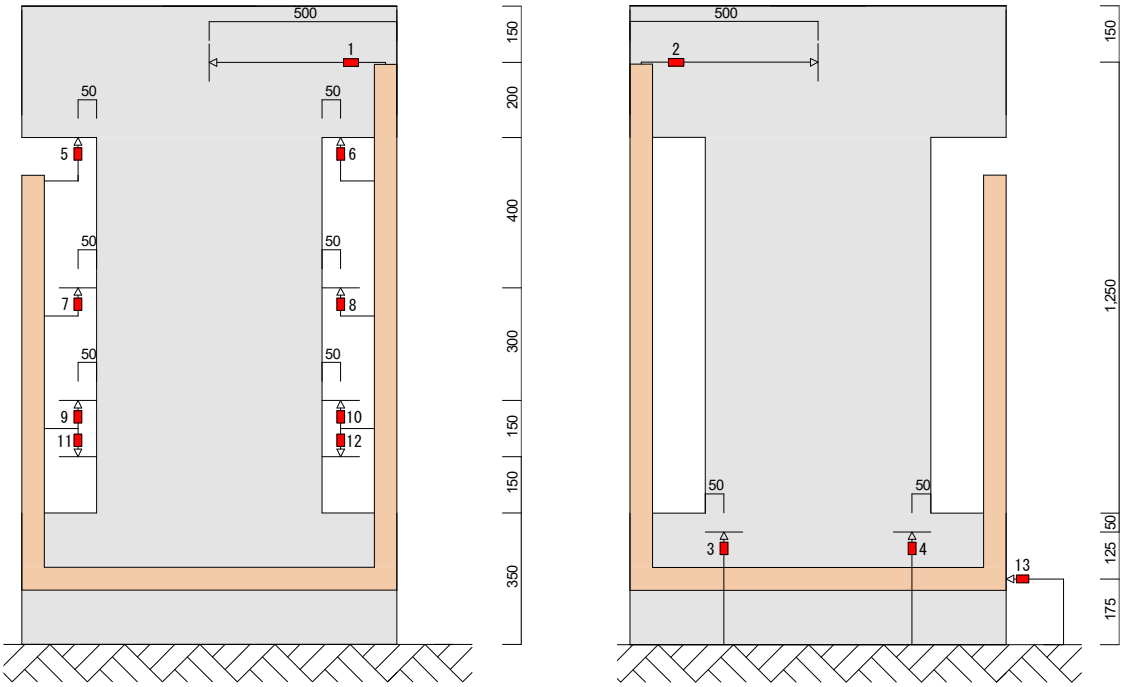

(1) North (2) South

(b) W20-Series

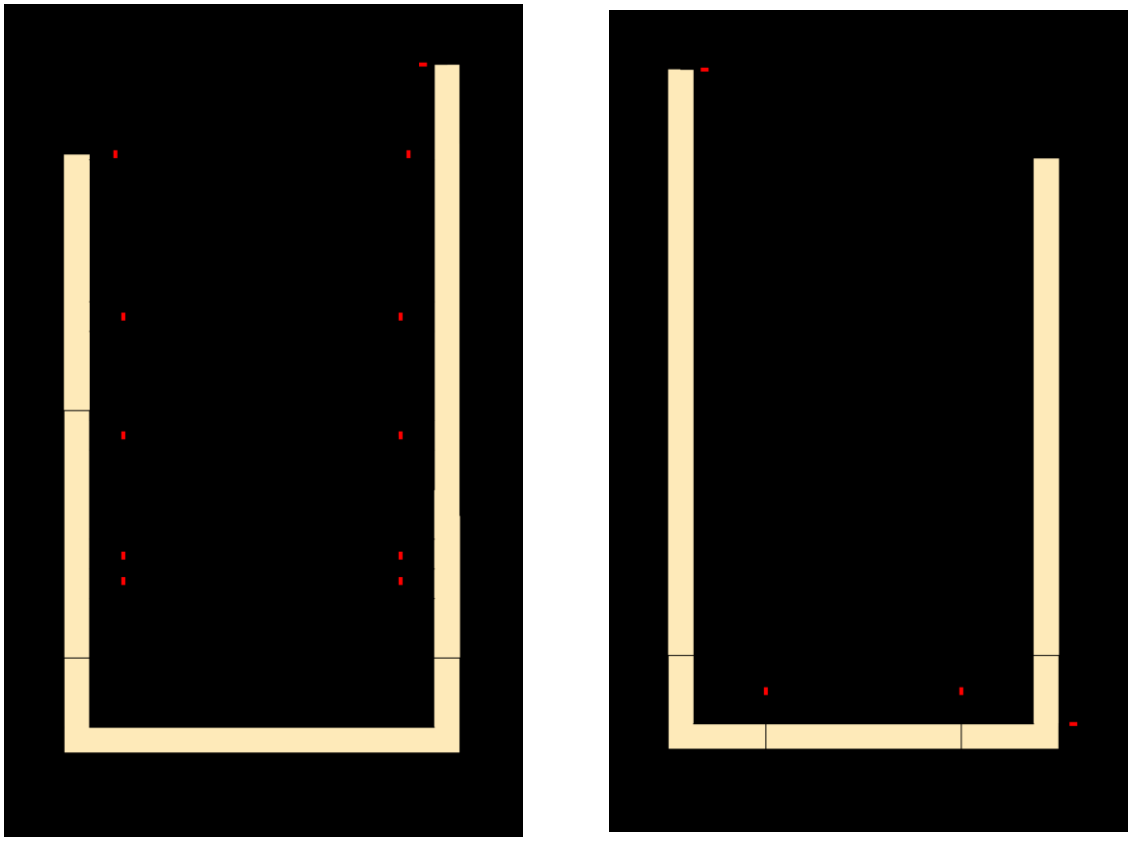

(c) W25-Series

Fig. 2.2-6 Continued

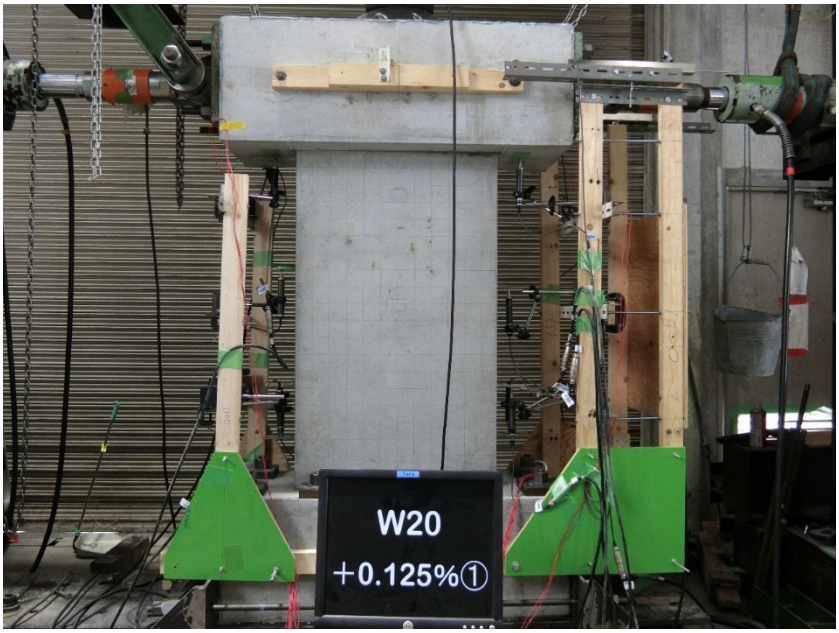

Fig. 2.2-7 Overall view of a testing specimen

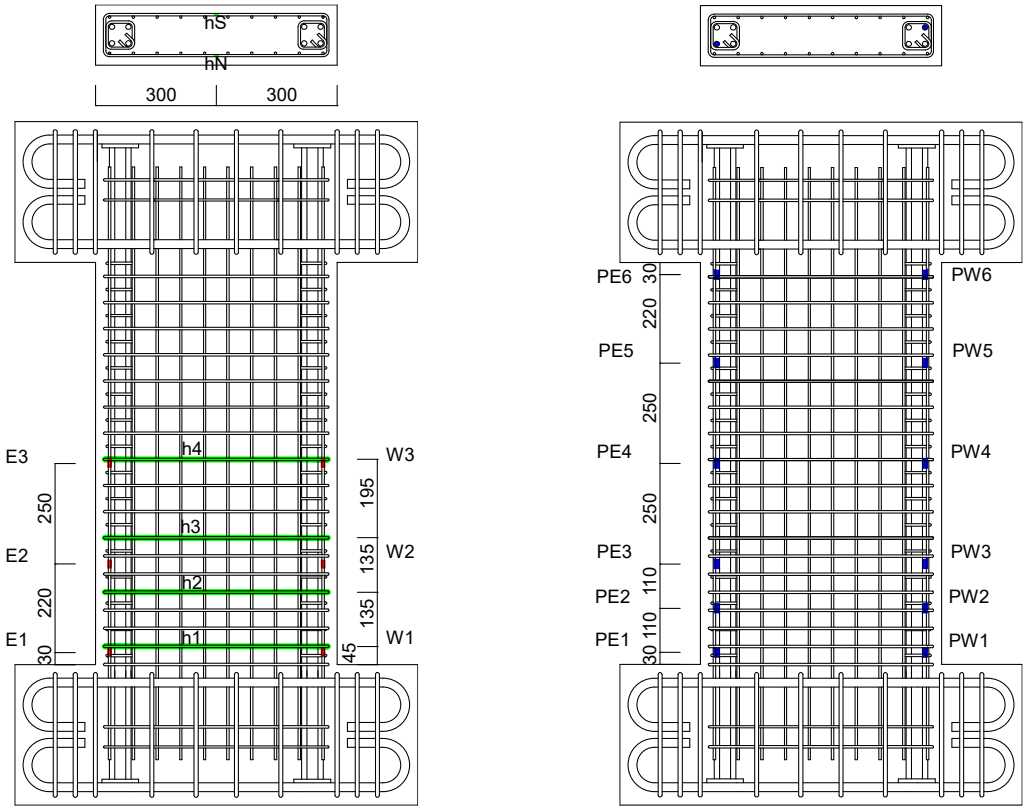

(1) Wall web (2) Concentrated rebars

(a) W20-F-Series

Fig. 2.2-8 Locations of strain gages

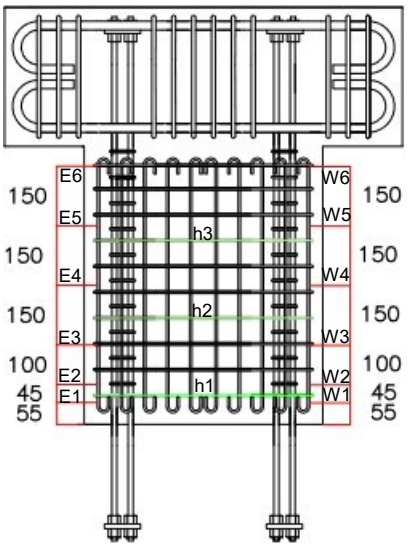

(1) Wall web

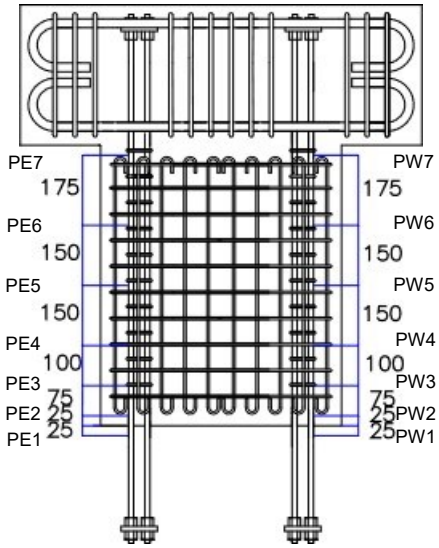

(2) Concentrated rebars

(b) W15-Series

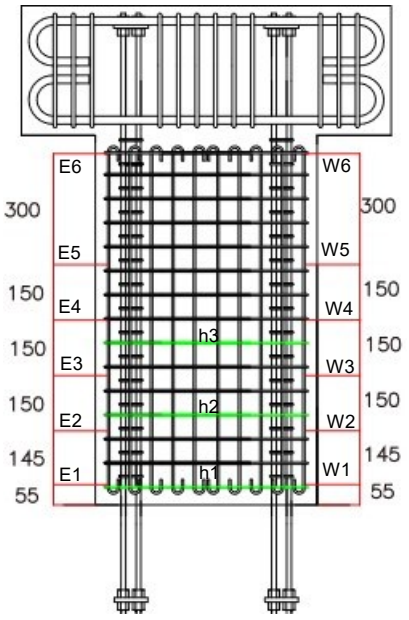

(1) Wall web

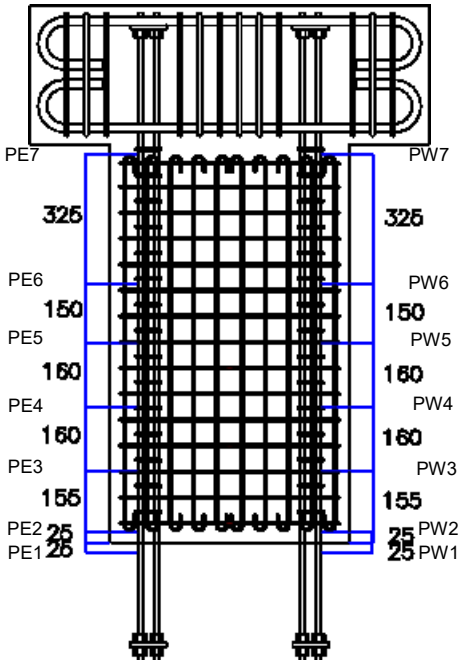

(2) Concentrated rebars

(c) W20-HU-073

Fig. 2.2-8 Continued

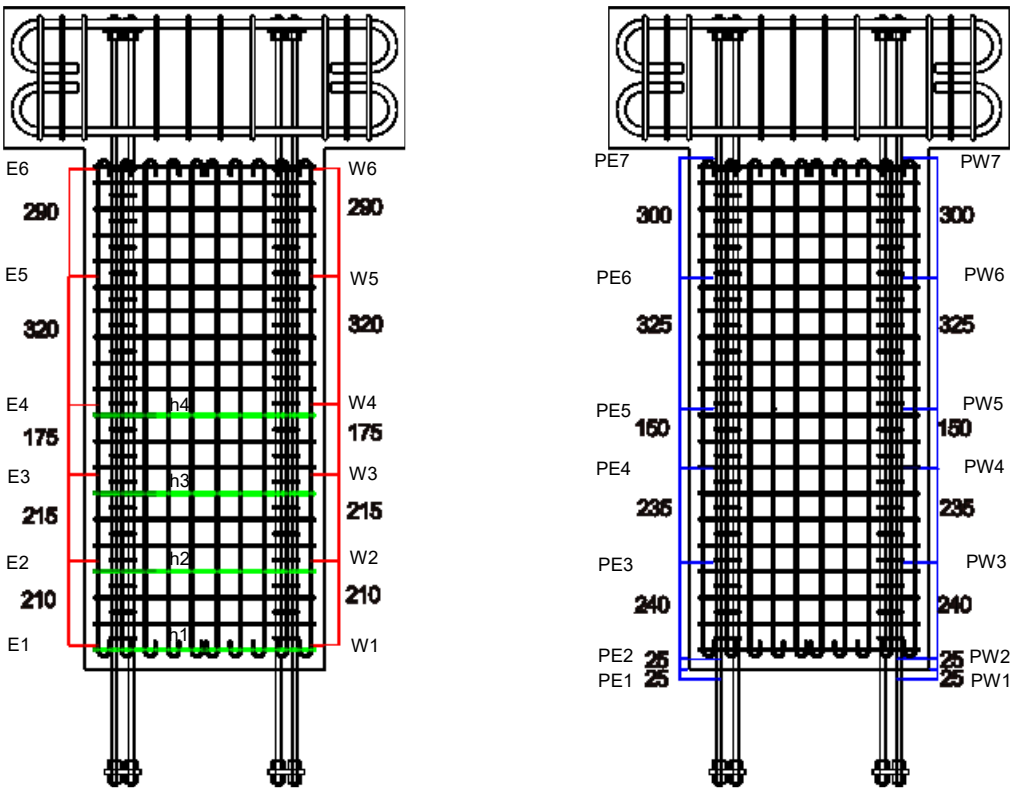

(1) Wall web (2) Concentrated rebars

(d) W25-HU-073

Fig. 2.2-8 Continued

2.3 Observed behaviors and results

2.3.1 Crack and damage of shear walls

This section summarized the developments of cracks that were observed from web side of each specimen. In the figures of this section, the grids have a spacing of 50 mm, the red lines and blue lines represent the cracks that were drawn at the peak drifts of the targeted levels in both push and pull direction of lateral loading, respectively, while the blacked portions express the spalled-off cover concrete.

For the tested shear wall W20-FD-15, when the lateral force reached +70kN, the first flexure crack was confirmed at the boundary between the bottom loading stub and wall panel on the north side. When the lateral force reached -50kN, flexure crack was confirmed at wall toe of south side. When the lateral force reached ±110kN, the first flexure-shear crack was found. Then, the initial spalling of cover concrete was observed when drift ratio reached 1.5%. With the spalling-off of the cover concrete became more and more significant, the exposure of the DL bars accompanying with the local buckling was first confirmed at R = -2.5%. the wall toe

on the north-east side and R = +3.0%. south-west side separately. During the loading cycle of R = 3.5%., when drift ratio reached +3.1%., at the wall toe on the north-east side, tensile rupture of the DL bars was confirmed. Besides, the local buckling of DL bars was also observed at the wall toe on the north-west side. And when drift ratio reached R = -3.5%., tensile rupture of the DL bars was confirmed at the wall toe on the south-west side.

At the last loading cycle, when drift ratio nearly reached R = +5.0%., at the wall toe on the west side of wall panel, the local buckling of concentrated rebars was confirmed. At the drift ratio R = -0.4%. and R = -1.6%., tensile rupture of the concentrated rebars was observed at the wall toe on the north-west side and south-west side respectively. Due to the descent of lateral resistance force and axial load, the test was terminated before drift ratio reached R = -5.0%.

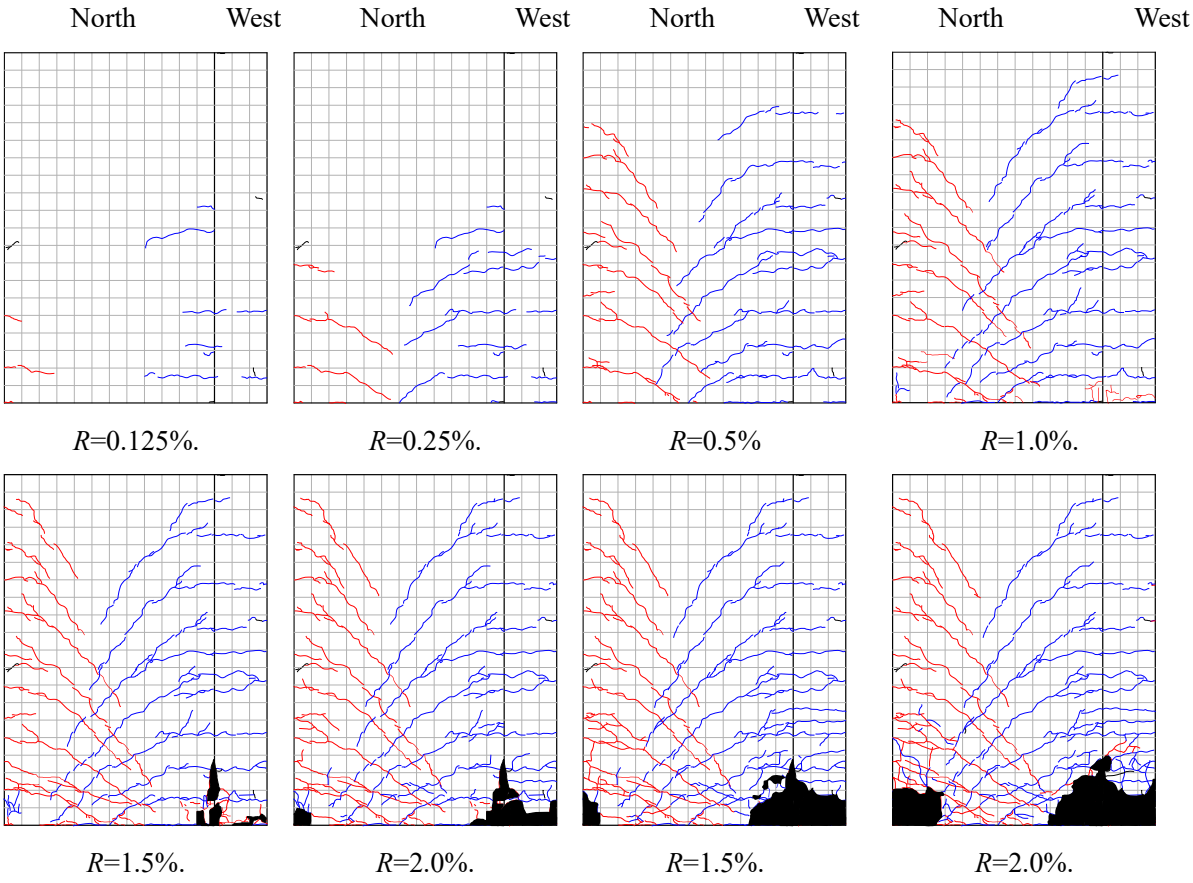

Fig. 2.3-1 Cracks patterns observed on specimen W20-FD-15

For the tested shear wall W20-FU-15, When the lateral force reached 40kN, the first flexure crack was confirmed at the boundary between the bottom loading stub and wall panel. When the lateral force reached +120kN and -100kN, the first flexure-shear crack was found on north and south side respectively. And then, the initial spalling of cover concrete was observed when drift ratio reached 2.0%. With the spalling-off of the cover concrete became more and more significant, the exposure of the DL bars accompanying with the local buckling was first confirmed at R = -2.5%. the wall toe on the north-east side and R = +3.0%. north-west side separately. At the last loading cycle, before drift ratio nearly reached R = +3.5%., obvious expansion of flexure and shear cracks were observed, and due to the dramatically descent of lateral resistance force and axial load, the test was terminated at that drift level.

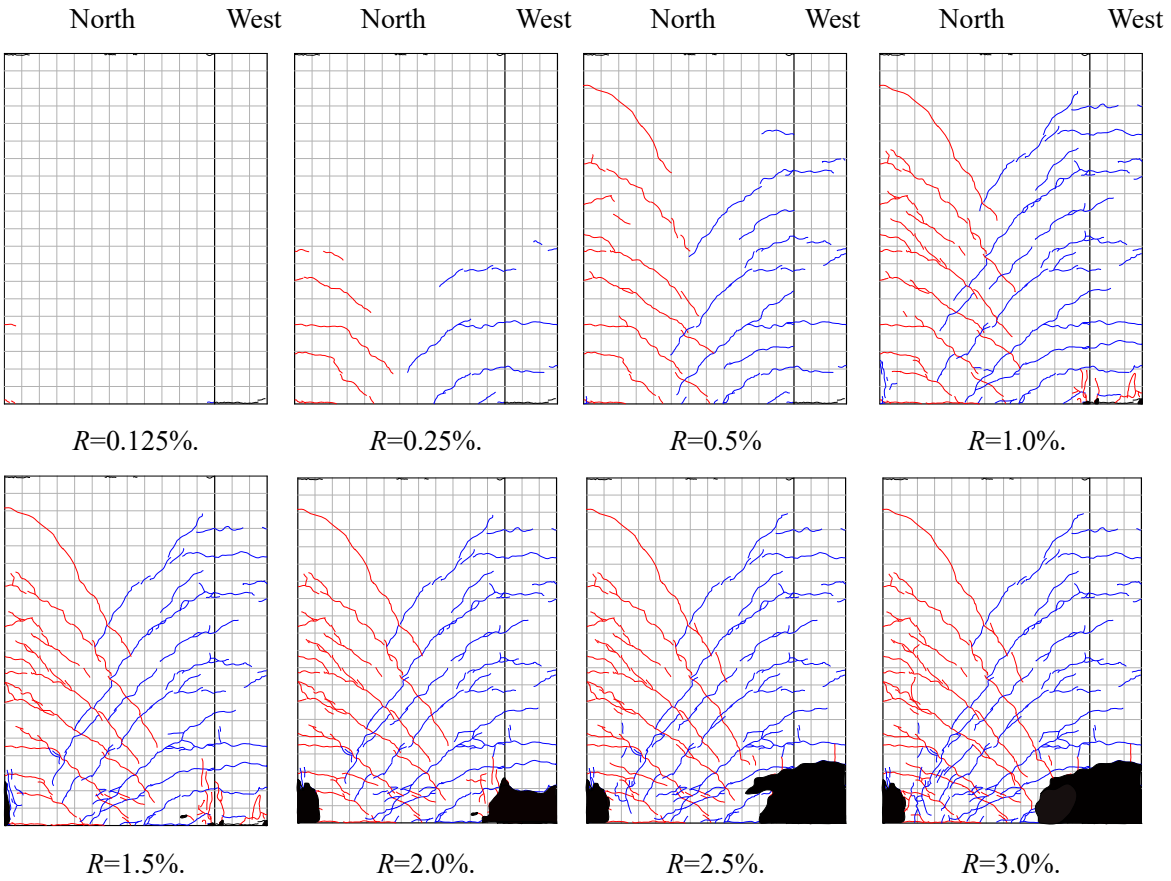

Fig. 2.3-2 Cracks patterns observed on specimen W20-FU-15

For specimen W15-HU-15, When the lateral force reached +40kN, the first flexure crack was confirmed at the boundary between the bottom loading stub and wall panel on the both side of the wall panel. When the lateral force reached +160kN, accompanying with the development of the flexure crack at position of 190 mm from the wall base the first flexure-shear crack on the north side was confirmed. At the compression zone of wall panel, the first vertical crack was found when drift ratio reached R = -0.375%. Then, the initial spalling of cover concrete was observed when drift ratio reached ±1.5%. The spalling-off of the cover concrete became more and more significant and the exposure of the HD bars was first confirmed at R = ±2.5%. At the last loading cycle, before drift ratio nearly reached R = -2.7%., obvious expansion of flexure and shear cracks were observed, and due to the dramatically descent of lateral resistance force, the test was terminated at the drift ratio of 4.0%.

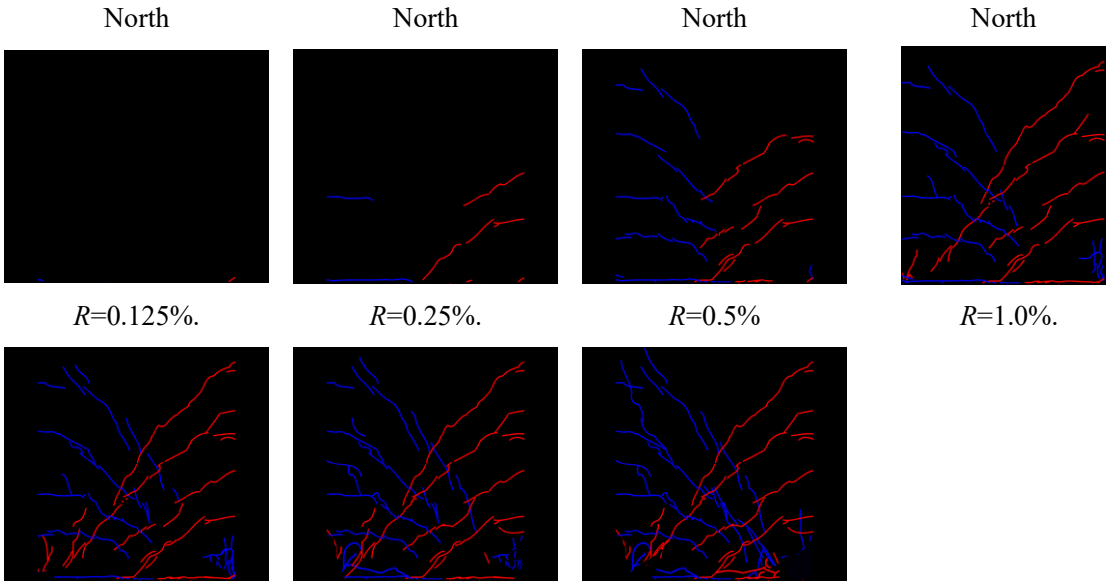

Fig. 2.3-3 Cracks patterns observed on specimen W15-HU-15

For specimen W15-HU-073, the first flexure crack was confirmed at the boundary between the bottom loading beam and wall panel when the lateral force was 40kN. Accompanying with the development of the flexure crack at position of 120 mm from the wall base, the first flexure-shear crack was found when drift ratio reached 0.125%. Then, the initial spalling of concrete was observed when drift ratio reached 1%. Significant spalling-off of concrete along with the exposure of the DL bars were first confirmed at the drift ratio of 2.5%. The shear crack that located at 480 mm away from base run through north (web) surface of specimen when drift ratio reached 3.5%. Accompanied with degradation of the lateral resistance and exposure of the HD bars in the wall panel was confirmed. After reaching the peak point in pull direction at the drift ratio of -4%. Obvious expansion of flexure and shear cracks were observed, and the test was terminated at that drift level.

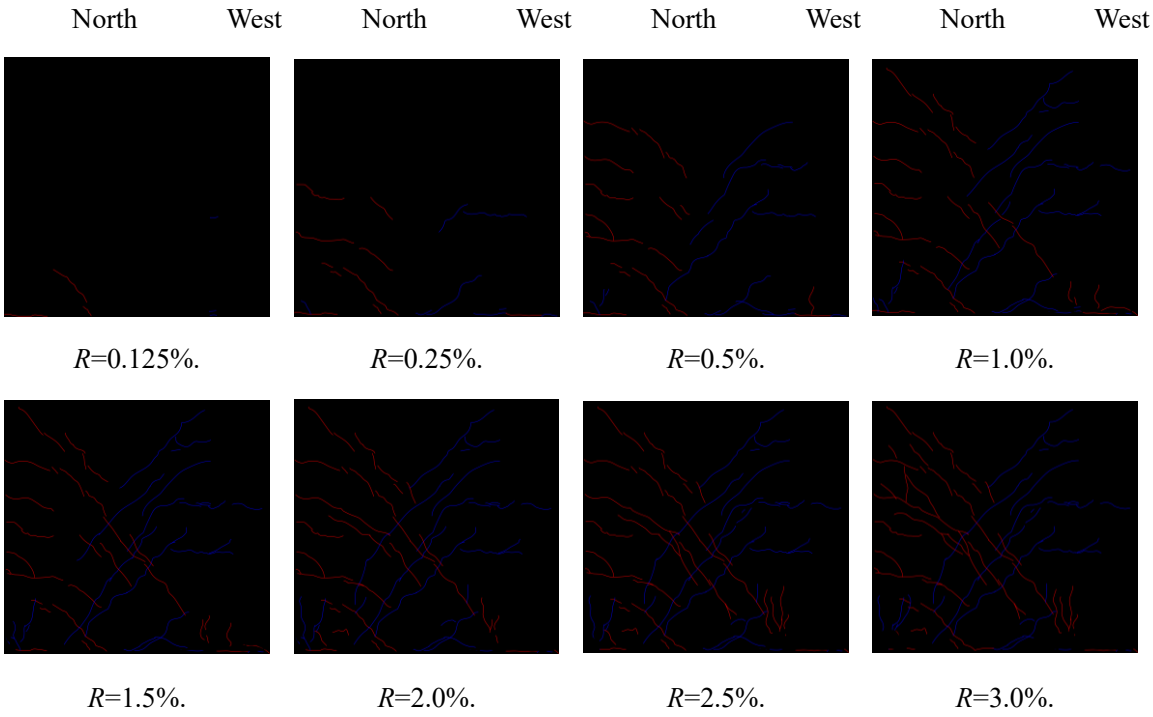

Fig. 2.3-4 Cracks patterns observed on specimen W15-HU-073

For specimen W20-HU-073, the first flexure crack was confirmed at boundary between the bottom loading beam and wall panel at the drift ratio of 0.125%. The first shear crack was found when drift ratio reached 0.375%. The initial spalling-off of concrete was observed at drift ratio of 2%, and obvious spalling-off of the concrete as well as exposure of the HD bars were first confirmed when drift ratio reached 2.5%. At the drift ratio of 3.5%, shear crack that located at 280mm away from base run through north (web) surface of the specimen.

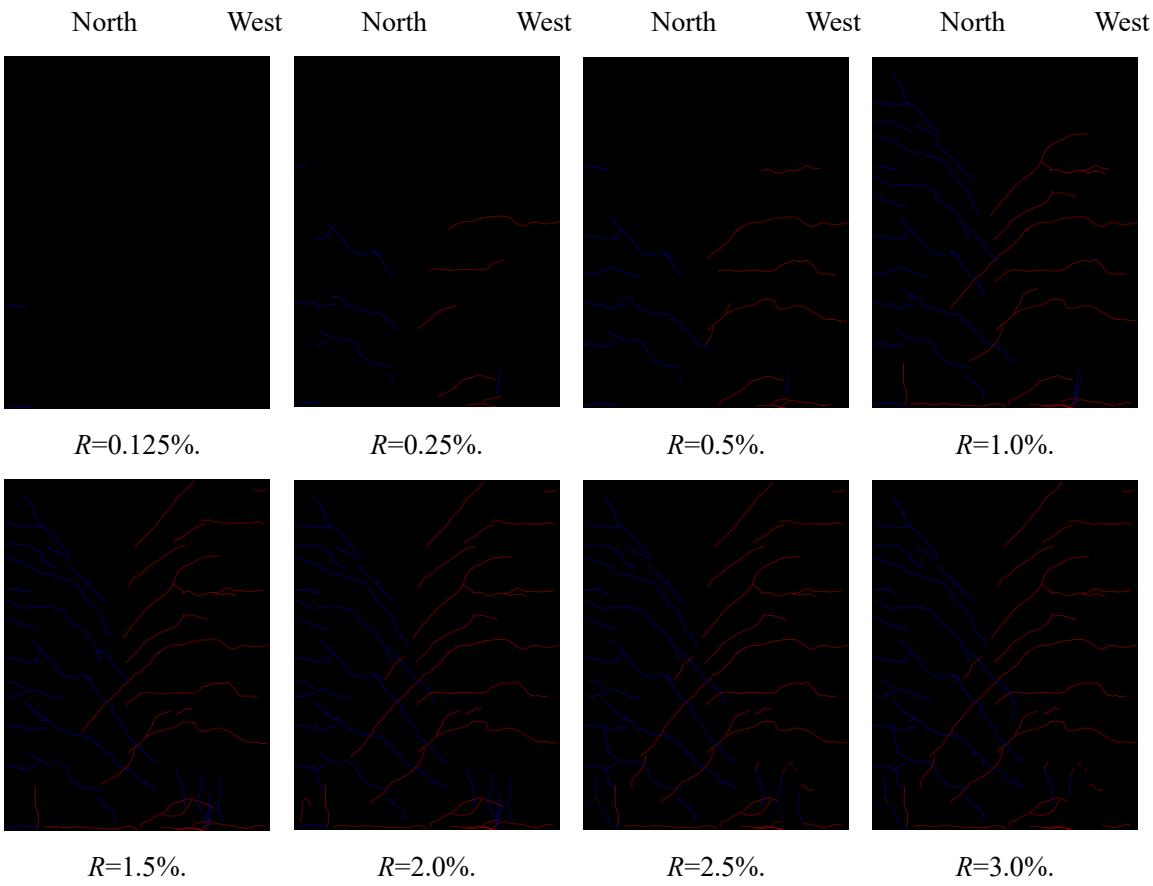

Fig. 2.3-5 Cracks patterns observed on specimen W20-HU-073

As for specimen W25-HU-073, the first flexure crack was confirmed at boundary between the bottom loading beam and the wall panel at the drift ratio of 0.125%. Accompanying with the development of the flexure crack at position of 240 mm from the bottom loading beam, the first flexure-shear crack was found when drift ration reached 0.25%. When drift ratio reached 1.5%, the initial spalling-off of concrete at the extreme corner of wall panel was confirmed and spalling-off of concrete became significant at from the drift ratio of 2.5% on.

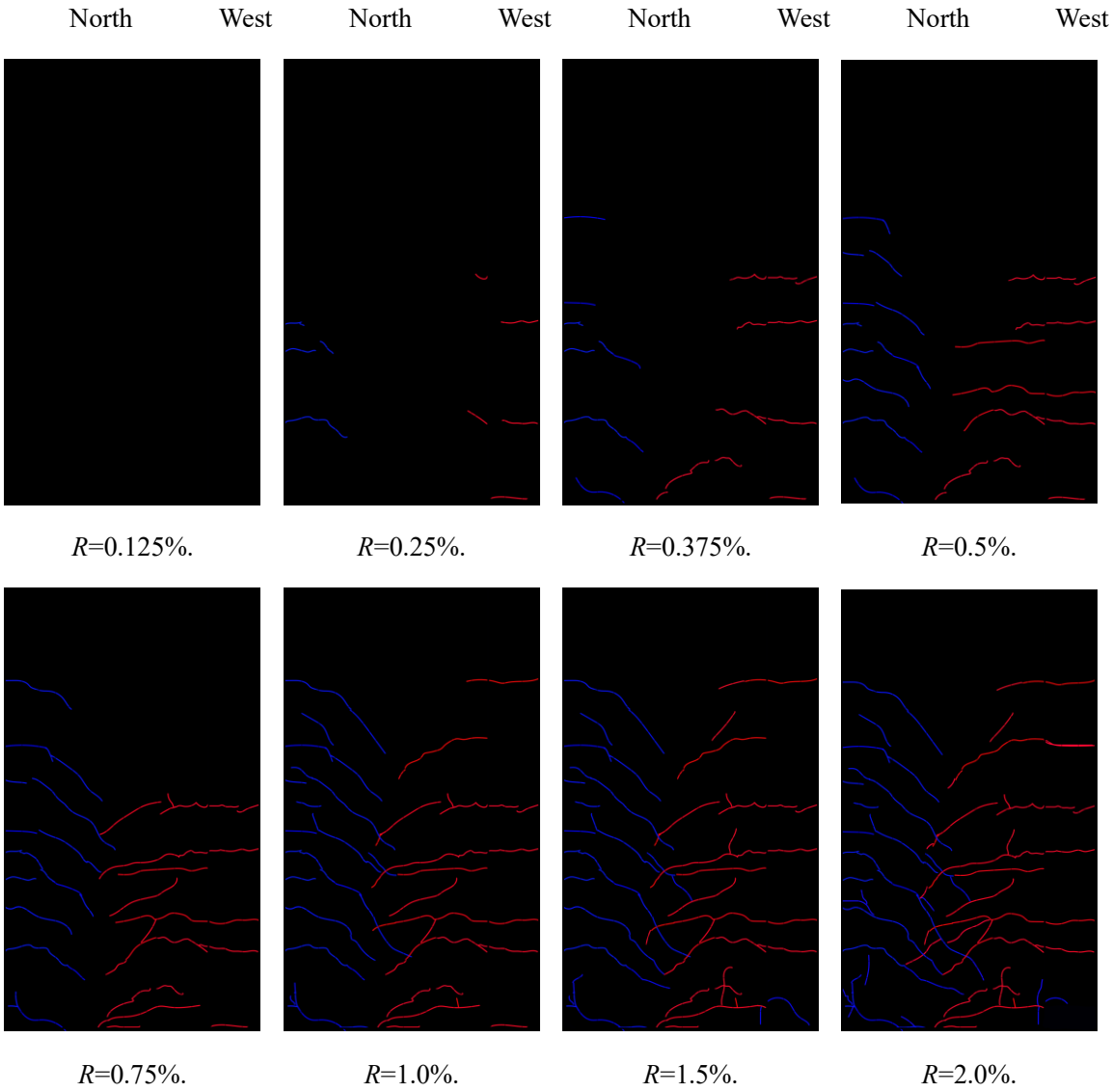

Fig. 2.3-6 Cracks patterns observed on specimen W25-HU-073

For all three specimens of HU-073-Series, no local buckling of the DL bars in the wall panel was observed. As compared with the previous results of W20-FD-15 and W20-FU-15, because the DL bars were not anchored into the top and bottom beams, they tended to sustain less lateral loading and absorb less energy, and hence mitigate damage near the wall toes. As obvious in Fig. 2.3-7, severe damage of concrete at the wall toe of specimen W20-FU-15 with the ordinary arrangement method of DL bars was observed, while the new arrangement method of DL bars perfectly reduce the damage caused by the local buckling of DL bars at drift ratio of 3%, which provided specimen W20-HU-073 larger deformability and prevent shear domain failure.

(a) W20-FU-15 (R=3%) (b) W20-HU-073 (R=3%)

Fig. 2.3-7 Effect of the new arrangement method for D6 DL bars

On the other hand, this new arrangement of DL bars might reduce the shear reinforcements of the bottom loading beam, and damage the loading beam adjacent to the wall toes. As shown in Fig. 2.3-8, severe damage at the panel-beam joint were observed for all three specimens. This fact implies that the adjacent members should be stiff enough to take full advantage of the new arrangement method. In the specimen with shear span ratio of 1.5, the flexure cracks were spread about 600 mm upper from the wall base, while for specimens with shear span ratio of 2.0 and 2.5, the flexure cracks were spread about 875 mm and 1050 mm in height, respectively. Distribution of the flexural cracks implies that the length of potential plastic hinge region of RC walls should be associated with the shear span of them.

Fig. 2.3-8 Damage at beam-wall joint (specimen W15-HU-073 at the loading cycle of 4%.)

2.3.2 Lateral force – drift ratio hysteretic behaviors

The lateral resistance force (V) versus drift ratio (R) relationships of all specimens are shown in Fig. 2.3-9, while the red dashed lines represent the P-Δ effect by the axial load on the lateral resistance force. The measured lateral capacities averaging the peak lateral forces in both directions are shown in Table 2.2-1.

As can be seen in Fig. 2.3-9, the lateral force of specimen W20-FD-15 leveled off after yielding of the concentrated rebars was confirmed at R = 0.75%., and reached its maximum lateral load carrying capacity at R = -1.5%. and R = +2.0%. separately. Then, the lateral resistance of specimen W20-FD-15 began to decrease nearly in accordance with the P-Δ effect, and maintained more than 80% of the maximum lateral force till drift ratio of R = 4.0%. which exhibited typical ductile behavior.

As for the specimens reinforced by SBPDN rebars, their lateral force all stably increased along with drift, and all specimens exhibited drift-hardening capability up to the drift level of 3.0%. The lateral resistance forces of specimens W15-HU-073 and W20-HU-073 reached peaks at R = 3.0%. and decreased slightly at R = 3.5%. As for specimen W25-HU-073, due to the limitation in the stroke length of the horizontal loading jacks, the cyclical loading was terminated after the cycle at R = 3.0%.

In order to ascertain the ultimate failure state of the walls reinforced with SBPDN rebars, after the reversed cycling of lateral load, all specimens were monotonically pushed up to the drift level of 7.0%. However, before drift ratio nearly reached R = +3.5%., along with obvious expansion shear cracks were observed at the wall panel of specimen W20-FU-15, came the sharply descent of lateral and axial resistance force, which can be considered as shear failure after flexural type hysteresis property. Similar to specimen W20-FU-15, at the last loading cycle of specimen W15-HU-15, the quickly decrease of lateral resistance force was confirmed before drift ratio reached 2.7%., but the specimen did not lose the gravity-sustaining capacity.

As for the specimens that the DL bars were not anchored into the adjacent beams and the applied axial load ratio was 0.073, although severe damage at the wall toes was confirmed (see Fig. 2.3-8), and the lateral resistance decreased along with drift ratio due to the increasing of P-Δ effect, all specimens still maintained more than 60% of the maximum lateral force till the end of tests at R = 7.0%. without losing their gravity-sustaining capacity, no shear failure was observed in this group.

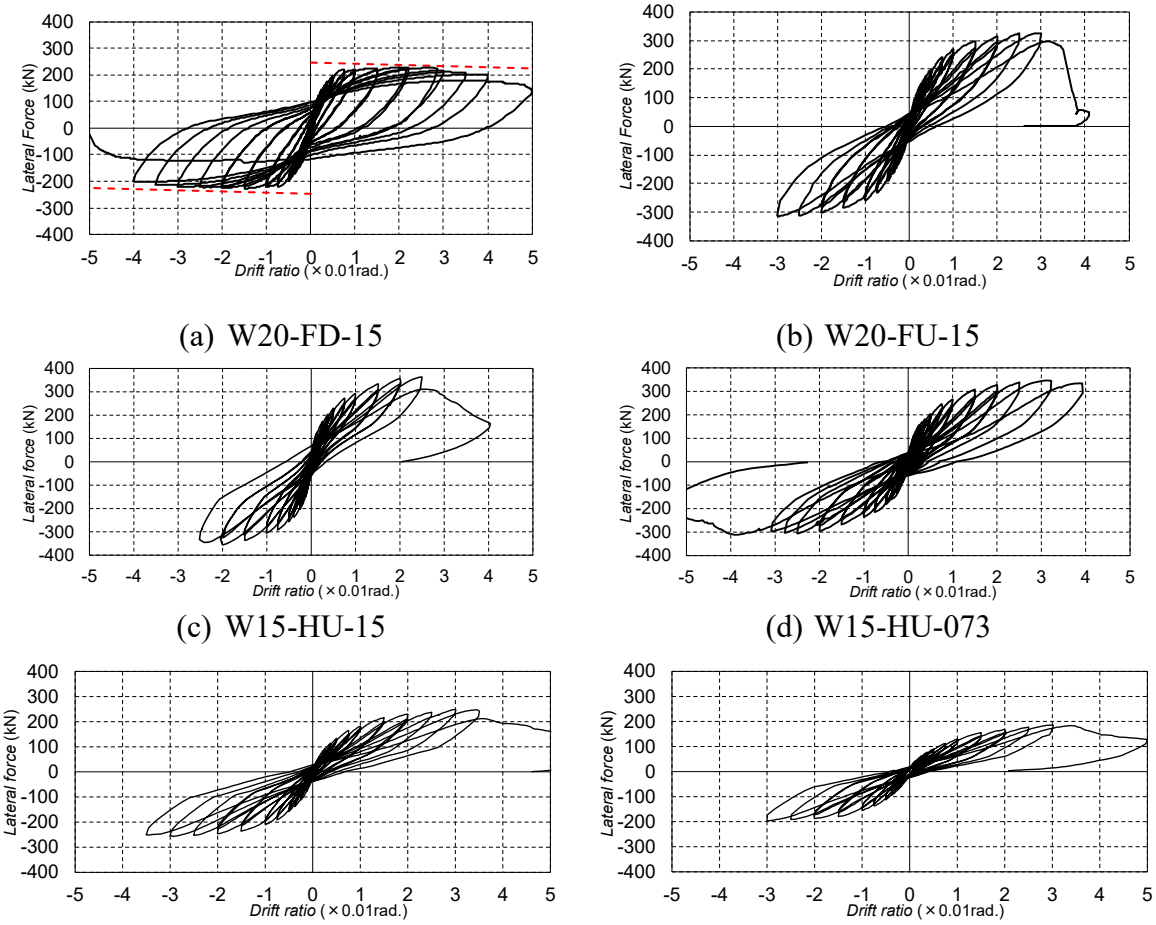

(a) W20-FD-15 (b) W20-FU-15

(c) W15-HU-15 (d) W15-HU-073

(e) W20-HU-073 (f) W25-HU-073

Fig. 2.3-9 Measured lateral load-drift ratio relationships

To see the effects of the main experimental variables on overall seismic performance of RC shear walls more clearly, the envelope curves in both directions are compared in Fig. 2.3-10.

(a) Effect of the type of concentrated rebars: it is obvious in Fig. 2.3-10(a) that the envelope curves of these two specimens were almost the same till drift ratio of 0.75%. From that drift on, however, the lateral resistance of the specimen with SD345 rebars leveled off along with drift due to the commencement of yielding of its concentrated rebars. On the other hand, since the yielding of SBPDN rebars were not confirmed, the lateral resistance of specimen W20-FU-15 kept increasing up to large deformation till drift ratio reached R reached 3.0%.

(b) Effect of axial load ratio: to see if it is feasible to utilize drift-hardening RC shear walls for low-rise buildings, in which shear deformation play the main role in the overall deformation, without premature shear failure, two short specimens with the same shear span ratio of 1.5 and different axial load level was compared in Fig. 2.3-10(b). As can be seen, they all exhibited obvious drift-hardening capability since both of them were reinforced by SBPDN rebars, but the specimen with higher axial load ratio indicated higher initial stiffness and maximum lateral force (about 10% higher). However, the specimen with lower axil load ratio did not failed by shear deformation till amazing large drift ratio R of 7.0%.

(c) Effect of the arrangement of DL bars and axial load ratio: to verify the effectiveness of the new arrangement method for DL bars in the wall panel, two specimens that have the same steel amount and type, and same shear span ratio are compared in Fig. 2.3-10(c). Measured results indicate that the since the specimen with the new arrangement method of DL bars had relatively low initial stiffness and maximum lateral resistance capacity (about 20% lower), this is because the low axial load ratio of specimen W20-HU-073 and the new method reduced the flexural strength of the wall. However, comparing with specimen W20-FU-15 whose DL bars were fixed with normal method, specimen W20-HU-073 maintained more than 60% of the maximum lateral force till the drift ratio of 7.0%. without shear failure and losing its gravity-sustaining capacity.

(d) Effect of the shear span ratio: to see the influence of shear span ratio on seismic behavior of the tested shear walls, comparisons were conducted in terms of the lateral force and drift ratio relationships, and the moment at the end section versus drift ratio envelope curves and shown in Fig. 2.3-10(d). It can be seen that the lower the shear span ratio, the higher the initial stiffness and the maximum lateral resistance force. In addition, since these three specimens have the same section and reinforcements details, there is little, in any, difference among the flexural strength of these three specimens, implying that influence of shear span ratio on flexural property of the wall section can be ignored.

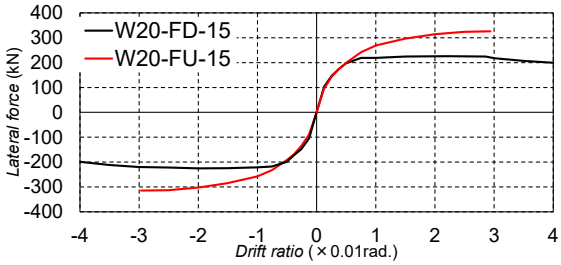

(a) Effect of the type of concentrated rebars

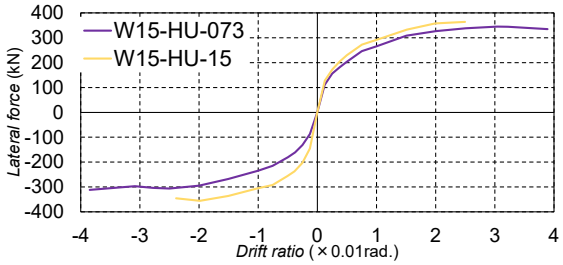

(b) Effect of axial load ratio

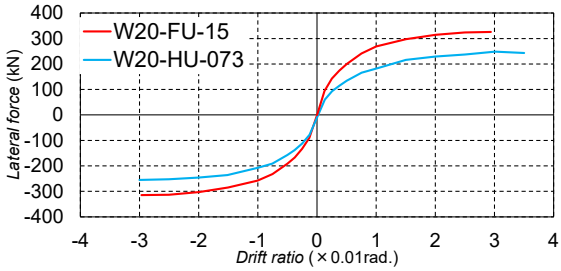

(c) Effect of the arrangement of DL bars and axial load ratio

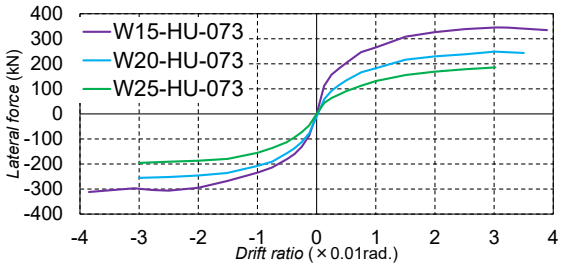

(1) $V - R$ relationships

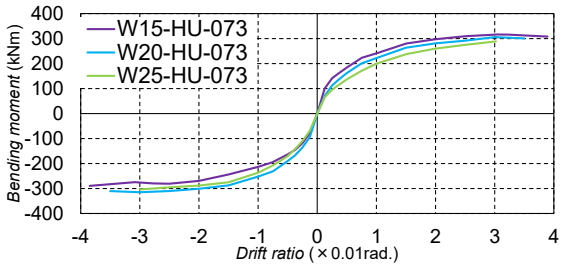

(2) Maximum flexural strengths of the wall sections

(d) Effect of the shear span ratio

Fig. 2.3-10 Effects of main experimental parameters.

2.3.3 Strains measured in reinforcements

To better understand the reason for the drift-hardening capability of the RC shear walls reinforced by the SBPDN rebars, and to verify the effect of the new arrangement method of DL bars, this section summarized the measured axial strain versus drift ratio relationships of all the rebars for each specimen, while the red dashed horizontal lines represent the yield strain of the rebars. And the title of each graph, for example W1 – 30mm, represents the result measured by the strain gauges located at the section of 30mm away from the wall base for specimens on the west side, which is related to the details provided in Fig. 2.2-8.

Form Fig. 2.3-11, one can see that the DL bars of specimen W20-FD-15 and W20-FU-15 yielded by tensile at a very early stage before drift ratio reached 0.5%. On contrary, for the specimens with the new arrangement method of DL bars, measured results indicate that the DL bars did not yield by tensile, they only yielded at the bottom end by compression. And from the results measured with height over 200mm, the strains did not reach the yielding strain, and they increased gradually during loading but decreased sharply at the beginning of unloading, this could be considered as the result of the slippage between concrete and the DL bars. Furthermore, local buckling of the DL bars in specimens of HU-Series was not confirmed, this could be the reason that this method mitigated the damage of concrete near the wall toes.

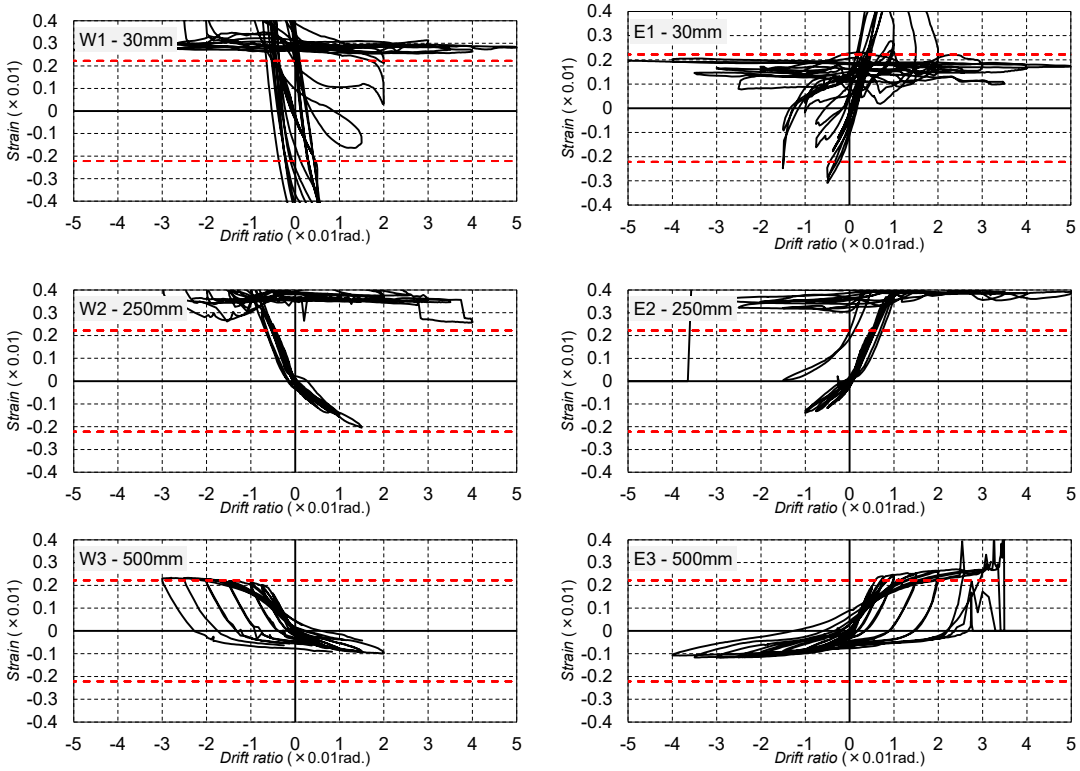

(a) W20-FD-15

Fig. 2.3-11 Measured strains-drift ratio relationships of DL rebars

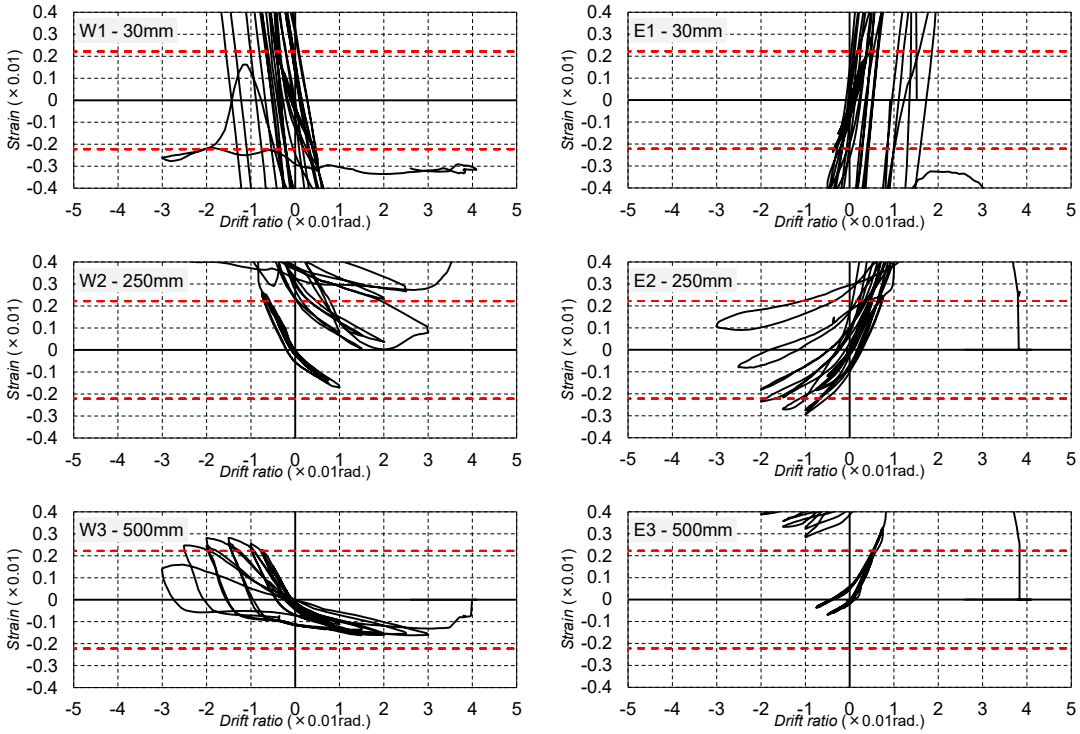

(b) W20-FU-15

Fig. 2.3-11 Continued

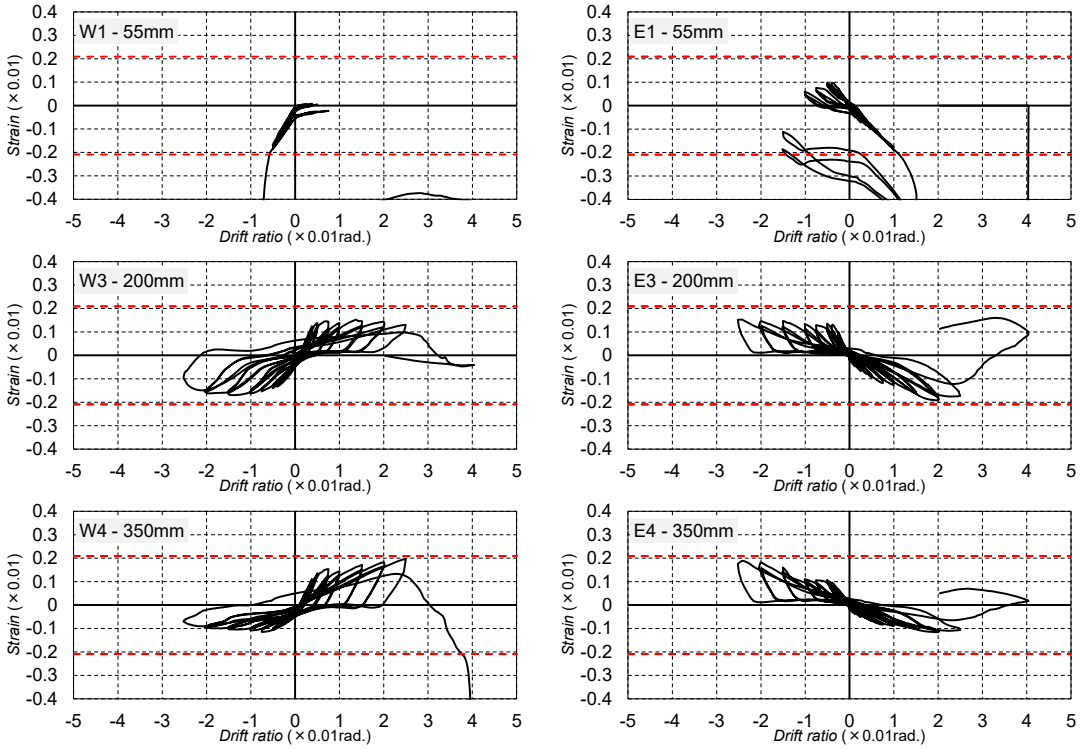

(c) W15-HU-15

Fig. 2.3-11 Continued

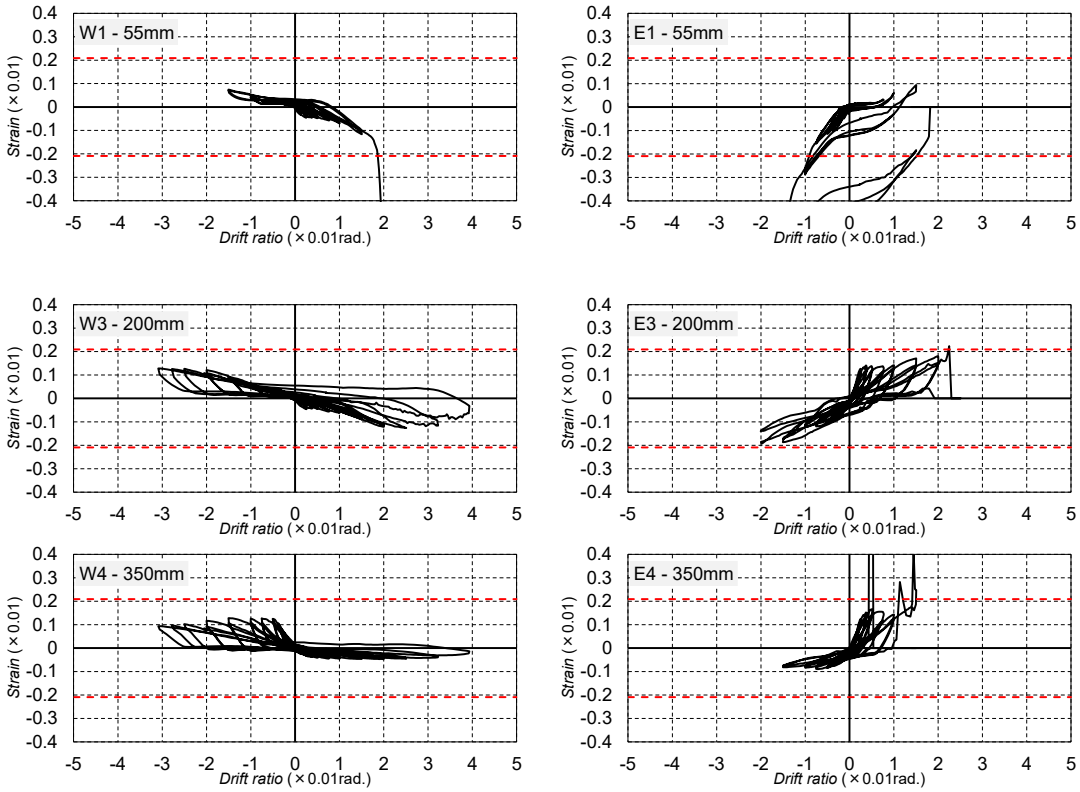

(d) W15-HU-073

Fig. 2.3-11 Continued

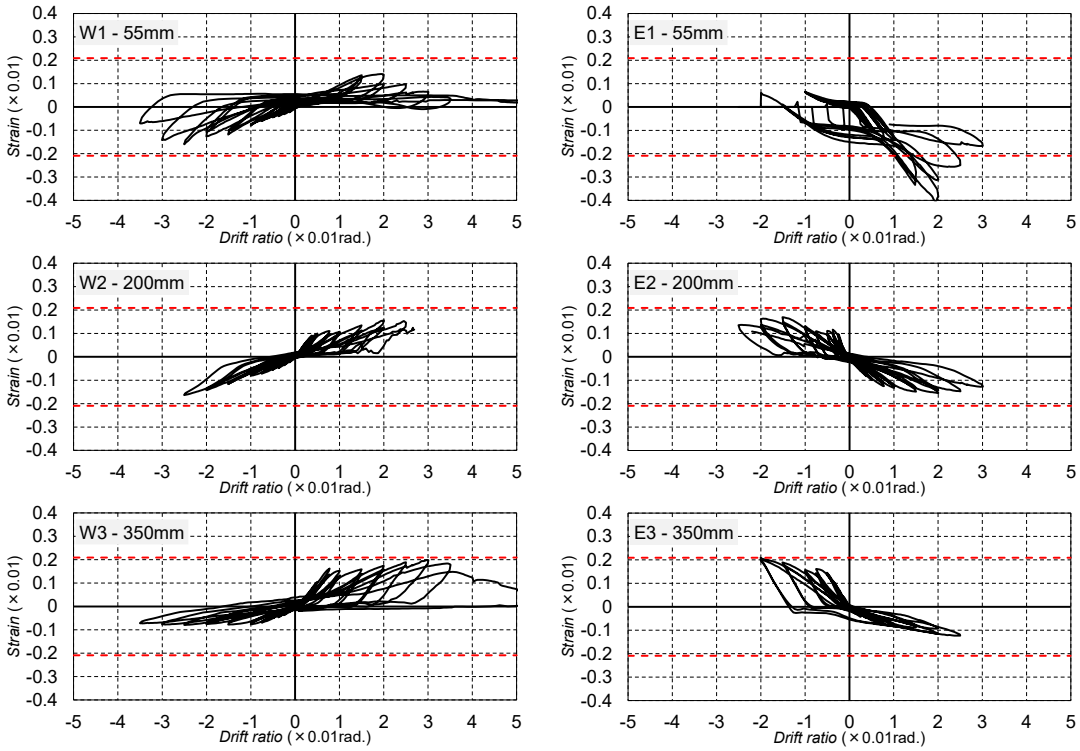

(e) W20-HU-073

Fig. 2.3-11 Continued

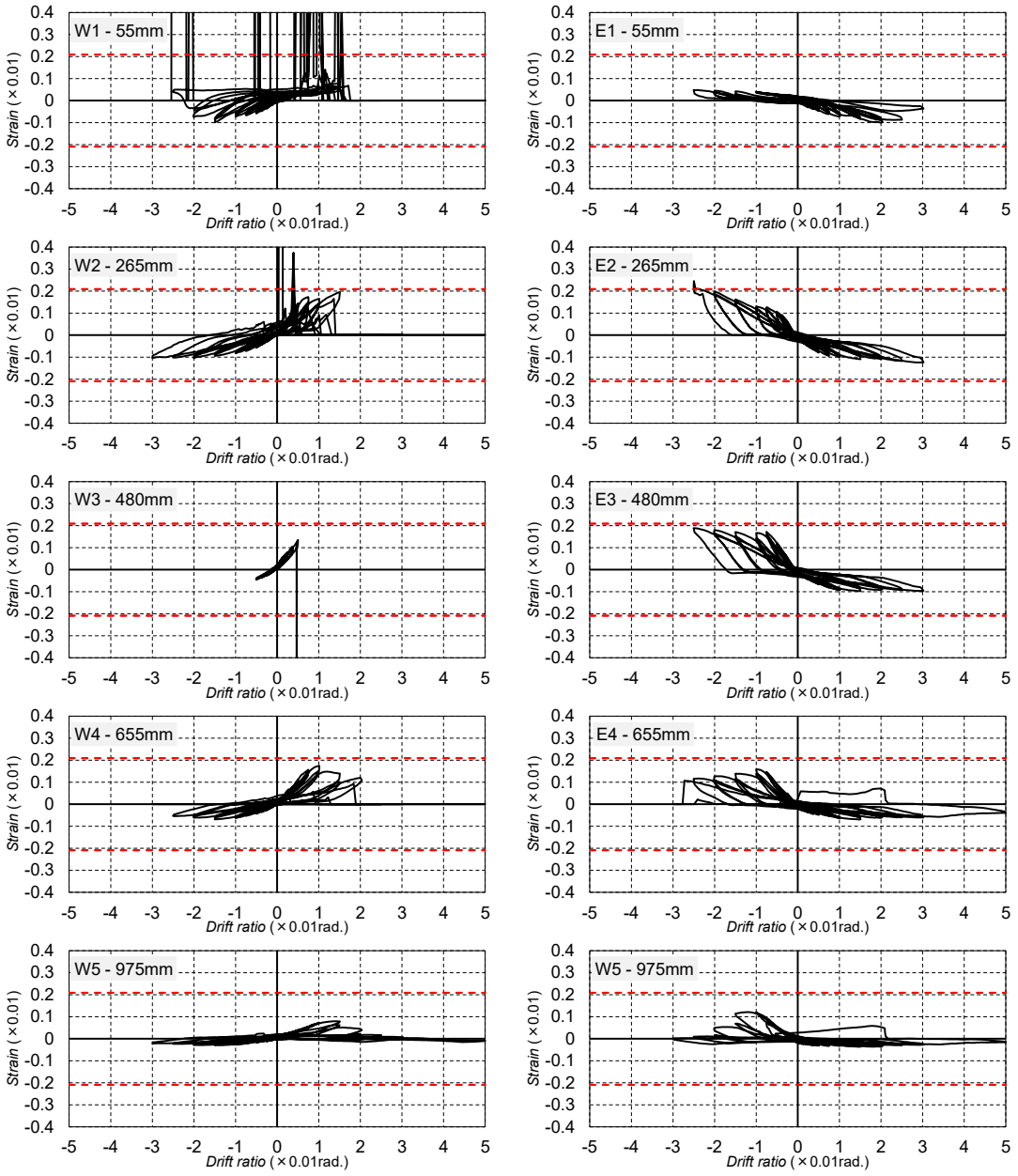

(f) W25-HU-073

Fig. 2.3-11 Continued

Fig. 2.3-12 shows the strains of horizontal reinforcements. It can be seen that the HD rebars of specimens with shear span ratio of 1.5 or axial load ratio of 0.15, yielded before drift ratio reached 2.0%. While the HD rebars of specimen W20-HU-073 yielded when drift ratio beyond 2.0%., and the HD rebars specimen W25-HU-073 did not yield till the end of test. So, the RC walls with low axial load level and high shear span ratio sustain less shear deformation, and sufficient shear reinforcements are required for drift-hardening RC walls to avoid brittle shear failure.

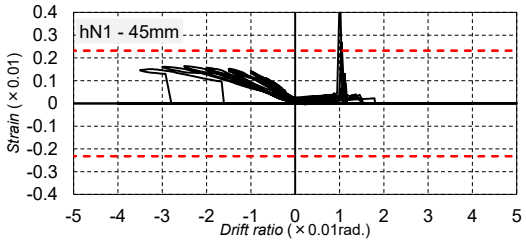

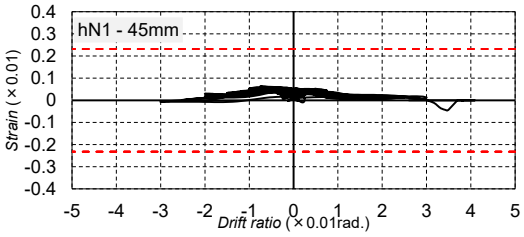

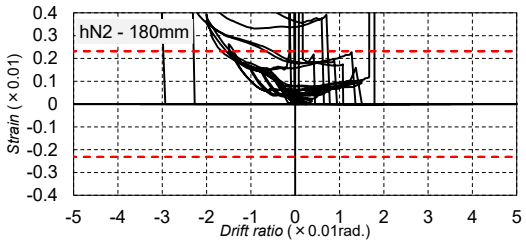

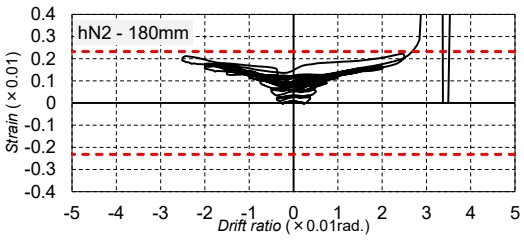

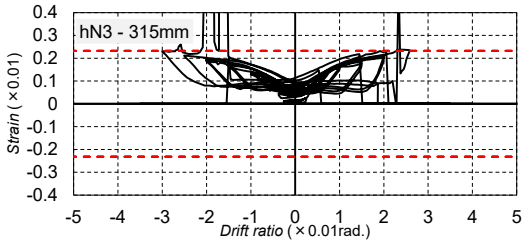

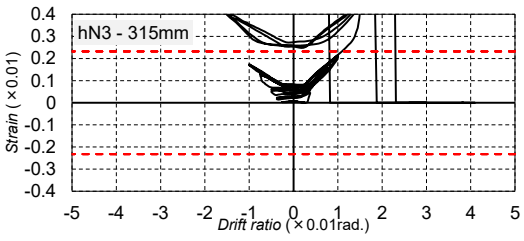

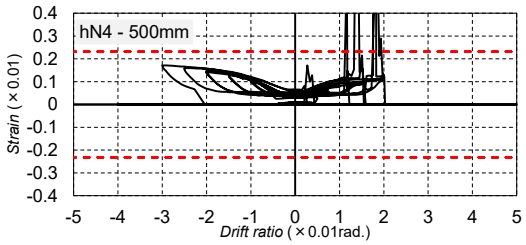

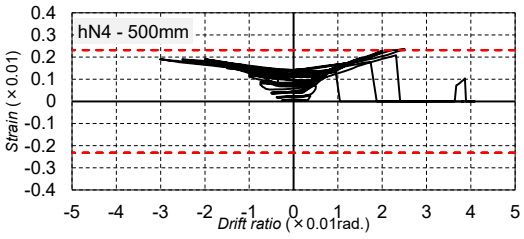

(a) W20-FD-15 (b) W20-FU-15

Fig. 2.3-12 Measured strains-drift ratio relationships of HD rebars

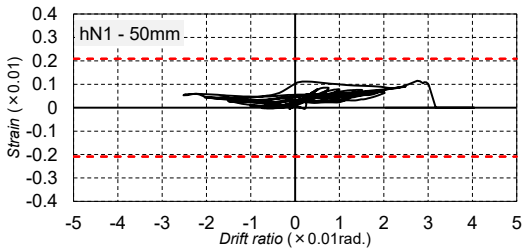

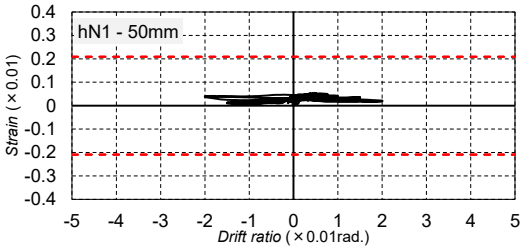

(c) W15-HU-15 (d) W15-HU-073

Fig. 2.3-12 Continued

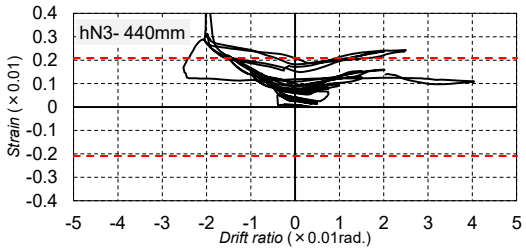

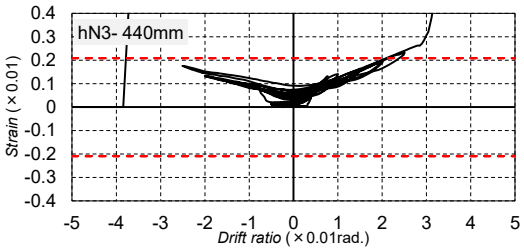

(c) W15-HU-15 (d) W15-HU-073

Fig. 2.3-12 Continued

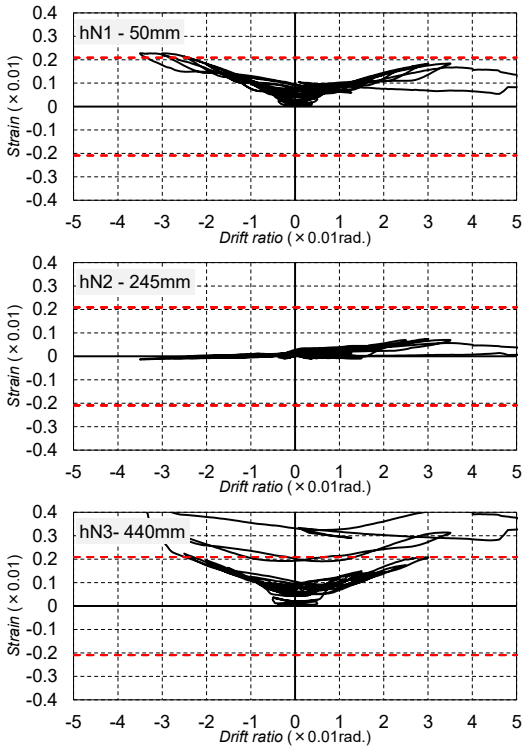

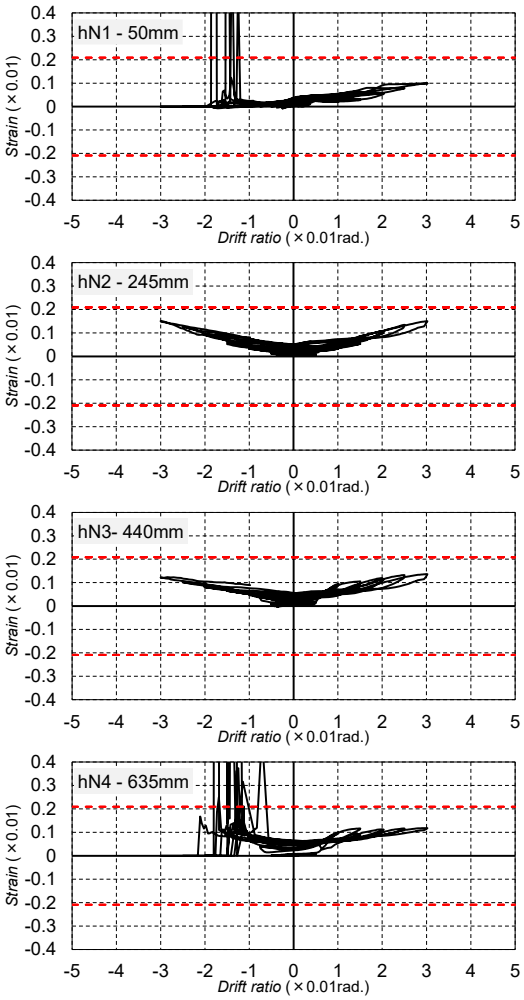

(e) W20-HU-073 (f) W25-HU-073

Fig. 2.3-12 Continued

To investigate the reason for the steady increase in the lateral force at large drift of the specimens reinforced by SBPDN rebars, the measured axial strains of all concentrated rebars are shown in Fig. 2.3-13. It is apparent that the SD345 rebars reached their yield strain at the drift ratio of 0.75%. However, the axial strains of SBPDN rebars exhibited stable increase along with the drift ratio, and did not reach its yield strain even at the drift ratio of 3.0%., which accounted for the increase in steel stress. This observation means that SBPDN rebars could provide lateral resistance even at large deformation, so that covered the loss in lateral resistance caused by the P-Δ effect after the significant spalling of cover concrete had commenced,

enabling the overall lateral resistance of the shear walls to increase along with the drift, in other words, the utilization of SBPDN rebars as concentrated rebars can assure RC walls drift-hardening capability.

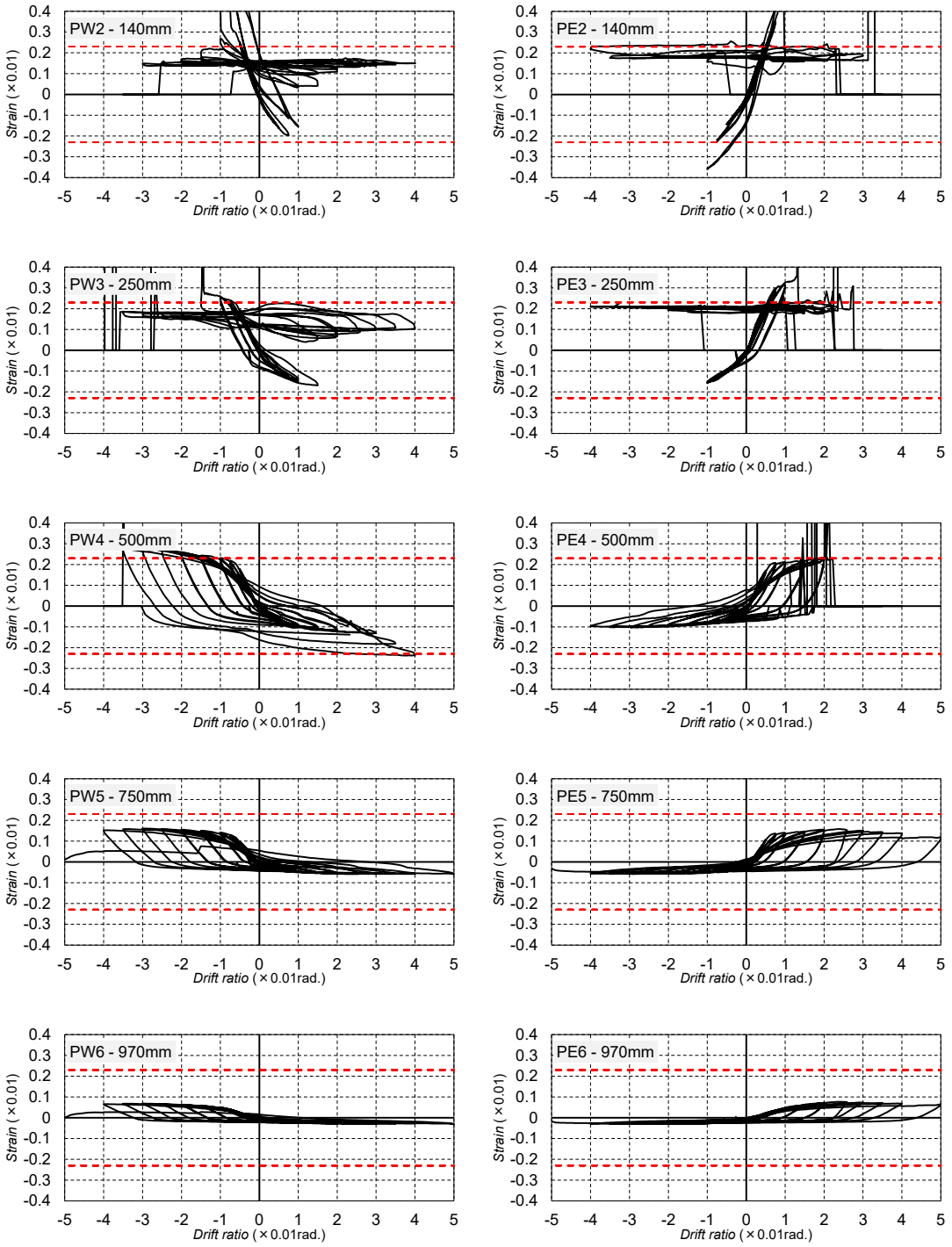

(a) W20-FD-15

Fig. 2.3-13 Measured strains-drift ratio relationships of concentrated rebars

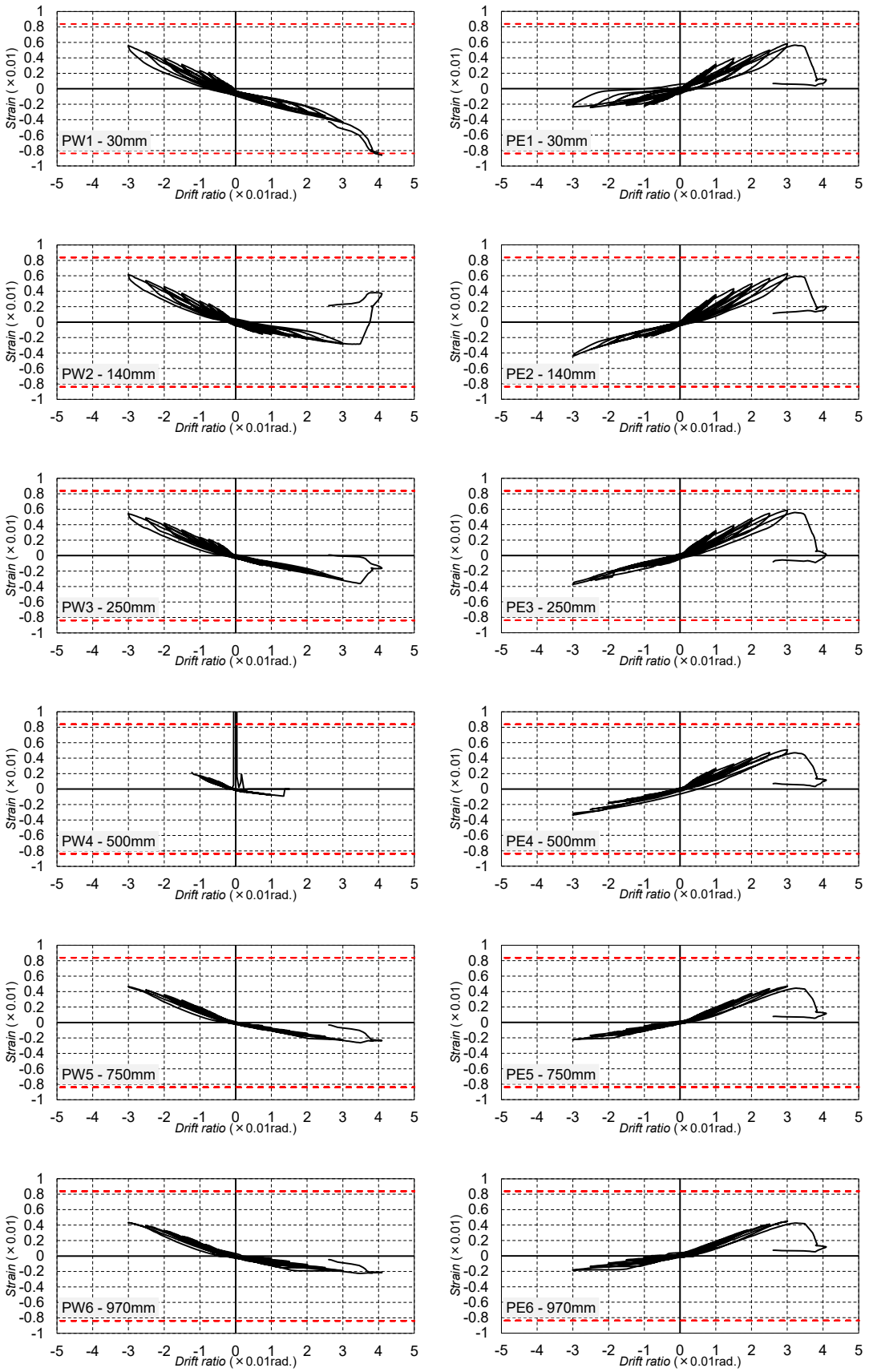

(b) W20-FU-15

Fig. 2.3-13 Continued

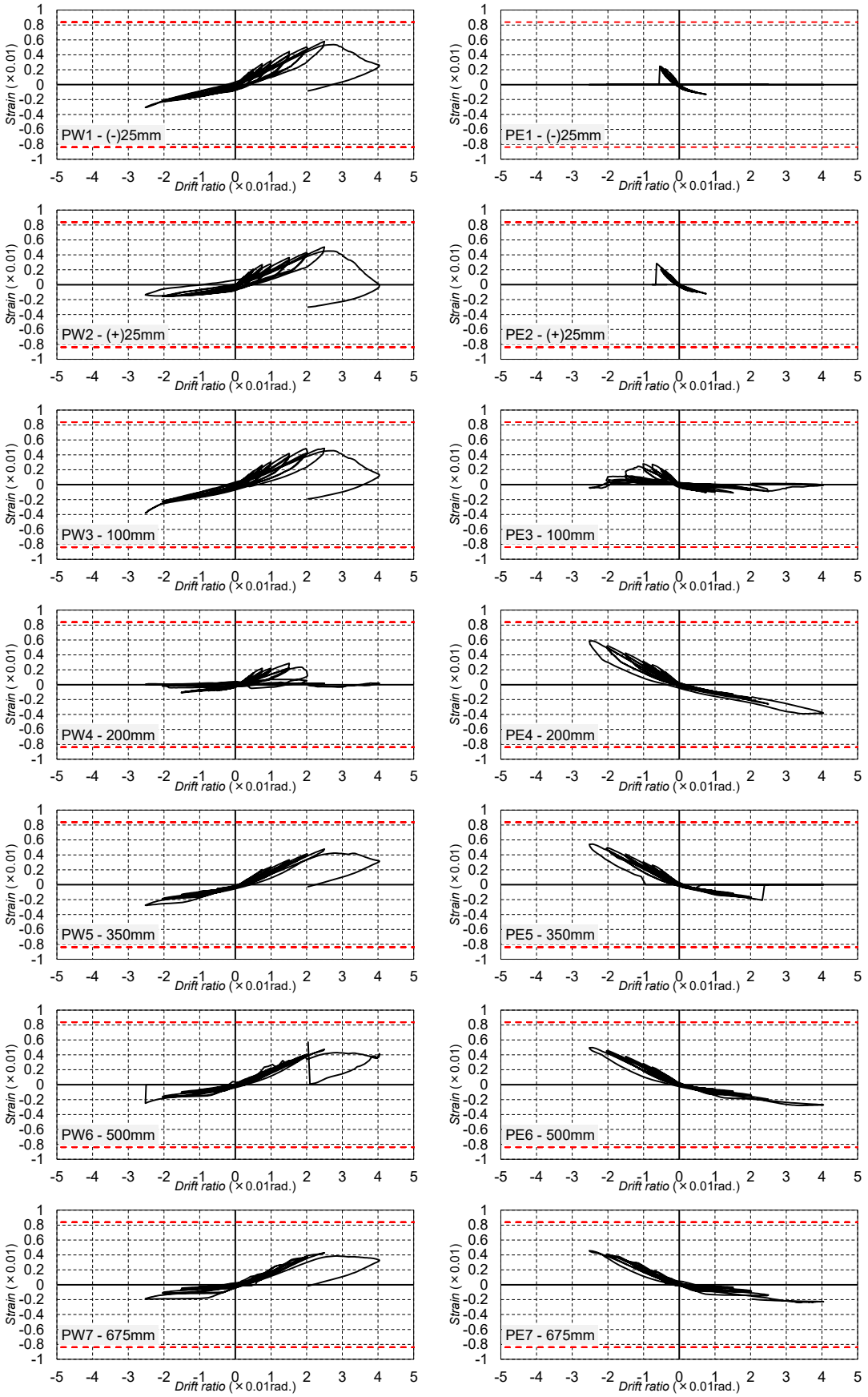

(c) W15-HU-15

Fig. 2.3-13 Continued

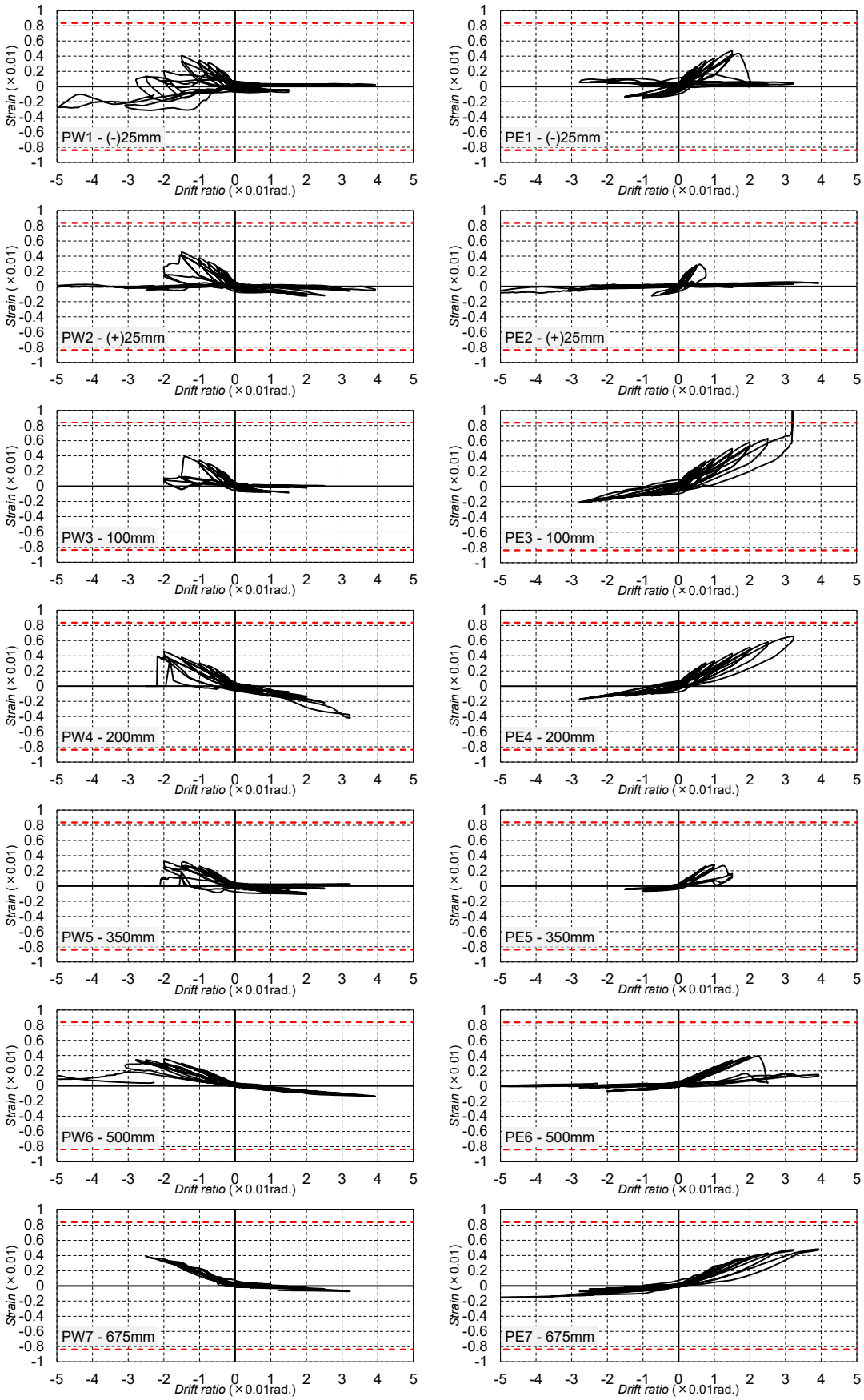

(d) W15-HU-073

Fig. 2.3-13 Continued

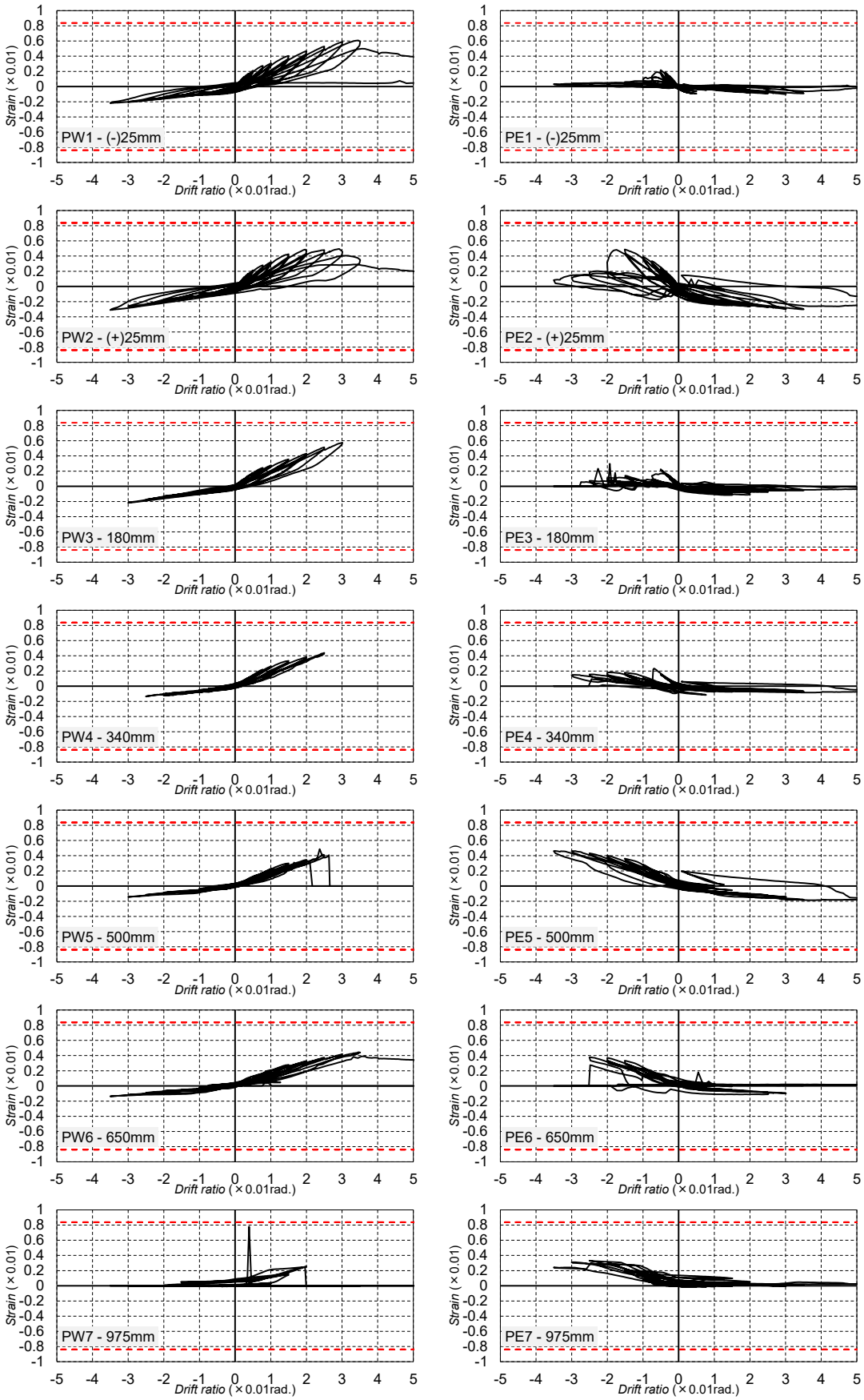

(e) W20-HU-073

Fig. 2.3-13 Continued

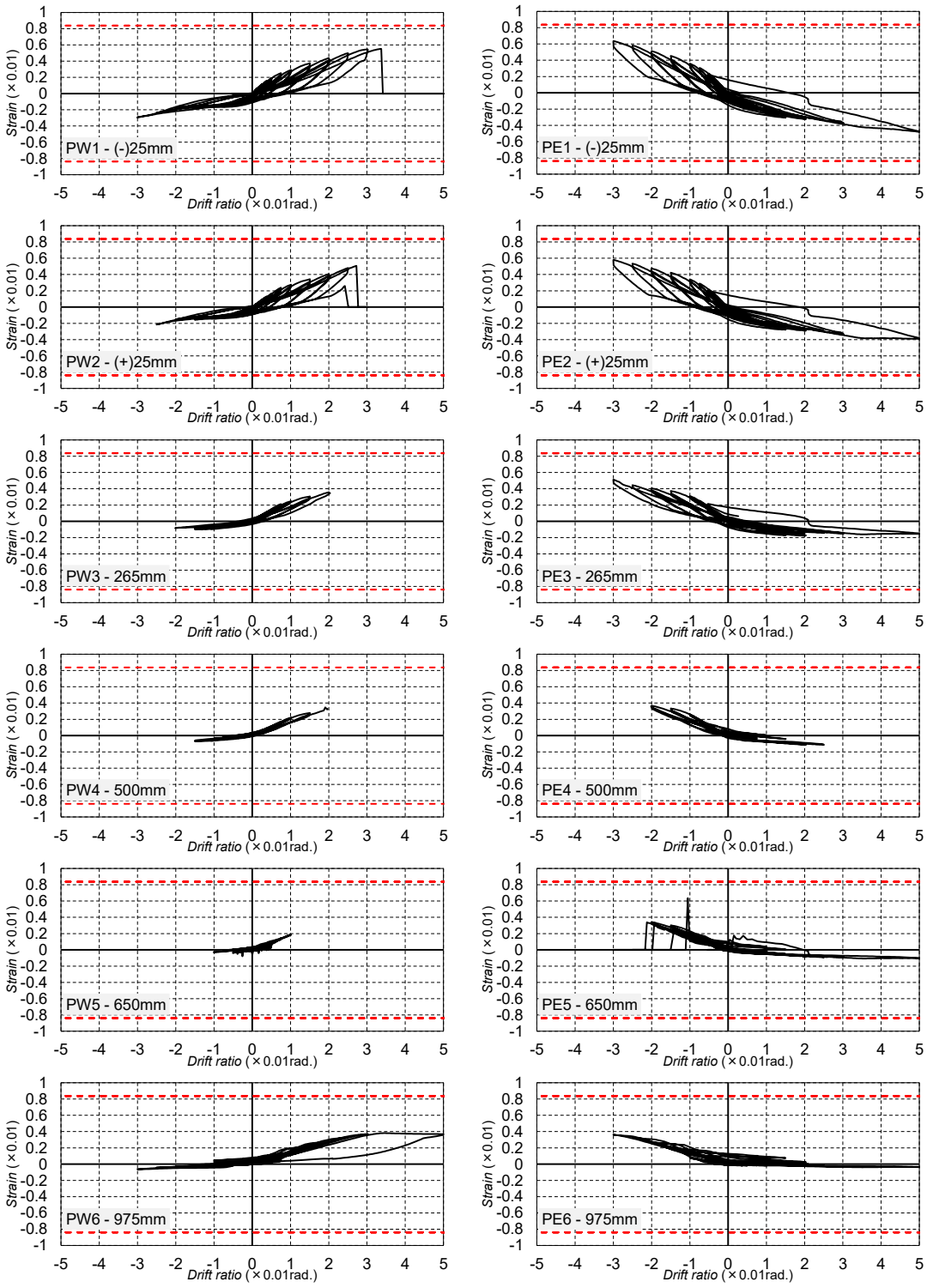

(f) W25-HU-073

Fig. 2.3-13 Continued

Fig. 2.3-14 indicates the strain profiles of concentrated rebars along the height of wall panels measured at the targeted drift ratios. The vertical red dashed lines in Fig. 2.3-14 represent the yield strains. And only the maximum tensile strains on the initially tensile side at each several controlling drift ratios were shown in Fig. 2.3-14. It is apparent that the strains of SD345 rebars tended to concentrated within the end region of wall panel about 0.5D (D is the depth of wall section about 600mm), and extreme low strains were measured at the top of the wall panel even at large deformation.

The strains measured in SBPDN rebars indicated similar behaviors to those of SD345 rebars till drift ratio reached 0.75%. However, after that drift level, the strains of SBPDN rebars exhibited a nearly uniform distribution along the height of wall panel, regardless of the shear span and axial load ratio and arrangement of DL bars. Low bond strength of SBPDN rebar made it possible for the axial strain to be transmitted from the limited plastic hinge region of shear walls to the adjacent region, where concentrated rebars have been conventionally assumed as remaining in elastic region. It is this transmission of axial strain along the entire length of rebars that delays the yielding of SBPDN rebars, and enables the lateral resistance force of RC walls reinforced by SBPDN rebars to keep increasing along with deformation and mitigating damage degree.

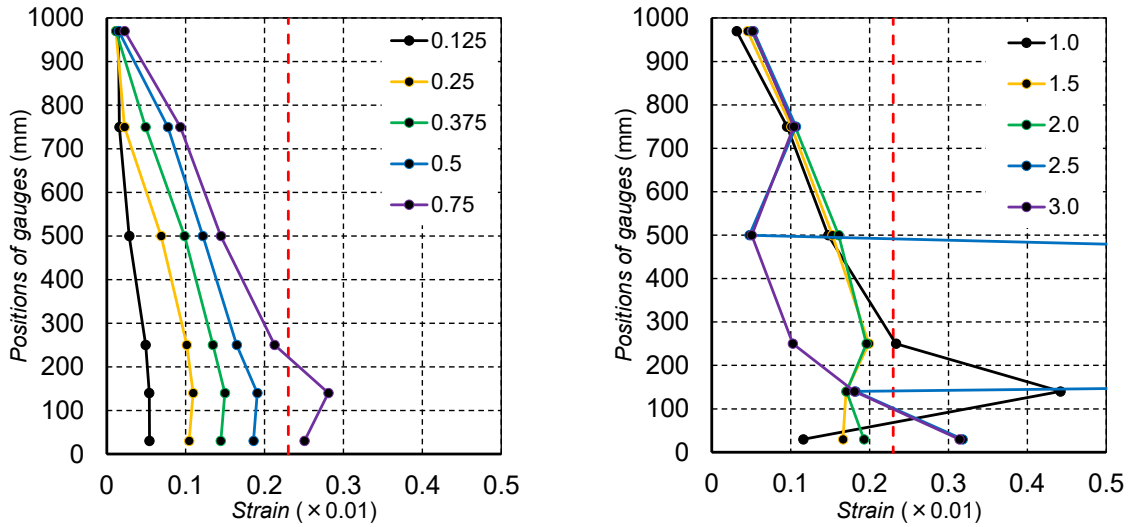

（1）R=0.125～0.75%.　　（2）R=1.0～3.0%.

(a) W20-FD-15

Fig. 2.3-14 Strains distribution of concentrated rebars

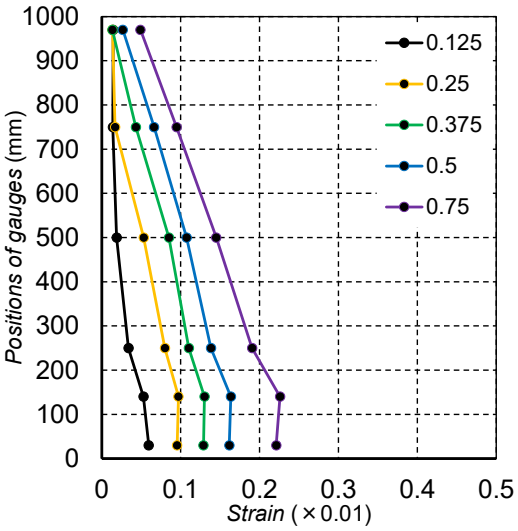

（1）R=0.125～0.75%.

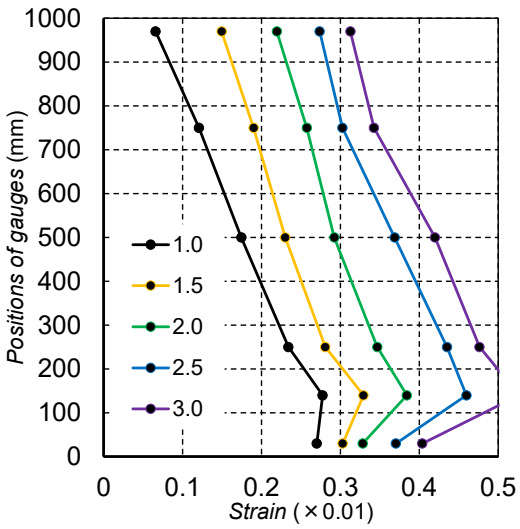

（2）R=1.0～3.0%.

(b) W20-FU-15

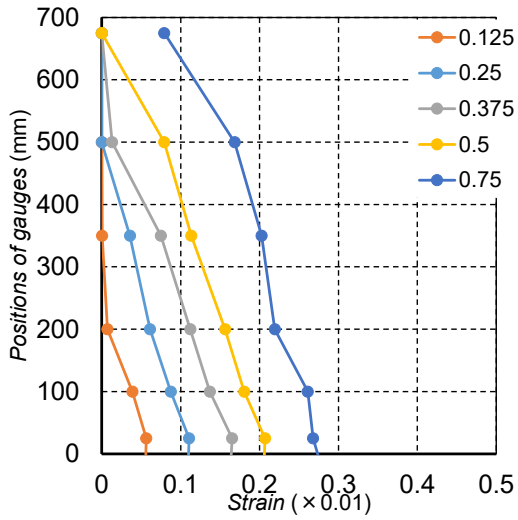

（1）R=0.125～0.75%.

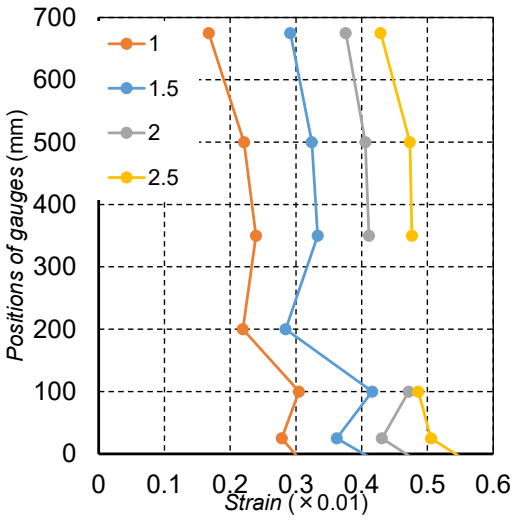

（2）R=1.0～2.5%.

(c) W15-HU-15

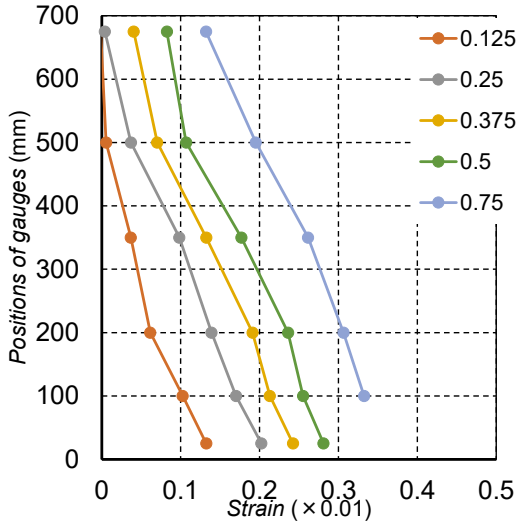

（1）R=0.125～0.75%.

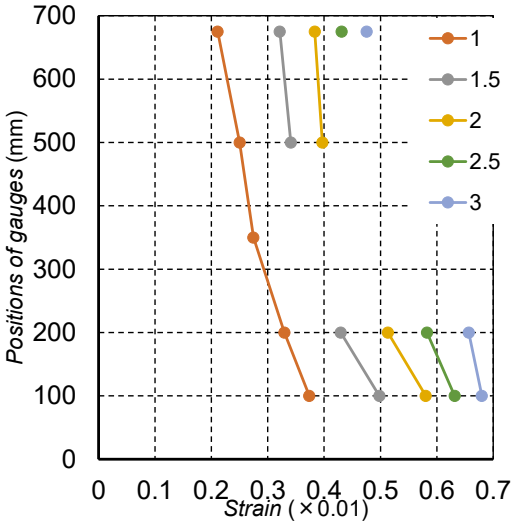

（2）R=1.0～3.0%.

(d) W15-HU-073

Fig. 2.3-14 Continued

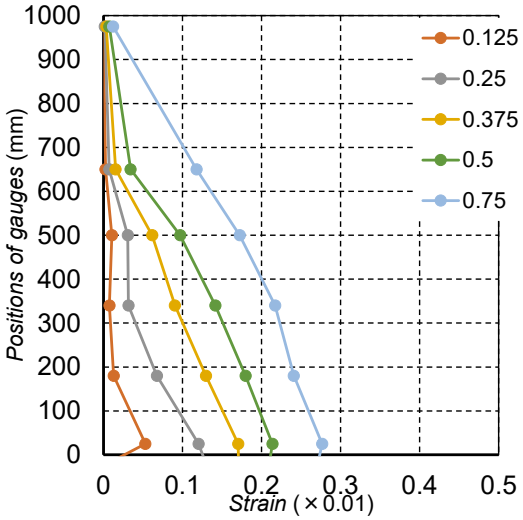

（1）R=0.125～0.75%.

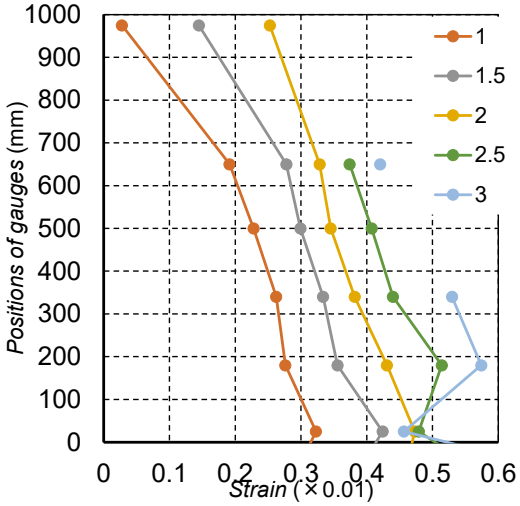

（2）R=1.0～3.0%.

(e) W20-HU-073

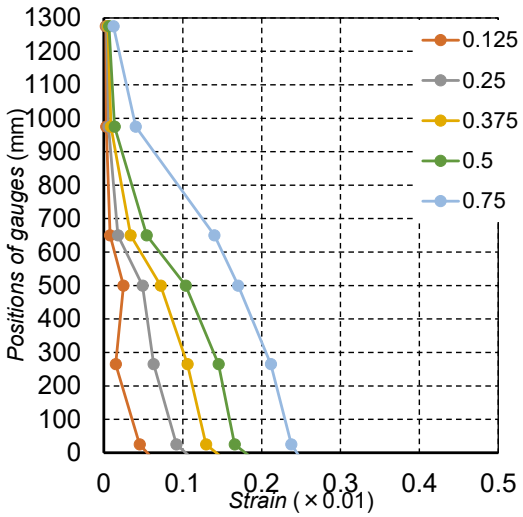

（1）R=0.125～0.75%.

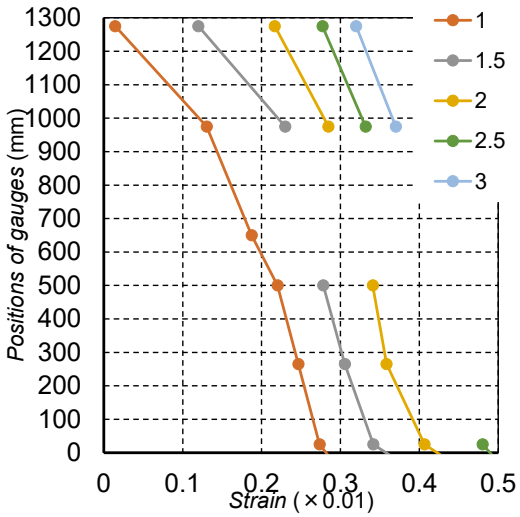

（2）R=1.0～3.0%.

(f) W25-HU-073

Fig. 2.3-14 Continued

2.3.4 Overall vertical axial deformation

Fig. 2.3-15 shows the overall vertical axial strain ε_v of all specimens, which were measured when the drift ratio returned to zero after the first loading cycle of each controlling drift ratio. In these graphs, minus represents the shortening while plus means elongation of the wall panel, and the calculation of the overall vertical axial strain is defined by equation Eq. (2.3.4-1), in which H is the height of where the DTs located (H = 700mm, 1000mm, and 1300mm for specimen with shear span ratio of 1.5, 2.0, and 2.5 respectively), and δ is the measured deformation on east and west side by the relative DTs shown in Fig. 2.2-6.

$$\varepsilon_v = 0.5 \times (\delta_E + \delta_W) / H \qquad (2.3.4\text{-}1)$$

(a) Effect of the type of concentrated rebars: one can be seen from Fig. 2.3-15(a) that after the yielding of SD345 rebars, specimen W20-FD-15 was elongated along with the increase of drift ratio. While since the concentrated SBPDN rebars of specimen W20-FU-15 did not yield, its overall axial almost remained at the same level.

(b) Effect of axial load ratio: because different axial load ratios were applied for specimen W15-HU-15 and W15-HU-073, the specimen with lower exhibited less axial deformation, but they showed the same tendency till drift ratio of 2.0%. However, after that drift level, since W15-HU-15 was finally failed by failure, its overall axial strain decreased quickly. On the other hand, due to the insufficient reinforcement at the beam-concealed column joint, the wall panel was 'pulled out'.

(c) Effect of the arrangement of DL bars and axial load ratio: since the DL bars of specimen W20-FU-15 yielded and buckled, the axial strain of this specimen slightly increased till drift ratio of 1.5%. and then slightly decreased. On contrary, since no yielding and local buckling of DL bars were confirmed for specimen W20-HU-073, the axial strain of this specimen kept increasing from the beginning.

(d) Effect of the shear span ratio: all specimens in this group exhibited similar behavior, that they were all elongated from the beginning. While, the ascent of overall axial strain of the specimen with higher shear span ratio tend to be more sharply than those of specimen with lower shear span ratio.

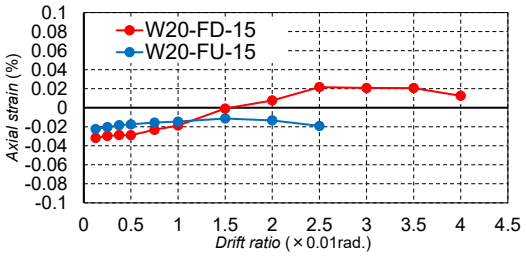

(a) Effect of the type of concentrated rebars

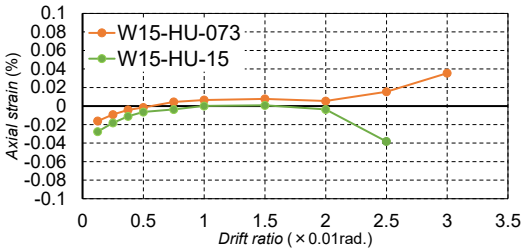

(b) Effect of axial load ratio

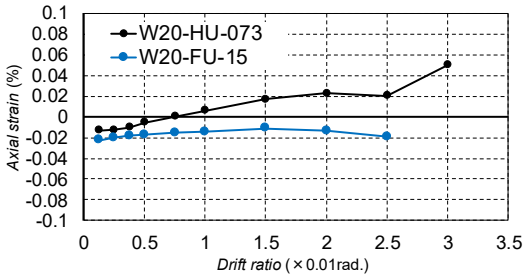

(c) Effect of the arrangement method of DL bars and axial load ratio

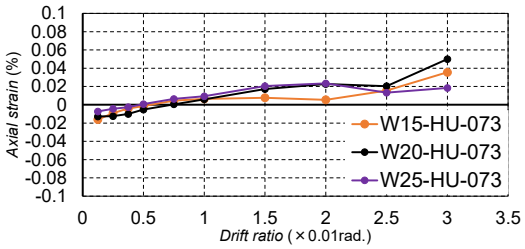

(d) Effect of shear span ratio

Fig. 2.3-15 Measured overall axial strain

2.3.5 Residual drift ratio

Fig. 2.3-16 shows the average residual drift ratio of the initially push and pull directions measured at each targeted drift level. One can be seen in Fig. 2.3-16(a) that no difference was observed in the measured residual deformation among specimens W20-FD-15 and W20-FU-15 till drift ratio reached 0.75%. After that drift on, due to the to the yielding of the SD345 concentrated rebars, the sharp increase of residual drift ratio observed in specimen W20-FD-15. On the other hand, the residual drift ratios of specimens with SBPDN rebars became much smaller than that of specimen with SD345 rebars.

The test results indicated that regardless of the axial load ratio, shear span ratio, and the arrangement method of DL bars, the residual drift ratios of RC walls reinforced by SBPDN rebars could be kept below 0.4%. to 0.6%. after being unloaded at R = 3.0%. It is also interesting to be noticed from Fig. 2.3-16(b) and Fig. 2.3-16(d) that the RC walls that has higher shear span ratio or axial load ratio, which were reinforced by SBPDN rebars, left slightly less residual deformation. Moreover, Fig. 2.3-16(b) also indicates that the new arrangement method of DL bars influences little on the residual deformation till drift ratio of 1.5%. but after that drift on, the residual drift ratio of specimen W20-FU-15 became larger than those of specimen W20-HU-073, this could be considered as the results of the yielding of DL bars.

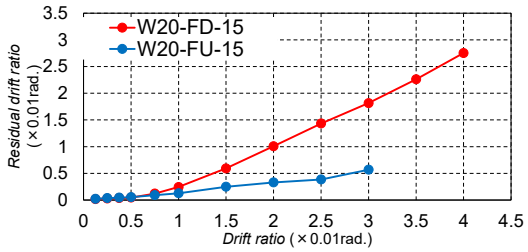

(a) Effect of the type of concentrated rebars

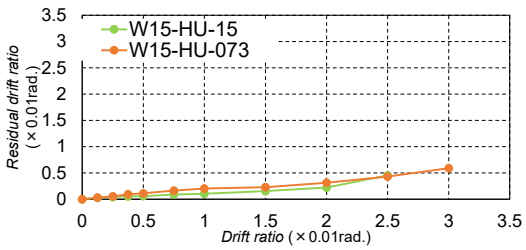

(b) Effect of axial load ratio

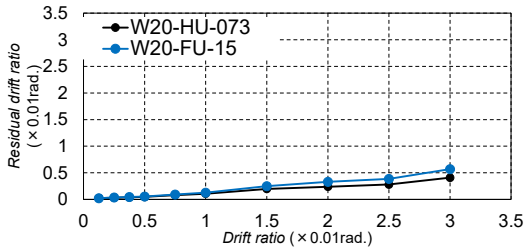

(c) Effect of the arrangement of DL bars and axial load ratio

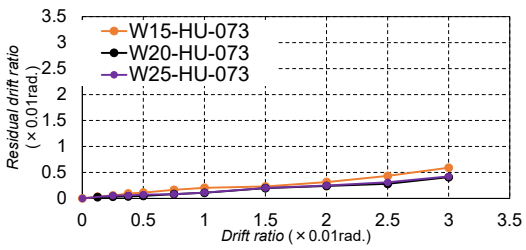

(d) Effect of shear span ratio

Fig. 2.3-16 Measured residual drift ratios

2.3.6 Equivalent viscous damping (Energy dissipation capacity)

To evaluate the seismic energy absorption capacity of RC shear walls, the equivalent viscous damping coefficient h_{eq} that is proposed by Jacobsen was applied as an index, and calculation details of h_{eq} can be found in [2.4]. Fig. 2.3-17 shows the measured equivalent viscous damping coefficient versus drift angle relationships for all specimens.

As obvious in Fig. 2.3-17(a), the energy dissipation capacity of specimen reinforced by SD435 rebars and SBPDN rebars were almost the same before drift ratio reached 0.75%. However, from that drift ratio on, after the concentrated rebars of specimen W20-FD-15 yielded, the h_{eq} of specimen W20-FD-15 exhibited abrupt increase along with drift ratio. On the other hand, as can be noticed that all shear walls reinforced by SBPDN rebars indicated stable energy absorption capacity with a nearly constant equivalent viscous damping coefficients until drift ratio reached 3.0%. which can be considered that the drift hardening RC shear walls behaved in an approximately nonlinear elastic manner until R = 3.0%. Moreover, the difference caused by axial load level, shear span ratio, and the arrangement method of DL bars was not significant, which indicated that the h_{eq} is mainly influenced by the concentrated rebars of RC shear walls.

Although according to the comparison of h_{eq} between ductile and drift hardening shear walls, that the duty of earthquake energy dissipation was not mainly carried by the later one, it is worth noticed the fact that higher h_{eq} indicates more unrepairable damage, so it is still necessary to evaluate the energy dissipation capacity because it will be the important index to design dampers, which can dissipate the most energy and can be easily and economically replaced after major earthquake.

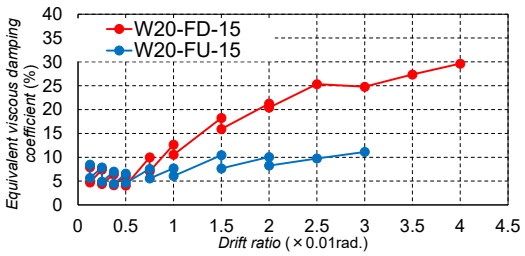

(a) Effect of the type of concentrated rebars

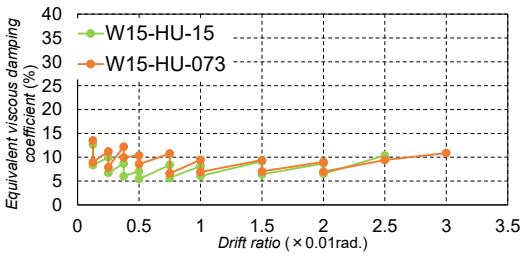

(b) Effect of axial load ratio

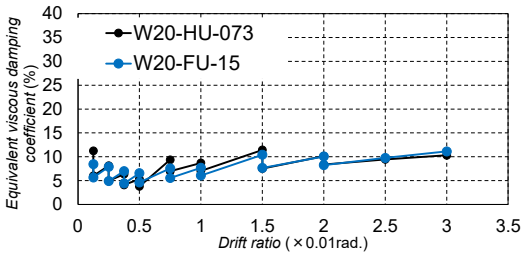

(c) Effect of the arrangement of DL bars and axial load ratio

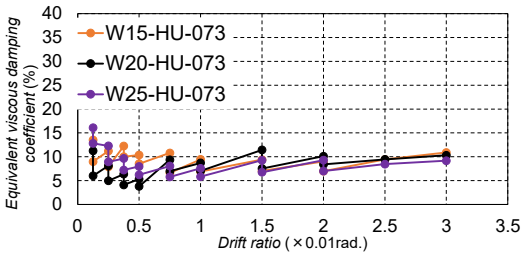

(d) Effect of shear span ratio

Fig. 2.3-17 Measured equivalent viscous damping coefficients

2.4 Conclusions

In order to avoid premature shear failure of reinforced concrete (RC) walls with SBPDN rebars, this chapter proposes a new arrangement of distributed longitudinal (DL) bars in the wall panel with the DL bars not being anchored into the adjacent beams. For the purpose of verifying the seismic performance of the combination of SBPND rebars and the new arrangement method for DL bars, a total of six 1/3-scale cantilever rectangular concrete walls were fabricated and tested under reversed cyclic lateral loading while subjected to constant axial load. Besides the arrangement method of DL bars, the other main experimental variables included the steel type of the concentrated rebars (SD345 (D13) deformed bars and SBPDN1275/1420 (U12.6) bars), the shear span ratio (1.5, 2.0, and 2.5), and the axial load ratio (0.073 and 0.15). Based on the experimental works described in this chapter, the following conclusions cab be drawn:

1) For specimens whose DL bars were anchored into the adjacent beams, the specimen reinforced by (SD345 (D13) deformed bars showed excellent ductility and energy absorption capacity. The utilization of SBPDN rebars at the edge zones of wall section could assure RC walls high and stable lateral load resistance up to the drift ratio of 3.0% under axial load with axial load ratio of 0.15.

2) For specimens with axial load ratio of 0.073, regardless of their shear span ratio, SBPDN rebars could provide obvious drift hardening capability till drift ratio of 3.5%. Combination with the new arrangement of DL bars could mitigate the damage of concrete near the wall toes, and prevent the wall with shorter shear span from premature shear failure. Experimental results also implied that the adjacent members should be stiff enough to take full advantage of the new arrangement method.

3) Larger axial load ratio resulted in larger initial stiffness and maximum lateral resistance force,

on the other hand, decreased the deformation capability of drift hardening concrete walls from 3.5% to 2.5% or 3.0% depending on the amount of distributed horizontal bars within the potential hinge region of the wall panel.

4) For all the rectangular RC shear walls reinforced by SBPDN rebars, regardless of their shear span ratio, axial load ratio and the arrangement of DL bars, the residual drift ratio can be controlled as low as 0.6%., after the walls experienced large drift ratio of up to 3.0%. This residual drift ratio is only one third of that measured in the test wall reinforced with normal-strength deformed rebars SD345.

5) For the shear walls with the new arrangement method, measured axial strain in the DL bars indicated that when the specimen under larger lateral deformation, the D6 DL bars in the wall panel might resist some of the axial stress caused by bending moment. Therefore, to accurately evaluate the ultimate capacities of the walls whose DL bars are not anchored into the adjacent beams, the influence of DL bars should be taken into consideration.

References

[2.1] Wallace JW, "Performance of structural walls in recent earthquakes and tests and implications for US building codes", 15th World Conference on Earthquake Engineering, 2012.

[2.2] Sun Y. et al. (2006): Analytical Study of Cyclic Response of Concrete Members Made of High-Strength Materials, the Eighth U.S. National Conference on Earthquake Engineering, Paper No. 1581.

[2.3] Architectural Institute of Japan (AIJ). Standard for structural calculation of reinforced concrete structures. Japan: Maruzen Co. Ltd; 2010.

[2.4] Fujitani T. et al. (2018), "Effect of the type of concentrated rebars on seismic performance and evaluation of rectangular RC cantilever shear walls", Proceedings of the JCI, 40(2), pp. 313-318, (in Japanese).

[2.5] Funato Y., Sun Y., Takeuchi T., and Cai G., "Modeling and Application of Bond Characteristic of High-strength Reinforcing Bar with Spiral Grooves," Proceedings of the Japan Concrete Institute, V.34, No.2, 2012, pp.157-162, (in Japanese).

CHAPTER THREE

Influence of construction method on seismic behaviors of concrete walls reinforced by SBPDN rebars

3.1 Introduction

As described in Chapter two, the utilization of weakly bonded ultra-high strength rebar (referred to as SBPDN rebar) in the edge zones of wall section could assure reinforced concrete walls drift-hardening capability up to the drift ratio of 3.0%., and the combination with the new arrangement of distributed longitudinal (DL) bars in wall panel could mitigate the damage of concrete near the wall toes, and prevent the drift-hardening concrete wall with shorter shear span from premature shear failure. Moreover, since the DL bars need not be anchored into foundation, it may provide a potential construction method for precast concrete walls.

The precast concrete walls system provides an economical construction system for structural industry [3.1]. Comparing with the cast-in-place concrete walls, the precast walls are relatively easy to manufacture and extremely energy efficient. However, in seismically active regions, the use of precast concrete structural systems has primarily been limited to low rise structures [3.2]. The main reason for their exclusion from use in medium and high-rise applications is the lack of knowledge of how this type of construction will perform when hit by strong earthquakes. Another problem is that the connection to the foundation has to resist the overturning moments caused by lateral load [3.3]. The resistance to overturning moment from lateral seismic loading appears as a vertical force couple at the wall edge zones as shown in Fig. 3.1-1. Because the moment arm of the lateral force is generally larger than the wall length, at one base connection, a large uplift force is created, while at the other base corner, a compression force is developed.

The capacity of the corner tension connector is limited due to the thin wall section where the connector plate must be anchored [3.4].

As shown in Fig. 3.1-1, this chapter proposes a new connection method for precast concrete walls reinforced by SBPDN rebars aiming at developing precast DHC walls. As displayed in Fig. 3.1-1, the connector, which consists of nuts and washer, is simply embedded into the foundation. It was expected that this method can fully take the advantages of using SBPDN rebars at the wall-base joint for precast concrete walls. The primary objectives of this chapter are listed below:

1) To obtain experimental information on the seismic performance of precast concrete walls reinforced with SBPDN rebars and fabricated by the proposed connection method.

2) To verify if the use of SBPDN rebars can provide precast concrete shear walls the same drift-hardening capability and deformability as the walls that are fabricated by conventional construction method.

3) To investigate the influence of axial load ratio and shear span ratio on the seismic performance of precast concrete shear walls.

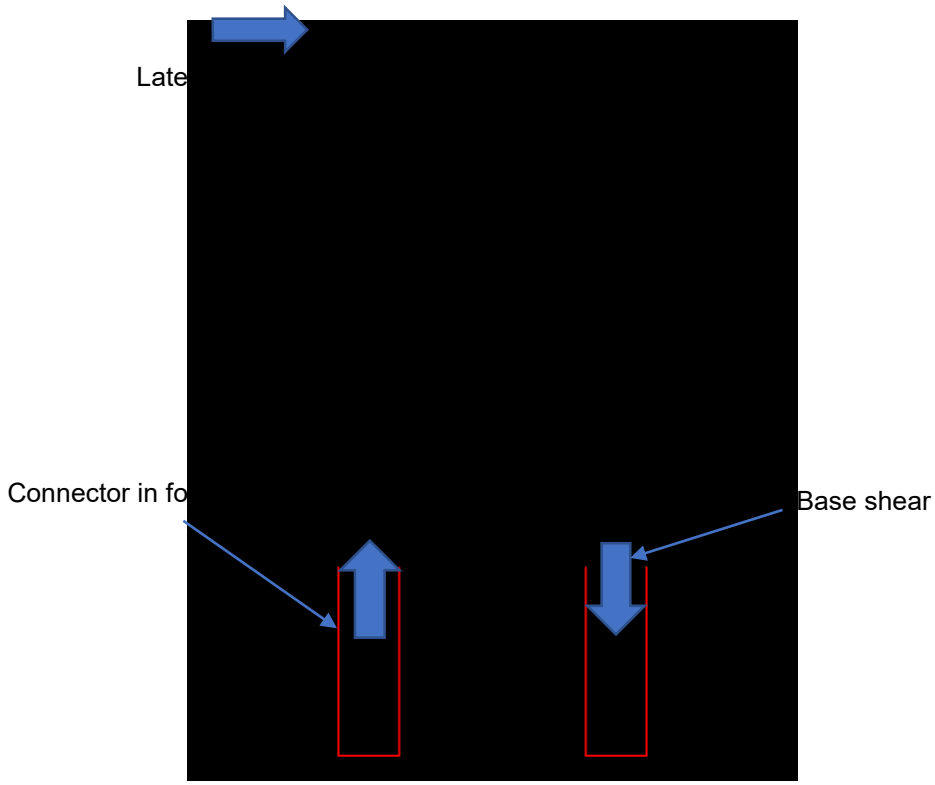

Fig. 3.1-1 Concept of the proposed connection method

3.2 Experimental program

3.2.1 Outlines of test specimens

To achieve the aforementioned goals of this chapter, a total of five 1/3-scale cantilever rectangular concrete shear walls were designed, fabricated, and tested under reversed cyclic lateral loading while subjected to constant axial load. All the specimens were fabricated by the proposed precast method as shown in Fig. 3.2-1. To be specific, the wall panel with the concentrated SBPDN rebars and the bottom base were fabricated separately, two sheath ducts were embedded into bottom base to make it hollow as the connector, and the surfaces of concrete at the wall-base joint were made uneven to increase the bond between concrete and the grouting material.

Fig. 3.2-1 Assembly of the precast wall

The experimental variables included, 1) the shear span ratio, 2) the applied axial load ratio, and 3) the diameter of sheath ducts.

Fig. 3.2-2 indicates the dimensions and reinforcement details of the specimens, while Table 3.2-1 lists the primary experimental parameters along with the main test results. As can be seen from Table 3.2-1 and Fig. 3.2-2, all specimens had the rectangular section of 150mm in thickness and 600mm in depth. The specimen of W15-Series had a shear span of 900 mm to give a shear span ratio of 1.5. As for specimens of W20-Series, their shear spans were 1200 mm to give a shear span ratio of 2.0.

The steel amount of distributed longitudinal (DL) bars and distributed horizontal (DH) bars in wall panel as well as of SBPDN rebars is the same for all test walls. The DL bars consisted of twenty D6 deformed bars uniformly placed with a spacing of 59 mm to give a steel ratio of 0.70%., while the DH bars were comprised of D6 deformed bars with a spacing of 65 mm. The DL bars were anchored at wall panel ends with 180-degree hooks as shown in Fig. 3.2-2, and the DH bars were placed in a closed form to sustain shear force and provide effective confinement effect. Eight SBPDN rebars with nominal diameter of 12.6mm were placed at the edge zones of wall panel. each SBPDN rebar was anchored to a steel plate (having a thickness of 9mm) by bolts at both ends. In addition, D6 deformed bars with a space of 65mm (less than 6 times the diameter of the concentrated rebars) were applied as transverse confinement to prevent the initial local buckling of concentrated rebars.

An axial load ratio (n) of 0.15 were applied for specimen WP15-D10H35-15 and WP20-D10H35-15, while n = 0.075 for the other specimens except WP20-D10H35-073 had an n of 0.073.

The diameters of sheath ducts for WP15-D12H35-075 and WP20-D12H35-075 were 120 mm, while the diameter of 100 mm for the rest of the tested specimens.

Table 3.2-1 Primary experimental parameters and main test results

Specimen	a/D	n	f'_c (N/mm^2)	f'_g (N/mm^2)	Longitudinal rebars		Concentrated SBPDN rebars		Transverse rebars		D_s	E_s	Q_{exp}
					Type	ρ_{wv}(%.)	Type	ρ_s(%.)	Type	ρ_{wh}(%.)	(mm)	(mm)	(kN)
WP15-D10H35-15	1.5	0.15	32.37	64.56	20-D6 Not Fixed	0.70	8-U12.6	0.58	D6@65	0.65	100	310	289
WP15-D12H35-075		0.075	34.95	52.95							120		262
WP20-D10H35-073	2.0	0.073	36.13	56.77							100		229
WP20-D10H35-15		0.15	44.91	63.49									248
WP20-D12H35-075		0.075	44.67	73.94							120		200

a/D: shear span ratio; n: axial load ratio; f'_c: concrete cylinder strength; f'_g: cylinder strength of grouting materials; ρ_{wv}: reinforcement ratio of longitudinal rebars; ρ_s: reinforcement ratio of concentrated rebars; ρ_{wh}: volumetric ratio of transverse reinforcement; D_s: diameter of sheath ducts; E_s: embedment depths of sheath ducts; Q_{exp}: measured maximum lateral force (average);

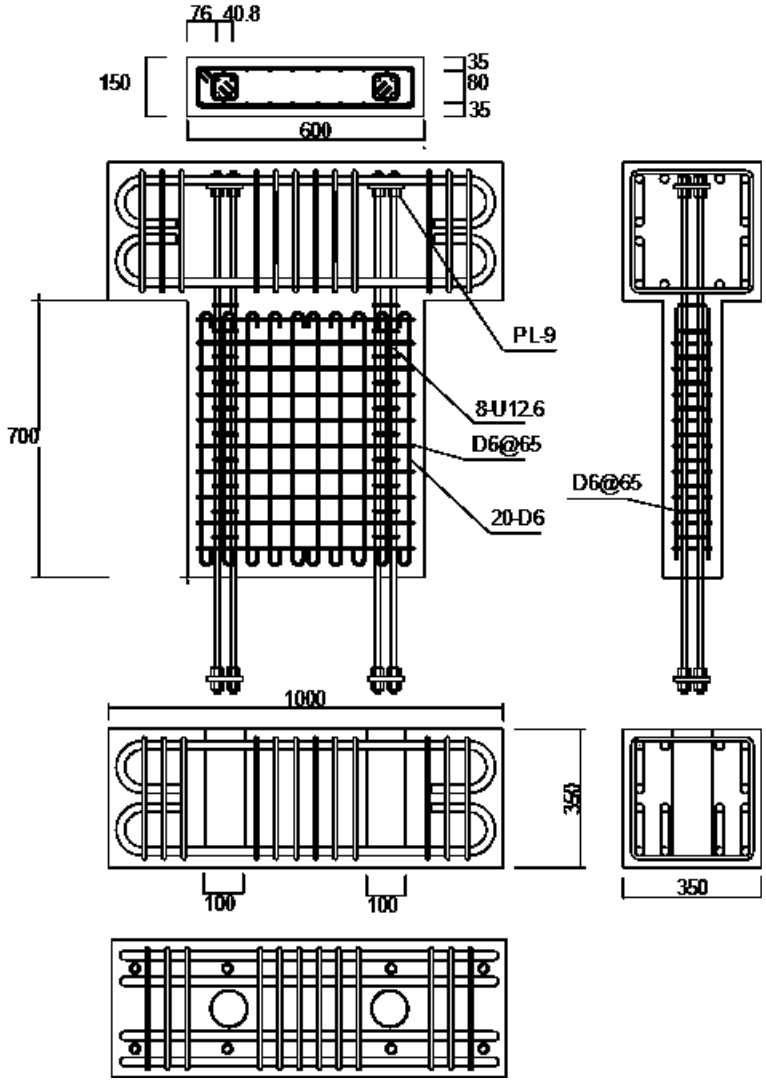

(a) WP15-D10H35-15

Fig. 3.2-2 Reinforcement details of test shear walls (Unit: mm)

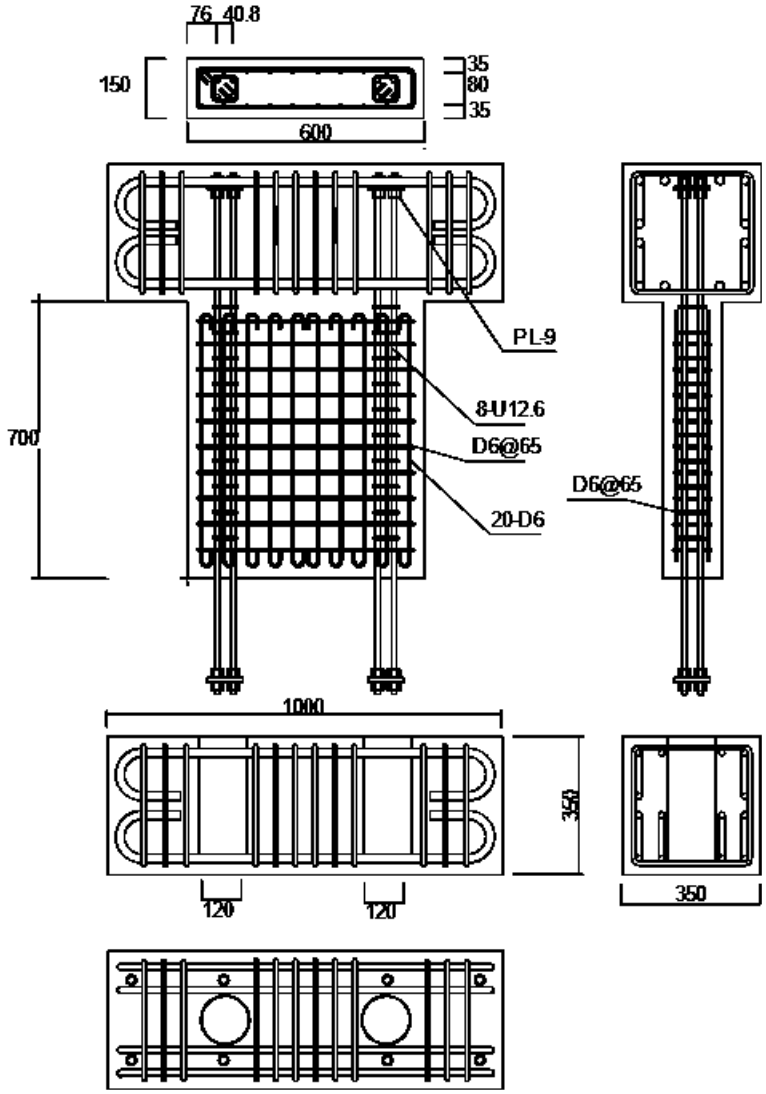

(b) WP15-D12H35-075

Fig. 3.2-2 Continued

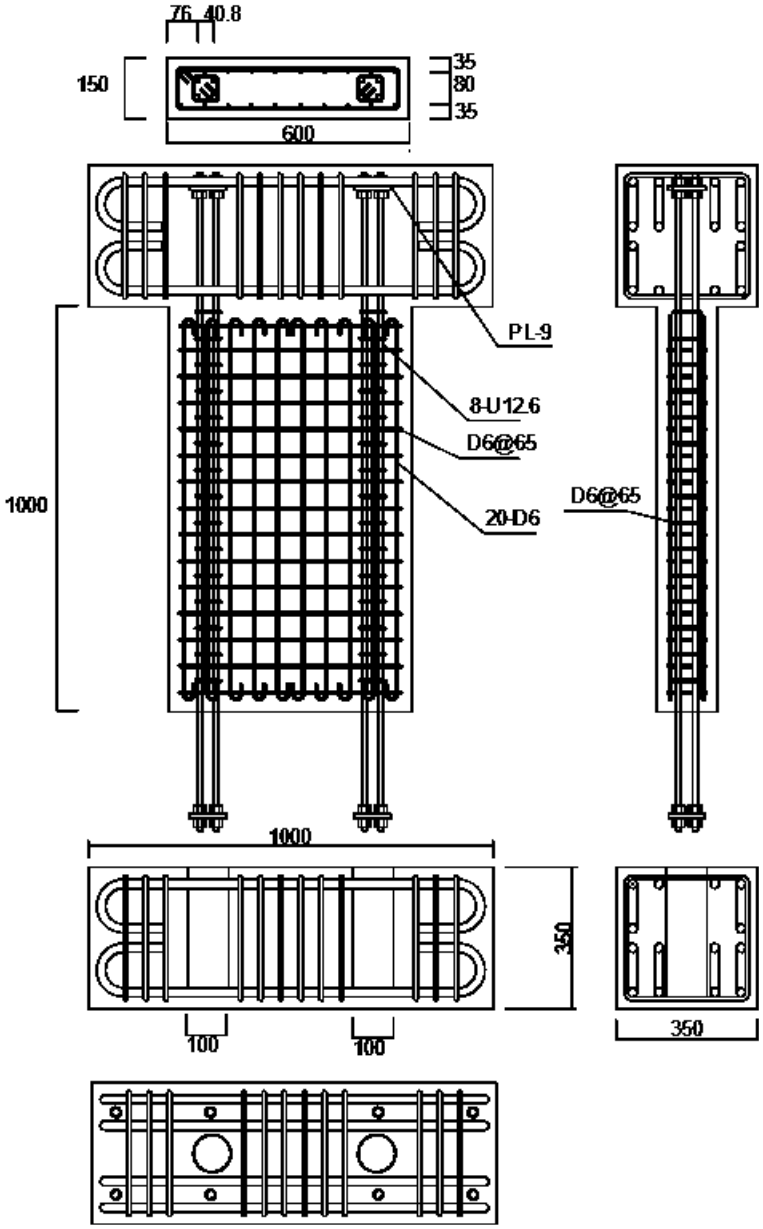

(c) WP20-D10H35-073 and WP20-D10H35-15

Fig. 3.2-2 Continued

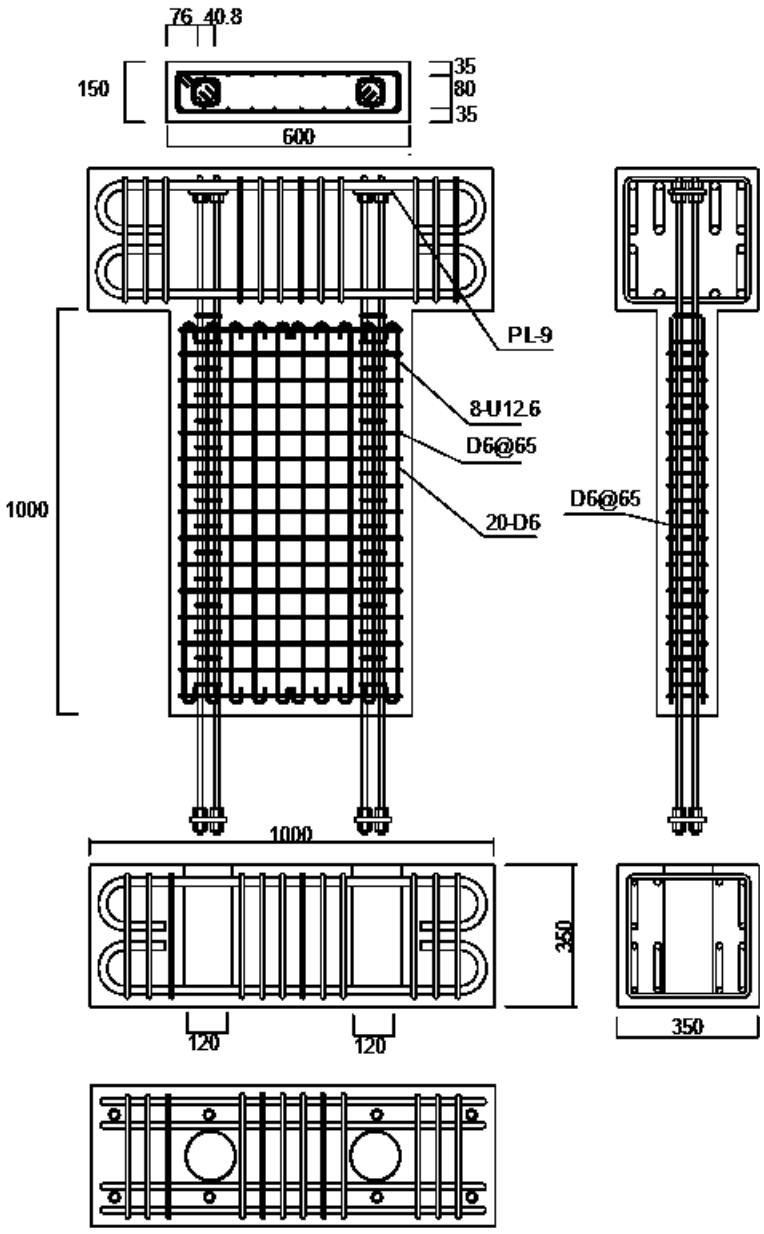

(d) WP20-D12H35-075

Fig. 3.2-2 Continued

3.2.2 Material properties

The ultra-high strength SBPDN 1275/1420 rebar with yield strength of about1380 MPa and spiral grooves on its surface as shown in Fig. 3.2-3. Mechanical properties together with the tensile stress-strain curves of the used steels are summarized in Table 3.2-2 and Fig. 3.2-4 separately. As the SBPDN 1275/1420 rebar did not exhibit apparent yield plateau in their stress-strain relations, the yielding strengths of them were determined by the 0.2%. offset yielding method.

U12.6 (SBPDN1275/1420)

Fig. 3.2-3 Surface of the concentrated rebars

(a) D6 rebars (SD295A)

D6	E_s (kN/mm^2)	f_y (N/mm^2)	ε_y (×0.01)	f_u (N/mm^2)
No.1	187.96	379.9	0.202	511.8
No.2	181.04	387.4	0.214	515.5
No.3	183.37	393.6	0.215	523.5
Average	184.13	386.96	0.210	516.95

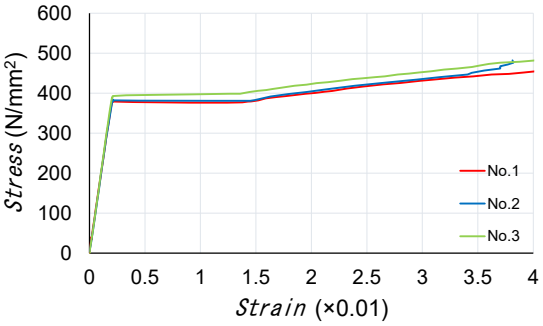

(b) U12.6 (SBPDN1275/1420)

U12.6	E_s (kN/mm^2)	f_y (N/mm^2)	ε_y (×0.01)	f_u (N/mm^2)
No.1	213.90	1377.8	0.844	1461.6
No.2	208.00	1373.0	0.860	1456.8
No.3	213.20	1387.4	0.846	1460.0
Average	211.70	1379.38	0.850	1459.47

※0.2%. offset method was used.

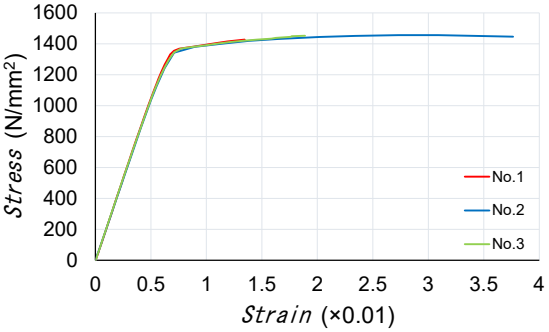

Table 3.2-2 Mechanical properties of the steels

Fig. 3.2-4 Stress-strain relationships of the steels

Note

E_s : Young's modulus
f_u : ultimate stress
f_y : yield stress
ε_y : yield strain

Ready-mixed concrete made of Portland cement and coarse aggregates with maximum particle size of 20mm was used to fabricate the specimens. Table 3.2-3 shows the mix proportions of concrete along with measured slumps and air contents. Concrete strengths were evaluated at the same day of loading by testing three standard cylinders (diameter: 100mm, height: 200mm), which were cured under the same condition to the shear walls, and test results are shown in Table 3.2-1 for each specimen.

Table 3.2-3 Mix proportions for concrete

Date	W/C	Water (kg/m^3)	Cement (kg/m^3)	Fine aggregate (kg/m^3)	Coarse aggregate (kg/m^3)	Additives	Slump (mm)	Air content (%.)
2019/10/01	0.57	180	316	869	882	2.94	212	3.8
2020/08/04				883	879		201	4.9
2020/08/26							184	4.1

The #1000-series sheath ducts with spiral groove on its surface, which are made of galvanized steel sheet according to Japanese standard JIS G3302, were applied in this experiment and shown in Fig. 3.2-5.

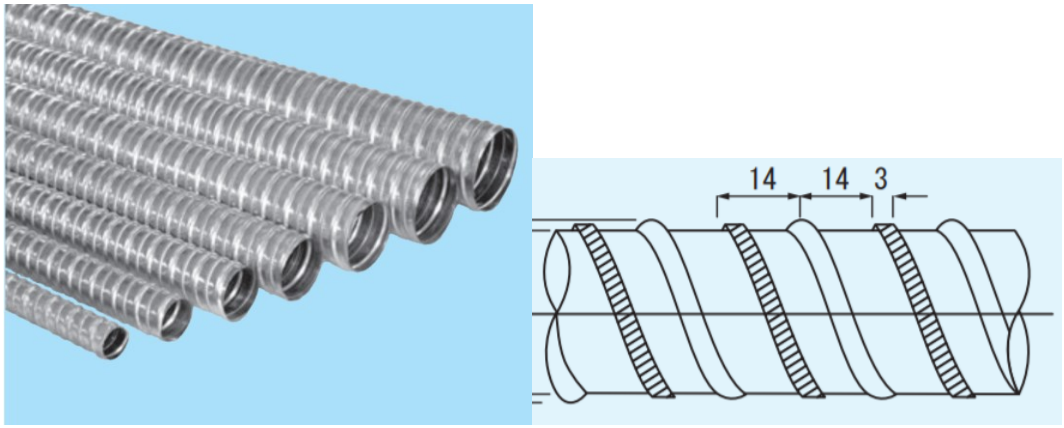

Fig. 3.2-5 Surface of the applied sheath ducts

A cementitious non-shrinkage mortar that excels in fluidity named PRE U-LOX was used as the grouting material for this experiment, and its material properties for each pack are summarized in Table 3.2-4. As shown in Fig. 3.2-5, the cement was completely mixed up by a hand mixer more than 120 second as is recommended. Compression strength of grouting material were evaluated at the same day of loading by testing three standard cylinders (diameter: 50mm, height: 100mm), which were cured more than 21 days under the same condition to the shear walls, and according to Japanese standard JIS A 1108, compression strength of grouting material is expected to beyond 60 N/mm^2 and test results are shown in Table 3.2-1 for each specimen.

Fig. 3.2-5 Mixing of the grouting material

Table 3.2-4 Mix properties for each pack of grouting material

Water (kg)	Cement (kg)	Mix temperature (°C)	Density (kg/L)	Volume (L)	Expansion and contraction rate (%.)	Static elastic modulus ($\times 10^4$ N/mm^2)
4.5	25	20	2.213	13	+0.24	2.95

3.2.3 Test setup and loading program

The experiments were conducted using the setup shown in Fig. 3.2-6. The loading apparatus was designed to subject the shear wall to reversed cyclic lateral load and constant axial compression. A vertical hydraulic jack with a capacity of 1000 kN, which was connected to stiff loading frame via a roller, was used to apply constant axial compression. The reversed cyclic lateral load was applied by two 500 kN horizontal hydraulic jacks. The lateral loading was controlled by drift ratio (R), which is defined as the ratio of the lateral displacement at the loading point of lateral force (Δ) to the shear span (a) of each shear wall, and the east direction was applied as the initial tensile direction (plus direction).

The loading program is shown in Fig. 2.2-5. To find out the first flexure or shear crack, the lateral loading was initially controlled by force before reaching drift ratio of 0.125%. After then, two complete loading cycles were applied at each specified level of targeted drifts (0.25%., 0.375%., 0.5%., 0.75%., 1%., 1.5%., and 2%.), and one cycle was applied at each level of targeted drift after drift ratio was beyond 2%.

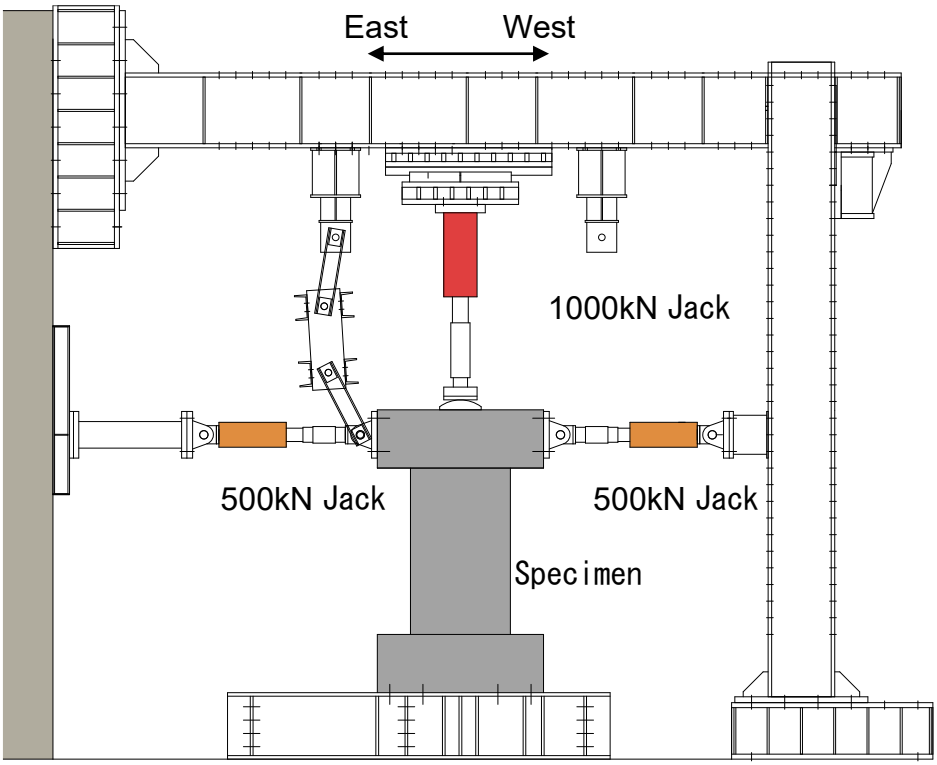

Fig. 3.2-6 Schematic view of test setup for shear walls

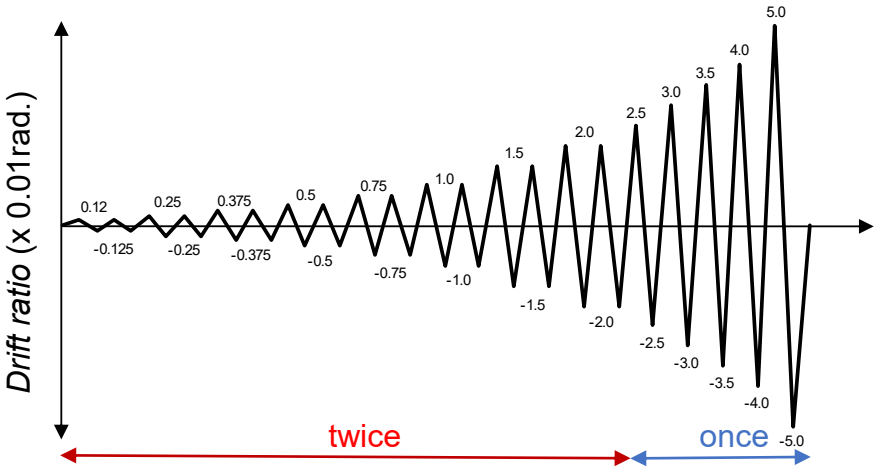

Fig. 3.2-7 Loading program

3.2.4 Instrumentation and measurement

Fig. 3.2-8 shows the locations of displacement transducers (DTs) for the tested specimens with the shear span ratio of 1.5(a) and 2.0(b) respectively. As shown in Fig. 3.2-8, two DTs were installed to measure the lateral displacement, and the average value measured by DTs No.1 and 2 were used as the lateral displacement of specimen. The other eight (four pairs of) DTs No.5 to 12 were installed to measure the local vertical displacement at several targeted heights of specimens. Besides, DTs No.3 and 4 were applied to record the rotation while No.13 for recording the horizontal displacement of the rigid bottom stub. Overall view of testing is shown in Fig. 3.2-9.

To measure the axial strain generated in the rebars of the walls, strain gauges were embedded for each specimen. Details of these measurements can be found in Fig. 3.2-10. Red, green, and blue marks represent the locations of embedded strain gauges for LD rebars, HD rebars and concentrated rebars separately.

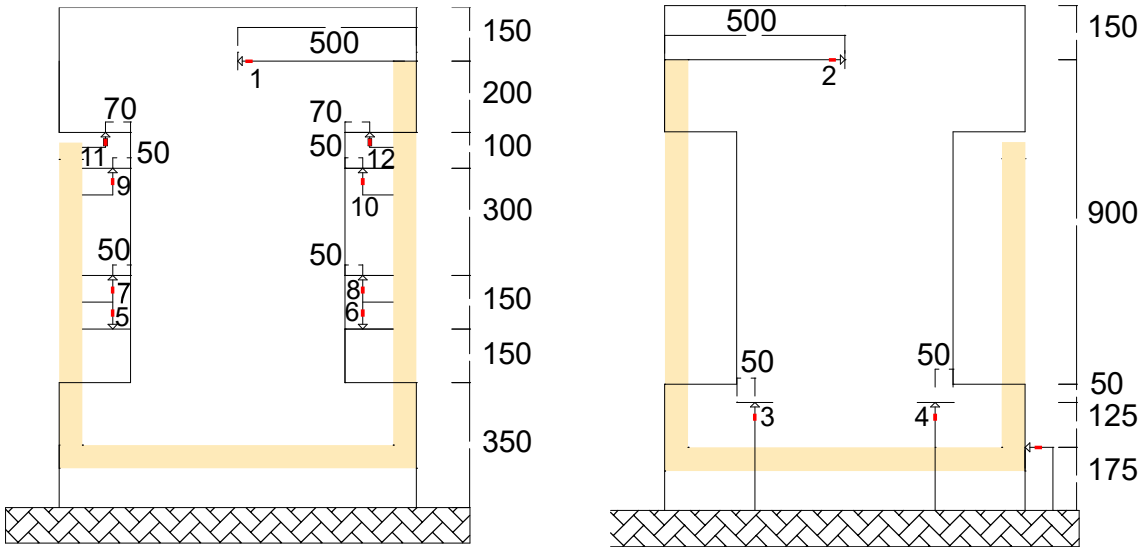

(1) North (2) South

(a) WP15-Series

Fig. 3.2-8 Positions of displacement transducers (DTs) (Unit: mm)

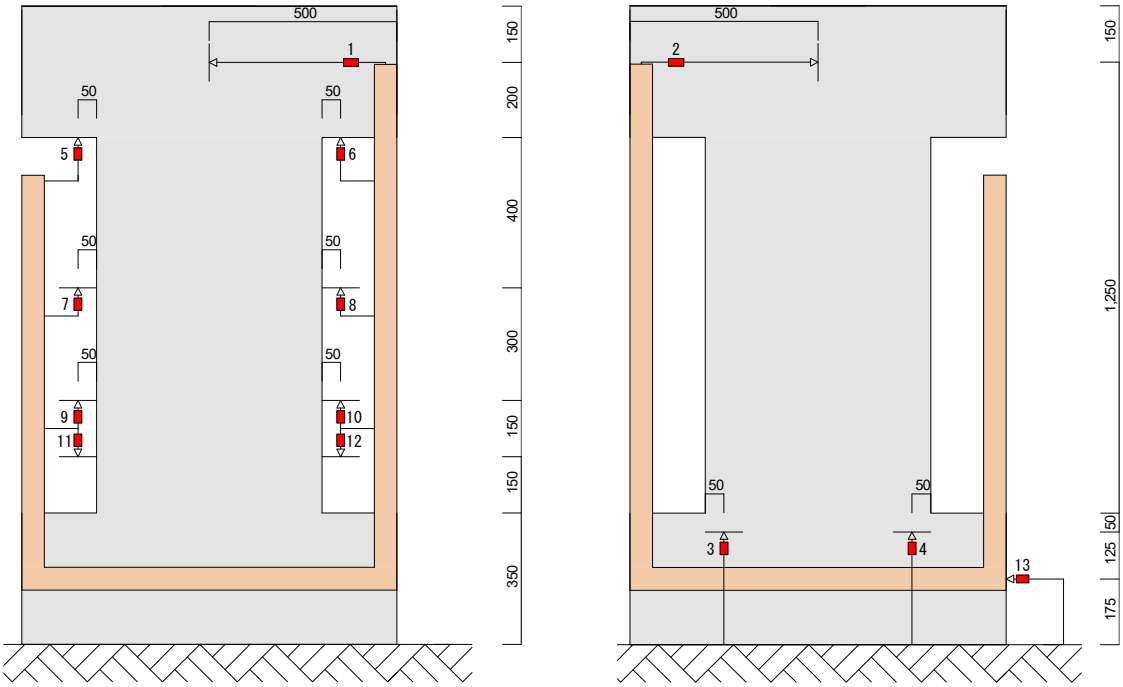

(1) North (2) South

(b) WP20-Series

Fig. 3.2-8 Continued

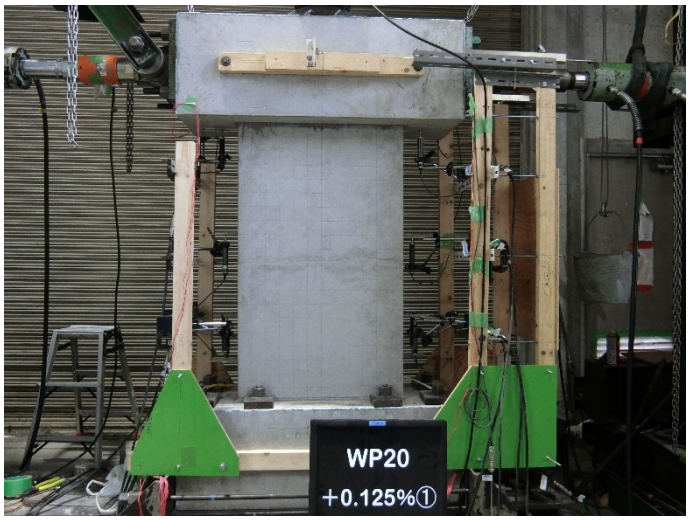

Fig. 3.2-9 Overall view of a testing specimen

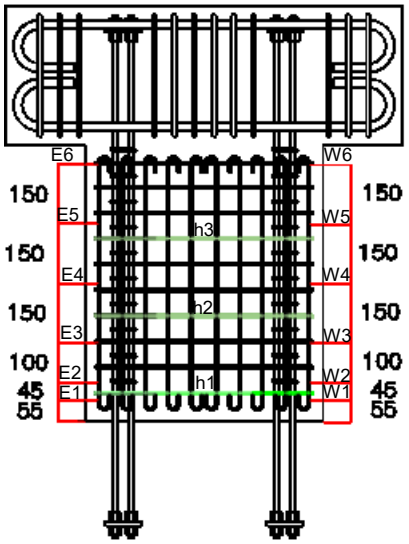

(1) Wall web

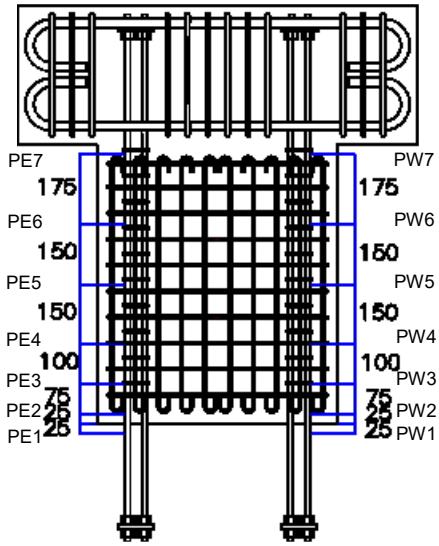

(2) Concentrated rebars

(a) WP15-Series

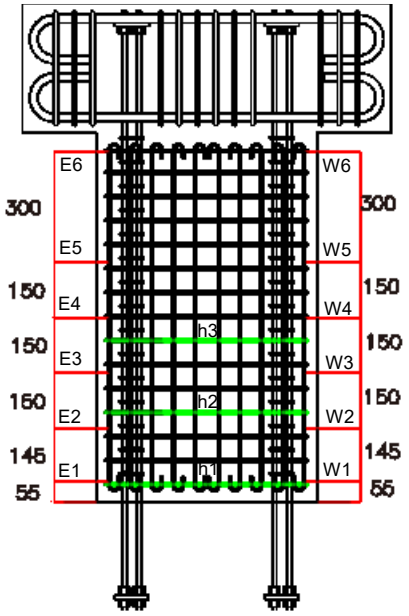

(1) Wall web

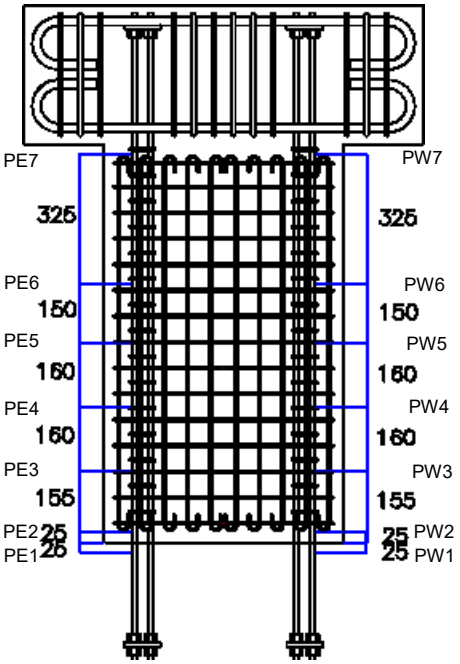

(2) Concentrated rebars

(b) WP20-Series

Fig. 3.2-10 Locations of strain gages

3.3 Observed behaviors and results

3.3.1 Crack and damage of shear walls

This section summarized the developments of cracks that were observed from web side of each specimen. In the figures of this section, the grids have a spacing of 50 mm, the red lines and blue lines represent the cracks that were drawn at the peak drifts of the targeted levels in both push and pull direction of lateral loading, respectively, while the blacked portions express the spalled-off cover concrete.

For specimen WP15-D10H35-15, as shown in Fig. 3.3-1, the first flexure crack was confirmed at boundary between the grouting material and wall panel when lateral force reached 100kN. The first shear crack was found when lateral force reached 160kN. The initial spalling-off of concrete was observed at drift ratio of 1.0%. After that, as can be seen in Fig. 3.3-2(a) when drift ratio reached 1.5%., the cover concrete on the top surface of the foundation was lifted up. And obvious spalling-off of the concrete was first confirmed when drift ratio reached 2.0%. At the drift ratio of 4.0%, in order to watch the damage at wall-base joint, the crashed cover concrete at the wall toe on the west side was cleaned up, and as shown in Fig. 3.3-2(b), it was observed that the sheath ducts had been pulled out.

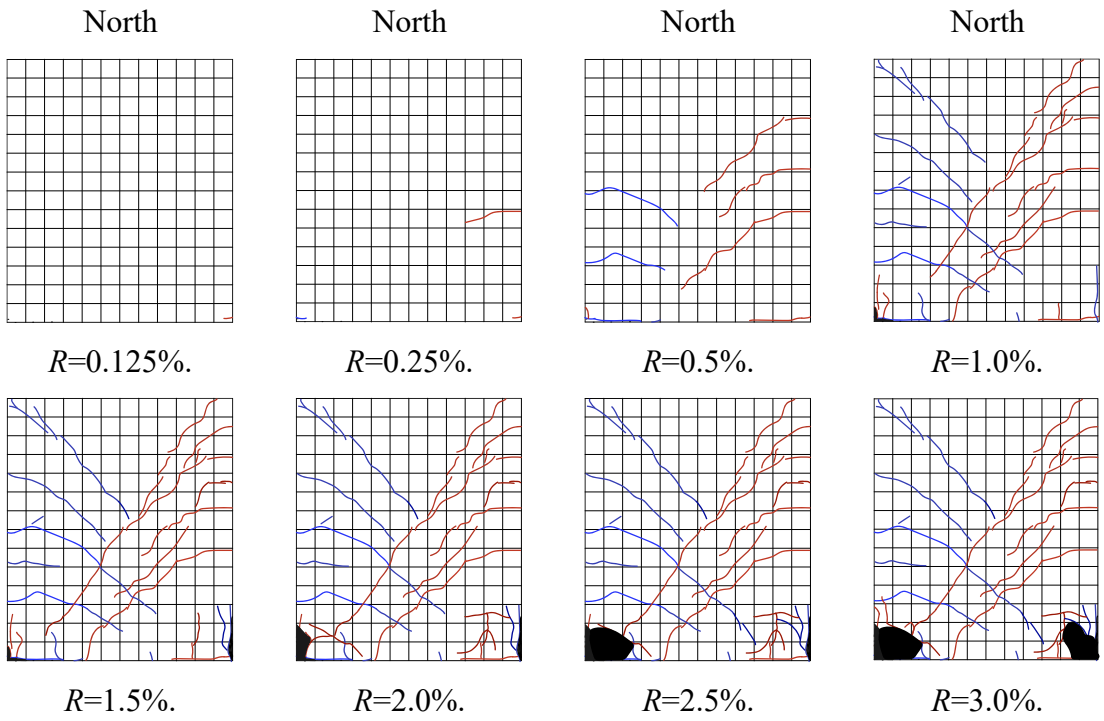

Fig. 3.3-1 Cracks patterns observed on specimen WP15-D10H35-15

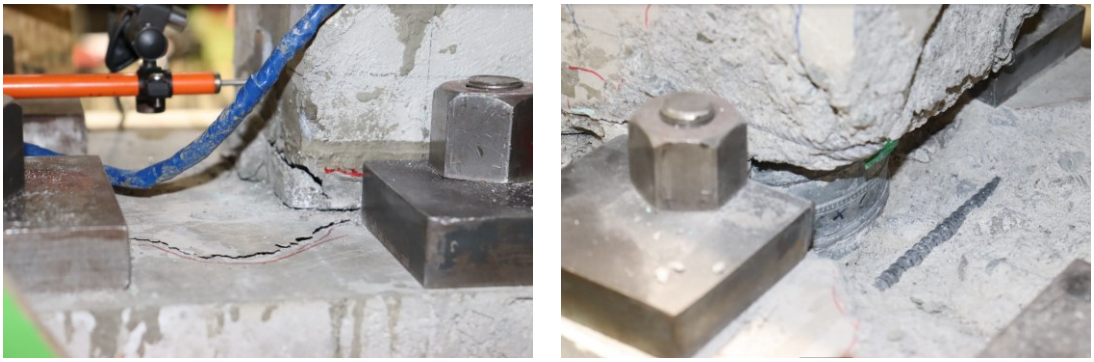

(a) R=1.5%. (b) R=4.0%.

Fig. 3.3-2 Damage observed on specimen WP15-D10H35-15

The first flexure crack was noticed at boundary between the grouting material and wall panel of specimen WP15-D12H35-075 when lateral force reached 40kN, as indicated in Fig. 3.3-3. The first shear crack was found when lateral force reached 120kN. Then, the first flexure crack run thought the surface of wall panel, which indicated that the concrete of wall panel was

completely separated from the grouting material at the drift ratio of 1.0%. After that, as can be seen in Fig. 3.3-4(a) when drift ratio reached 1.5%., the cover concrete on the top surface of the foundation was lifted up. Flaking of the cover concrete surface was observed at 2.0%., from that drift ratio, spalling off of the cover concrete visibly grown, and the exposure of the DH bars was fist confirmed at 2.5%. Similar to specimen WP15-D10H35-15, the sheath ducts had been found to be pulled out at the drift ratio of 4.0%. as displayed in Fig. 3.3-4(b).

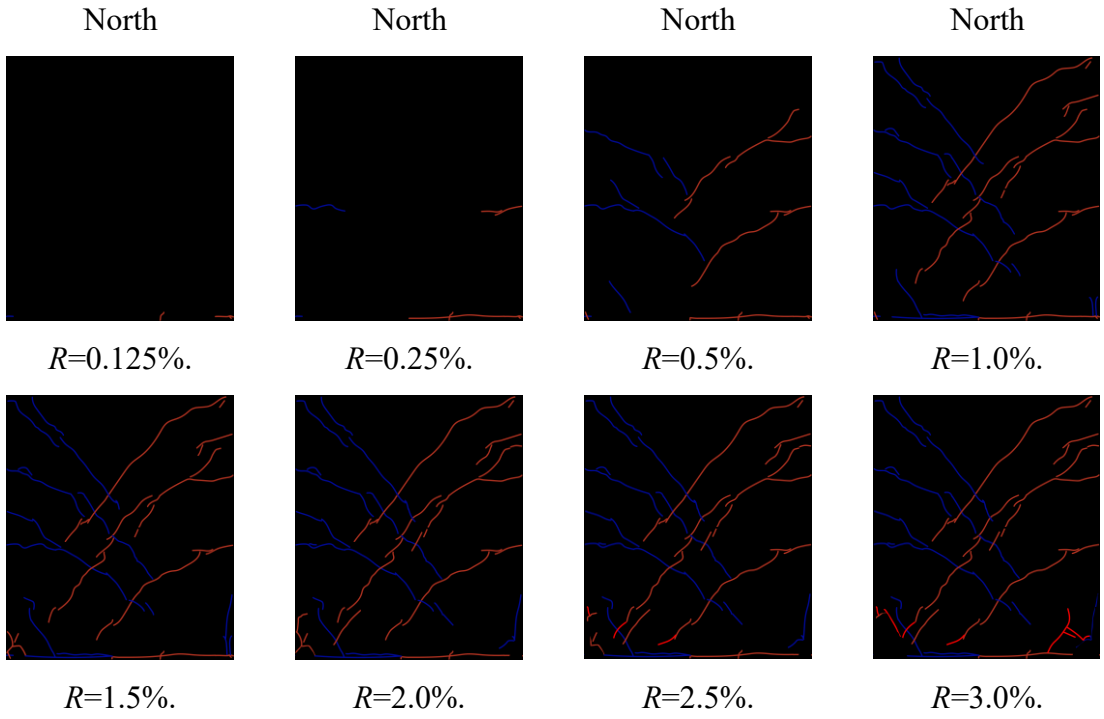

Fig. 3.3-3 Cracks patterns observed on specimen WP15-D12H35-075

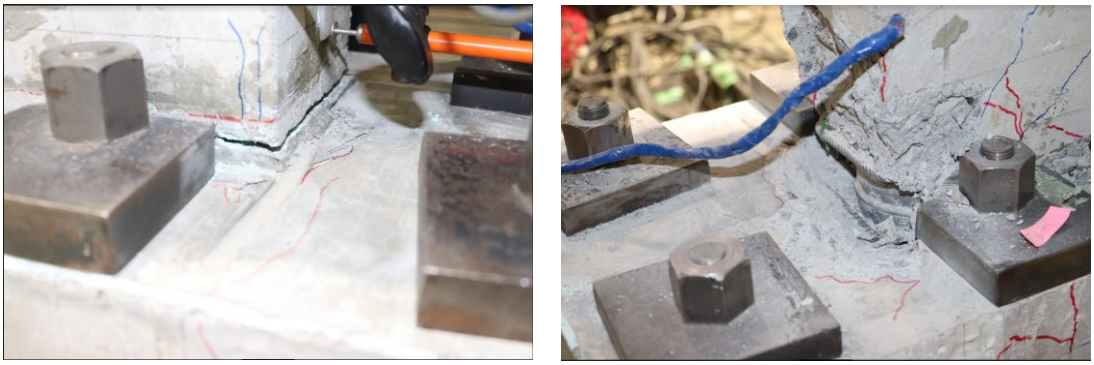

(a) R=1.5%. (b) R=4.0%.

Fig. 3.3-4 Damage observed on specimen WP15-D12H35-075

For specimen WP20-D10H35-073, the first flexure crack was noticed when drift ratio reached 0.125%., as indicated in Fig. 3.3-5, and the first shear crack was found at R = 0.375%. The initial flaking of concrete was observed at drift ratio of 1.5%. From that drift ratio on, spalling off of the cover concrete visibly grown till R = 2.5%. along with the exposure of the DH bars was fist confirmed. Then when drift ratio approached 3.0%, severe damage of concrete near wall-base joint was observed as shown in Fig. 3.3-6.

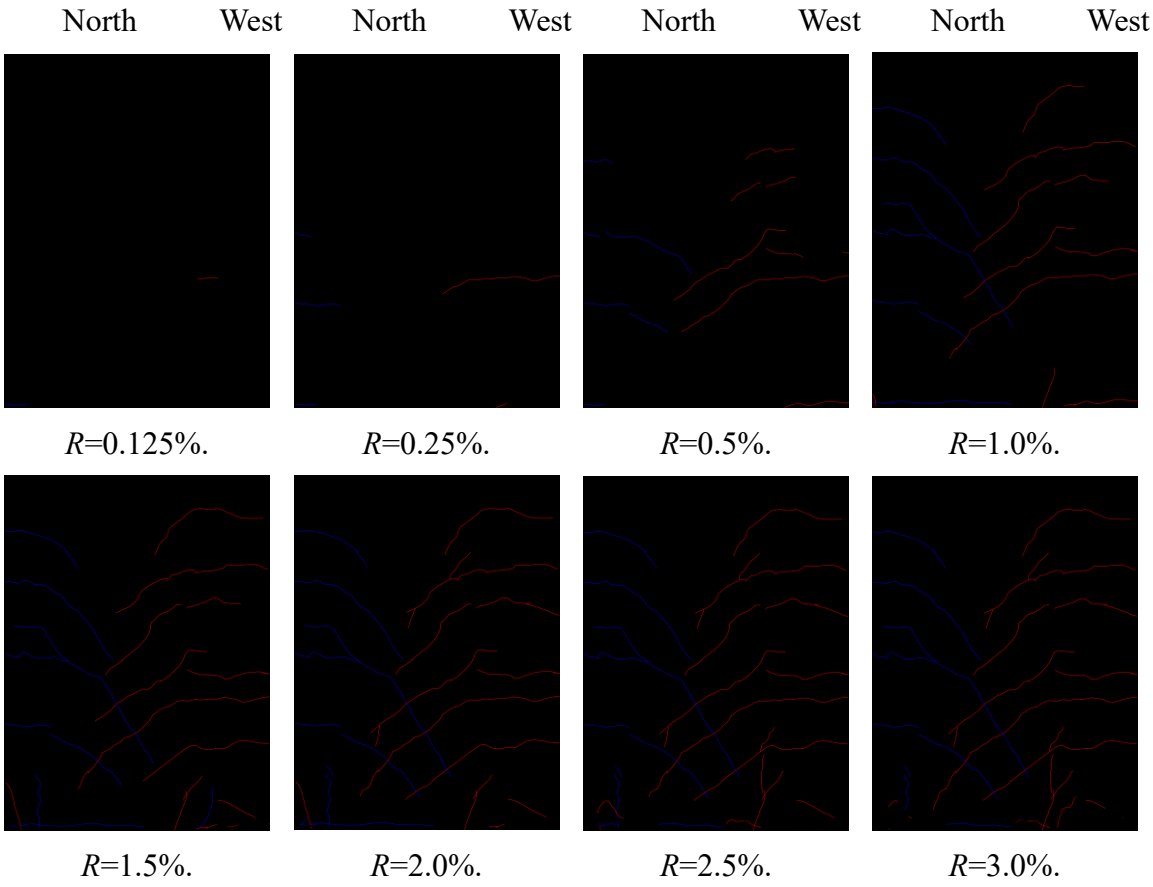

Fig. 3.3-5 Cracks patterns observed on specimen WP20-D10H35-073

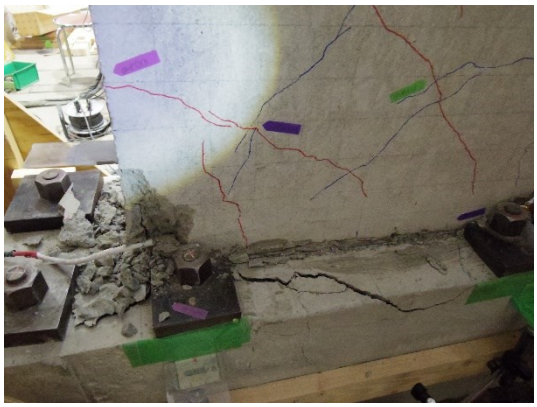

R=3.0%.

Fig. 3.3-6 Damage observed on specimen WP20-D10H35-073

Fig. 3.3-7 shows the cracks patterns of specimen WP20-D10H35-15, the first flexure crack was noticed at boundary between the grouting material and wall panel when lateral force reached 90kN. The first shear crack was found when lateral force reached 150kN. After that, flaking of the cover concrete surface was observed at R=1.5%., and as displayed in Fig. 3.3-8(a) when drift ratio reached 2.0%., the cover concrete on the top surface of the foundation was lifted up. Along with the spalling off of the cover concrete grown severely, the exposure of the DH bars

was fist confirmed at R=2.5%. Finally, the sheath ducts had been found to be pulled out when drift ratio approached 4.0%. as indicated in Fig. 3.3-8(b).

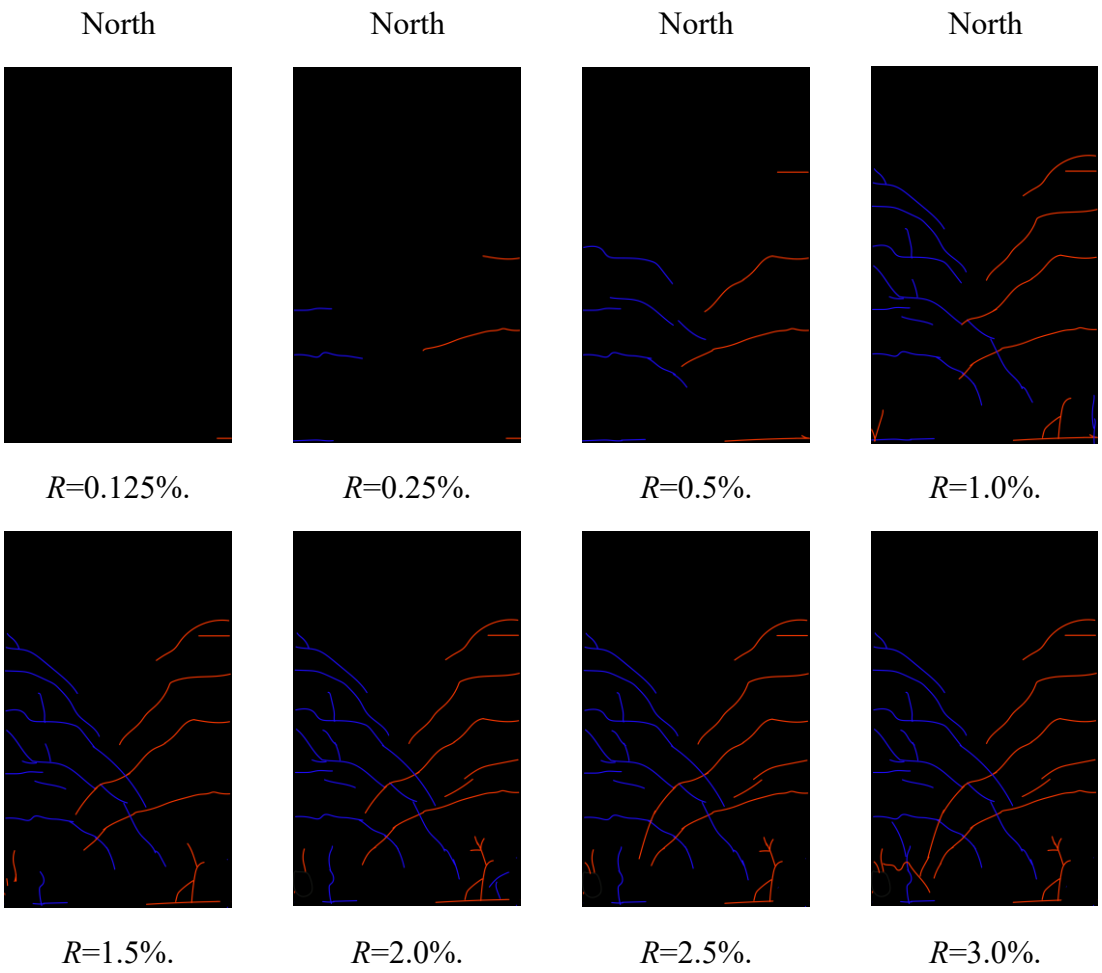

Fig. 3.3-7 Cracks patterns observed on specimen WP20-D10H35-15

(a) R=2.0%. (b) R=4.0%.

Fig. 3.3-8 Damage observed on specimen WP20-D10H35-15

The first flexure crack was noticed at boundary between the grouting material and the foundation of specimen WP20-D12H35-07, as exhibited in Fig. 3.3-9, when lateral force reached 40kN. The first shear crack was found when drift ratio reached 0.25%. After that, flaking of the cover concrete surface at wall toe along with the lifting up of concrete on the top

surface of the foundation were observed at R=1.5%. From that drift ratio on, spalling off of the cover concrete visibly grown, and the exposure of the DH bars was fist confirmed at 2.5%. Then, as indicated in Fig. 3.3-10(a), at the wall-base joint of east side, the grouting material was found to be pulled out from the sheath duct at the drift ratio of -3.5%. On the other hand, while R=+4.0%. it was noticed that the sheath duct was pullout out from foundation on the west side as shown in Fig. 3.3-10(b). Because the construction quality is difficult to control by the utilized equipment, the strength of the grouting material filling in the two sheath ducts could be different, and this could be considered as the reason to the different failure modes.

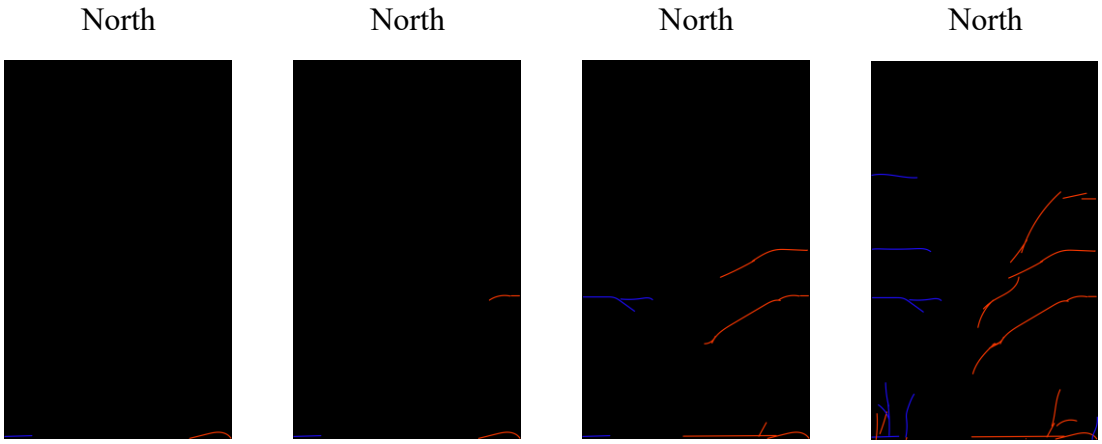

R=0.125%. *R*=0.25%. *R*=0.5%. *R*=1.0%.

Fig. 3.3-9 Cracks patterns observed on specimen WP20-D12H35-075

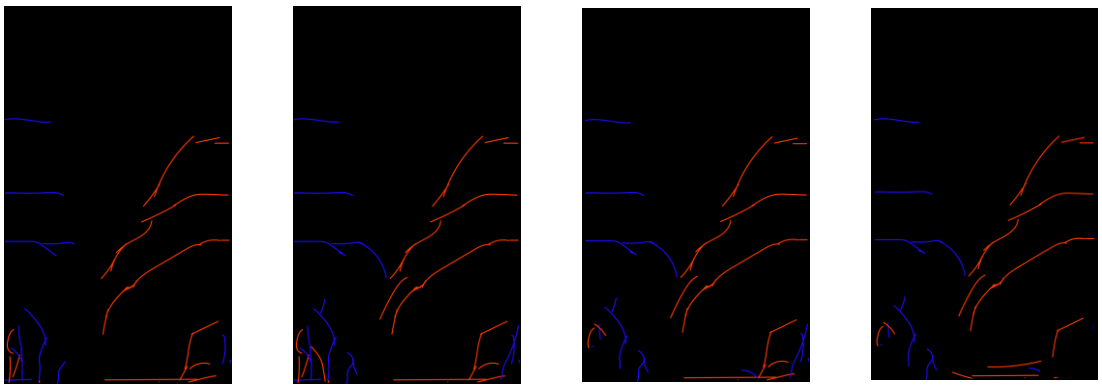

R=1.5%. *R*=2.0%. *R*=2.5%. *R*=3.0%.

Fig. 3.3-9 Cracks patterns observed on specimen WP20-D12H35-075

Fig. 3.3-11 summarized all the crack patterns that were observed at the ultimate state on the north surface of the tested specimens. As can be seen in these figures, the precast specimens indicated less cracks than the conventional-fabricated specimens. As for the precast group, the specimen with higher axial load level exhibited more cracks, while the specimen of which sheath ducts had larger diameter shows less cracks. Besides, once the damage at the wall-base joint was observed at any drift ratio, the cracks of the precast specimens stop developing from that drift ratio on. Hence, the bond failure of connector prevents the transmission of shear and flexure deformation to the wall panel.

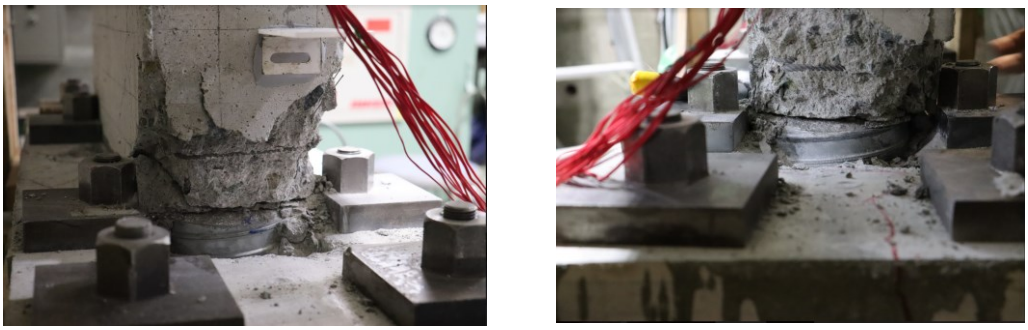

(a) R=-3.5%. (b) R=+4.0%.

Fig. 3.3-10 Damage observed on specimen WP20-D12H35-075

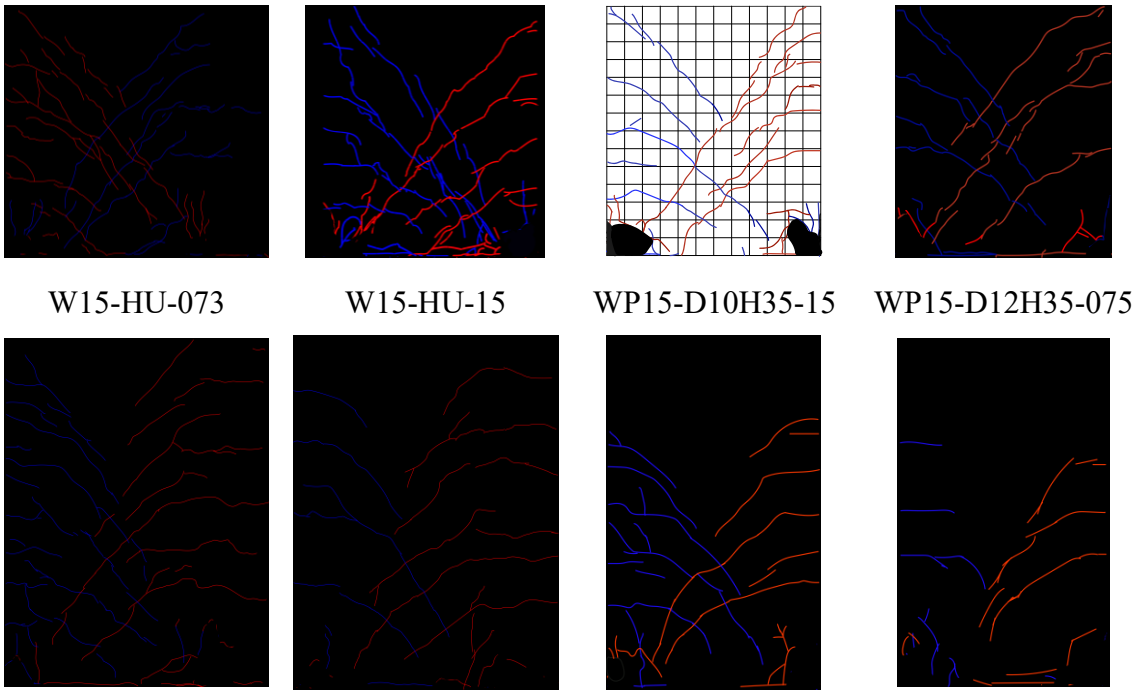

W15-HU-073 W15-HU-15 WP15-D10H35-15 WP15-D12H35-075

W20-HU-073 WP20-D10H35-073 WP20-D10H35-15 WP20-D12H35-075

Fig. 3.3-11 Cracks patterns measured at R=3.0%. for all specimens

3.3.2 Lateral force – drift ratio hysteretic behaviors

The measured lateral resistance force (V) versus drift ratio (R) relationships of all specimens are shown in Fig. 3.3-12, while the measured lateral capacities that averaging the peak lateral forces in both directions are shown in Table 3.2-1.

As can be seen in Fig. 3.3-12, for specimen with shear span ratio of 1.5, lateral force of both specimen WP15-D10H35-15 and WP15-D12H35-075 reached peak at the drift ratio of 1.5%. when the damage of concrete was observed at the wall-base joint. From that drift ratio, onwards, the lateral resistance of the specimen began to degrade gradually, which indicated approximate ductile behavior.

The specimen with shear span ratio of 2.0 exhibited similar behavior, after the commencement

of damage at the concrete around the connectors, specimen WP20-D10H35-15 and WP20-D12H35-075 reached its maximum lateral load carrying capacity at R = +1.5%. and R = -2.0%. separately. Then, the lateral resistance force of the abovementioned specimens began to decrease nearly in accordance and maintained more than 70%. of the maximum lateral force till drift ratio of R = 4.0%. Except specimen WP20-D10H35-073, whose lateral force kept increasing till drift ratio of 2.5%., and descend more sharply than the others, which could be considered as the result of the better grouting quality and severe damage at the wall-base joint as described in Fig. 3.3-6.

It is noteworthy that from the drift ratio when the damage of concrete was observed at the wall-base joint, onwards, the unloading curvatures for all the precast shear walls began to become irregular. Specifically, at that loading cycle, the lateral force down to zero fast and leave large deformation, then along with the two horizontal jacks completely be free, the specimen 'slip' back to its original position and the axial load degrade gradually during this process. It is assumed that once the wall panel together with the sheath ducts were pullout from the foundation at the peak of each targeted drift ratio, they were pushed back by the axial load after unloading of lateral force.

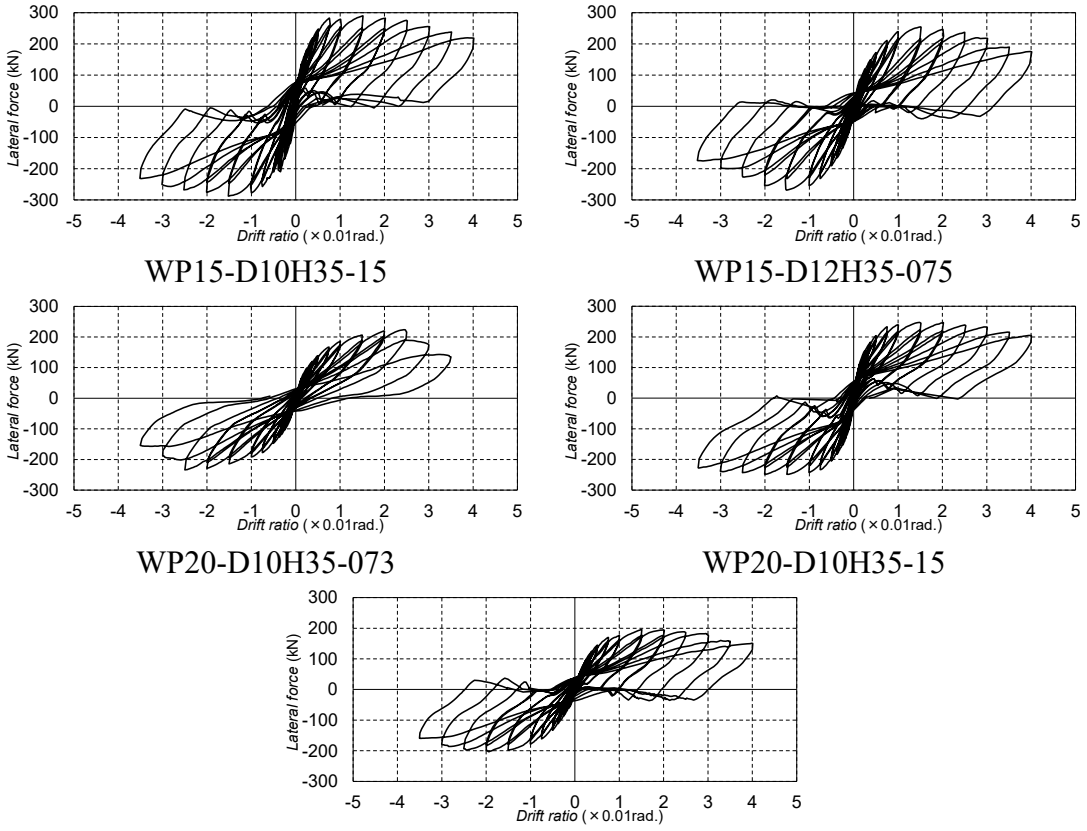

Fig. 3.3-12 Measured lateral load-drift ratio relationships

In order to clearly see the effects of the main experimental variables on overall seismic performance of drift-hardening RC shear walls, the envelope curves in both directions are compared in Fig. 3.3-13.

Effect of the construction method were summarized in Fig. 3.3-13(a), specimens W15-HU-15, W15-HU-073, and W20-HU-073 that were fabricated conventionally, which were described in Chapter 2 were compared as the control group. It is obvious that the lateral resistance forces of the conventional group stably increased up to such a large drift level as 3.0%, obvious drift-hardening capability were observed in this group.

For the precast specimens with shear span ratio of 1.5 and axial load ratio of 0.15, the initial stiffness and lateral force of shear wall W15-HU-15 and WP15-D10H35-15 are almost the same until the drift ratio of 0.75%. However, from that drift ratio on, the difference between these two specimens kept growing, the lateral force of W15-HU-15 kept increasing and reached its shear force loading capacity at the drift ratio of 2.5%. on the other hand, specimen W15-HU-15 exhibited an approximate ductile failure mode descend and did not reached its designed shear resistance capability until drift ratio of 3.0%.

For the specimens with shear span ratio of 1.5 while n=0.075 and 0.073, the lateral force of W15-HU-073 was higher than that of WP15-D12H35-075 from the beginning and indicated the same tendency till R=1.0%. Then, their gap became larger from that drift on, since W15-HU-073 exhibited obvious drift hardening capability while lateral force of WP15-D12H35-075 degrade gradually.

As for the specimens with shear span ratio of 2.0, these two specimens indicated the same seismic behavior till drift ratio of R=2.0%., but same to the other groups, the lateral force of precast specimen WP20-D10H35-073 decreased from that ratio. According to comparison that is shown in Fig. 3.3-13(a), the damage of the concrete at the wall-base joint decreased the lateral force of precast shear walls, resulted in the premature loss of drift hardening capability.

Fig. 3.3-13(b) illustrated the lateral force of two specimens with the only difference was the diameter of their sheath ducts. Specimen WP20-D10H35-073 and WP20-D12H35-075 exhibited the same behavior till R=2.0%., but the one whose sheath ducts had larger diameter indicated lower lateral resistance force, which could be considered that the connector with smaller diameter can provide large bond strength between concrete, and this will be discussed later in section 3.3.7.

It is obvious in Fig. 3.3-13(c) that the higher axial load ratio led to higher overall lateral resistance force, but the axial load ratio of 0.15 could not stop the connectors being pullout from the foundation.

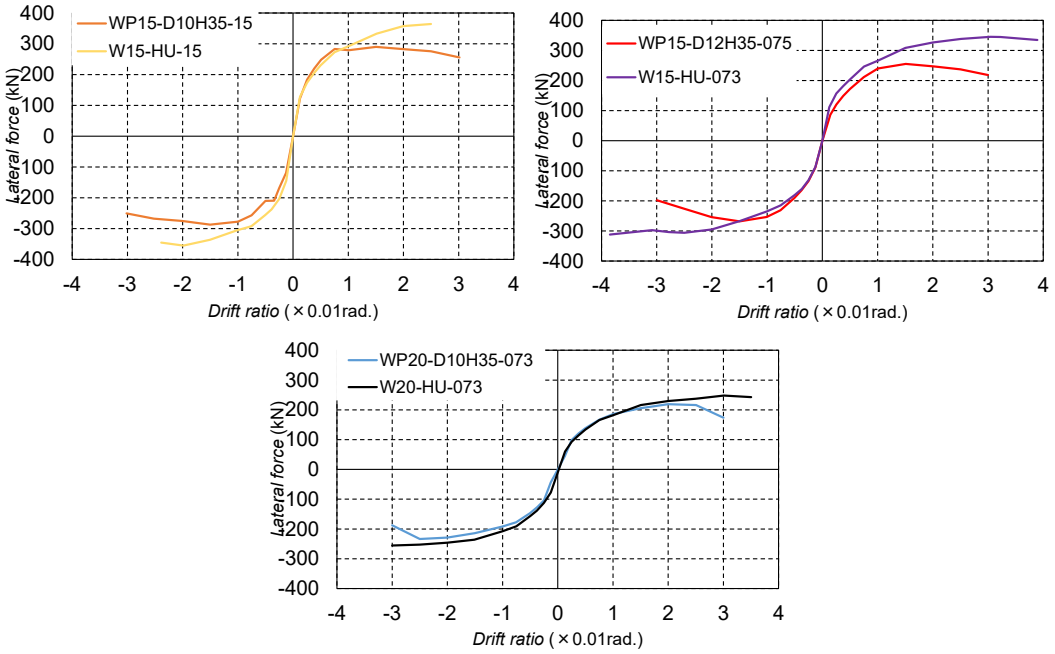

(a) Effect of construction method

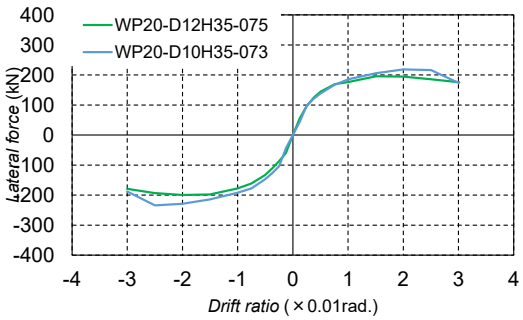

(b) Effect of diameter of sheath ducts

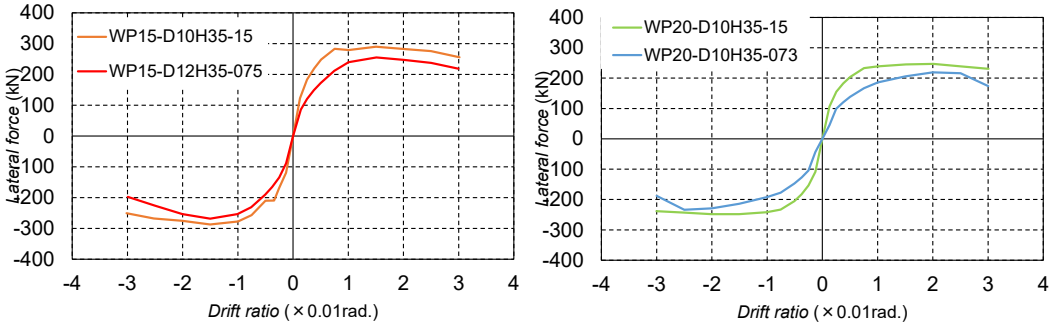

(c) Effect of axial load ratio

Fig. 3.3-13 Effects of main experimental parameters.

3.3.3 Strains measured in reinforcements

The measured axial strains of concentrated rebars for all tested shear walls are shown in Fig. 3.3-14. And the title of each graph, for example W1 – 30mm, represents the strain measured by the strain gauges located at the section of 30mm away from the wall base for specimens on the west side, which is related to the details provided in Fig. 3.2-10. It is apparent that the axial strains of SBPDN rebars exhibited similar behaviors to the lateral force, they all indicated stable increase till the drift ratio when the damage around the connector was observed, and from that drift on, the axial strains of concentrated rebars remained at a constant level and decrease gradually along with the increasing drift ratio. Although the axial strains of concentrated rebars did not reached its yield strain (0.85%.), the bond failure between concrete and sheath ducts could no longer fix the SBPDN rebars at bottom ends, the proposed connection method could not assure the precast shear walls drift hardening capability.

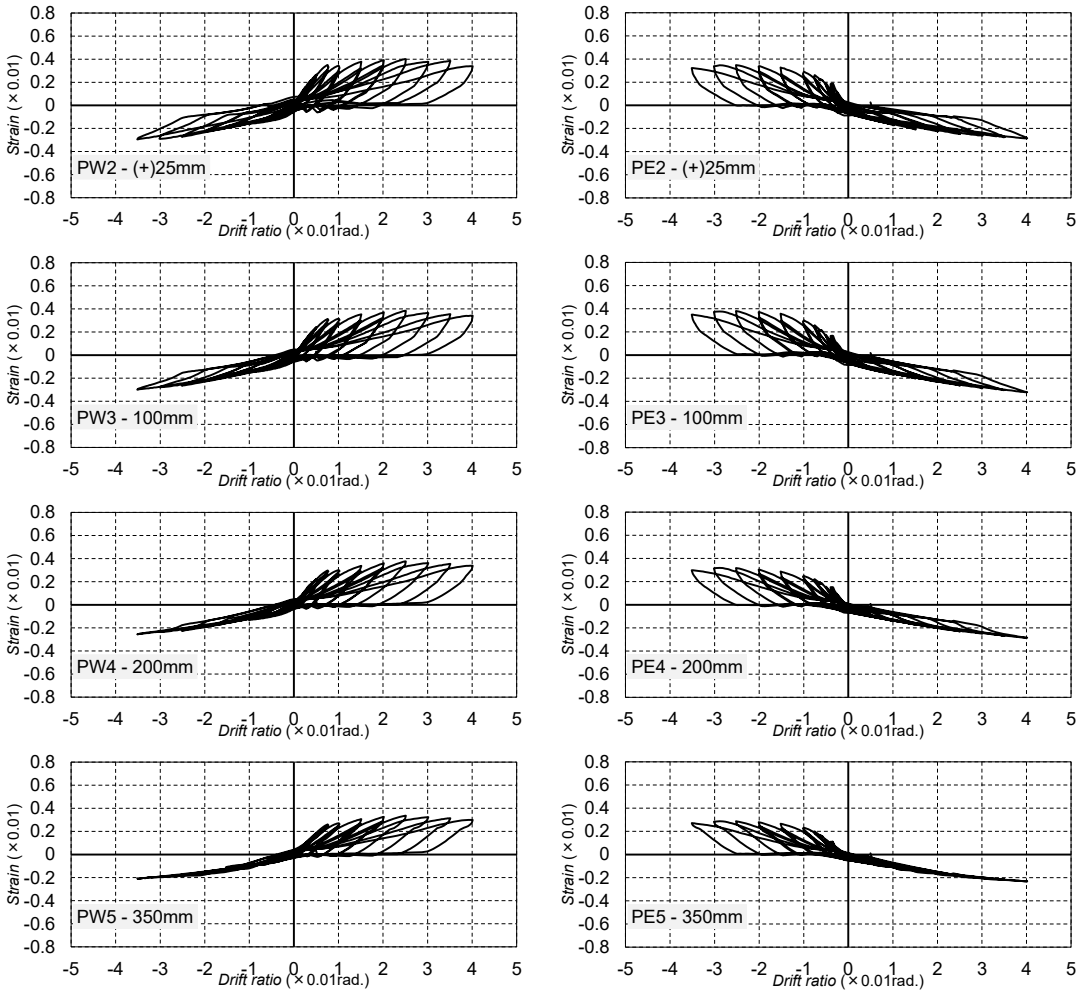

(a) WP15-D10H35-15

Fig. 3.3-14 Measured strains-drift ratio relationships of concentrated rebars

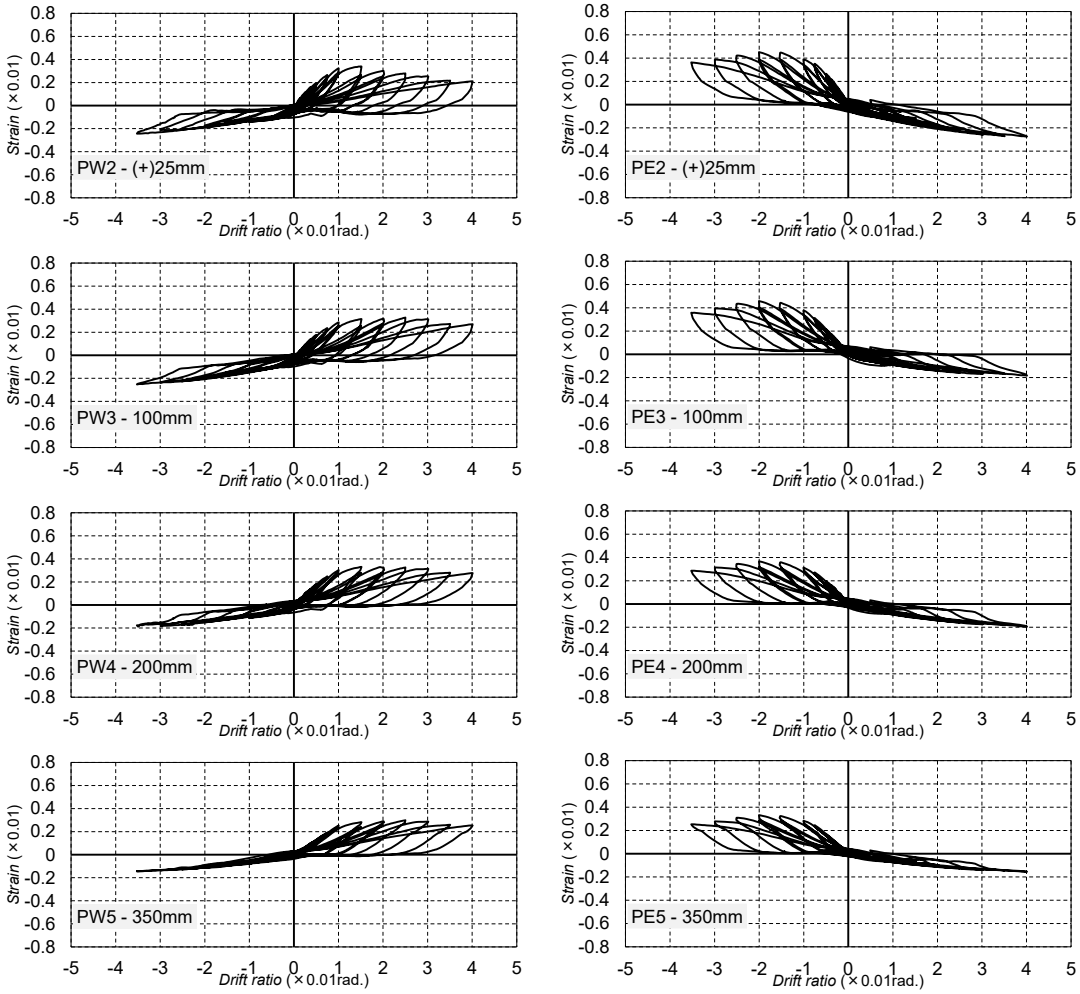

(b) WP15-D12H35-075

Fig. 3.3-14 Continued

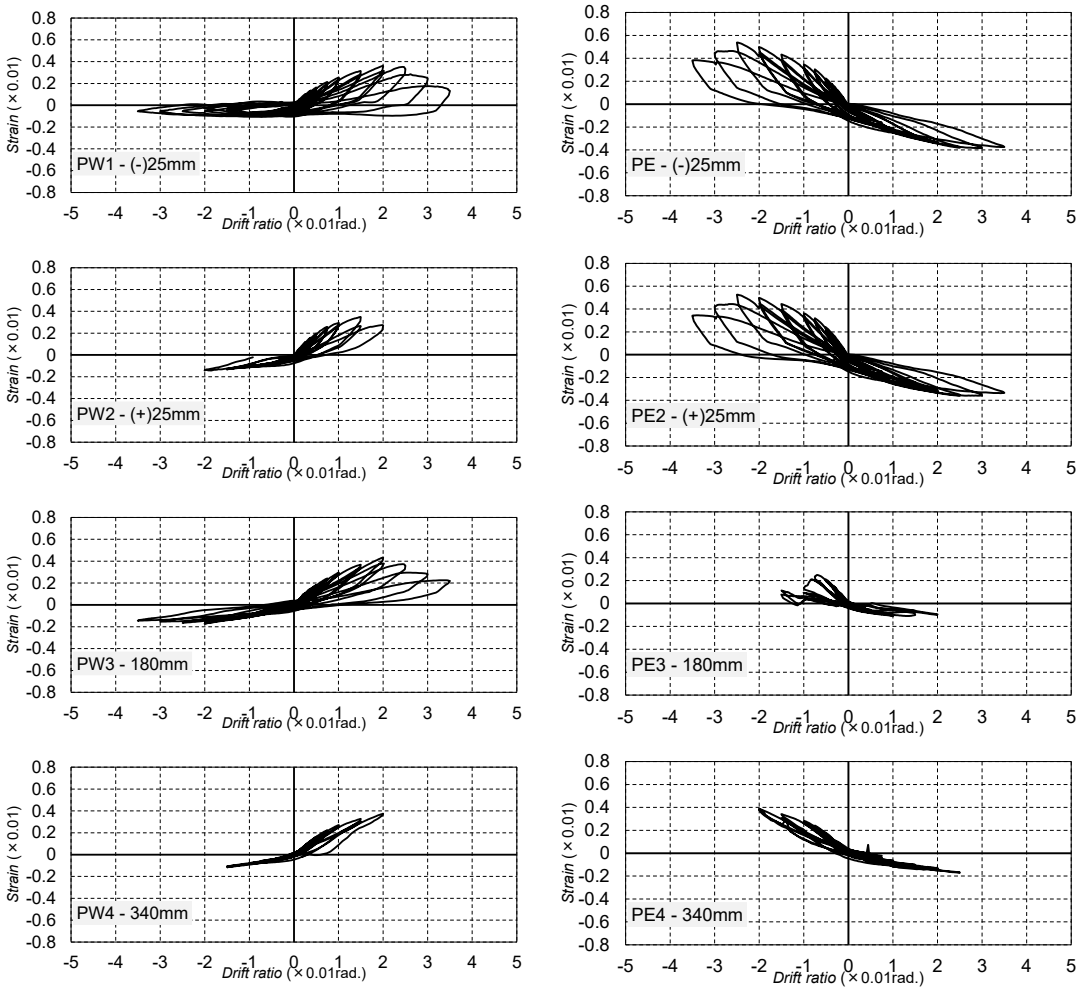

(c) WP20-D10H35-073

Fig. 3.3-14 Continued

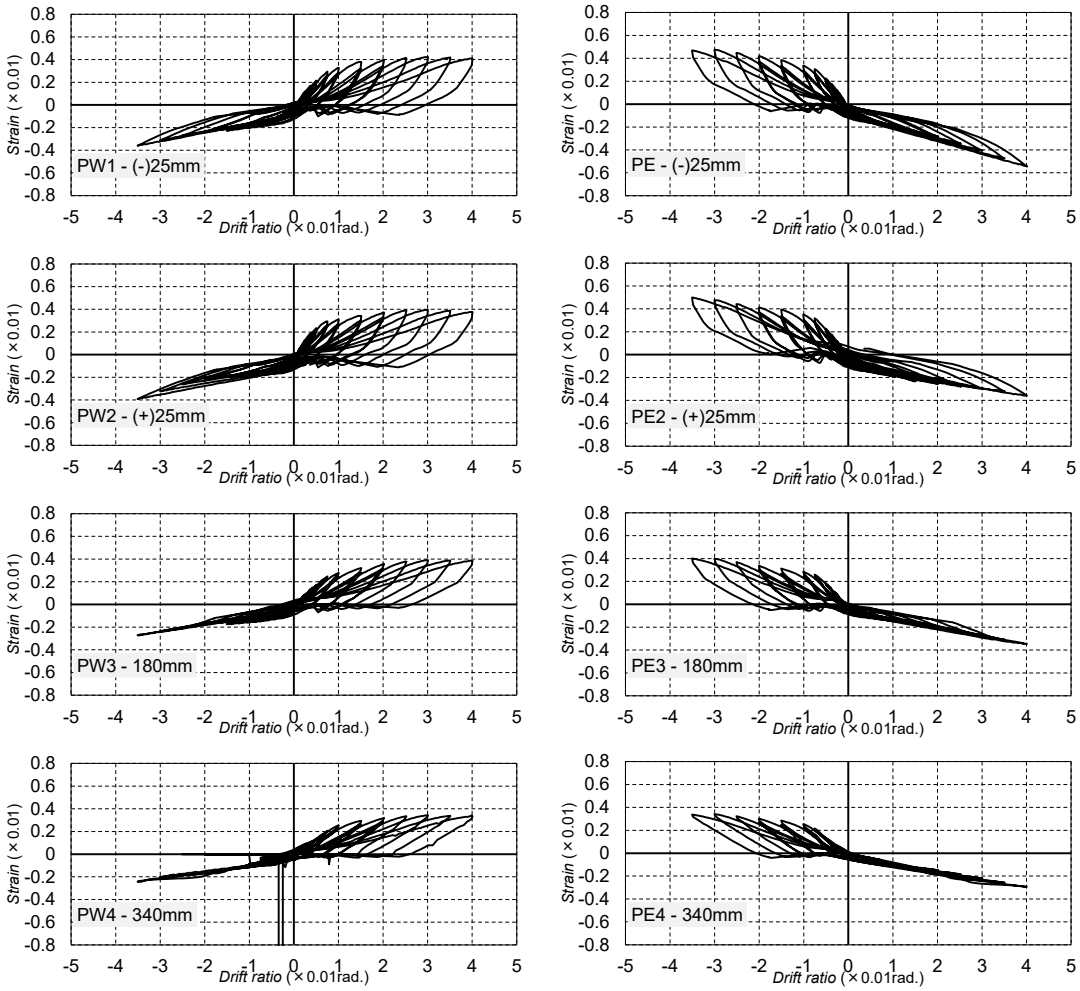

(d) WP20-D10H35-15

Fig. 3.3-14 Continued

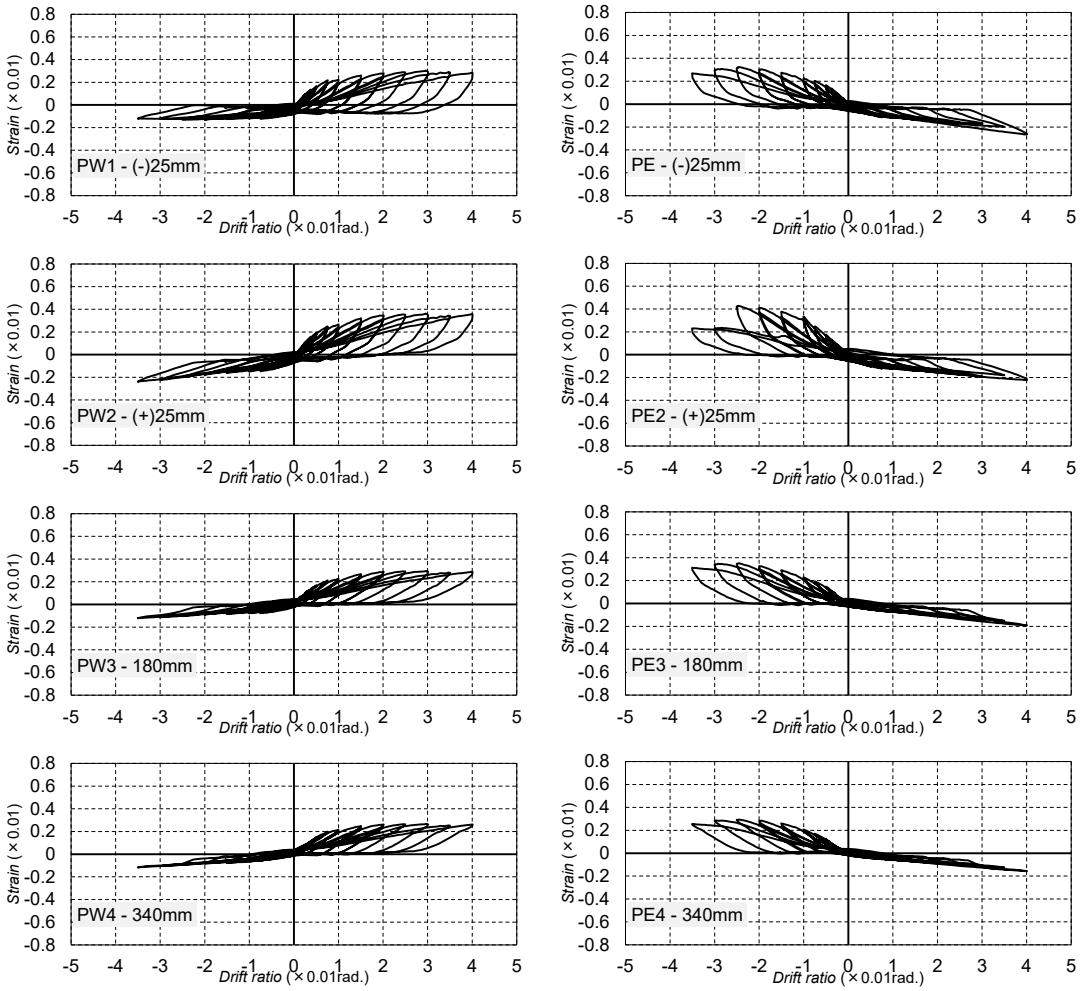

(e) WP20-D12H35-075

Fig. 3.3-14 Continued

The distributions of strains of concentrated rebars along height of wall panel are shown in Fig. 3.3-15. The strains measured in SBPDN rebars of precast specimens indicated similar behaviors to those of conventional fabricated specimens till drift ratio reached 0.75%. After that drift level, they all exhibited a nearly uniform distribution along the height of wall panel, but the strains of SBPDN rebars distributed faster but stop increasing at relative drift ratio when the damage of wall-base joint was confirmed. In addition, it can be noticed that the specimen with higher axial load ratio had higher strain in concentrated rebars, which coincides with the fact that the larger the applied axial load, the larger the lateral resistance of shear walls.

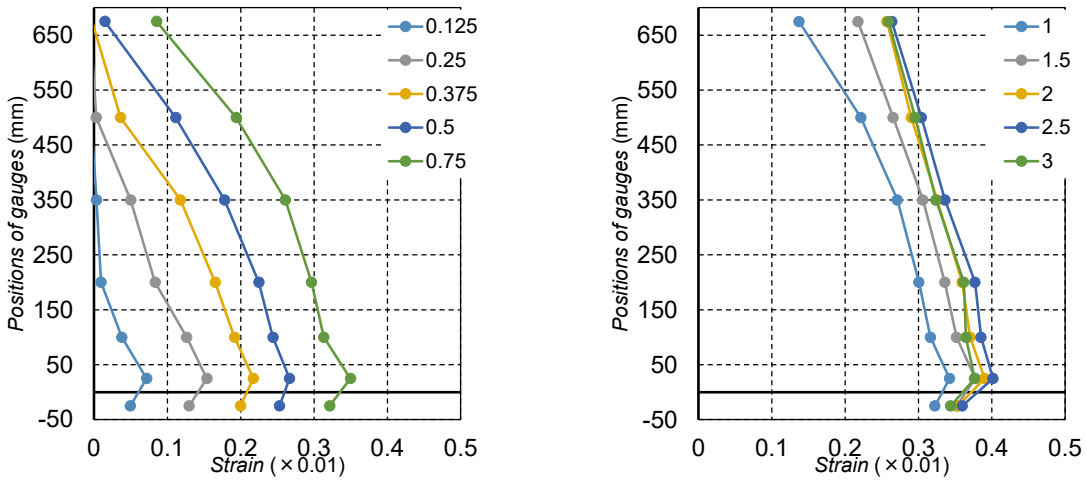

（1）R=0.125～0.75%　　（2）R=1.0～3.0%

(a) WP15-D10H35-15

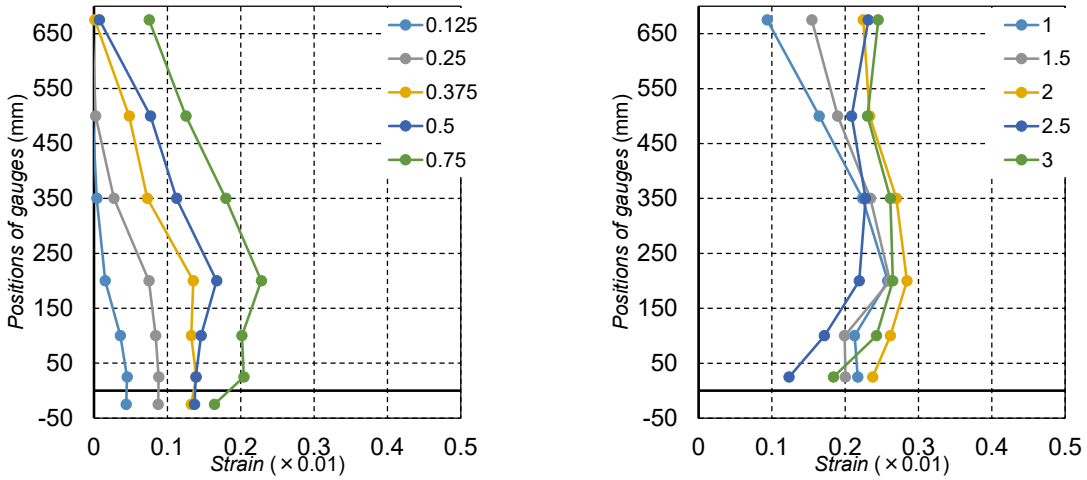

（1）R=0.125～0.75%　　（2）R=1.0～3.0%

(b) WP15-D12H35-075

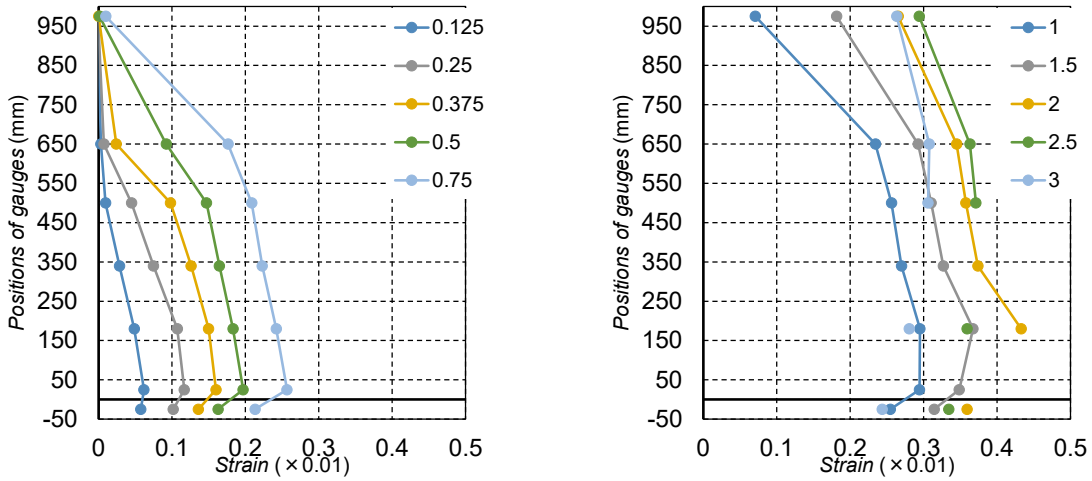

（1）R=0.125～0.75%　　（2）R=1.0～3.0%

(c) WP20-D10H35-073

Fig. 3.3-15 Strains distribution of concentrated rebars

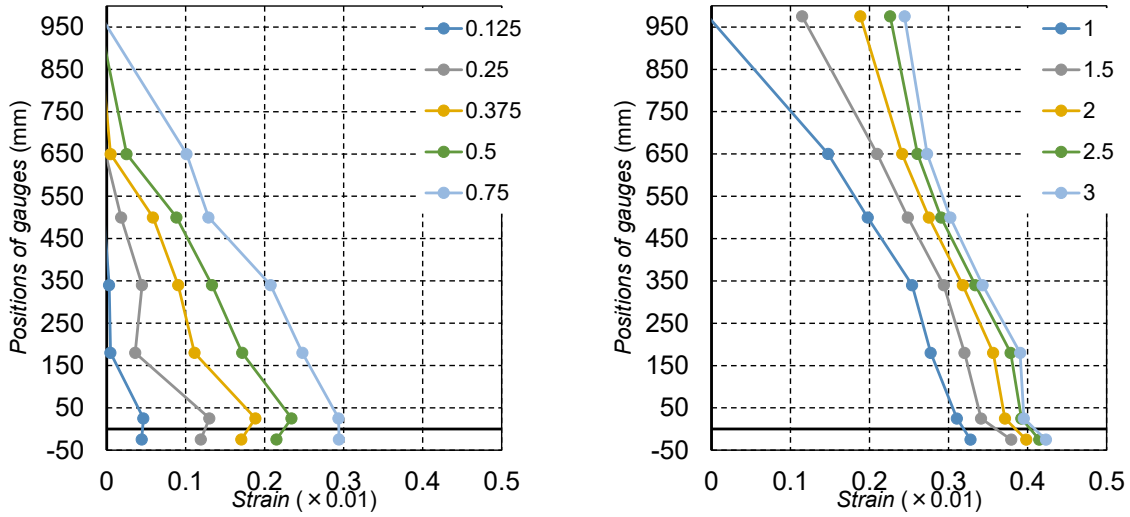

（1）R=0.125～0.75%　　（2）R=1.0～3.0%

(d) WP20-D10H35-15

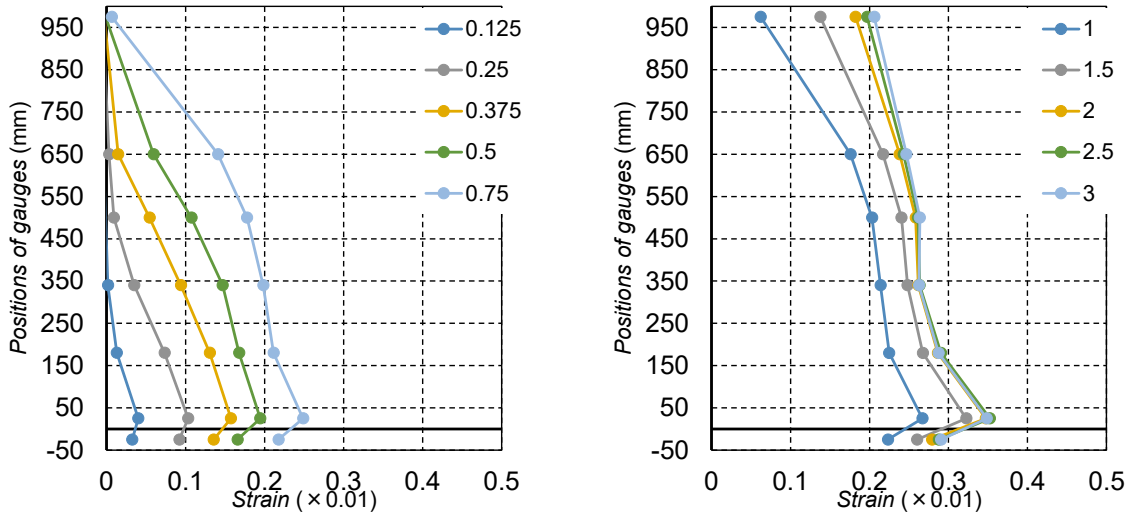

（1）R=0.125～0.75%　　（2）R=1.0～3.0%

(e) WP20-D12H35-075

Fig. 3.3-15 Continued

3.3.4 Overall vertical axial deformation

Fig. 3.3-16 shows the overall vertical axial strain versus drift angle relationship for all specimens, details of the calculation can be found in Chapter 2 section 2.3.4. It is obvious in Fig. 3.3-16 (a) that since the conventional fabricated specimen with an axial load ratio of 0.15 finally indicated shear failure at large deformation, its overall vertical axial strain increased gradually and declined rapidly at the drift ratio of 2.5%. while the precast specimen indicated a stable overall vertical axial strain. As for the lower axial load ratio group, specimen W15-HU-073 exhibited stable increase of overall vertical axial strain, while the recast specimen was lifted up dramatically after drift ratio of 1.0%.

As can be seen in Fig. 3.3-16 (b), two specimens exhibited the same behavior till drift ratio of 1.5%. after that drift ratio on, overall vertical axial strain of the specimen with larger diameter

of sheath ducts ascended faster, but since these two specimens had the same failure mode, they were lifted up to the almost same level at the drift ratio of 3.0%.

Fig. 3.3-16 (c) display the influence of axial load ratio on the precast shear walls, the precast specimen with lower axial load was gradually 'lifted up', on the other hand, the precast shear walls with higher axial load ratio were almost constant till the end of test, which indicated that the specimens were 'pushed back' by the axial load.

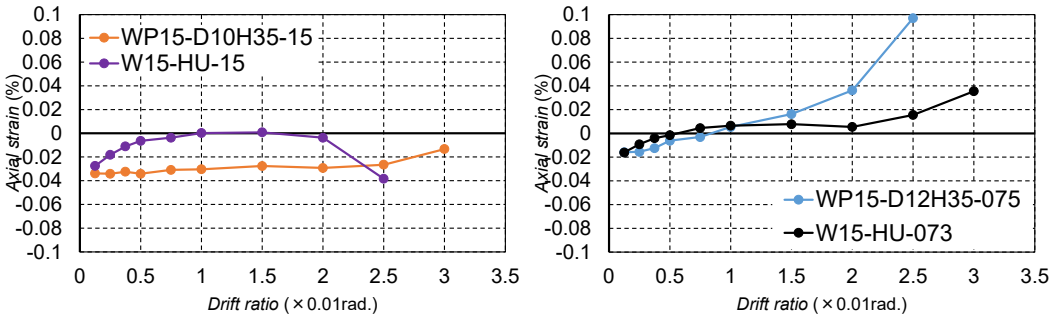

(a) Effect of construction method

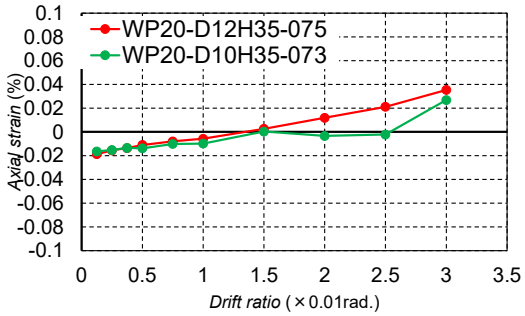

(b) Effect of diameter of sheath ducts

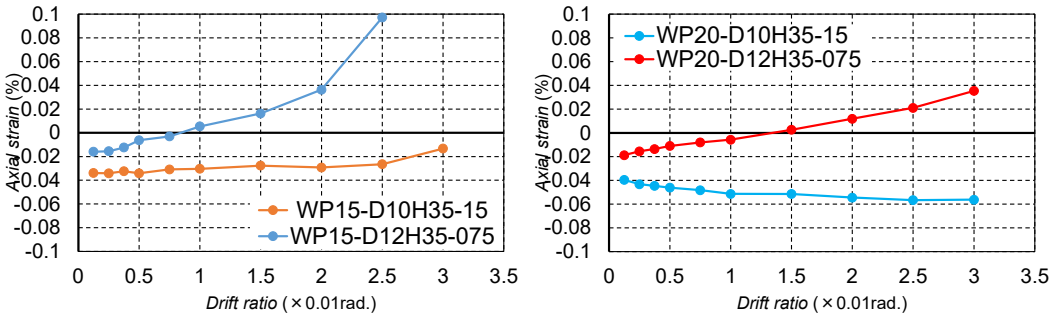

(c) Effect of axial load ratio

Fig. 3.3-16 Measured overall axial strain

3.3.5 Residual drift ratio

Fig. 3.3-17 summarized the average residual drift ratio of the plus and minus directions measured at each targeted drift ratio. Since the hysteretic behaviors of the precast specimen became irregular during unloading, the residual drift ratios were measure when the specimens were completely stabilized. And one can be seen in Fig. 3.3-17 that, even the connectors were

lifted up, the SBPDN rebars could still control the residual drift ratio of precast shear walls under a very low level.

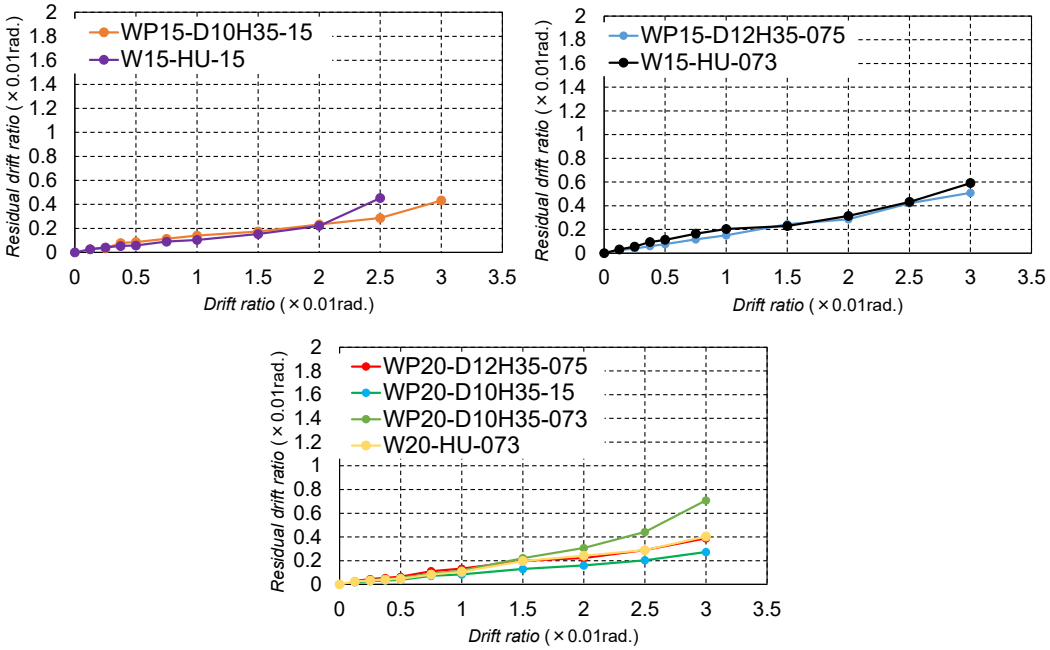

Fig. 3.3-17 Measured residual drift ratios

3.3.6 Equivalent viscous damping (Energy dissipation capacity)

Fig. 3.3-18 shows the measured equivalent viscous damping coefficient for all tested specimens. For the specimens with shear span ratio of 1.5, until drift ratio of 1.0%., all specimens indicated stable energy absorption capacity with a nearly constant equivalent viscous damping coefficient. After that drift ratio on, the conventional fabricated specimens behaved in an approximately nonlinear elastic manner, on the other hand, the precast specimens exhibited a stable ascent in equivalent viscous damping coefficient, which the damage at the wall-base joint is irreparable.

One can be seen from Fig. 3.3-18(b), that before the drift ratio of 1.5%, the precast specimen with different diameter of sheath ducts had almost the same energy absorption capacity. Then, the equivalent viscous damping coefficient of the specimen whose sheath ducts had lager diameter increased faster, but they finally had the same value at the drift ratio of 3.0%. because they behaved the same failure mode.

As shown in Fig. 3.3-18(c), the influence of axial load ratio on the energy dissipation capacity of could be ignored.

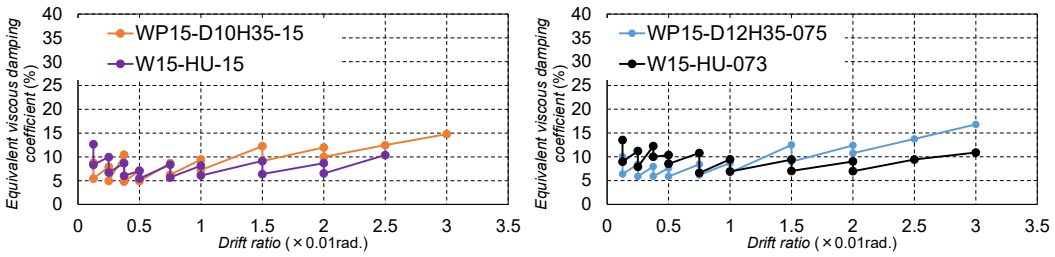

(a) Effect of construction method

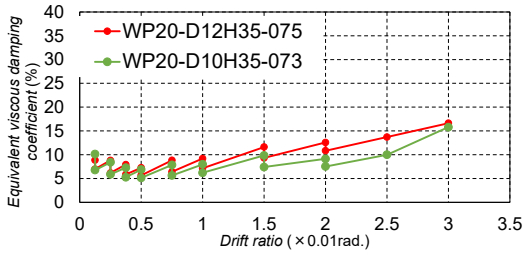

(b) Effect of diameter of sheath ducts

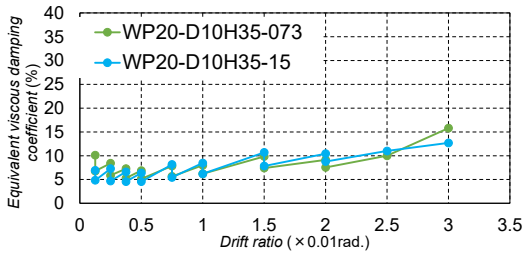

(c) Effect of axial load ratio

Fig. 3.3-18 Measured equivalent viscous damping coefficients

3.3.7 Evaluation of bond strength between sheath ducts and concrete

In order to better understand bond failure at the wall-base joint, this section proposed a method to estimate the maximum bond strength (τ_{max}) between sheath ducts and the concrete according to the tested results in this Chapter. Specifically, since all the axial strain measure in the SBPDN rebars did not reach their yield train (0.85%), which indicated that these rebars remained linear elastic, therefore, the stress of each rebars can be calculated by the Hooke's Law. The τ_{max} can be computed by the following equation.

$$\tau_{max} = \frac{4A_s\varepsilon_{max}E_s}{\pi D_s H_s} \tag{3.3-1}$$

In Eq. (3.3-1), where A_s = 125 mm^2 is the nominal diameter of each SBPDN rebars and E_s = 211.7 kN/mm^2 is the Young's modulus that was summarized in Table 3.2-2. ε_{max} is the mean of measured maximum tensile strain in the concentrated rebars at the four positions shown in Fig. 3.3-19. D_s and H_s are the diameter and embedment depths of sheath ducts, respectively. And the calculated results were summarized in Table 3.3-1. As can be seen in this Table 3.3-1, the applied sheath ducts with larger diameters indicated lower bond strength. Besides, the

average τ_{max} of sheath ducts with diameter of 100 mm is 4.6 N/mm^2, hence in order to completely take the advantages of utilization of SBPDN rebars in the precast shear walls, based on Eq. (3.3-1), the embedment depths of sheath ducts should be at least 480 mm to provide sufficient bond strength for SBPDN rebars to develop strain along with drift till the yield strain.

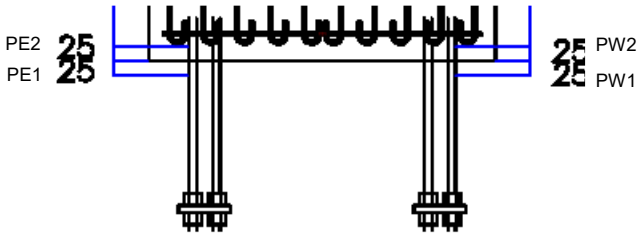

Fig. 3.3-19 Locations of strain gages

Table 3.3-1 Evaluated bond strength and main test results

Specimen	*a/D*	*n*	ε_{max}	τ_{max}	D_s	H_s	Q_{exp}
			%.	(N/mm^2)	(mm)	(mm)	(kN)
WP15-D10H35-15	1.5	0.15	0.35	3.77	100	310	289
WP15-D12H35-075		0.075	0.39	3.51	120		262
WP20-D10H35-15	2.0	0.15	0.45	4.87	100		248
WP20-D10H35-073		0.073	0.48	5.16			229
WP20-D12H35-075		0.075	0.35	3.21	120		200

a/D: shear span ratio; *n*: axial load ratio; *Ds*: diameter of sheath ducts; H_s: embedment depths of sheath ducts; Q_{exp}: measured maximum lateral force (average);

3.4 Conclusions

In this chapter, to verify if the use of SBPDN rebars can provide precast concrete shear walls the same drift-hardening capability as the cast-in-site walls, five 1/3-scale cantilever concrete shear walls were fabricated by the proposed connecting method, and tested under reversed cyclic lateral loading while subjected to constant axial load. From the experiments described in this chapter, the following conclusions can be drawn:

1) Comparing with the drift hardening shear walls fabricated by conventional construction method, the precast specimens exhibited nearly identical lateral resistance till the drift ratio of 2.0%. After that drift level on, the bond failure occurred between connection portion and concrete due to insufficient anchorage length of the connection portion, triggering the degradation of lateral resistance. However, the degradation is gradual, and all precast walls remained over 80% of their maximum lateral forces at the drift of 3.0%.

2) While the bond failure between the connector and concrete caused degradation of lateral resistance at large drift, the use of SBPDN rebars could still control the residual drift ratio below 0.6% after unloading from the drift of 3.0%.

3) The precast specimen under higher axial load exhibited higher lateral resistance force, but the axial load could not prevent the lift of connector at wall-base joint by the transferred shear force.

4) The bond strength between sheath ducts and concrete was evaluated on the basis of the measured strains of longitudinal rebars. The evaluated bond strength (4.6 N/mm^2) implied that to completely take the advantages of utilization of SBPDN rebars in the precast concrete walls, the embedment depths of sheath ducts should be at least 480 mm (about five times of the diameter of sheath duct) to provide sufficient bond strength for SBPDN rebars to develop strain along with drift till the yield strain.

References

[3.1] Sri Sritharan. et al., "Precast concrete wall with end columns (PreWEC) for earthquake resistant design", Earthquake Engng Struct. Dyn. 2015; 44: 2075–2092.

[3.2] American Concrete Institute (ACI), "Acceptance criteria for special unbonded post-tensioned precast structural walls based on validation testing and commentary." ACI ITG-5.1-07, 2007.

[3.3] Brian J. Smith. Et al., "Behavior of Precast Concrete Shear Walls for Seismic Regions: Comparison of Hybrid and Emulative Specimens", Journal of Structural Engineering, 2013, Vol. 139, No. 11, ISSN 0733-9445.

[3.4] Holden, T., Restrepo, J., and Mander, J., "A comparison of the seismic performance of precast wall construction: emulation and hybrid approaches." Research Rep. 2001-4, Univ. of Canterbury, New Zealand.

CHAPTER FOUR

Influence of anchorage detailing on Seismic behavior of precast concrete walls reinforced with SBPDN rebars

4.1 Introduction

In Chapter Two, it has been experimentally verified that the use of SBPDN as concentrated rebar can provide concrete walls drift-hardening capability up to the drift ratio of at least 3.0%. Meanwhile, it has also been confirmed that the utilization of SBPDN rebars can control the residual deformation of concrete walls under 15% of the experienced peak deformation. However, due to its low bond strength, which is about 3 MPa and is only about one-fifth of ordinary deformed rebar [4.1], all SBPDN rebars need to be fixed by steel plate via high strength nuts (see Fig. 4.1-1(a)) to prevent the slippage of SBPDN rebars at both ends. On the other hand, previous research also proved that if the SBPDN rebar was screwed (see Fig. 4.1-1(b)) its bond strength could be enhanced to 21.8 MPa. Thus, lap joint with screwed thread is a potential fixation method for SBPDN rebars and is expected to simplify fabrication of precast concrete walls reinforced with SBPDN rebars.

According to the experimental works conducted by Wei et al. [4.2] on concrete columns reinforced with SBPDN rebars, the embedment length of 20d for SBPDN rebar in precast concrete component could not effectively prevent the slippage of SBPDN rebar 2.0% drift [4.2]. The experimental results described in chapter three also indicated that sufficient embedment length of SBPDN rebar is necessary for the precast DHC walls to develop drift-hardening capability up to larger drift than 2.0%.

Based on the above-mentioned background, this chapter will be devoted to

1) Clarifying the influence of embedment length of SBPDN rebar on seismic performance of the precast DHC walls through cyclic testing of three test walls and comparison with the experimental results described in chapter three.

2) Verifying the effectiveness of anchorage by screwed threads at the ends of SBPDN rebars instead of combination of the end-plate and nuts.

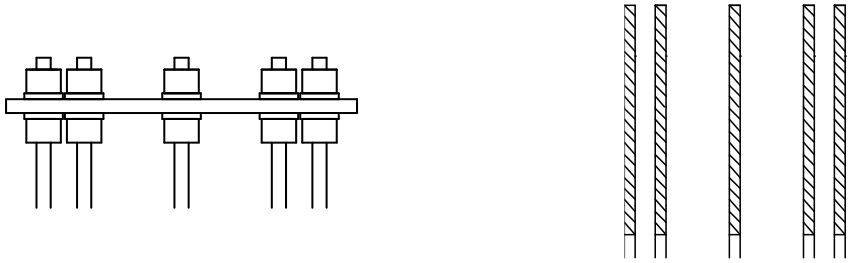

(a) steel plate (b) screwed threads

Fig. 4.1-1 Anchorage of SBPDN rebars

4.2 Experimental program

4.2.1 Outlines of test specimens

To achieve the aforementioned goals of this chapter, a total of three 1/3-scale cantilever rectangular concrete shear walls were designed, fabricated, and tested under reversed cyclic lateral loading while subjected to constant axial load. All the specimen was fabricated by the proposed precast method as described in Chapter Three, section 3.2.1.
The experimental variables included, 1) the shear span ratio, 2) the anchorage of SBPDN rebars at wall-base joint.

Fig. 4.2-1 indicates the dimensions and reinforcement details of the specimens, while Table 4.2-1 lists the primary experimental parameters along with the main test results. As shown in Table 4.2-1 and Fig. 4.2-1, all specimens had the rectangular section of 150mm in thickness and 600mm in depth, and the sheath ducts with diameter of 100mm and embedment depth of 510mm were applied for all specimens, it was expected that they can provide sufficient bond strength till the yielding of SBPDN rebars. The specimen of WP15-Series had a shear span of 900 mm to give a shear span ratio of 1.5. As for specimens of WP20-Series, their shear spans were 1200 mm to give a shear span ratio of 2.0.

The steel amount of longitudinal distributed (LD) bars and horizontal distributed (HD) bars in wall panel as well as of SBPDN rebars is the same for all test walls. As can be seen in Fig. 4.2-1, for specimen WP15-D10H55P-075 and WP20-D10H55P-075, each SBPDN rebar was anchored to a steel plate (having a thickness of 9mm) by bolts at both ends. As for specimen WP15-D10H55N-075, instead of the steel plate, each SBPDN rebar was screwed at bottom end along the splice length of 20d (where d represented the nominal diameter of SBPDN rebar), and the embedment depth of the screwed threads was 40d.

Table 4.2-1 Primary experimental parameters and main test results

Specimen	a/D	n	f'_c (N/mm^2)	f'_g (N/mm^2)	Longitudinal rebars		Concentrated SBPDN rebars		Transverse rebars		D_s	H_s	Anchorage of SBPDN rebars	Q_{exp}
					Type	ρ_{wv}(%)	Type	ρ_s(%)	Type	ρ_{wh}(%)	(mm)	(mm)		(kN)
WP15-D10H55P-075	1.5	0.075	34.68	64.96	20-D6 Not Fixed	0.70	8-U12.6	0.58	D6@65	0.65	100	510	steel plates	337
WP15-D10H55N-075			43.65	66.16									screwed lap joint	341
WP20-D10H55P-075	2.0		44.89	75.19									steel plates	253

a/D: shear span ratio; *n*: axial load ratio; f'_c: concrete cylinder strength; f'_g: cylinder strength of grouting materials; ρ_{wv} : reinforcement ratio of longitudinal rebars; ρ_s: reinforcement ratio of concentrated rebars; ρ_{wh}: volumetric ratio of transverse reinforcement; D_s: diameter of sheath ducts; E_s: embedment depths of sheath ducts; Q_{exp}: measured maximum lateral force (average);

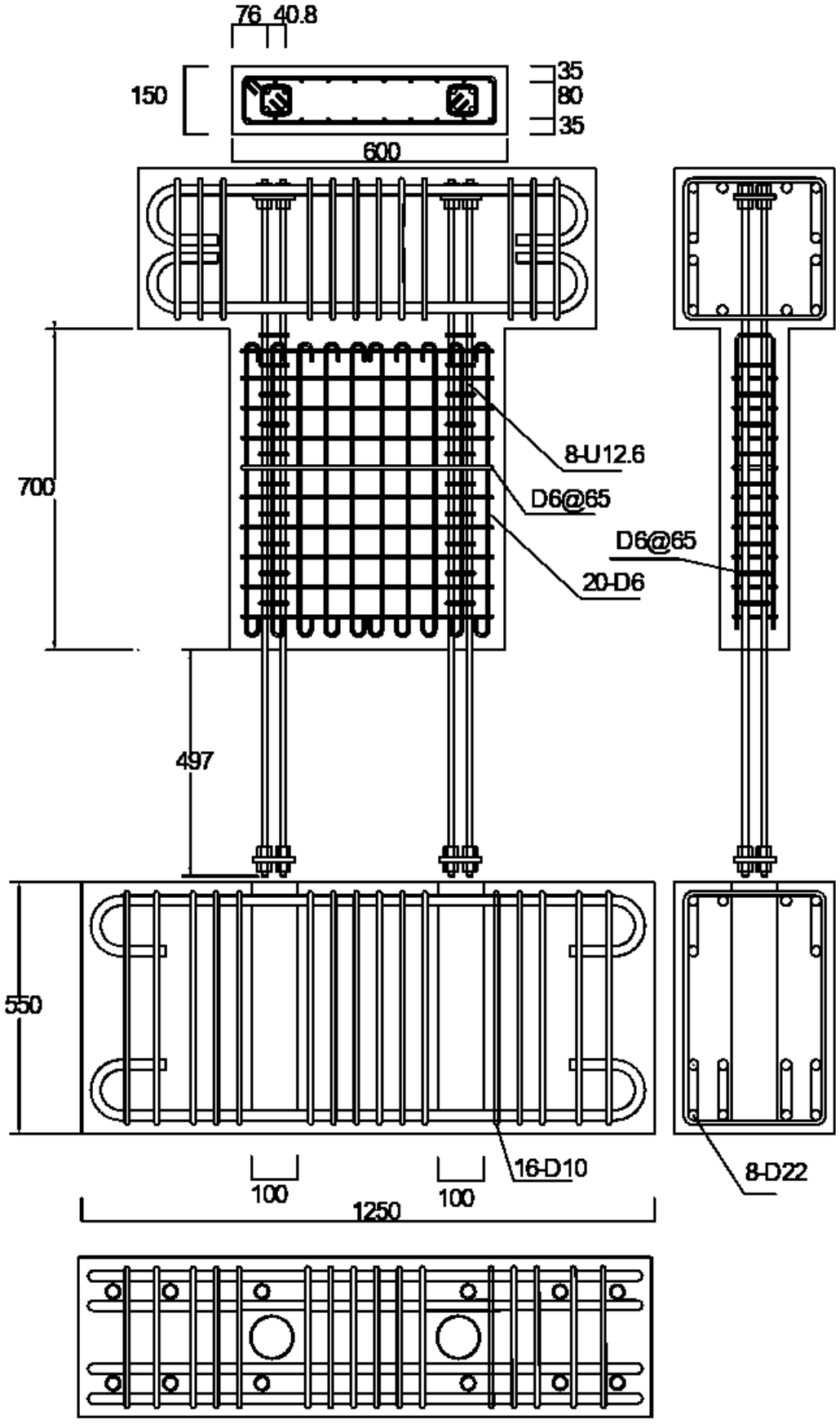

(a) WP15-D10H55P-075

Fig. 4.2-1 Reinforcement details of test shear walls (Unit: mm)

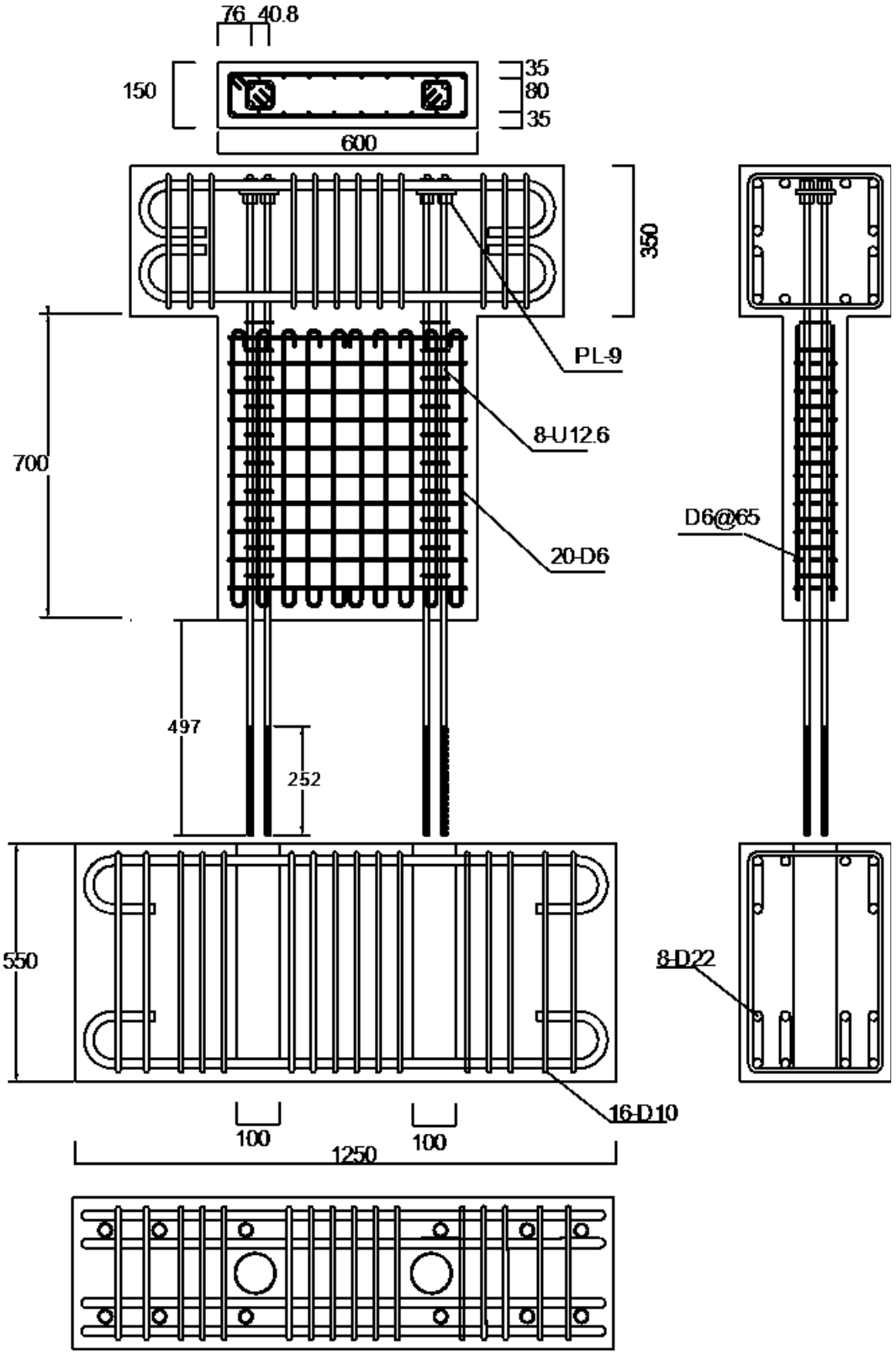

(b) WP15-D10H55N-075

Fig. 4.2-1 Continued

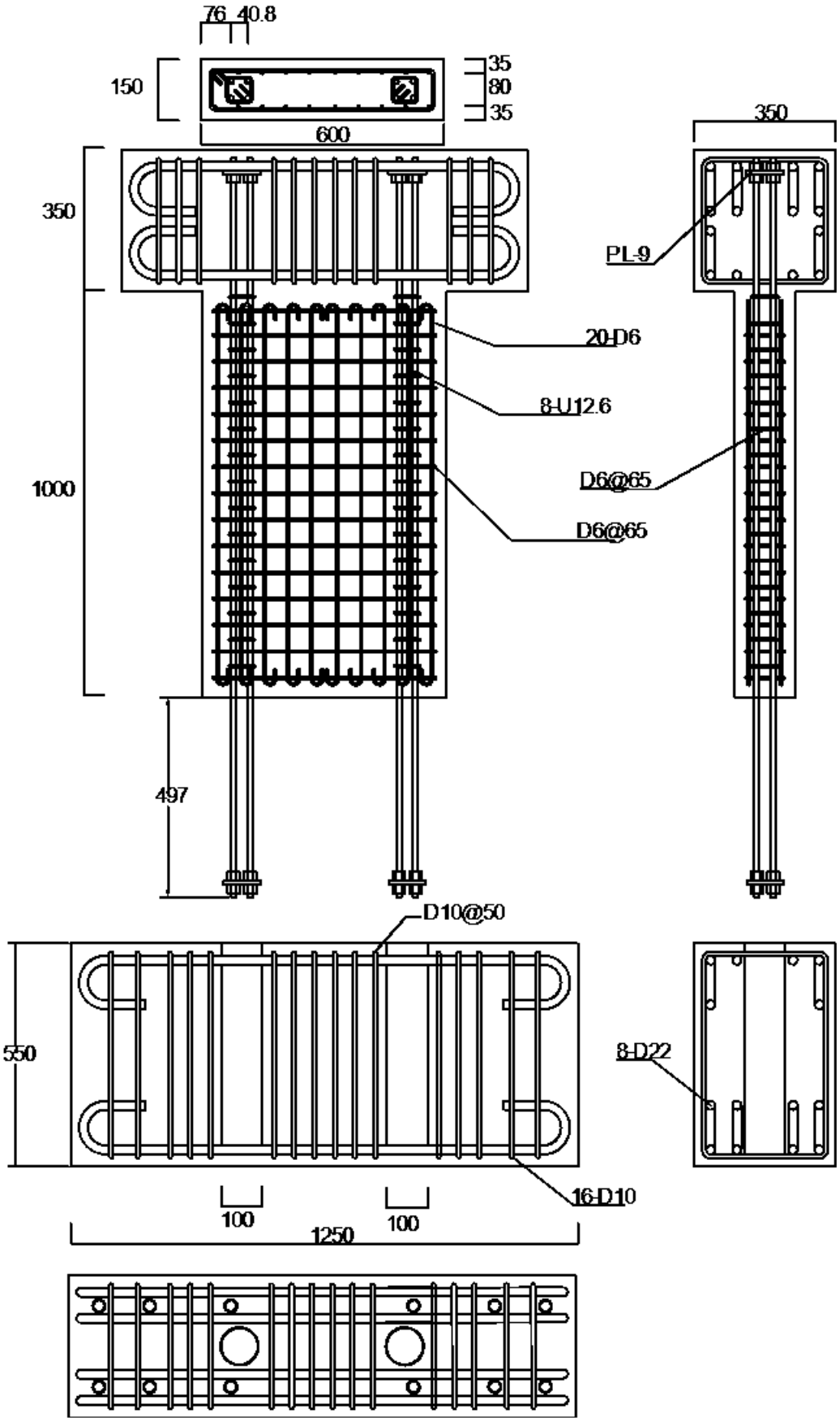

(c) WP20-D10H55P-075

Fig. 4.2-1 Continued

4.2.2 Material properties

The ultra-high strength SBPDN 1275/1420 rebar with yield strength of about1380 MPa and spiral grooves on its surface as shown in Fig. 4.2-2(a). Previous experimental works by Funato et al indicated that the bond strength of SBPDN rebar is about 3 MPa when it was embedded in concrete with compression strength of about 40 MPa, which is about one-fifth comparing with ordinary rebar [4.1]. However, it had also been proved that if the SBPDN rebar was screwed as shown in Fig. 4.2-2(b), its bond strength was increased to 21.8 MPa.

Mechanical properties together with the tensile stress-strain curves of the used steels are summarized in Table 4.2-2 and Fig. 4.2-3 separately. As the SBPDN 1275/1420 rebar did not exhibit apparent yield plateau in their stress-strain relations, the yielding strengths of them were determined by the 0.2% offset yielding method.

(a) Ordinary (b) Screwed thread

Fig. 4.2-2 Surface of U12.6 (SBPDN1275/1420) bars

(a) D6 rebars (SD295A)

D6	E_s (kN/mm^2)	f_y (N/mm^2)	ε_y (×0.01)	f_u (N/mm^2)
No.1	187.96	379.9	0.202	511.8
No.2	181.04	387.4	0.214	515.5
No.3	183.37	393.6	0.215	523.5
Average	184.13	386.96	0.210	516.95

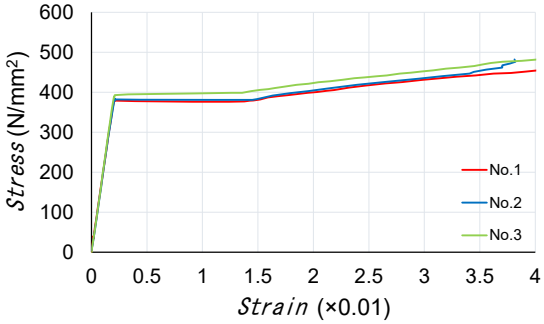

(b) U12.6 rebars (SBPDN1275/1420)

U12.6	E_s (kN/mm^2)	f_y (N/mm^2)	ε_y (×0.01)	f_u (N/mm^2)
No.1	213.90	1377.8	0.844	1461.6
No.2	208.00	1373.0	0.860	1456.8
No.3	213.20	1387.4	0.846	1460.0
Average	211.70	1379.38	0.850	1459.47

※0.2% offset method were used.

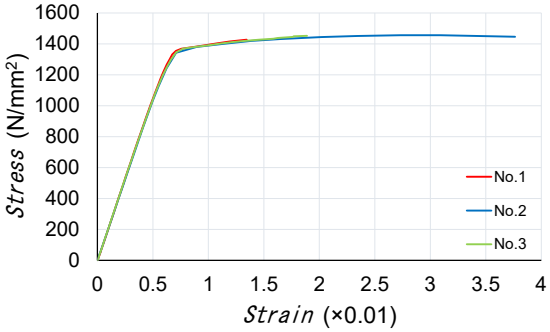

Table 4.2-2 Mechanical properties of the steels

Fig. 4.2-3 Stress-strain relationships of the steels

Note

E_s : Young's modulus
f_u : ultimate stress
f_y : yield stress
ε_y : yield strain

Ready-mixed concrete made of Portland cement and coarse aggregates with maximum particle size of 20mm was used to fabricate the specimens. Table 4.2-3 shows the mix proportions of concrete along with measured slumps and air contents. Concrete strengths were evaluated at the same day of loading by testing three standard cylinders (diameter: 100mm, height: 200mm), which were cured under the same condition to the shear walls, and test results are shown in Table 4.2-1 for each specimen.

Table 4.2-3 Mix proportions for concrete

Date	W/C	Water (kg/m^3)	Cement (kg/m^3)	Fine aggregate (kg/m^3)	Coarse aggregate (kg/m^3)	Additives	Slump (mm)	Air content (%)
2020/08/04	0.57	180	316	883	879	2.94	201	4.9
2020/08/26							184	4.1

The #1000-series sheath ducts with spiral groove on its surface, which are made of galvanized steel sheet according to Japanese standard JIS G3302, were applied in this experiment which were the same as shown in Chapter Three.

A cementitious non-shrinkage mortar that excels in fluidity named PRE U-LOX was used as the grouting material for this experiment, which was the same as described in Chapter Three. Compression strength of grouting material were evaluated at the same day of loading by testing three standard cylinders (diameter: 50mm, height: 100mm), which were cured more than 21 days under the same condition to the shear walls, and according to Japanese standard JIS A 1108, and test results are shown in Table 4.2-1 for each specimen.

4.2.3 Test setup and loading program

The experiments were conducted using the setup shown in Fig. 4.2-4. The loading apparatus was designed to subject the shear wall to reversed cyclic lateral load and constant axial compression. A vertical hydraulic jack with a capacity of 1000 kN, which was connected to stiff loading frame via a roller, was used to apply constant axial compression. The reversed cyclic lateral load was applied by two 500 kN horizontal hydraulic jacks. The lateral loading was controlled by drift ratio (R), which is defined as the ratio of the lateral displacement at the loading point of lateral force (Δ) to the shear span (a) of each shear wall, and the east direction was applied as the initial tensile direction (plus direction).

The loading program is shown in Fig. 4.2-5. To find out the first flexure or shear crack, the lateral loading was initially controlled by force before reaching drift ratio of 0.125%. After then, two complete loading cycles were applied at each specified level of targeted drifts (0.25%, 0.375%, 0.5%, 0.75%, 1%, 1.5%, and 2%), and one cycle was applied at each level of targeted

drift after drift ratio was beyond 2%.

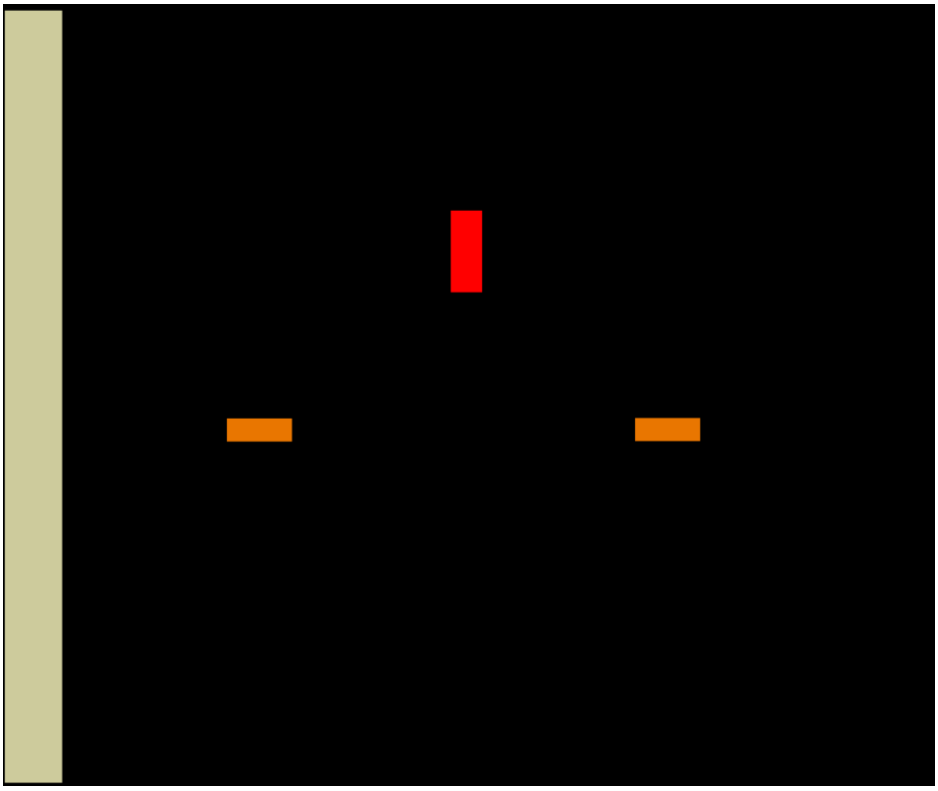

Fig. 4.2-4 Schematic view of test setup for shear walls

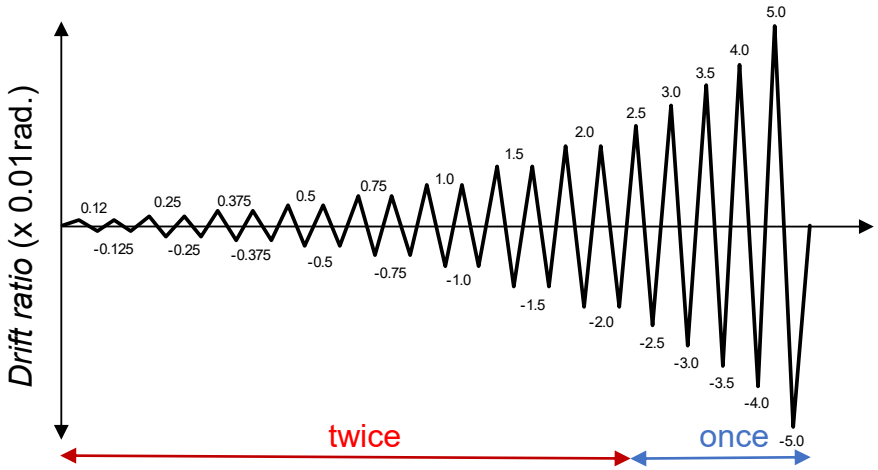

Fig. 4.2-5 Loading program

4.2.4 Instrumentation and measurement

Fig. 4.2-6 shows the locations of displacement transducers (DTs) for the tested specimens with the shear span ratio of 1.5(a) and 2.0(b) respectively. As can be seen, two DTs were installed to measure the lateral displacement, and the average value measured by DTs No.1 and 2 were used as the lateral displacement of specimen. The other eight (four pairs of) DTs No.5 to 12 were installed to measure the local vertical displacement at several targeted heights of specimens. Besides, DTs No.3 and 4 were applied to record the rotation while No.13 for recording the horizontal displacement of the rigid bottom stub. Overall view of testing is shown in Fig. 4.2-7.

To measure the axial strain generated in the rebars of the walls, strain gauges were embedded for each specimen. Details of these measurements can be found in Fig. 4.2-8. Red, green, and blue marks represent the locations of embedded strain gauges for LD rebars, HD rebars and concentrated rebars separately.

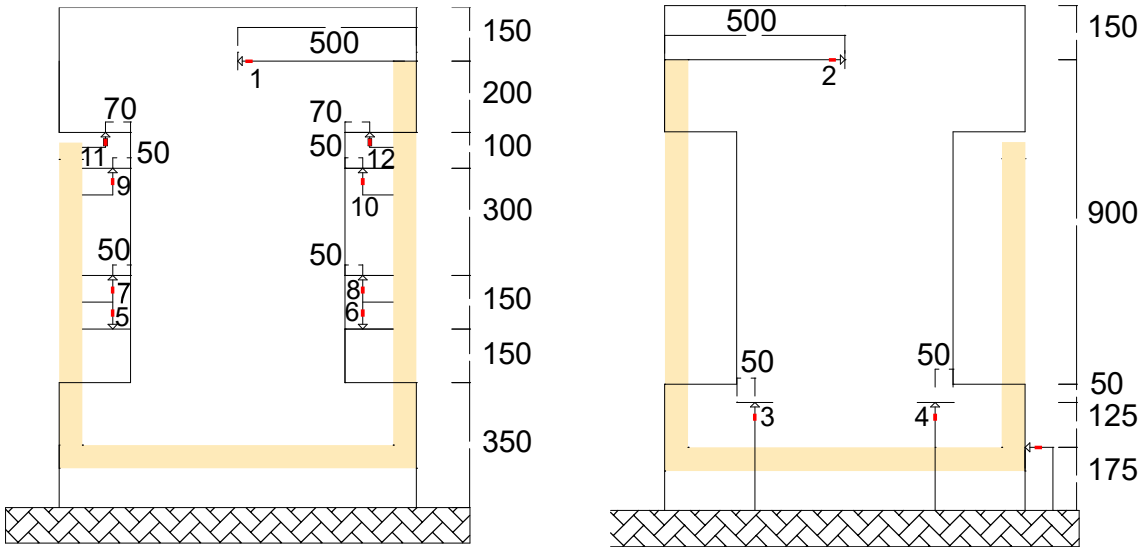

(1) North (2) South

(a) WP15-Series

Fig. 4.2-6 Positions of displacement transducers (DTs) (Unit: mm)

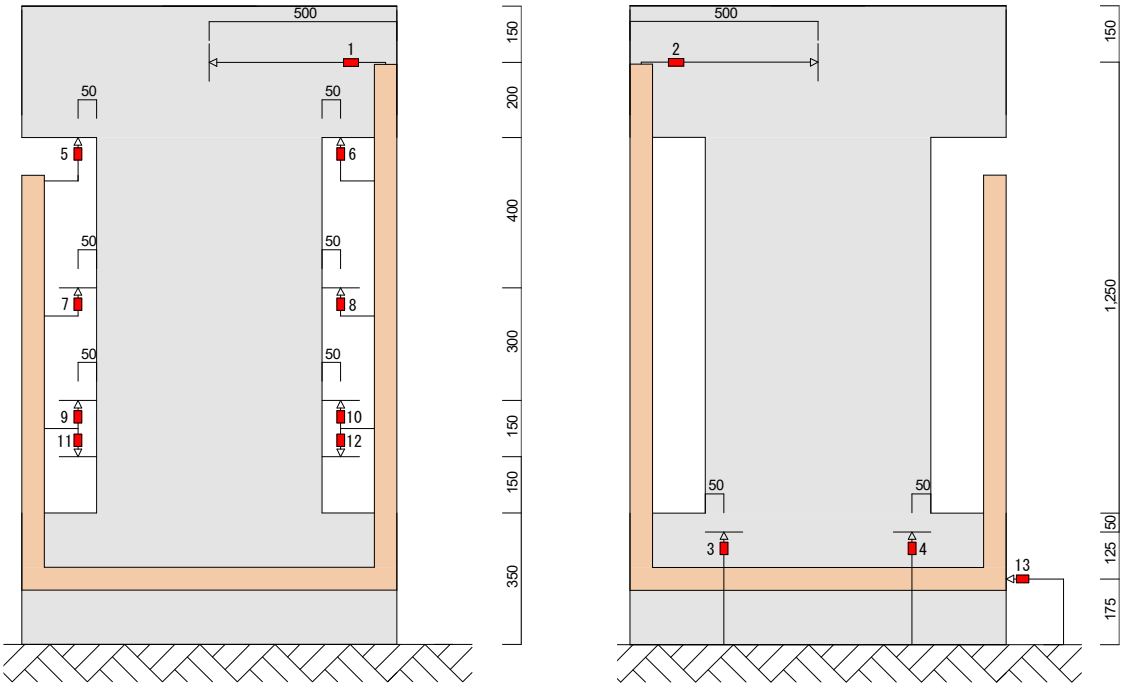

(1) North (2) South

(b) WP20-Series

Fig. 4.2-6 Continued

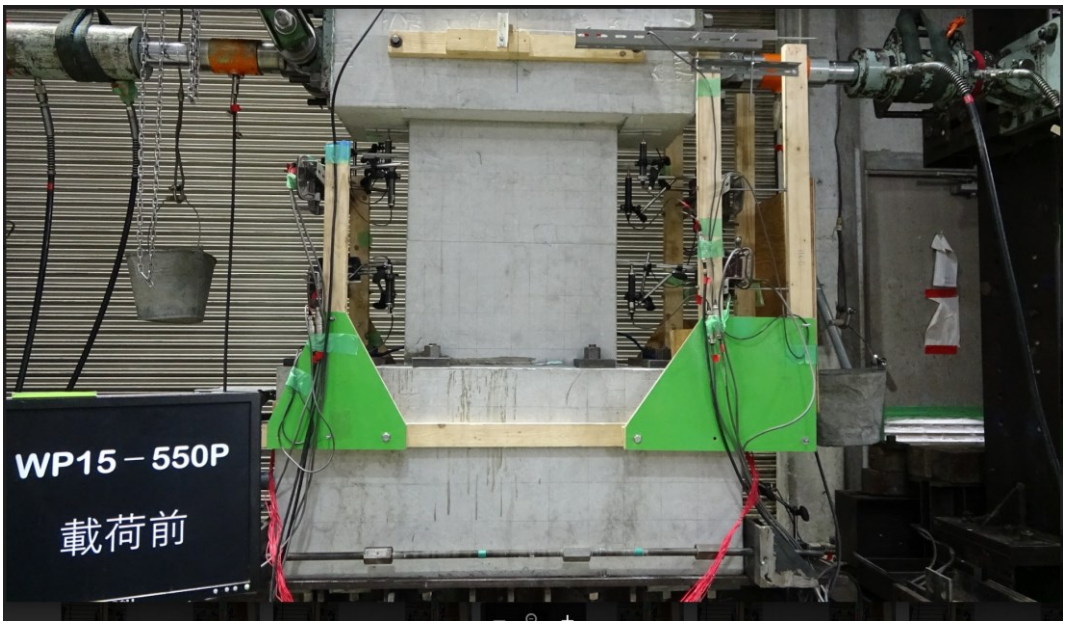

Fig. 4.2-7 Overall view of a testing specimen

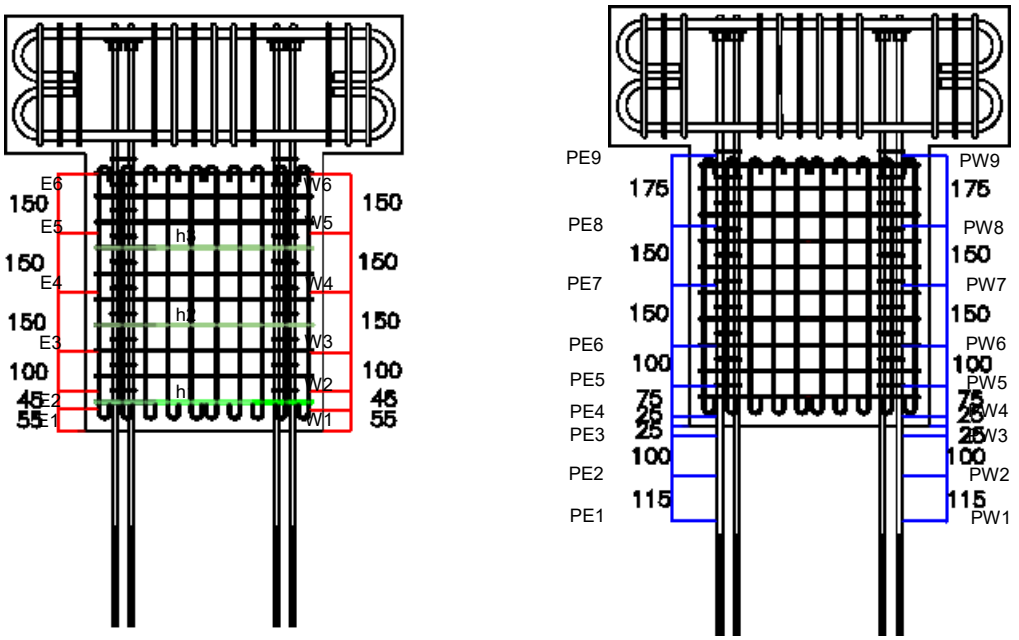

(1) Wall web (2) Concentrated rebars

(a) WP15-Series

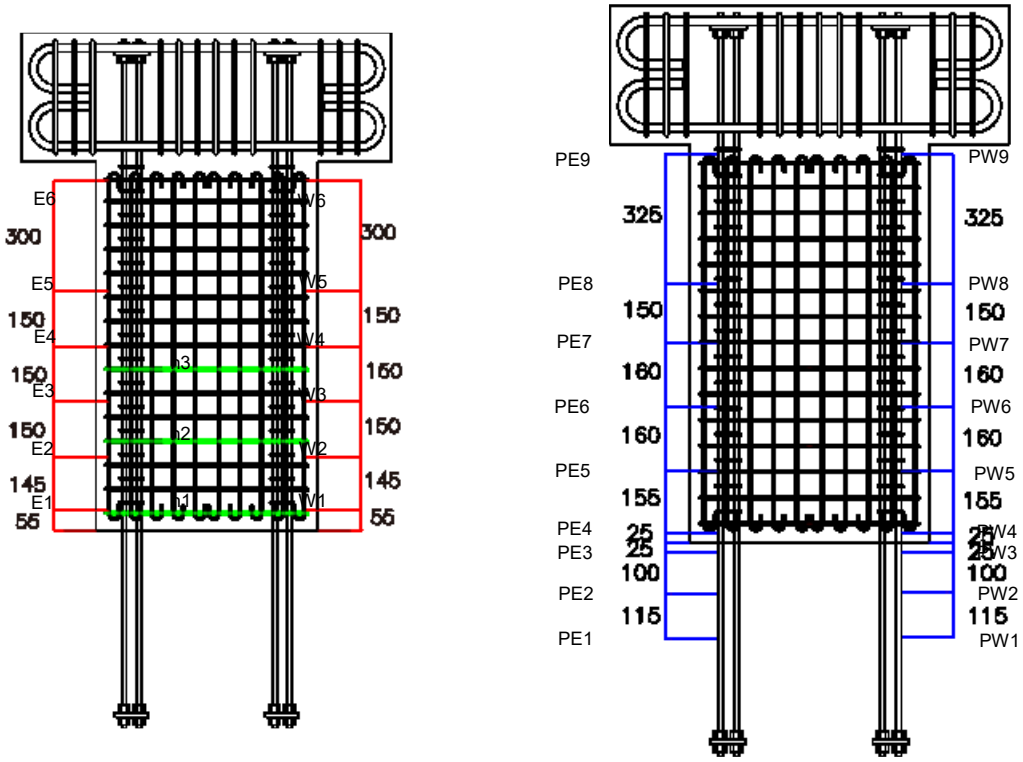

(1) Wall web (2) Concentrated rebars

(b) WP20-Series

Fig. 4.2-8 Locations of strain gages

4.3 Observed behaviors and results

4.3.1 Crack and damage of shear walls

This section summarized the developments of cracks that were observed from web side of each specimen. In the figures of this section, the grids have a spacing of 50 mm, the red lines and blue lines represent the cracks that were drawn at the peak drifts of the targeted levels in both push and pull direction of lateral loading, respectively, while the blacked portions express the spalled-off cover concrete.

For specimen WP15-D10H55P-075, as shown in Fig. 4.3-1, the first flexure crack was confirmed at boundary between the grouting material and wall panel when lateral force reached 70kN. The first shear crack was found when lateral force reached 110kN. The initial spalling-off of concrete was observed at drift ratio of 1.5%, along with the spalling off of the cover concrete visibly grown, and the exposure of the HD bars was fist confirmed at 2.5%. After that, as can be seen in Fig. 4.3-2(a) when drift ratio reached 3.0%, the cover concrete on the top surface of the foundation was slightly lifted up. Finally, at the drift ratio of 5.2%, obvious expansion of flexure and shear cracks were observed which is indicated in Fig. 4.3-2(b), and due to the dramatically descent of lateral resistance force, the test was terminated at the drift ratio of 5.5%.

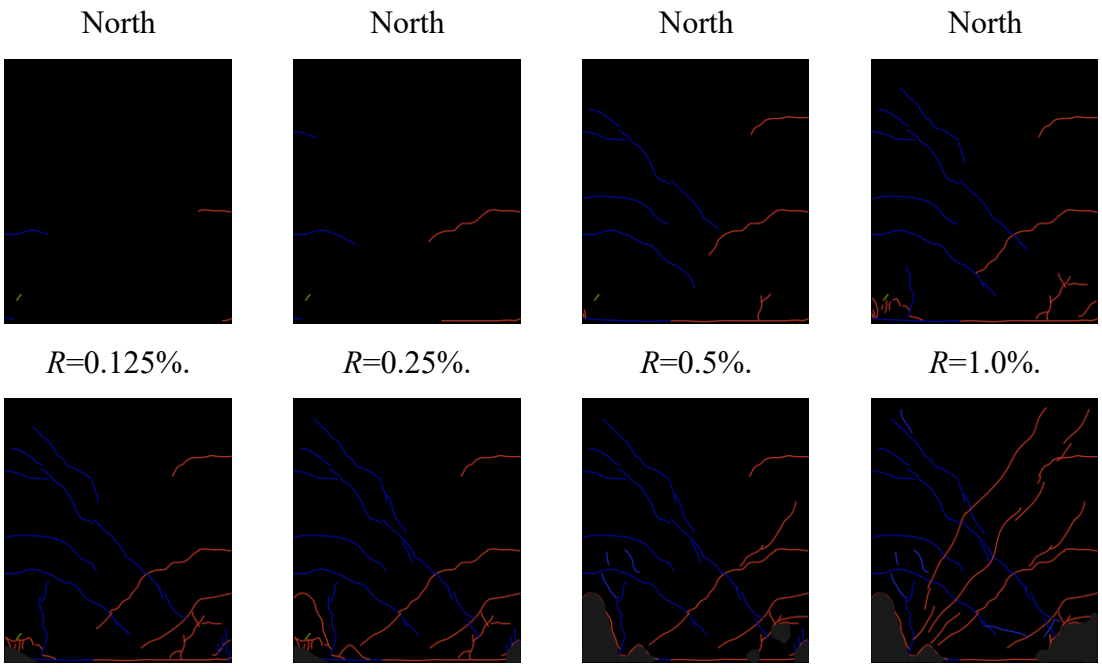

Fig. 4.3-1 Cracks patterns observed on specimen WP15-D10H55P-075

(a) R=3.0%. (b) R=5.2%.

Fig. 4.3-2 Damage observed on specimen WP15-D10H55P-075

For specimen WP15-D10H55N-075, as can be seen in Fig. 4.3-3, the first flexure crack was confirmed at boundary between the grouting material and wall panel when lateral force reached 50kN. The first shear crack was found when lateral force reached 150kN. The initial spalling-off of concrete was observed at drift ratio of 1.5%, along with the spalling off of the cover concrete visibly grown, and the exposure of the HD bars was fist confirmed at 2.0%. After that, as can be seen in Fig. 4.3-4(a) when drift ratio reached 3.5%, less damage than that of specimen WP15-D10H55P-075 was observed at the wall-base joint. Finally, at the drift ratio reached 5.0%, the SBPDN rebar was suspected of being pulled out from the grouting materials as was displayed in Fig. 4.3-4(b).

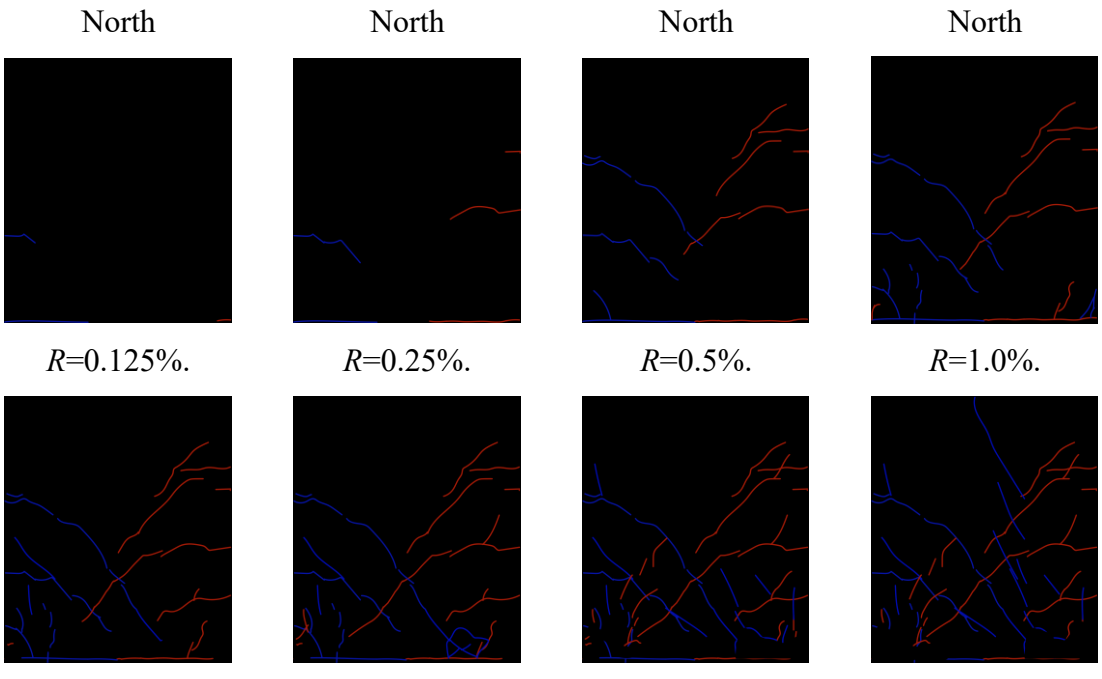

Fig. 4.3-3 Cracks patterns observed on specimen WP15-D10H55N-075

For specimen WP20-D10H55P-075, as is illustrated in Fig. 4.3-5, the first flexure crack was confirmed at boundary between the grouting material and wall panel when lateral

(a) R=3.5%. (b) R=5.0%.

Fig. 4.3-4 Damage observed on specimen WP15-D10H55N-075

force reached 60kN. The first shear crack was found when lateral force reached 100kN. The initial spalling-off of concrete was observed at drift ratio of 1.5%, and obvious spalling off of the cover concrete was fist confirmed at 2.5%. Meanwhile, the cover concrete on the top surface of the foundation was slightly lifted up as can be seen in Fig. 4.3-6. Due to the limitation in the stroke length of the horizontal loading jacks, the test was terminated at drift ratio of 4.0%, and no sever damage at the wall panel nor the wall-base joint were confirmed till the end of test.

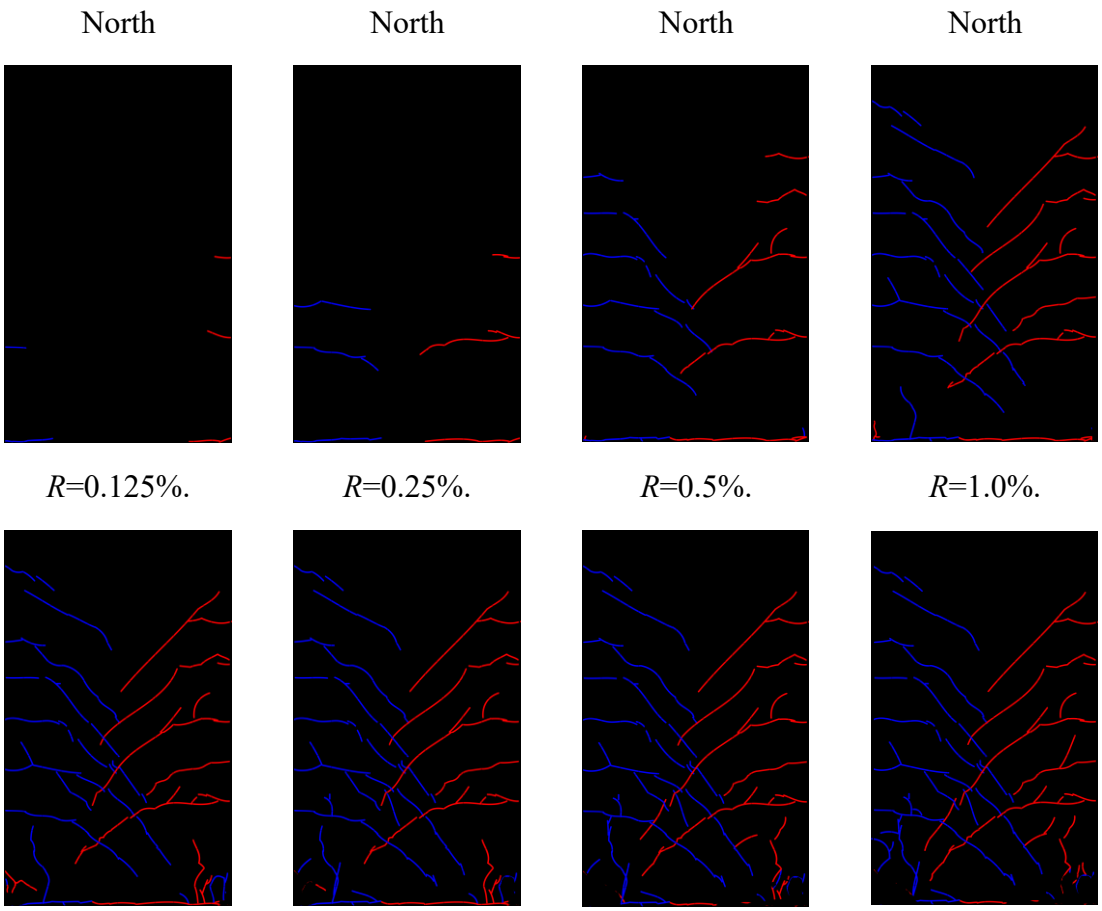

Fig. 4.3-5 Cracks patterns observed on specimen WP20-D10H55P-075

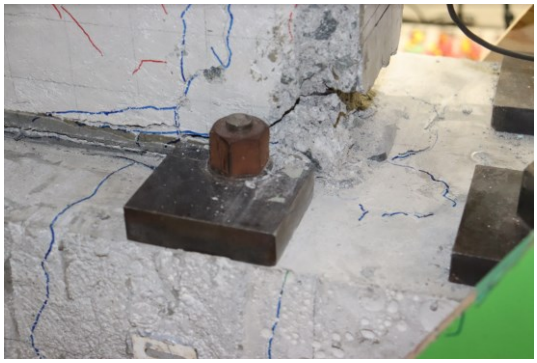

R=2.5%.

Fig. 4.3-6 Damage observed on specimen WP20-D10H55P-075

4.3.2 Lateral force – drift ratio hysteretic behaviors

The measured lateral resistance force (V) versus drift ratio (R) relationships of all specimens are shown in Fig. 4.3-7, while the measured lateral capacities that averaging the peak lateral forces in both directions are summarized in Table 4.2-1.

As can be seen in Fig. 4.3-7(a) and (b), for specimen with shear span ratio of 1.5, their lateral force all stably increased along with drift, all specimens exhibited drift-hardening capability up to the drift ratio of 3.0%. and the lateral force of specimen WP15-D10H55P-075, in which SBPDN rebars were anchored to steel plates, exhibited no obvious decrease till an extreme large drift ratio of 4.8%.

One can be seen in Fig. 4.3-7(c), lateral force of specimen WP20-D10H55P-075 stably ascend until large drift ratio of 3.5%, and almost remained the same level till R = 4.0%.

It is noteworthy that for the loading cycles beyond the drift ratio of 2.0%, although obvious damage of concrete was not observed at the wall-base joint, the residual deformation increased faster from that drift on, and the loading curvatures for all the precast shear walls became irregular. For example, at the beginning of the loading cycle with a targeted drift ratio of 2.5%, lateral force of specimen WP15-D10H55P-075 increased gradually along with the drift ratio as usual, but it suddenly dropped to zero when lateral deformation near zero, which indicated that even the damage around the connector could not be observed directly form the specimen, it still influenced the loading and residual deformation of precast shear walls, on the other hand, the proposed method with an embedment depth of 510mm could provide sufficient bond strength to assure precast specimen drift-hardening capability till drift ratio of 3.0%.

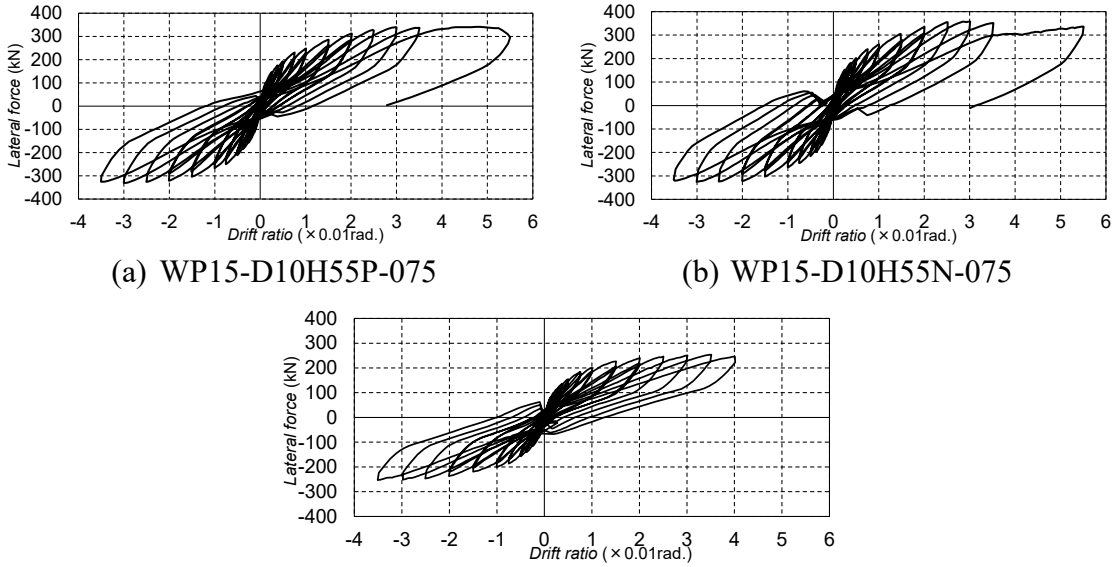

(a) WP15-D10H55P-075 (b) WP15-D10H55N-075

(c) WP20-D10H55P-075

Fig. 4.3-7 Measured lateral load-drift ratio relationships

To better see the performance of the applied anchor method of this chapter, the envelope curves in both pull and push direction of hysteretic loops are compared in Fig. 4.3-8.

On can be seen from 4.3-8(a) that lateral force of all specimen increased stably along with lateral deformation till drift ratio of 3.0%, hence the connectors with an embedment depth of 510mm could provide sufficient bond strength between concrete, which could assure precast shear walls the same drift hardening capability as the conventional fabricated walls.

Fig. 4.3-8(b) shows comparison of two specimens with the only difference is their anchorage of SBPDN rebars at bottom end, and it is obvious in Fig. 4.3-8(b) that the proposed simplified anchor method, which the SBPDN rebars were screwed along the splice length of 20d (where d is the nominal diameter of SBPDN bar) with a total embedment depth of 40d, could provide shear wall the same drift hardening capability till drift ratio of 3.0% as the anchorage of steel plates.

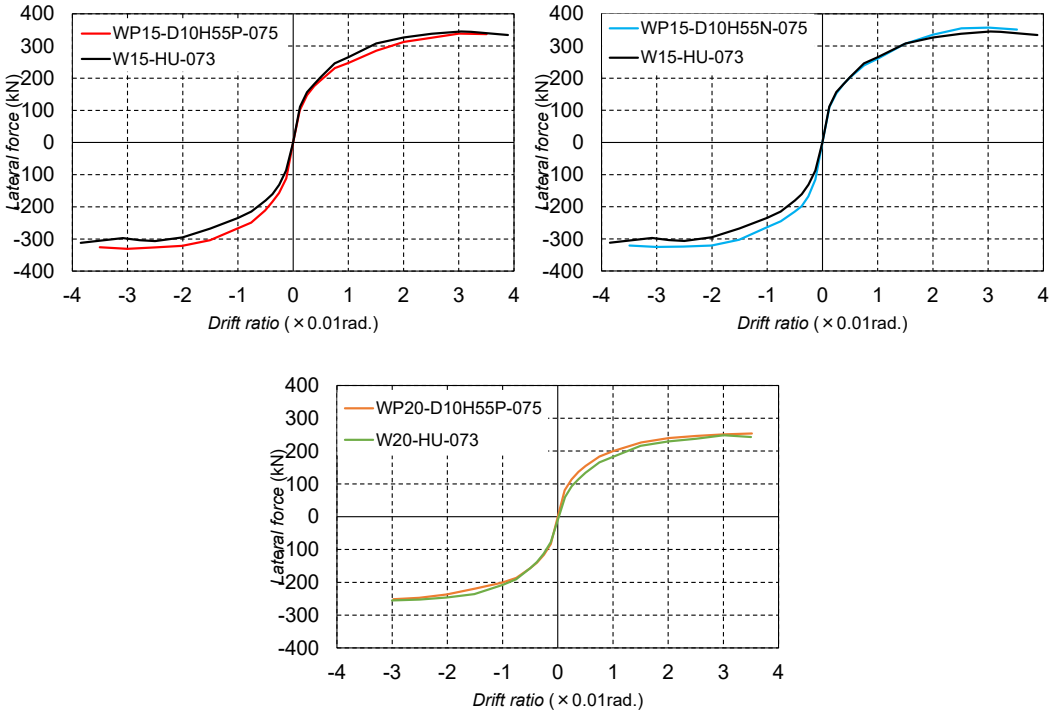

(a) Effect of construction method

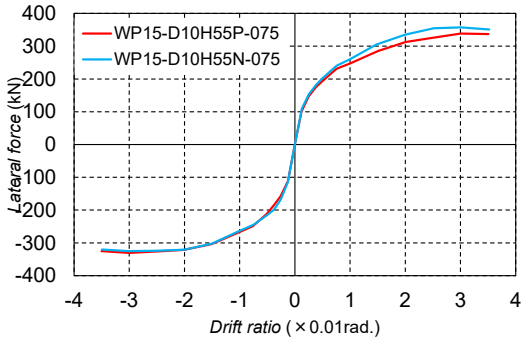

(b) Effect of anchorage at bottom end

Fig. 4.3-8 Effects of main experimental parameters.

4.3.3 Strains measured in reinforcements

The measured axial strains of concentrated rebars for all tested shear walls are shown in Fig. 4.3-9. And the title of each graph, for example W1 – 30mm, represents the strain measured by the strain gauges located at the section of 30mm away from the wall base for specimens on the west side, which is related to the details provided in Fig. 4.2-8. While the red dashed horizontal lines represent the yield strains.

As can be seen from Fig. 4.3-9, the axial strain of SBPDN rebars in all specimens exhibited stably ascent till drift ratio of 3.0%, and the strains measured in specimen WP20-D10H55P-075, which had a shear span ratio of 2.0 and the SBPDN rebars were anchored by steel plate, did not reached their yield strain (0.85%) till the end of test. n the other hand, it is noteworthy that the SBPDN rebars in specimen WP15-D10H55P-075 and WP15-D10H55N-075 yielded at

the drift ratio of 3.8% and 3.0%, respectively. However, even after the yielding of SBPDN rebars, the lateral force of specimen WP15-D10H55P-075 did not decrease until reached its maximum shear carrying capacity of the wall panel at the drift ratio of 5.2%. As for specimen WP15-D10H55N-075 whose SBPDN rebars were anchored by the screwed threads, at the last loading cycle when drift ratio beyond 3.5%, the measured axial strain in SBPDN rebars remain the same level along with the increased drift ratio, which indicated the slippage between SBPDN rebars and the grouting material.

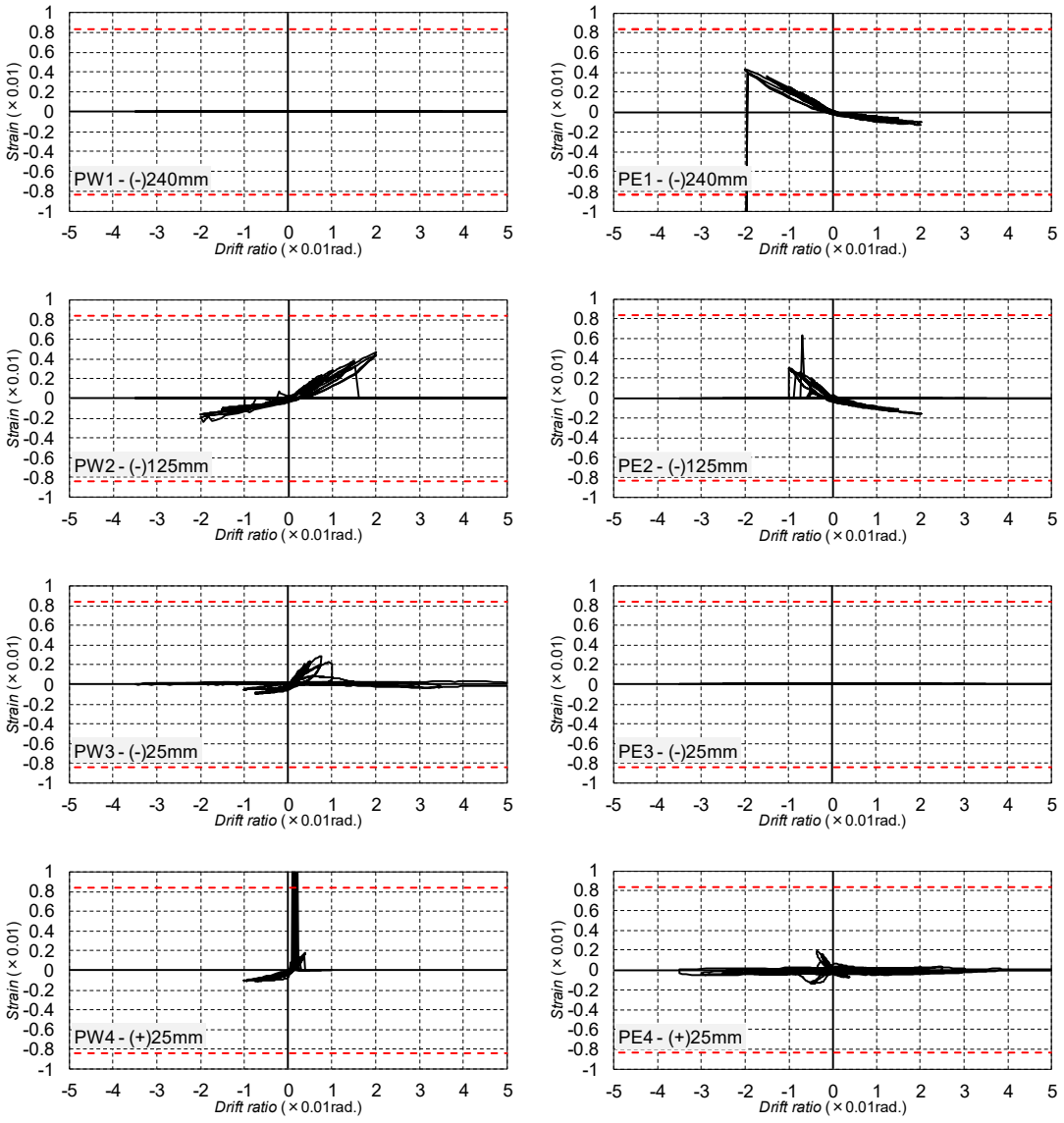

(a) WP15-D10H55P-075

Fig. 4.3-9 Measured strains-drift ratio relationships of concentrated rebars

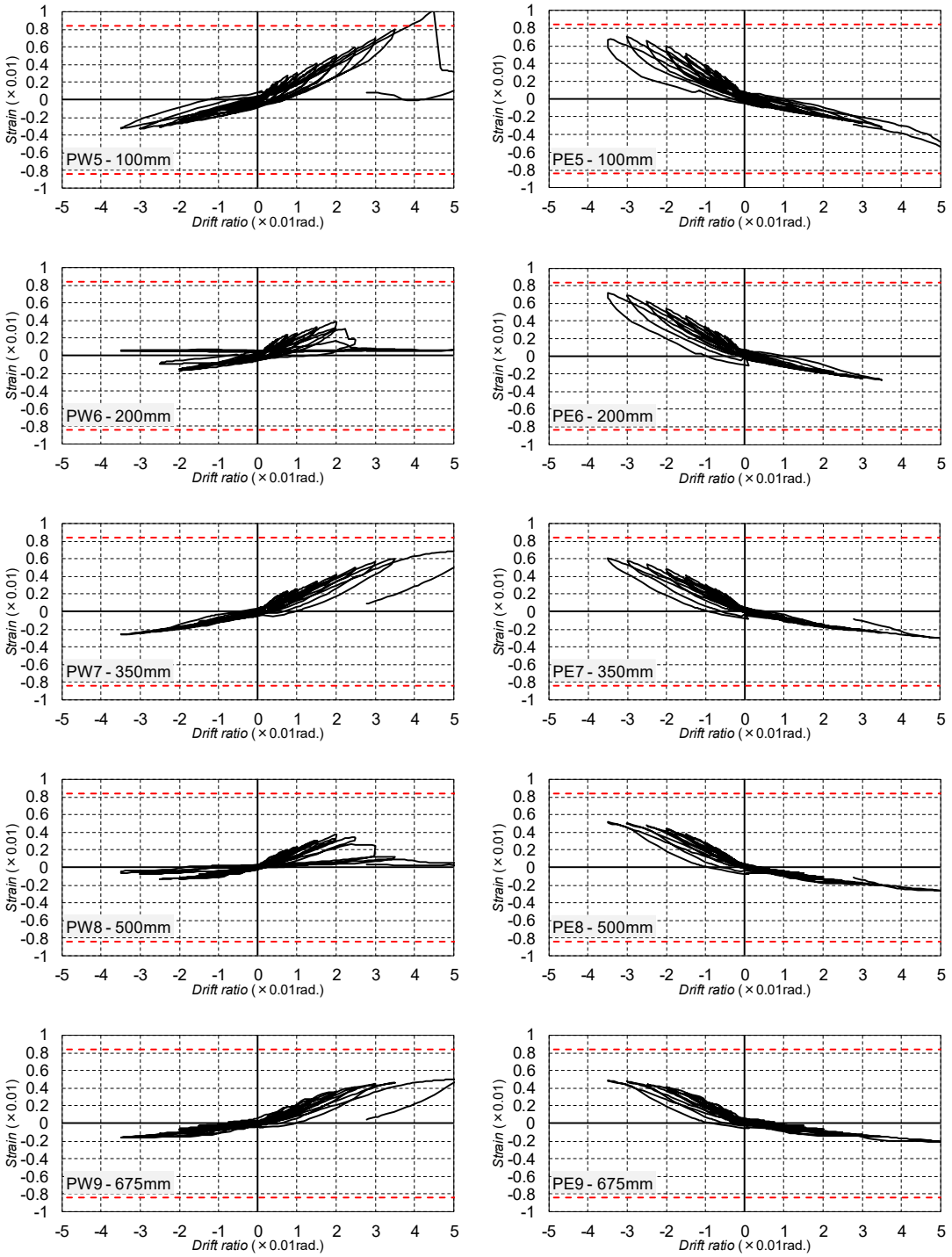

(a) WP15-D10H55P-075

Fig. 4.3-9 Continued

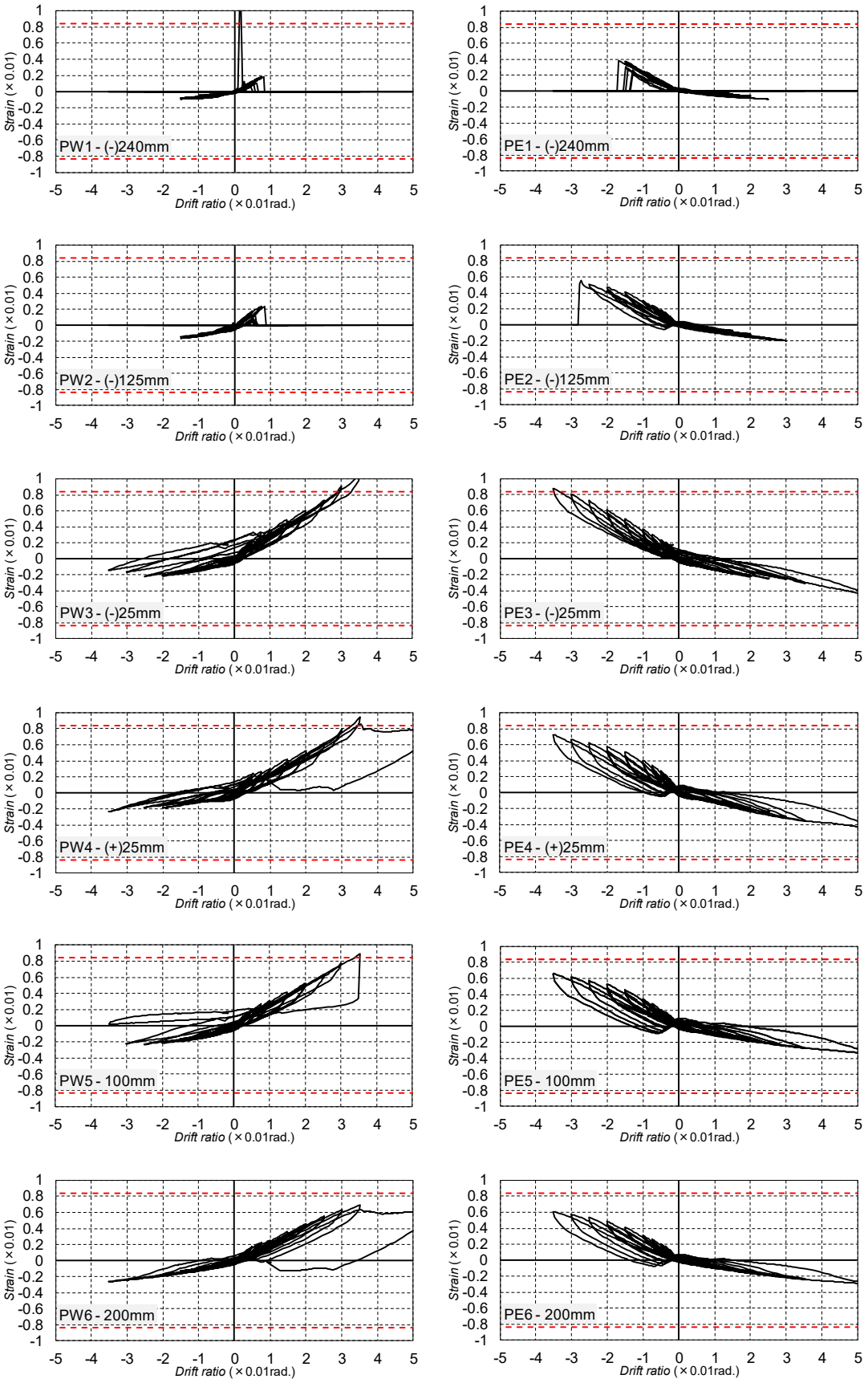

(b) WP15-D10H55N-075

Fig. 4.3-9 Continued

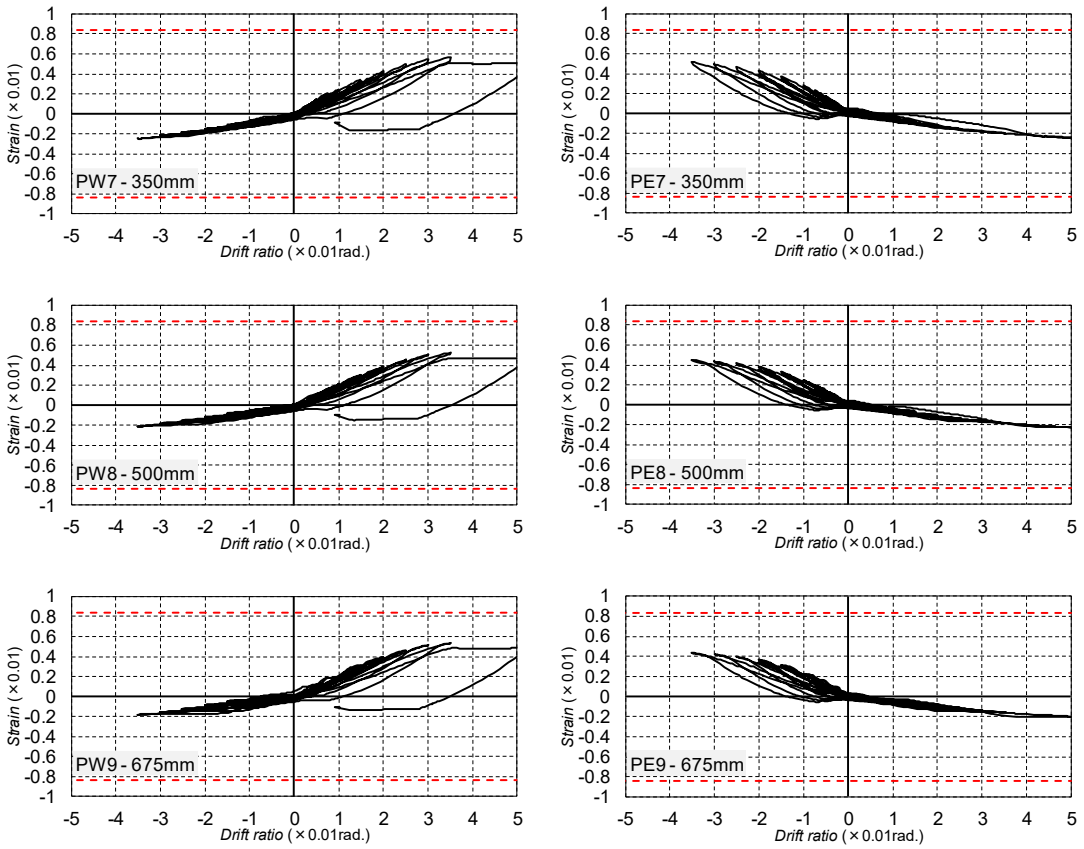

(b) WP15-D10H55N-075

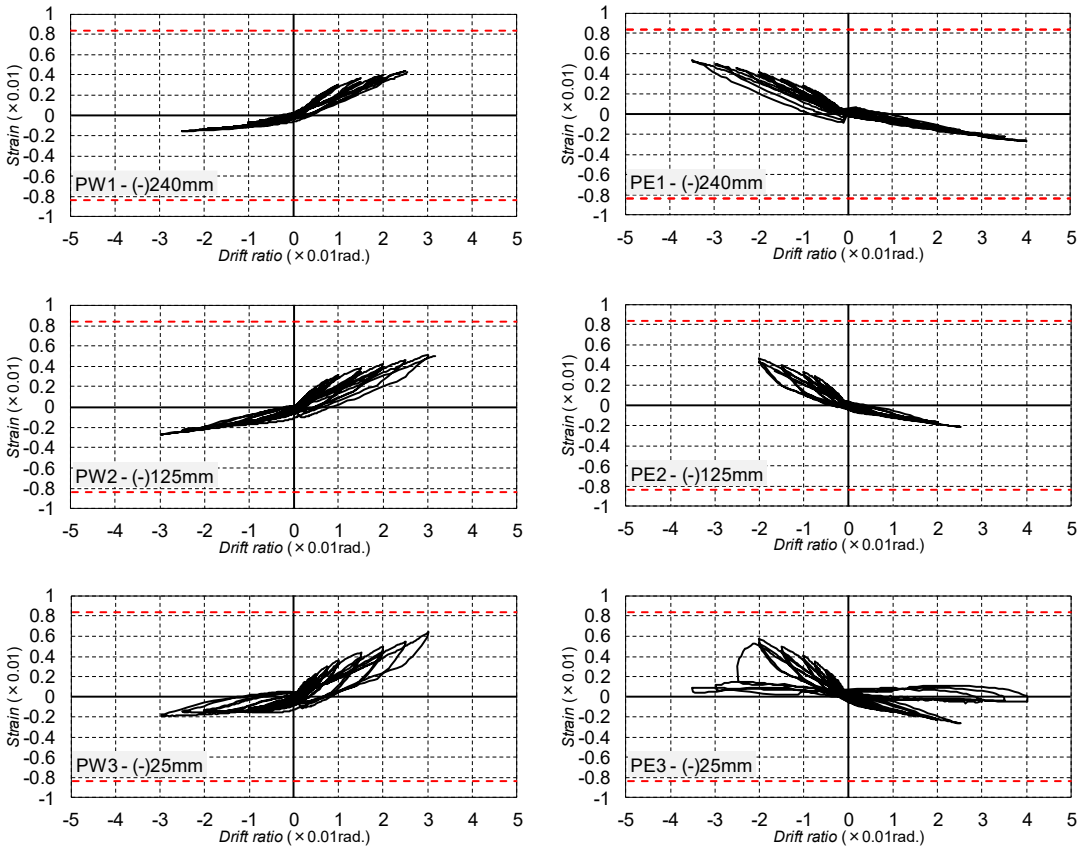

(c) WP20-D10H55P-075

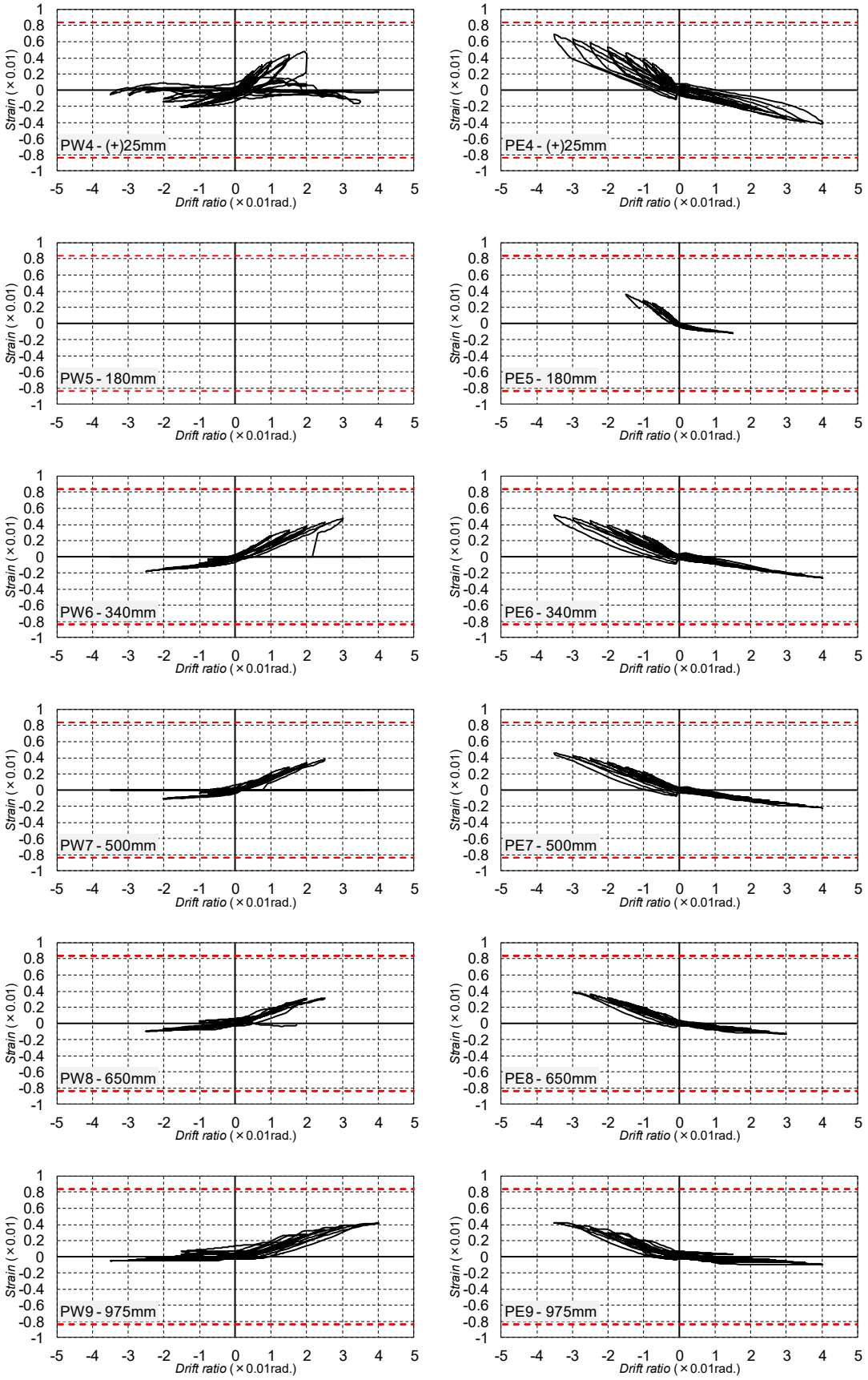

(c) WP20-D10H55P-075

Fig. 4.3-9 Continued

Fig. 4.3-10. indicates the strain profiles of concentrated rebars along the height of wall panels measured at each targeted drift ratios, and one can be seen that the strains of SBPDN rebars in the precast specimens exhibited a nearly uniform distribution along the height of wall panel, which is the same as in the conventional fabricated specimens. And as can be noted that, even in the wall-base joint zone, the strains of SBPDN rebars could still indicate an almost uniform distribution.

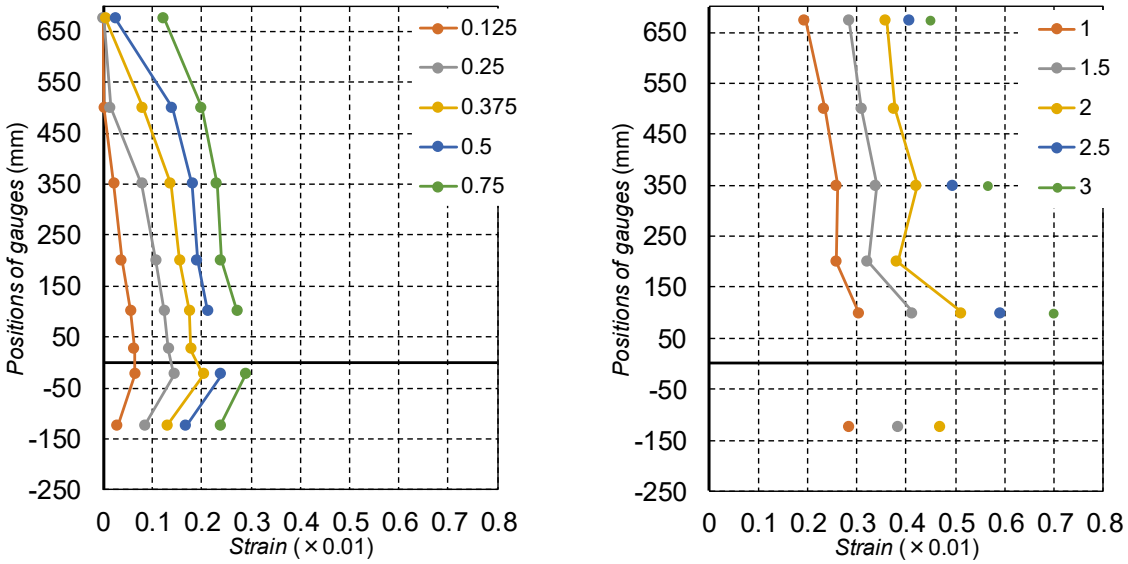

（1）R=0.125～0.75%.　　（2）R=1.0～3.0%.

(a) WP15-D10H55P-075

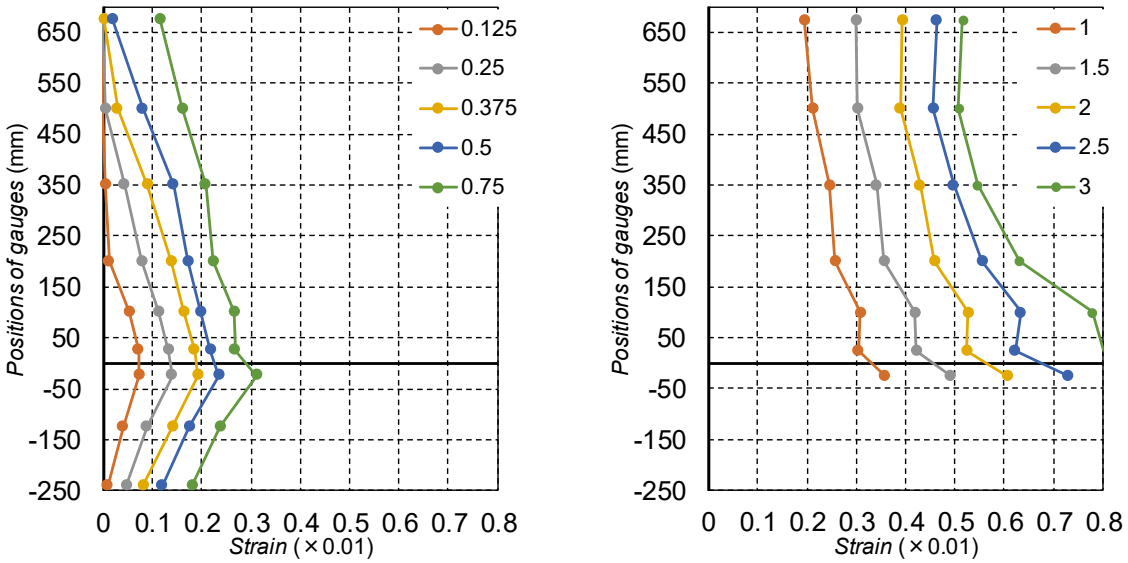

（1）R=0.125～0.75%.　　（2）R=1.0～3.0%.

(b) WP15-D10H55N-075

Fig. 4.3-10 Strains distribution of concentrated rebars

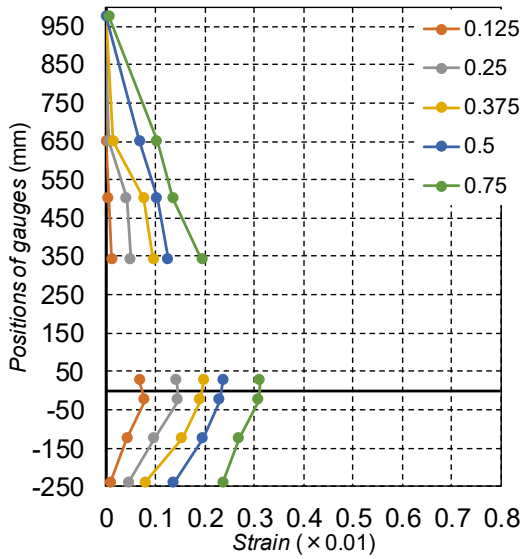

（1）R=0.125～0.75%.

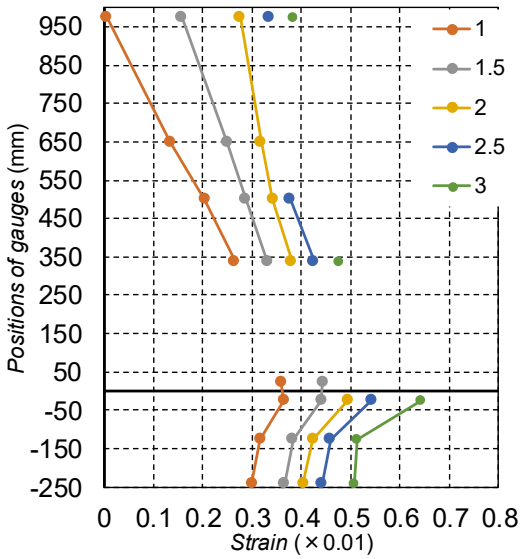

（2）R=1.0～3.0%.

(c) WP20-D10H55P-075

Fig. 4.3-10 Continued

4.3.4 Overall vertical axial deformation

Fig. 4.3-11 shows the overall vertical axial strain versus drift angle relationship for all specimens, details of the calculation can be found in Chapter 2 section 2.3.4. As can be seen in Fig. 3.3-16 (a), for the precast specimen WP15-D10H55P-075 and WP20-D10H55P-075, in which SBPDN rebars were anchored by steel plates, their overall vertical axial strain increased gradually along with drift ratio and no significant difference was observed between the conventional fabricated specimens. On the other hand, as shown in Fig. 3.3-16 (b), for the specimen WP15-D10H55N-075 whose SBPDN rebars were anchored by screwed threads, its overall vertical axial strain increased slightly faster after the drift ratio of 1.5%. This could be counted on the influence of the slippage between SBPDN rebars and the grouting material at the wall-base joint.

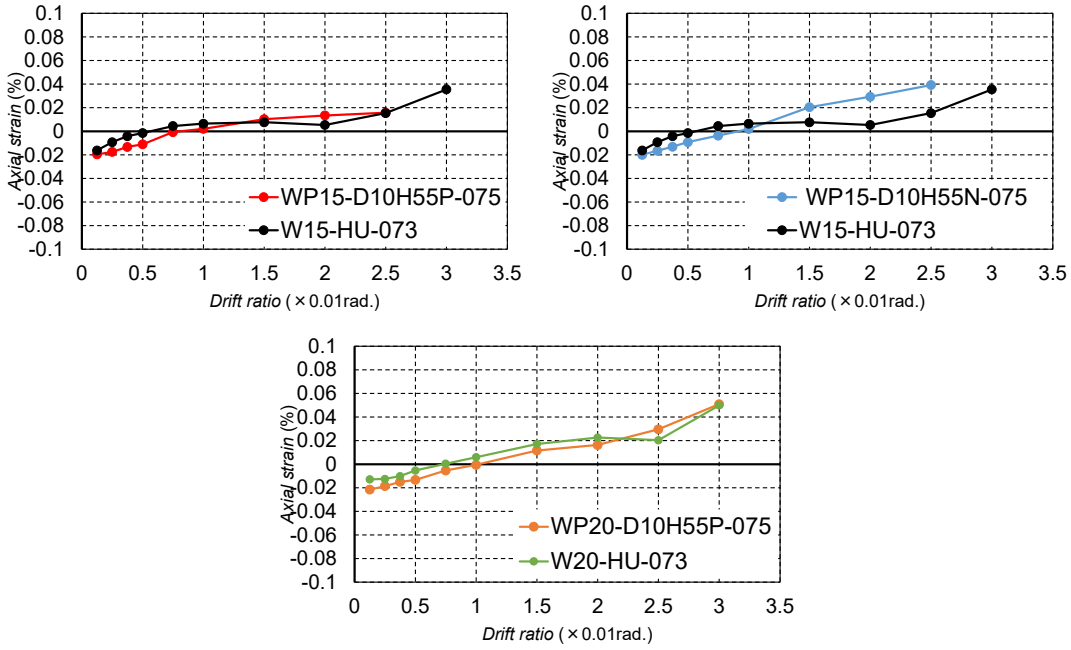

(a) Effect of construction method

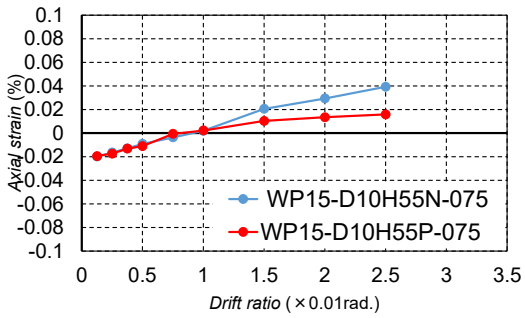

(b) Effect of anchorage at bottom end

Fig. 4.3-11 Measured overall axial strain

4.3.5 Residual drift ratio

Fig. 4.3-12 summarized the average residual drift ratio of the plus and minus directions measured at each targeted drift ratio. As displayed in Fig. 4.3-1, the residual drift ratios of all specimens were controlled under a very low level till 1.5%. However, from that drift ratio on, residual drift ratios measured from the precast specimens increased faster due to the damage around the connectors. Besides, for the precast specimen WP15-D10H55N-075 whose SBPDN rebars were anchored by screwed threads, its residual drift ratio ascended more sharply than that of the specimen anchored by steel plates, which could be considered as the influence of the slippage between SBPDN rebars and the grouting material at the wall-base joint.

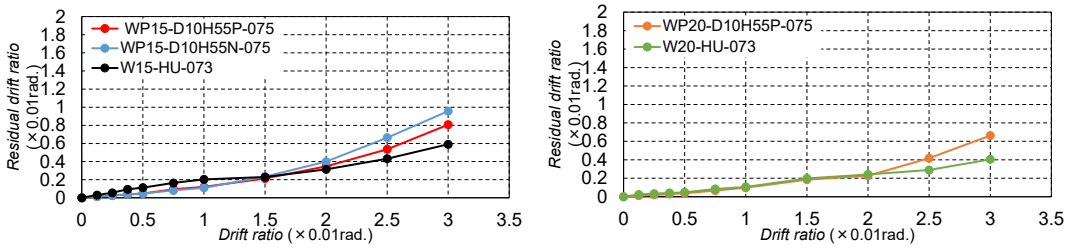

Fig. 4.3-12 Measured residual drift ratios

4.3.6 Equivalent viscous damping (Energy dissipation capacity)

Fig. 4.3-13 shows the measured equivalent viscous damping coefficient (*heq*) for all tested specimens. It can be seen that, all specimens indicated stable energy absorption capacity with a nearly constant equivalent viscous damping coefficient. Although the measured *heq* of the precast specimens were slightly lower till drift ratio of 1.0%. the influence of construction method and anchorage of SBPDN rebars on the overall energy absorption capacity could be ignored.

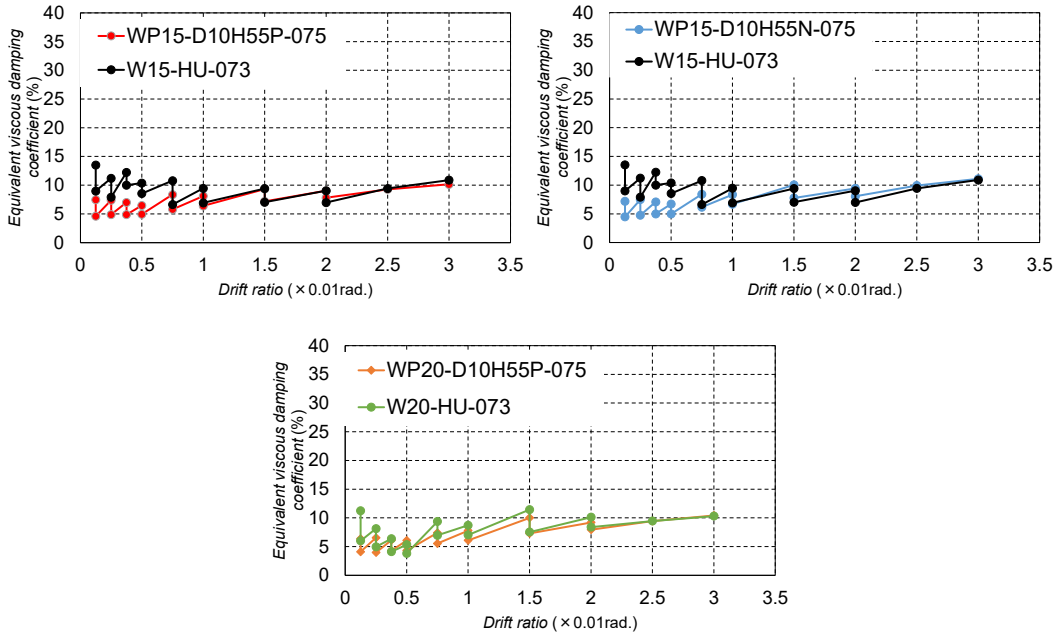

(a) Effect of construction method

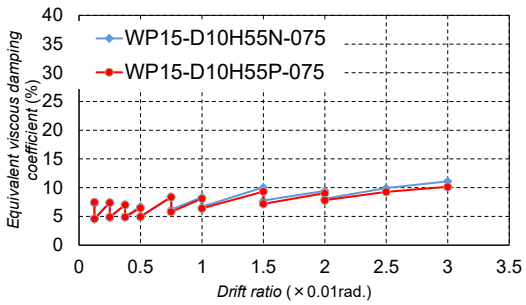

(b) Effect of anchorage at bottom end

Fig. 4.3-13 Measured equivalent viscous damping coefficients

4.4 conclusion

This chapter is intended to experimentally investigate the influence of anchorage detailing on seismic performance of precast concrete walls reinforced with SBPDN rebars. Three precast concrete walls were fabricated and tested under combined reversed lateral loading and constant axial compression, with the shear span ratio and the anchorage detailing (fixation by steel plate and nuts or by screwed threads of end portion) of SBPDN rebars at experimental variables. Based on the experimental results described in this chapter, the following conclusions cab be drawn:

1) If the embedment length of sheath ducts that accommodate SBPDN rebars was five times of the duct diameter, giving an embedment depth of 510 mm, both anchorage methods (by combination of the steel plate and nuts or by screwed threads of end portion) could provide sufficient bond strength to SBPDN rebars, and ensure the precast concrete walls drift-hardening capability till drift ratio of 3.0%.

2) No severe damage was observed around the anchorage portions with embedment length of 510 mm regardless of the difference of anchorage detailing. Both short walls with shear span ratio of 1.5 exhibited excellent deformability up to about 5.0% drift without obvious degradation of lateral resistance, while the lateral resistance of the test wall with shear span ratio of 2.0 at the drift of 4.0% remained almost the same value as the maximum lateral force.

3) The residual deformation of the precast walls was identical to that of the cast-in-site walls described in chapter two till the drift level of 2.0%. After that drift level, the residual drift of precast walls became 30% larger than the cast-in-site wall due to the slippage of anchorage portions at large deformation. The anchorage by nuts and steel plate was more effective than that by screwed threads at ends of SBPDN rebars in aspect of controlling the residual deformation at larger drift than 2.0%.

References

[4.1] Funato Y., Sun Y., Takeuchi T., and Cai G., “Modeling and Application of Bond Characteristic of High-strength Reinforcing Bar with Spiral Grooves,” Proceedings of the Japan Concrete Institute, V.34, No.2, 2012, pp.157-162.

[4.2] C. Wei. et al., “SEISMIC BEHAVIOR OF SQUARE CONCRETE BEAM-COLUMNS WITH CIRCULARLY DISTRIBUTED ULTRA-HIGH-STRENGTH REBARS”, 17th World Conference on Earthquake Engineering, 2021, Paper No. C000411.

CHAPTER Five

Analysis method to evaluate seismic behavior of concrete walls reinforced by SBPDN rebars

5.1 Introduction

Experimental results described in chapter two have indicated that the utilization of SBPDN rebars in the edge zones of wall section could assure concrete shear walls drift-hardening capability up to the drift ratio of 3.0%, and that the new arrangement of distributed longitudinal (DL) bars in the wall panel could mitigate the damage of concrete near the wall toes, preventing the DHC walls with shorter shear span ratio from premature shear failure. It has also been verified that the precast concrete walls reinforced by DBPFN rebars can exhibit the same drift-hardening capability as the cast-in-site walls if the embedment length of SBPDN rebars are sufficient long.

To promote the DHC walls, either cast-in-site or precast, however, it is necessary to develop an accurate and reliable analytical method to evaluate overall seismic behavior of the DHC walls. This method should be able to take effect of the slippage of weakly bonded SBPDN rebar into consideration, which is not available in the current seismic design codes [5.1-5.6].

Objectives of this chapter are, 1) to develop a numerical analysis method by modifying the method proposed by Sun et al, covering the effects of bond slippage of SBPDN rebars, shear deformation, plastic hinge length, and placement of DL bars in the wall panel, 2) to verify validity and accuracy of the refined analytical method through comparison between the theoretical predictions by the refined method and the measured results in terms of hysteresis loop, residual drift ratio, and the axial strain of concentrated rebars, and 3) to clarify whether the current code-prescribed design equations can be applied to predict ultimate capacities of the walls with SBPDN rebars.

5.2 Evaluation of ultimate capacities by current codes

Table 5.2-1 summarized the primary experimental parameters along with the main test results, in which these specimens had been described in Chapter Two. To verify the accuracy of seismic design code in Japan for evaluating ultimate capacities of concrete walls reinforced by SBPDN rebars, calculation results by the provided method were compared with the experimental results in this section.

Table 5.2-1 Primary experimental parameters and main test results

Specimen	*a/D*	*n*	f'_c (N/mm^2)	Longitudinal rebars		Concentrated SBPDN rebars		Transverse rebars		Q_{exp}
				Type	ρ_{wv}(%)	Type	ρ_s(%)	Type	ρ_{wh}(%)	(kN)
W20-FD-15	2.0	0.15	31.6	20-D6 Fixed	0.70	8-D13	0.58	D6@65 Height over 300mm	0.65	228
W20-FU-15			31.8			8-U12.6		D6@45 Height less than 300mm	0.94	320
W15-HU-15	1.5		34.0	20-D6 Not Fixed	0.70			D6@65	0.65	360
W15-HU-073		0.073	33.9							329
W20-HU-073	2.0		36.0							253
W25-HU-073	2.5		35.8							191

a/D: shear span ratio; *n*: axial load ratio; f'_c: concrete cylinder strength; ρ_{wv} : reinforcement ratio of longitudinal rebars; ρ_s: reinforcement ratio of concentrated rebars; ρ_{wh}: volumetric ratio of transverse reinforcement. Q_{exp}: measured maximum lateral force (average);

5.2.1 Ultimate bending strength

The equation recommended in Japanese code [5.5] will be adopted to compute the ultimate bending strength ${}_{cal}M_{mu1}$, and the corresponding lateral force of rectangular concrete walls can be written as follows:

$$calM_{mu1} = a_{pt}\sigma_{py}l_w + 0.5a_w\sigma_{wy}l_w + 0.5Nl_w \quad (5.2.1)$$

$$calQ_{mu1} = \frac{calM_{mu1}}{a} \quad (5.2.2)$$

Note

a : Shear span
a_{pt} : Total nominal Area of concentrated rebars at the tensile boundary zone
a_w : Total nominal Area of LD rebars
b : Thickness of wall panel
D : Width of wall panel
f'_c : Concrete cylinder strength
l_w : $0.9D$ for rectangular section
${}_{cal}M_{mu1}$: Ultimate bending strength
n : Axial load ratio

N : Axial load（$=n\ b\ D f'_c$）
${}_{cal}Q_{mu1}$: Lateral force calculated from the ultimate bending strength
σ_{py} : Yield strength of concentrated rebars at the tensile boundary zone
σ_{wy} : Yield strength of LD rebars

For comparison, the NewRC block method [5.7], which has been recommended for the concrete components made of high-strength materials, was also applied to calculate the ultimate bending strength of the walls. The corresponding lateral force will be referred as to ${}_{cal}Q_{mu2}$. This method based on the following assumption: 1) the plane section remains plane, 2) concrete does not resist tensile stress, and 3) constitutive laws of reinforcements are completely elasto-plastic. This method simply and reasonably replaces the actual stress distribution of concrete in compressive zone with an equivalent rectangular stress block as shown in Fig. 5.2-1. Equations to calculate the parameters defining the stress block are given by Eq. (5.2.3) through Eq. (5.2.8). Then, the flexure strength of the section shown in Fig. 5.2-2 can be calculated by Eq. (5.2.9), by increasing the depth of neutral axis from zero to the depth of section until satisfying the static equilibrium condition.

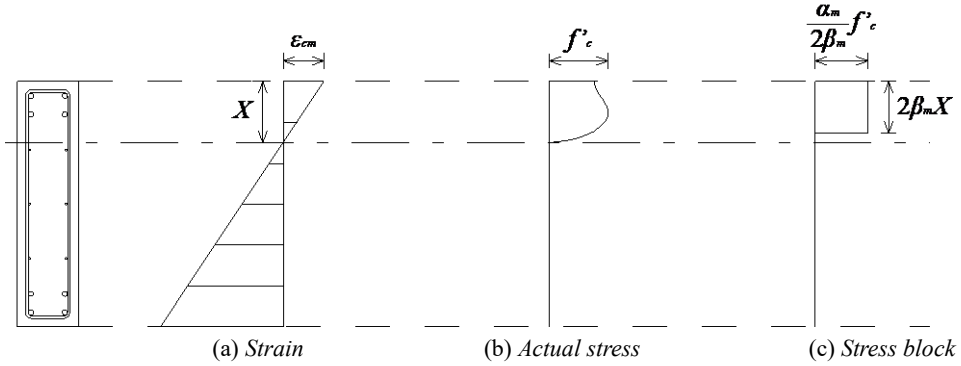

Fig. 5.2-1 Define of NewRC stress block

$$K = \frac{f'_{cc}}{f'_c} = 1.0 \tag{5.2.3}$$

$$\alpha_m = 0.831 - 0.076\left(\frac{f'_c}{42}\right) \tag{5.2.4}$$

$$\beta_m = 0.429 - 0.010\left(\frac{f'_c}{42}\right) \tag{5.2.5}$$

$$\xi = \frac{\varepsilon_{cm}}{\varepsilon_{co}} = 1.483 - 0.1\left(\frac{f'_c}{42}\right) \tag{5.2.6}$$

$$\frac{\varepsilon_{co}}{\varepsilon_o} = 1 + 4.7(K-1) \tag{5.2.7}$$

$$\varepsilon_o = 0.94 f'^{\,0.25}_c \times 10^{-3} \tag{5.2.8}$$

Note

f'_c : Concrete cylinder strength

K : Strength enhancement ratio of confined concrete
ε_o : Strain at the maximum stress of unconfined concrete
ε_{co} : Strain at the maximum stress of confined concrete
ε_{cm} : Crushing strain of concrete

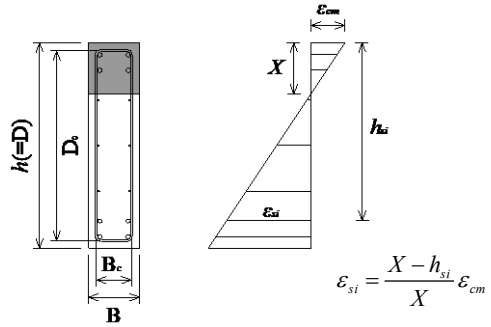

Fig. 5.2-2 Strain profile in wall cross section

$$M_{mu} = \alpha_m f'_{cc} bX\left(\frac{h}{2} - \beta_m X\right) + \sum_{i=1}^{n_s} f_{si} A_{si}\left(\frac{h}{2} - h_{si}\right) \quad (5.2.9)$$

Note
A_{si} : Area of longitudinal rebars at number i layer
b : Thickness of wall panel
f'_{cc} : Strength of confined concrete
f_{si} : Area of longitudinal rebars at number i layer
h : Depth of wall panel
h_{si} : Distance from the extreme compressive fiber
n_s : Number of layers of longitudinal rebars
X : Depth of neutral axis

5.2.2 Ultimate shear strength

The modified Ohno · Arakawa mean equation [5.5] is recommended by deign code of Japan to evaluate ultimate shear strength of shear walls, which is written as below:

$$_{cal}Q_{su} = \left\{\frac{0.068 p_{te}^{0.23}\left(f'_c + 18\right)}{\sqrt{a/D + 0.12}} + 0.85\sqrt{p_{wh}\sigma_{hy}} + 0.1\sigma_0\right\} bj \quad (5.2.10)$$

Note
a_t : Total nominal Area of concentrated rebars at the tensile boundary zone
a/D : Shear span ratio
b : Thickness of wall panel
D : Width of wall panel
d : 0.95D for rectangular section
f'_c : Concrete cylinder strength
J : 7/8d
p_{te} : Equivalent reinforcement ratio of tensile rebar（%）(=100a_t/b d)
p_{wh} : Reinforcement ratio of HD rebars
$_{cal}Q_{su}$: Ultimate Shear Strength
σ_{hy} : Yield strength of HD rebars
σ_o : Average axial stress over the cross section of wall panel

Moreover, the evaluation method of ultimate shear strength for concrete shear walls, which is recommended in the design guidelines of AIJ [5.6], which can consider the degradation of shear strength along with the drift was adopted and expressed by the following equations.

$$_{cal}V_{su} = bjp_{wh}\sigma_{wy}\cot\phi + \tan\theta(1-\beta)bD\nu\sigma_B/2 \tag{5.2.11}$$

$$\nu = \begin{cases} \nu_0 & R_u<0.005 \\ (1.2-40R_u)\nu_0 & 0.005 \leqq R_u<0.02 \\ 0.4\nu_0 & 0.02 \leqq R_u \end{cases} \tag{5.2.12}$$

$$\tan\theta = \sqrt{(H/D)^2+1} - H/D \tag{5.2.13}$$

$$\beta = (1+\cot^2\phi)p_{wh}\sigma_{hy}/\nu\sigma_B \tag{5.2.14}$$

$$\cot\phi = \begin{cases} \min\left[2.0,\ j/(D\tan\theta),\ \sqrt{(\nu_0\sigma_B/p_{wh}\sigma_{hy})-1}\right] & \text{(Method A)} \\ 1.0 & \text{(Method B)} \end{cases} \tag{5.2.15}$$

Note

b : Thickness of wall panel
D : Width of wall panel
H : Height of wall panel
j : 7/8d
p_{wh} : Reinforcement ratio of HD rebars
ν : Effective coefficient of concrete compressive strength
ν_0 : Effective coefficient of concrete in non-hinge region (=0.7-σ_B/2000)
σ_B : Unconfined concrete compressive strength
σ_{hy} : Yield strength of HD rebars
R_u : Potential drift ratio

5.2.3 Comparison of the calculated ultimate capacities

The calculated ultimate capacities are compared with the experimental results in Table 5.2-2. Because the D6 LD bars in wall panels of specimens HU-Series were not anchored into the adjacent loading beams, they are assumed not to sustain axial stress induced by bending moment, and both results that the D6 LD bars were considered or not are summarized in in Table 5.2-2.

One can be seen that, for specimen W20-FD-15 with normal rebars, both Eq. (5.2.1) and the NewRC block method predict its flexure strength very well with difference less than 10%. On the other hand, it is obvious from Table 5 that, even the flexure strength provided by D6 DL bars were ignored, Eq. (5.2.1) overestimates the flexure strength of RC walls reinforced with SBPDN rebars about 35%, because SBPDN rebars did not yield until R = 3.0%. Meanwhile, the calculated flexural strengths by NewRC block method agreed much better with the test results than those calculated by Eq. (5.2.1), but still overestimated the flexure strength by 1% - 18%, because it ignores the effect of the slippage of SBPDN rebars.

Table 5.2-2 Comparison of ultimate capacities

Specimen	Q_{mu1} (kN)	Q_{mu2} (kN)	Q_{su} (kN)	Q_{exp} (kN)	Q_{su} / Q_{mu1}	Q_{su} / Q_{mu2}	Failure mode
W20-FD-15	247	212	296	228	1.20	1.40	flexure
W20-FU-15	469	318	296	320	0.60	0.93	shear
W15-HU-15	625	429	324	360	0.52	0.76	shear
	551*	386*			0.59*	0.84*	
W15-HU-073	561	423	306	329	0.55	0.72	flexure
	485*	383*			0.63*	0.80*	
W20-HU-073	424	323	288	253	0.68	0.89	flexure
	367*	290*			0.78*	0.99*	
W25-HU-073	339	258	272	191	0.80	1.05	flexure
	293*	232*			0.93*	1.17*	

Q_{mu1}: Calculated ultimate flexural strength by Eq. (5.2.1)
Q_{mu2}: Ultimate flexural strength calculated by NewRC block method
Q_{su} : Calculated ultimate shear strength by Ohno · Arakawa mean method
Q_{exp} : Measured maximum lateral force
*The results with a * mark represent that the DL rebars were assumed not to sustain axial stress induced by bending moment.

As for the ultimate shear strength, for the two specimens W20-FU-15 and W15-HU-15 which exhibited shear dominant failure, the Ohno · Arakawa mean method overestimated their shear bearing capacities about 10%. Besides, the ratio of Q_{su} /Q_{mu1} and Q_{su} /Q_{mu2} shown in Table 5.2-2. indicated that the current design codes of Japan could not accurately predict the failure mode of DHC walls.

Due to the neglect of the effect of slippage of SBPDN rebars in RC members, the current design codes of Japan could not accurately evaluate ultimate capacity of DHC shear walls. For the purpose of finding a passible way to reasonably evaluate the ultimate flexure strength of DHC walls by the current design codes of Japan, instead of using the yield strain of SBPDN rebars, the measured axial strains in the concentrated SBPDN rebars at the maximum lateral resistance force were applied to calculate the ultimate flexure strength using NewRC block method and the equation recommended in Japanese code. The mean of measured strains and relative evaluation results were summarized in Table 5.2-3, it can be seen that Eq. (5.2.1) still overestimated the flexure strength of DHC walls, but the differences were less than 15%, which is much better than the results that using the yield strains. As for the results by NewRC block method, the calculated results overestimated the measured one if the D6 DL bars were assumed perfectly fixed; on the other hand, the measured results were underestimated by the calculated one if the D6 DL bars were neglected, but the differences are less than 10%. Therefore, if the effect of the D6 DL bars could be taken into consideration, the NewRC block method could predict the flexural strength of DHC walls accurately as long as the measured axial strain in SBPDN rebars were utilized.

Table 5.2-3 Ultimate capacities calculated with measured strains

Specimen	ε_{max}	Q_{mu1} (kN)	Q_{mu2} (kN)	Q_{exp} (kN)	Q_{exp} / Q_{mu1}	Q_{exp} / Q_{mu2}
W15-HU-15	0.58	493	421	360	0.73	0.86
		420*	373*		0.86	0.97
W15-HU-073	0.66	465	370	329	0.71	0.89
		389*	316*		0.85	1.04
W20-HU-073	0.60	333	268	253	0.76	0.94
		276*	226*		0.92	1.11
W25-HU-073	0.58	260	210	191	0.73	0.91
		214*	176*		0.89	1.08

Q_{mu1}: Calculated ultimate flexural strength by Eq. (5.2.1)
Q_{mu2}: Ultimate flexural strength calculated by NewRC block method
Q_{su} : Calculated ultimate shear strength by Ohno·Arakawa mean method
Q_{exp}: Measured maximum lateral force
ε_{max}: the mean of measured maximum tensile strain in the concentrated rebars
* The results with a * mark represent that the DL rebars were assumed not to sustain axial stress induced by bending moment.

Fig. 5.2-3 shows the ultimate shear strength calculated by the methods A and B recommended in the guidelines of AIJ [5.6], represented in purple lines and green lines, respectively. As apparent from Fig. 5.2-3, both methods underestimated the ultimate shear strength at large deformation for drift hardening specimens with a shear span ratio of 1.5 and specimen W20-FU-15. Although the calculated results by method B for specimen W20 and W25 were very close to their tested results, it is difficult to discuss the prediction accuracy since no shear failure at the wall panels were observed till the end of the experiments for the specimen with shear span of 2.0 and 2.5.

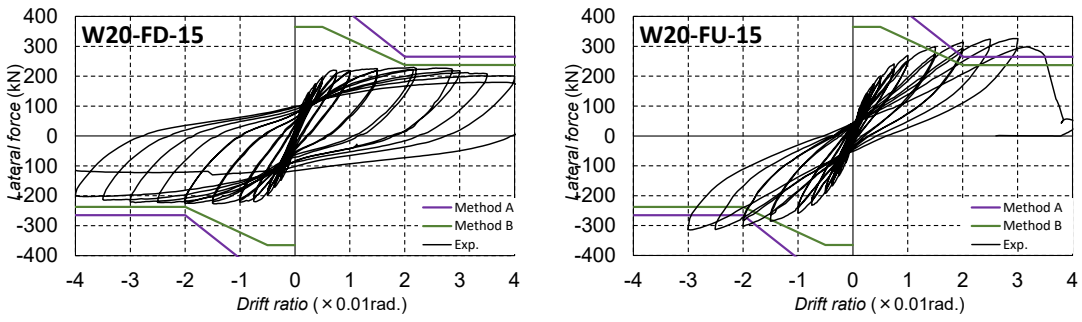

Fig. 5.2-3 Ultimate shear strength envelop provided by guidelines of AIJ

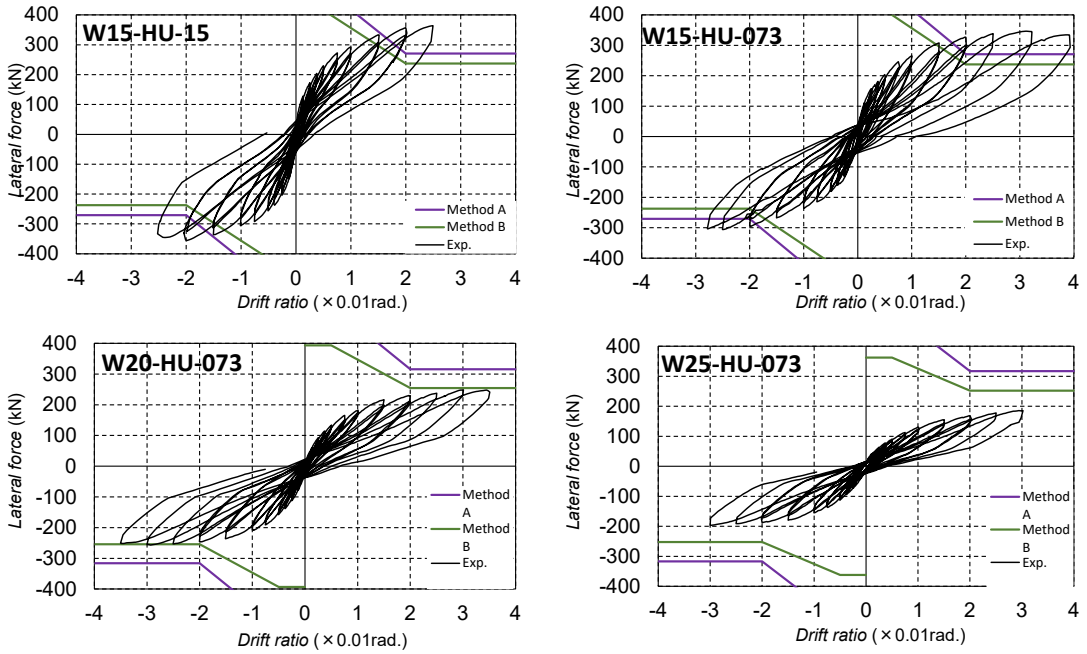

Fig. 5.2-3 Continued

5.3 Analytical method for assessing seismic behaviors of drift hardening shear walls

5.3.1 Description of analytical method

To promote the application of RC walls reinforced by SBPDN rebars to actual buildings, it is indispensable to develop a refined method to evaluate the ultimate capacities of the walls reasonably and accurately. As described in section 5.2, current design codes of Japan could not accurately evaluate ultimate capacity of drift hardening shear walls. To reasonably evaluate the seismic behavior of RC walls reinforced by SBPDN rebars, the analytical method that can take account of the effect of slippage of SBPDN rebars in RC members is necessary. In this study, to evaluate seismic performance of concrete shear walls made of high-strength steel with low bond strength, the finite springs method (FSM) refined by Kitajima [5.8] along with the bar-slipping model modified by Funato [5.9] were applied as the main calculation tool.

As can be seen in Fig. 5.3-1, in the proposed FSM, a concrete shear wall under seismic loading will be divided into three zones: 1) the elastic zone where the curvature is zero, 2) the plastic hinge zone in which the strain and stress of the longitudinal rebars are uniformly distributed, and produces a uniform curvature concentrating within the end region of the wall panel, 3) the joint zone that simulates the wall-base joint. And each zone is divided into finite fiber along the height of wall panel. While in each fiber as shown in Fig. 5.3-1, an initial slippage S_{bi} had been given to produce the overall slip S_b at the end region of each divided zone, and concentrated rebars were assumed to be completely fixed at both ends to give zero slippage as the convergence criteria.

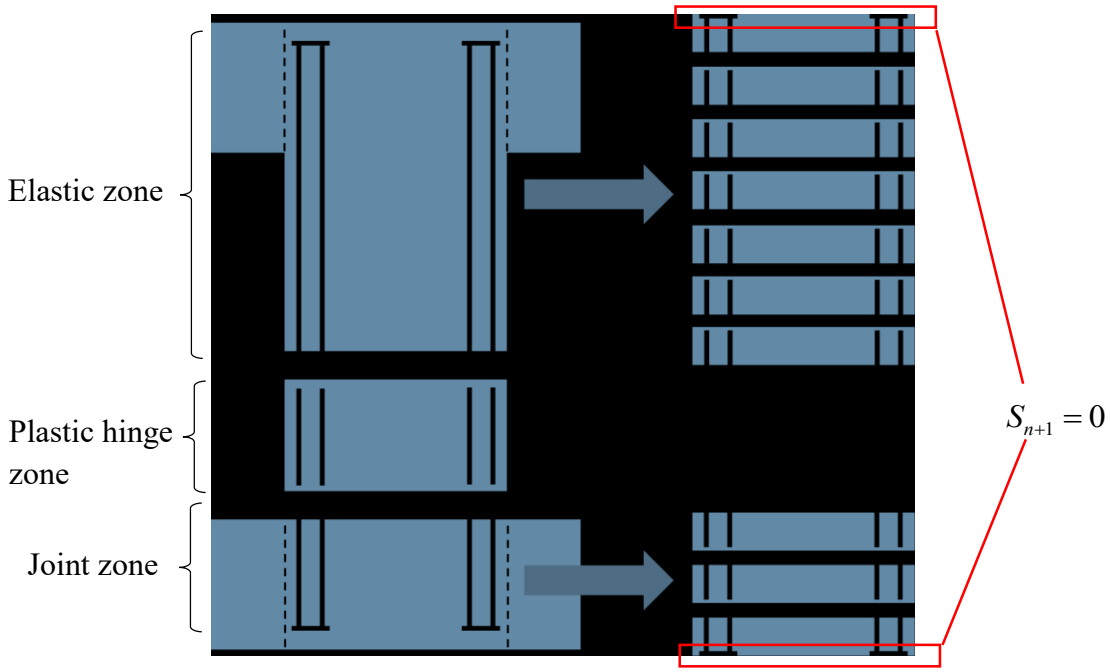

Fig. 5.3-1 schematic of concrete shear wall in the FSM

Behavior of SBPDN rebars in the joint zone can be provided by the following step: firstly, give an initial stress σ_0 and slip S_0 at the edge side of the first segment, and the next stress σ_1 and slip S_1 can be obtained by Eq. (5.3.1) and Eq. (5.3.2), separately. Where l is the length of the divided spring element, D_s is the diameter of the rebar, $\tau(\ )$ is bond stress on the basis of the bar-slip model, and $f_s^{-1}(\ )$ is the function to calculate the strain of rebar, which is based on the constitutive relationship of the applied steel.

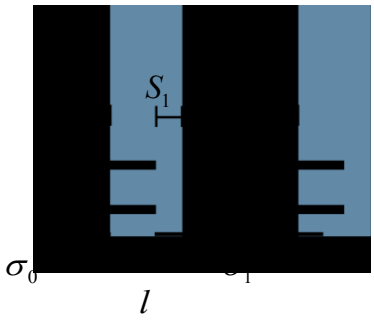

$$\sigma_1 = \sigma_0 - \tau(S_0) \times \frac{4l}{D_s} \tag{5.3.1}$$

$$S_1 = S_0 - f_s^{-1}(\sigma_1) \times l \tag{5.3.2}$$

Then, calculate the slip and stress at the next segment i+1 till i=n. If the boundary condition $S_{k+1} = 0$ is met, the assumed rebar stress σ_{k+1} is the stress.

$$\sigma_{k+1} = \sigma_k - \tau(S_k) \times \frac{4l}{D_s} \tag{5.3.3}$$

$$S_{k+1} = S_k - f_s^{-1}(\sigma_k) \times l \tag{5.3.4}$$

As for the plastic hinge region, one can be seen in Fig. 5.3-2 that the cross section of wall panel was divided into 60 elements. Based on the assumption that the concrete plane remains plane,

give an initial curvature ϕ, the flexure strength of the section can be obtained by the NewRC block method as described before.

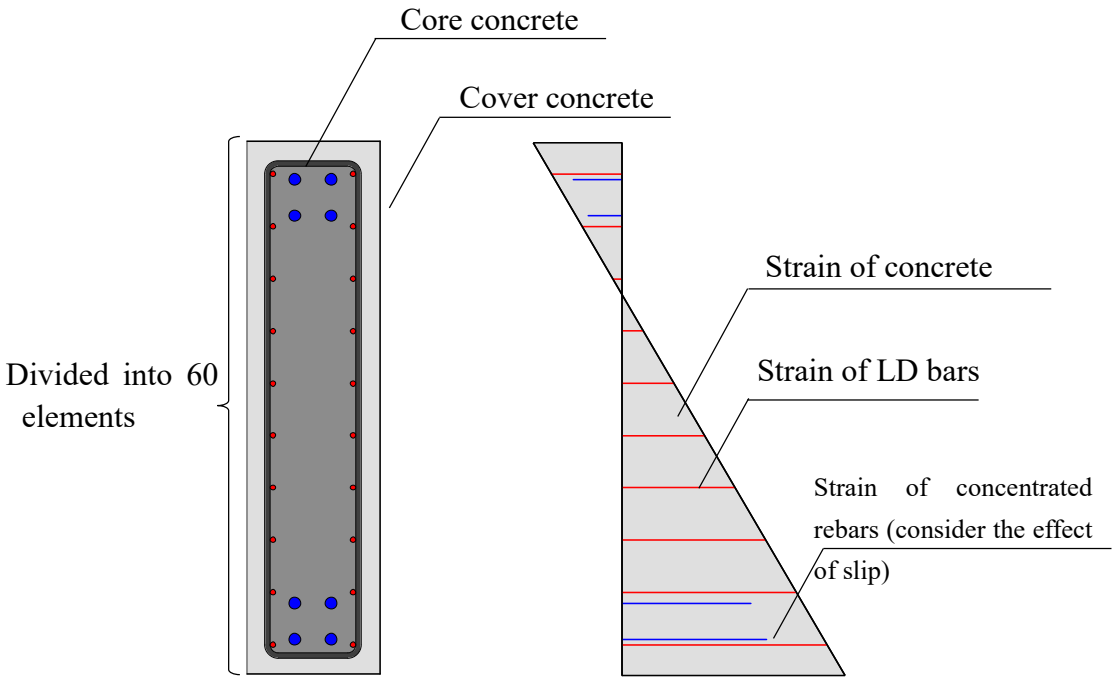

Fig. 5.3-2 Section discretion and strain profile in wall panel cross section

5.3.2 Stress-strain models of the applied materials

The FSM method described before can predict strain distribution of the wall section, and with the help of stress-strain models to calculate the flexure strength. Hence, in order to evaluate seismic behavior of drift hardening concrete shear walls, reliable and accurate constitutive laws of materials are necessary.

A reliable stress-strain model for concrete proposed by Sakino and Sun [5.10] which can take the confinement effect of stirrups into consideration, was applied in this analysis. Definition can be seen as below, in Eq. (5.3.4).

$$Y = \frac{AX + (D-1)X^2}{1 + (A-2)X + DX^2} \tag{5.3.5}$$

$$Y = f'_c / f'_{cc}$$

$$X = \varepsilon_c / \varepsilon_{c0}$$

$$A = E_c \varepsilon_{c0} / f'_{cc}$$

$$E_c = \left(0.69 + 0.33\sqrt{f'_c}\right) \times 10^4$$

$$K = \frac{f'_{cc}}{f'_c} = 1 + 11.5 \cdot \frac{\rho_{hw} \sigma_y}{f'_c} \left(\frac{d''}{C}\right)\left(1 - \frac{s}{2D_c}\right) \qquad \textit{(for rectangular common hoop)}$$

$$\varepsilon_0 = 0.94 f'_c{}^{0.25} \times 10^{-3}$$

$$\varepsilon_{c0} = \varepsilon_0 \begin{cases} [1 + 4.7(K-1)] & K \le 1.5 \\ [3.35 + 20(K-1.5)] & K > 1.5 \end{cases}$$

$$D = 2.25 - 0.017 f'_c + 1.6\sqrt{(K-1) f'_c / 23}$$

Note

C	:	center-to-center distance of transverse reinforcement（=Dc）
d''	:	nominal diameter of HD bars
E_c	:	Elastic modulus of concrete
f'_c	:	strength of unconfined concrete
f'_{cc}	:	strength of confined concrete
K	:	strength enhancement ratio
s	:	Spacing of transverse reinforcement
ε_o	:	Strain at the strength of unconfined concrete
ρ_h	:	volumetric ratio of transverse reinforcement

Fig. 5.3.3 indicates the unloading and reloading rules of the stress-strain model. If the unloading occurs at point A (ε_A, f_A), for example, the unloading curve is assumed to be a parabola with a peak point B (ε_B, f_B), which can be calculated by Eq. (5.3.6), The reloading curve is assumed to be a straight line that connects the reloading point B (ε_B, f_B) and C (ε_C, f_C), which is assumed that $f_C = 0.9 f_A$.

$$B(\varepsilon_B,\ f_B) = \left(\varepsilon_A - \frac{f_A}{E_c},\ 0 \right) \tag{5.3.6}$$

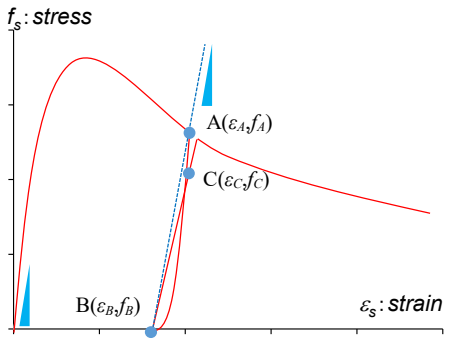

Fig. 5.3-3 Complete stress-strain curve of confined concrete under compression

As for the constitutive law of concentrated rebar, because SBPDN rebars did not exhibit apparent yield plateau in their stress-strain relations, the famous Menegotto-Pinto model [5.11], which had been modified by Kitajima et al. based on test results of ultra-high strength bars [5.8], was applied in this analysis. As shown in Fig. 5.3-4, this model has two asymptotes with initial elastic modulus E_s and a tangent (gradient $E_t = QE_s$) at the peak point, and the equation of the curve is expressed by Eq. (5.3.7). The unloading and reloading models suggested by Kitajima et al. are indicated in Fig. 5.3-5, which were applied for SBPDN rebar. There are three cases for unloading and/or reloading as described below:

1) for the unloading or reloading occur at point A, based on the envelop of Menegotto-Pinto

model, the target point C is located on the reversed curve with the point (ε_{mo},0) as its origin. The absolute strain ε_{ss} at point C is assumed to be equal to the experienced maximum strain in the initial direction. 2) for the reloading from point D at the unloading curve: the target point will be point A, which is the start point of the previous unloading curve. 3) for the unloading from point E on the reloading curve: the start point D of the previous reloading curve will be taken as the target point. And once the strains of the start point and target point are specified, the unloading and/or reloading curves can be defined by the Menegotto-Pinto function as described in Eq. (5.3.7).

$$f_s = E_s \varepsilon_s \left\{ Q + \frac{1-Q}{\left[1+\left(\varepsilon_s / \varepsilon_{ch}\right)^N\right]^{1/N}} \right\} \tag{5.3.7}$$

$$Q = 0.1\left(\varepsilon_{su}\right)^{-2.5}$$

$$\varepsilon_{ch} = \frac{f_{su} - QE_s\varepsilon_{su}}{E_s(1-Q)}$$

$$N = 3.0$$

Note

f_s	:	Tensile stress
f_{sy}	:	Yield stress
f_{su}	:	Ultimate stress
f_{ch}	:	characteristic stress
ε_s	:	Strain of SBPDN rebar
ε_{sy}	:	Strain at the yield stress
ε_{su}	:	Strain at the ultimate stress
ε_{ch}	:	characteristic strain
E_s	:	Young's modulus
E_t	:	Tangential stiffness
Q	:	The ratio of the tangential stiffness at the peak to the initial stiffness
N	:	Curvature coefficient

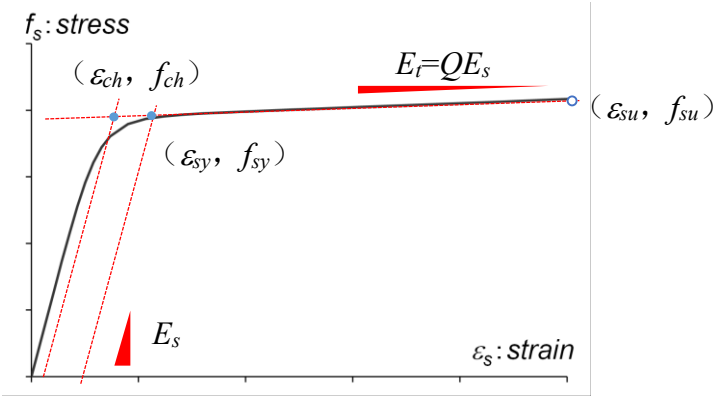

Fig. 5.3-4 Envelope curve of the modified Menegotto-Pinto model

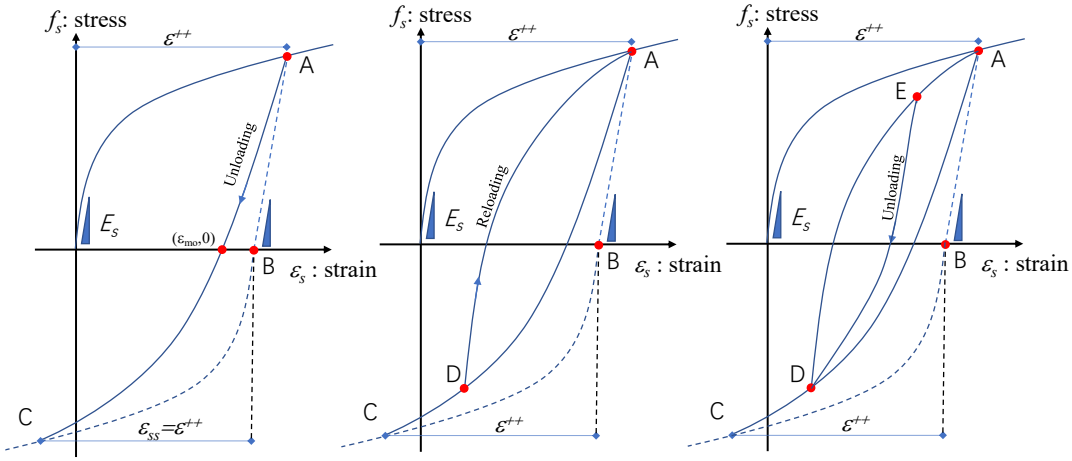

Fig. 5.3-5 Unloading and reloading rules for stress-strain curve of reinforcing steel

As previous research indicated that the bond strength of SBPDN rebar is about 3 MPa when it was embedded in concrete with compression strength of about 40 MPa, which is about one-fifth comparing with ordinary rebar [5.9]. Therefore, to reliably assess seismic behavior of concrete shear wall reinforced by SBPDN rebars, it is indispensable to consider the effect of bond slip, and develop a bond stress-slip model for SBPDN rebar.

Funato et al. have proposed a bond stress-slip model and its envelope curve is displayed in Fig. 5.3-6 along with the coordinates of key points, while the unloading and/or reloading rules are indicated in Fig. 5.3-7. Because the bond strength of a rebar is affected by the concrete strength, the modified maximum bond strength of SBPDN rebar, which related to strength of confined concrete, is indicated in Eq. (5.3.8), where f'_c is strength of unconfined concrete and K is strength enhancement ratio. Besides, significant parameters including residual bond stress and maximum slip, which is based on the experiment results, were recommended as 0.13 τ_{max} and 0.015mm for the SBPDN rebars, respectively.

$$\tau_{max} = 3.0\sqrt{\frac{Kf'_c}{40}} \tag{5.3.8}$$

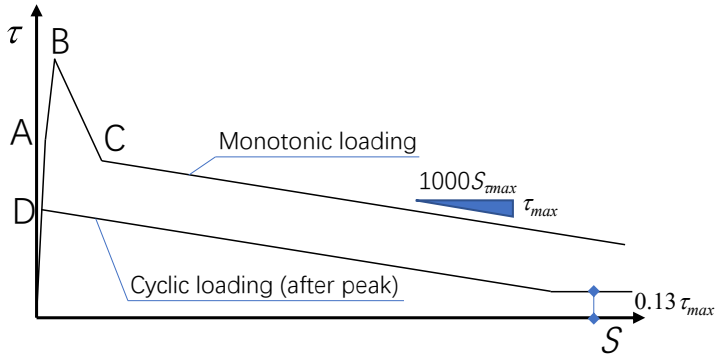

$S_{\tau max}$=0.015mm
A（$1/3S_{\tau max}$，$2/3\,\tau_{max}$）
B（$S_{\tau max}$，τ_{max}）
C（$5S_{\tau max}$，$3/5\,\tau_{max}$）
D（$1/5S_{\tau max}$，$2/5\,\tau_{max}$）

Fig. 5.3-6 The envelope bond stress-slip relationship of SBPDN rebar

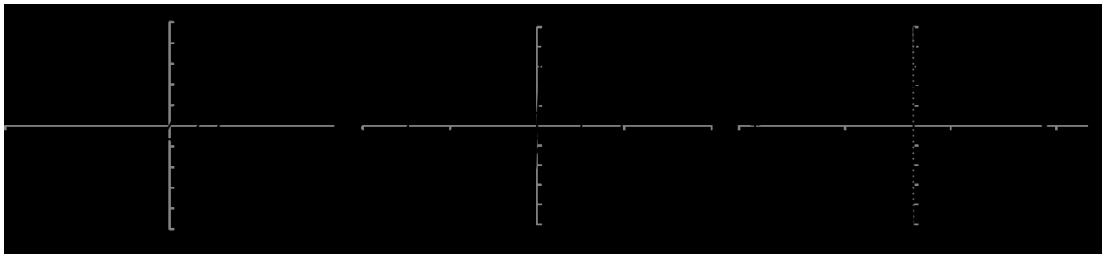

(a) before peak (b) after peak (c) asymptotes after peak

Fig. 5.3-7 Unloading and/or reloading bond stress – slip curves of SBPDN rebar

5.3.3 Effect of shear deformation and length of potential plastic hinge region

As described before, the plastic hinge zone in which the strain and stress of the longitudinal rebars are uniformly distributed, and produces a uniform curvature concentrating within the end region of the wall panel, thus the length of plastic hinge zone plays a predominant role in accurately predicting the overall seismic behavior. Besides, for the analysis of concrete column, the length of plastic hinge region is commonly assumed to be 1*D*, where *D* is the depth of the column section, and the effect of shear deformation is usually ignored. However, to accurately evaluate the shear walls with different shear span ratio by the same assumption is unreasonable, and the shear deformation of the squat shear wall is necessary to be considered.

To calculate the proportion of flexure and shear deformation and the length of potential plastic hinge region from the experimental data, it is assumed that the overall deformation of the walls (Δ) consists of only flexure (Δ_f) and shear (Δ_s) deformation, as described in Eq. (5.3.9). The curvature concentrates in the potential plastic hinge region as a constant and the curvature outside the hinge region is neglected, which is the same to the proposed FSM method. Based on these two assumptions, the measured proportion of flexural deformation α and parameter β about the length of potential plastic hinge region *Lp* were defined by Eq. (5.3.10) and (5.3.11), separately, where *D* is the depth of the wall panel.

$$\Delta = \Delta_s + \Delta_f \tag{5.3.9}$$

$$\Delta_f = \alpha \cdot \Delta \qquad 0 < \alpha < 1 \tag{5.3.10}$$

$$L_p = \beta \cdot D \qquad 0 < \beta < 1.5 \tag{5.3.11}$$

To derive the parameter α and β, firstly, as can be seen in Fig. 5.3-8, a pair of displacement transducers (DTs) were set at the same height from the wall base, and details can be found in Chapter Two, section 2.2.4. For the first of each loading cycle in the loading program, the difference of measured displacement from the drift ratio of zero to the targeted level were divided by the distance between the two DTs, to calculate the tested angel of rotation at each position $\tan_{exp}\psi_i$. Considering that the vertical displacements measured by the DTs might be not reliable when the drift ratio was larger than 1.5%., due to the spalling of cover concrete, only the calculated results of $\tan_{exp}\psi_i$ until the drift ratio of 1.5%. are produced.

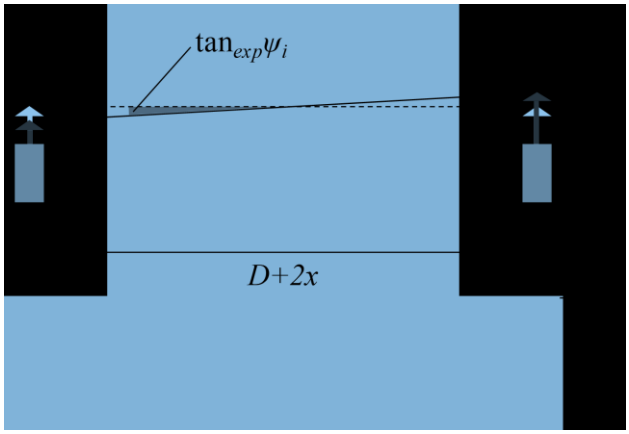

Fig. 5.3-8 Define of tan$_{exp}\psi_i$

Note

$_{exp}\psi_i$	:	Calculated angel of rotation at each position
h_i	:	Height of each displacement transducer
x	:	Distance between the shear wall and each displacement transducer.
D	:	Width of wall panel

Then, the angel of rotation caused by shear and flexure deformation, referred to as tan$_s\psi_i$ and tan$_f\psi_i$, respectively, could be derived by their relationships between tan$_{exp}\psi_i$.

Specifically, Fig. 5.3-9(a) exhibited the model of shear deformation, tan$_s\psi_i$ could be represented by the Eq. (5.3.12) to (5.3.16), where H is the shear span of wall panel, $\delta(h_i)$ and $v(h_i)$ are the lateral and vertical displacement caused by shear deformation at relative position, respectively.

$$\tan\theta_s = \frac{\Delta_s}{H} \tag{5.3.12}$$

$$\delta(h_i) = \Delta_s \cdot \frac{h_i}{H} \tag{5.3.13}$$

$$v_{push}(h_i) = (x + \delta(h_i))\tan\theta \tag{5.3.14}$$

$$v_{pull}(h_i) = (x - \delta(h_i))\tan\theta \tag{5.3.15}$$

$$\tan_s\psi_i = \frac{(v_{push}(h_i) + v_{pull}(h_i))}{x \times 2 + D} \tag{5.3.16}$$

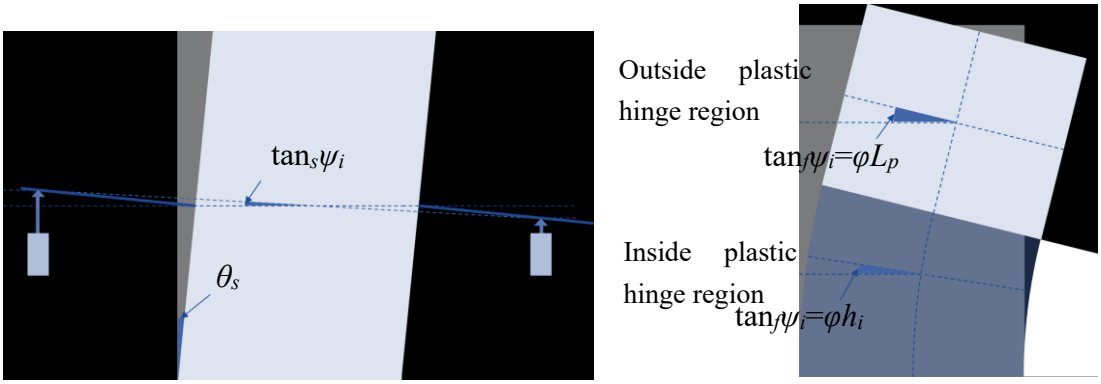

(a) shear deformation (b) flexure deformation

Fig. 5.3-9 Geometric model of shear and flexure deformation

As for tan$_f\psi_i$, it is assumed that curvature concentrates in the potential plastic hinge region as a constant and the curvature outside the hinge region is neglected, so the curvature ϕ inside the plastic hinge region, as shown in Fig. 5.3-9(b), can be provided by Eq. (5.3.17), where L is the length of wall panel. And the tan$_f\psi_i$ at each position, inside or outside the plastic hinge region, can be obtained by Eq. (5.3.18)

$$\phi = \frac{\Delta_f}{\{L-(L_p/2)\}L_p} \tag{5.3.17}$$

$$\tan_f \psi_i = \begin{cases} \phi \cdot h_i & h_i \le L_p \\ \phi \cdot L_p & L_p < h_i \end{cases} \tag{5.3.18}$$

Finally, the relationships between α and β can be derived by Eq. (5.3.19) and (5.3.20), the values of α and β can be obtained when ξ is the minimum for each loading cycle.

$$\tan_{cal}\psi_i(\alpha,\beta) = \tan_s \psi_i + \tan_f \psi_i \tag{5.3.19}$$

$$\xi = \sum_{i=1}^{n}\left(\tan_{\exp}\psi_i - \tan_{cal}\psi_i(\alpha,\beta)\right)^2 \tag{5.3.20}$$

The calculated results of α and β until the drift ratio of 1.5%. are shown in Table 5.3-1 and Table 5.3-2, respectively. It was found that the larger the shear span ratio, the larger the proportion of flexural deformation and the longer the length of potential plastic hinge region.

Table 5.3-1 Proportion of flexural deformation α

Drift ratio (%.)	0.125	0.25	0.375	0.5	0.75	1	1.5	average
W15-Series	0.61	0.63	0.71	0.71	0.73	0.71	0.71	0.69
W20-Series	0.80	0.80	0.83	0.85	0.82	0.81	0.84	0.83
W25-Series	0.87	0.73	0.78	0.81	0.82	0.82	0.86	0.82

Table 5.3-2 The factor of measured potential plastic hinge region β

Drift ratio (%.)	0.125	0.25	0.375	0.5	0.75	1	1.5	average
W15-Series	1.13	0.68	0.34	0.32	0.30	0.28	0.27	0.45
W20-Series	0.64	0.64	0.58	0.58	0.37	0.35	0.31	0.47
W25-Series	1.16	1.12	0.84	0.73	0.66	0.36	0.32	0.69

5.3.4 Analytical assumptions and procedures

With all the reliable tools described above, to utilize the FSM method to evaluate the overall seismic behavior of RC walls reinforced with SBPDN rebars, the following assumption are made: 1) concrete only resist compression stress, 2) the concrete plane remains plane after bending and cover concrete do not spall off, 3) the constitutive model of concrete proposed by Sakino and Sun which can take the confinement effect of stirrups into consideration, was applied in this analysis, 4) the bond-slip relationship of the SBPDN rebars follows the model proposed by Funato et al, and the modified Menegotto-Pinto model is utilized as the constitutive model of SBPDN rebars, 5) an uniform curvature concentrating within the end region of the wall panel was produced, 6) strain and stress of the longitudinal rebars are uniformly distributed in the plastic hinge region, and the proportion of flexure deformation is given by the results shown in Table 5.3-1, the length of the potential plastic hinge region is determined and based on the test results shown in Table 5.3-2, and the average values of α and β were used in the calculation, 7) the concentrated rebars are completely fixed at both ends without slippage.

According to the abovementioned basic assumptions and relative models, processes of analysis can be described as follows: (1) As shown in Fig. 5.3-1, a concrete shear wall can be divided into elastic zone, plastic hinge zone and joint zone. (2) Calculate the curvature φ_k of the shear in the hinge zone based on the fifth assumption for a given drift ratio R_k. (3) Give an initial value ε_k to the strain at the center of section, and the strain distribution of concrete ε_{ci} across the section depth can be obtained following the second assumption. (4) The distribution of rebar strain which the slip effect has been considered can be computed by the iterative procedures as described in section 5.3.1. (5) Use the strain obtained above to calculate the concrete stress and the rebar stress according to respective constitutive law. (6) Calculate the internal axial load N and the bending moment M by the NewRC block method. (7) If the axial load N balances the applied axial load P within a tolerable error, the calculated M is taken as the bending moment M_k corresponding to the given R_k. If not, try a new center strain ε_k, and repeat from step (4). (8) Calculate the lateral force V_k corresponding to R_k which can satisfy static equilibrium. (9) Give a new R_k and repeat the above steps till the target drift ratio.

5.4 Verification of the numerical analysis models

To verify the reliability and accuracy of the proposed method for evaluating the seismic performance of drift-hardening concrete shear walls, the refined analytical method will be compared with the experimental ones presented in Chapter Two and Chapter Four of this paper.

Comparison will be made in three important aspects, 1) the lateral force V versus drift ratio R relationship, 2) residual drift ratio, and 3) the strain of concentrated rebars versus drift ratio relationship, the strains were measured at the sections 25mm away from the end of wall base on the initial tensile side, and the horizontal red dotted lines superimposed in each figure represent the yield strain of the used rebars.

Fig. 5.4-1 displayed the results of two specimens whose LD bars were fixed into wall base. For specimen W20-FD-15, in which ordinary steel bars were applied as its concentrated rebars, one can be seen from Fig. 5.4-1(a) that the analytical result slightly overestimated the measured one before the drift ratio of 0.5%, when the concentrated rebars yielded during the test, and then it exhibited accurate agreement with the experimental curves with difference of less than 10% on the conservative side. Fig. 5.4-1(b) indicated that the analytical residual drift ratio of specimen W20-FD-15 was the same to the tested one before the drift ratio of 0.5%, but the difference grown lager after that drift ratio. And Fig. 5.4-1(c) illustrated the comparison for strain of concentrated rebars versus drift ratio relationship, which express the reason for the above-mentioned differences. As shown in Fig. 5.4-1(c), the analytical strain yielded at the drift ratio of 0.25%., which was faster than the measured one, led to the higher initial stiffness of the analytical result. And since the constitutive law for normal steel is assumed to be completely elasto-plastic without hardening stage, and the unloading curve was assumed to follow the elastic modulus of the steel, which resulted in slightly lower ultimate strength and more residual strain for the analytical results.

As for drift hardening specimen W20-FU-15 which was reinforced by SBPDN rebars, it is obvious in Fig. 5.4-1(a) that the theoretical hysteresis loops traced the experimental curves accurately up to drift ratio of 3.0%. It can be noted that even the analytical result underestimated the measured one less than 10% from drift ratio 0.75%. to 2.0%., it accurately evaluated the experimental lateral resistance force at the drift ratio of 3.0%., which is presumed as the ultimate condition of the drift hardening shear wall. And as apparent in Fig. 5.4-1(b), the proposed method perfectly predicted the residual deformation of drift hardening shear walls. Fig. 5.4-1(c) displayed the strain measured in SBPDN rebars, although the proposed analytical method did not trace unloading curve of the tested results, the calculated steel strains can predict the measured strains very close up to the large deformation 2.5%. Besides, the theoretical strains exceed the measured ones after that drift about 10%, which can be attributed to that significant spalling off the cover concrete in this specimen made the SBPDN bars begin to slip, and regarding the increasing of steel strains. Therefore, it can be presumed that making some subtle modification in the proposed method to consider the influence of crushed cover concrete, may lead more accurate predictions of overall seismic performance of drift hardening concrete shear walls.

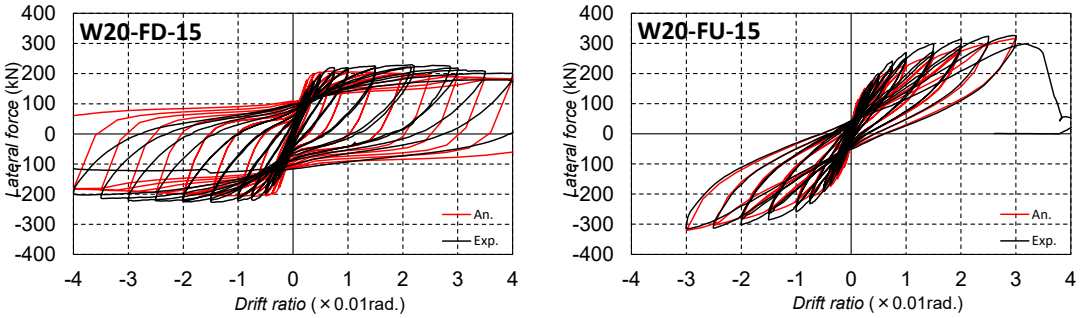

(a) *V-R* relationship

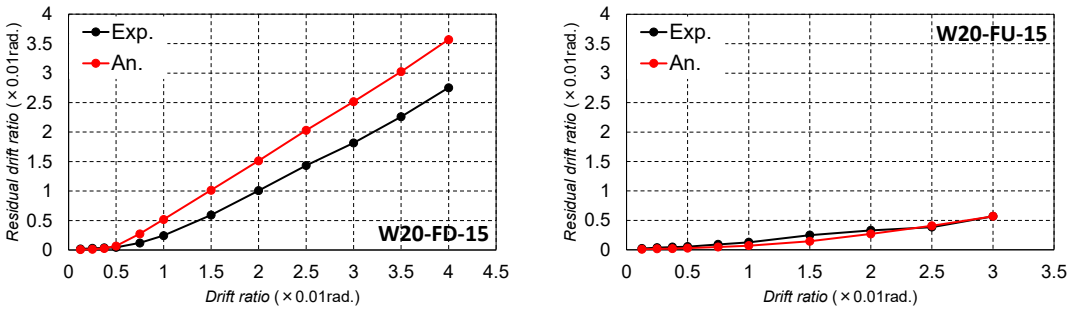

(b) Residual drift ratio

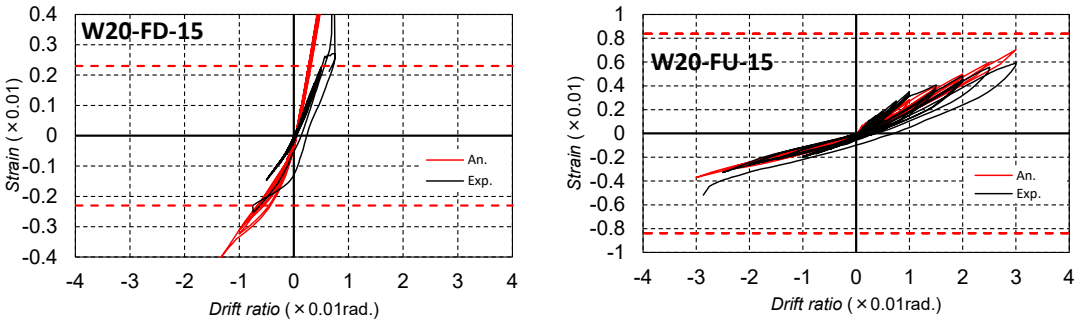

(c) Strain in concentrated rebars

Fig. 5.4-1 Comparisons between tested and analytical results

5.4.1 Effect of placement of the distributed longitudinal bars

A new arrangement of longitudinal distributed (LD) bars in the wall panel was proposed in Chapter Two, and experimental results indicated that the influence of the LD bars on seismic behaviors could not be ignored.

Fig. 5.4-2 compares the measured results with the calculated ones in terms of hysteretic responses and the residual drift ratios, for all the specimens whose LD bars were not anchored into the adjacent loading beams. To investigate the influence of the D6 LD bars in the wall panel, two calculated results are exhibited, the blue lines represent the results where the D6 LD bars are neglected while the red lines express the calculated results with the D6 LD bars being fully taken into consideration.

As shown in Fig. 5.4-2(a), for all specimens, red lines exhibited “fatter” hysteresis loops, which represents larger energy dissipation capacity. This could own to the blue lines only considered SBPDN rebars, which remained in the elastic condition, led to neglecting the plastic behavior

of the LD bars. One can see from Fig. 5.4-2(b) that at the initial stage of loading, the calculated envelopes in blue lines exhibit better agreement with the experimental curves than the blue lines, which implies that the LD bars in the wall did not directly sustain the axial stress induced by bending moment as expected. However, as the drift ratio increases, the calculated envelopes in red lines trace the experimental curves very well up at the drift of 0.75%., implying that the LD bars near the edge zone of the wall section will sustain axial stress induced by bending moment at large deformation. It is also obvious from Fig. 5.4-2(c) that complete ignorance of the D6 LD bars tends to underestimate the residual deformation, while full consideration of the LD bars overestimates the test result. These observations indicate that to accurately evaluate the ultimate capacity and residual deformation, the resistance to axial stress of the LD bars should be taken into consideration.

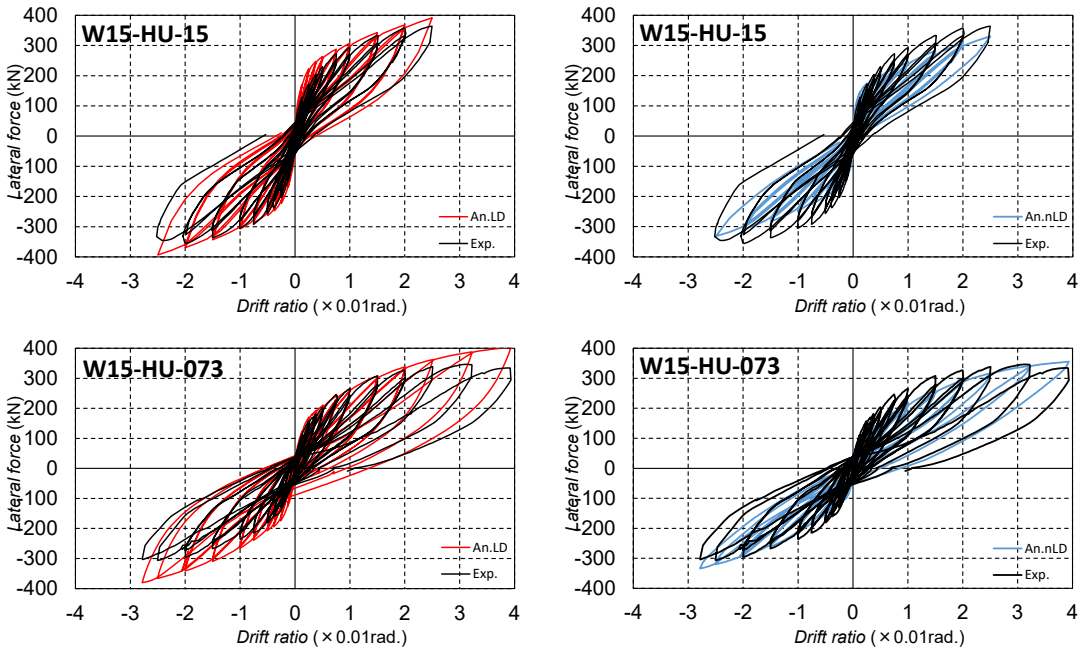

(a) *V*-*R* relationship

Fig. 5.4-2 Effect of arrangement for longitudinal distributed bars

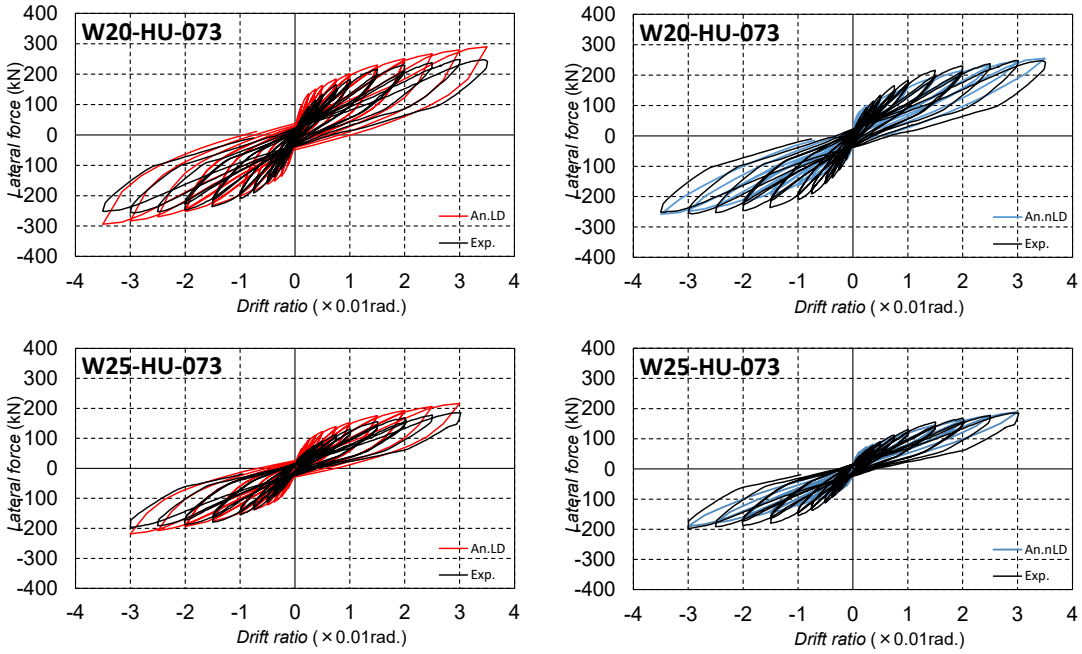

(a) *V*-*R* relationship

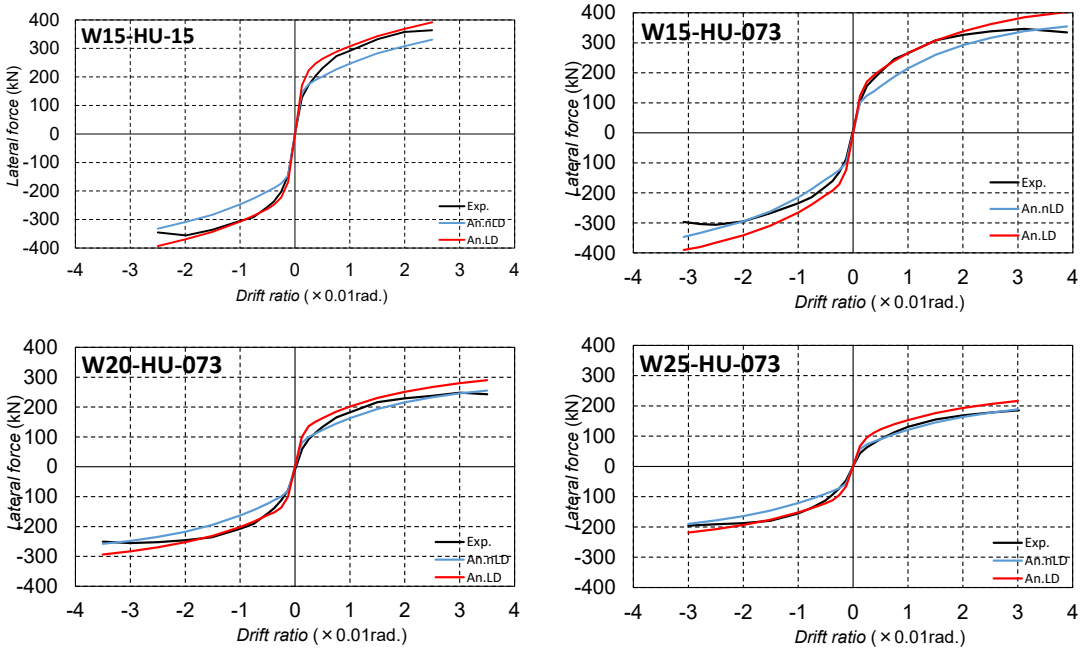

(b) Envelop of *V*-*R* relationship

Fig. 5.4-2 Continued

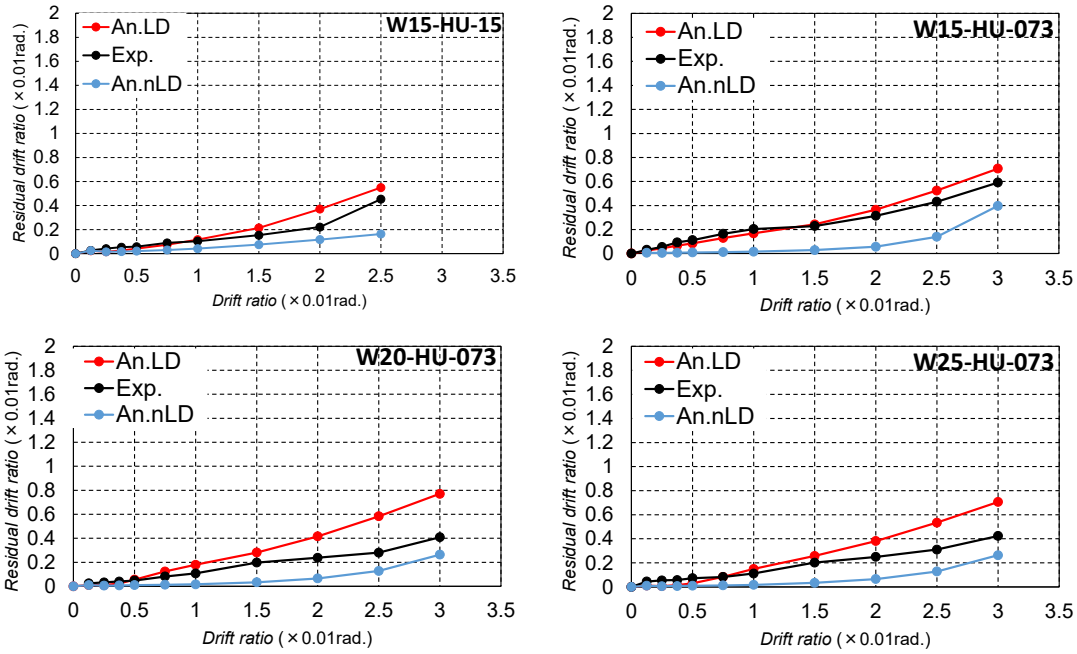

(c) Residual drift ratio

Fig. 5.4-2 Continued

Since the complicated behavior of LD bars is difficult to be predicted by the proposed method, based on the analytical results exhibited above and the experimental results described in Chapter Two, it is simply assumed that only the four LD bars located at the boundary zone of wall panel provide flexure resistance. The comparison of calculated results based on the assumption and the measured ones were summarized in Fig. 5.4-3.

One can be seen from Fig. 5.4-3(a) and (c) that the analytical predictions for all specimens exhibited very good agreement with the test curves till drift ratio of 2.5%. or 3.0%., in the terms of lateral resistance force and the strain in SBPDN rebars. On the other hand, as shown in Fig. 5.4-3(b) the predicted residual drift ratio slightly underestimated the tested one, but indicated better accuracy than both of the results in Fig. 5.4-2(b).

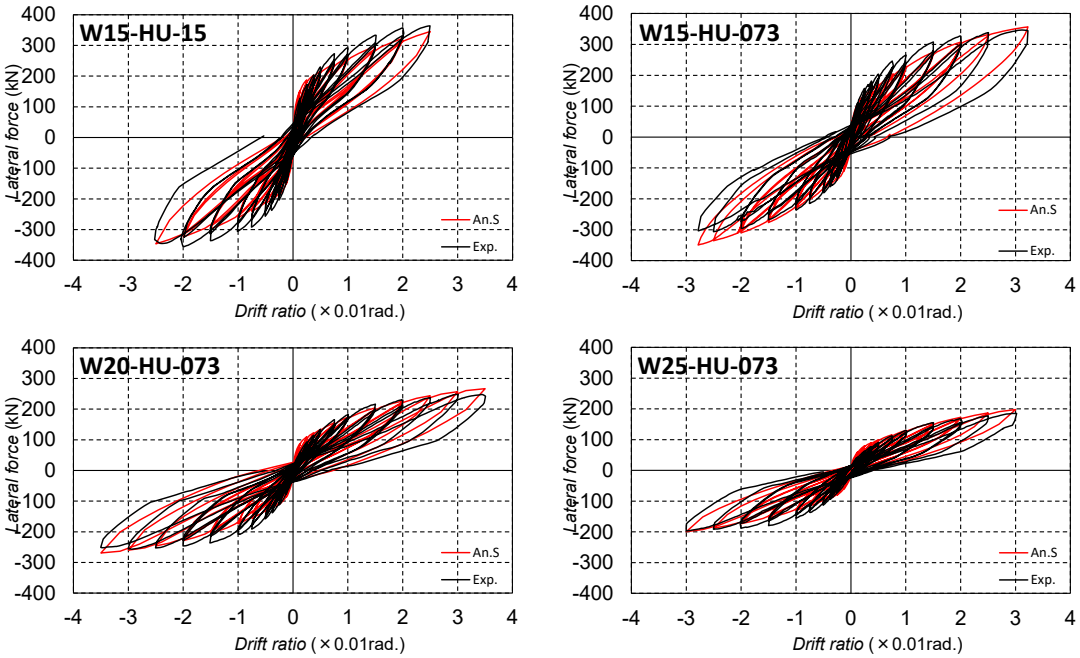

(a) *V-R* relationship

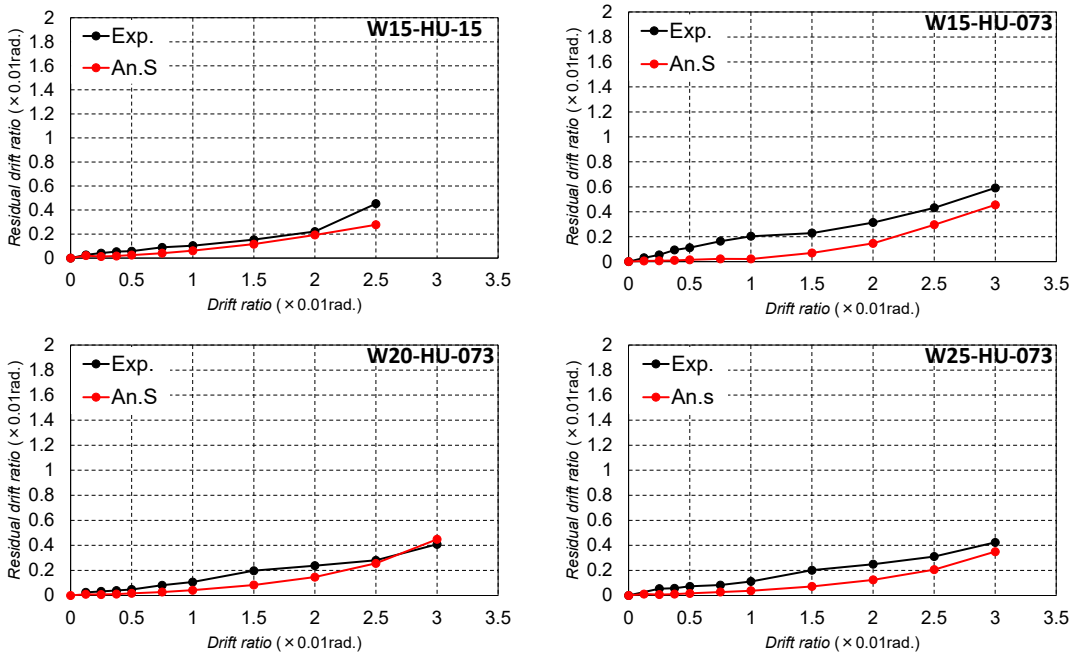

(b) Residual drift ratio

Fig. 5.4-3 Effect of the new arrangement for LD bars

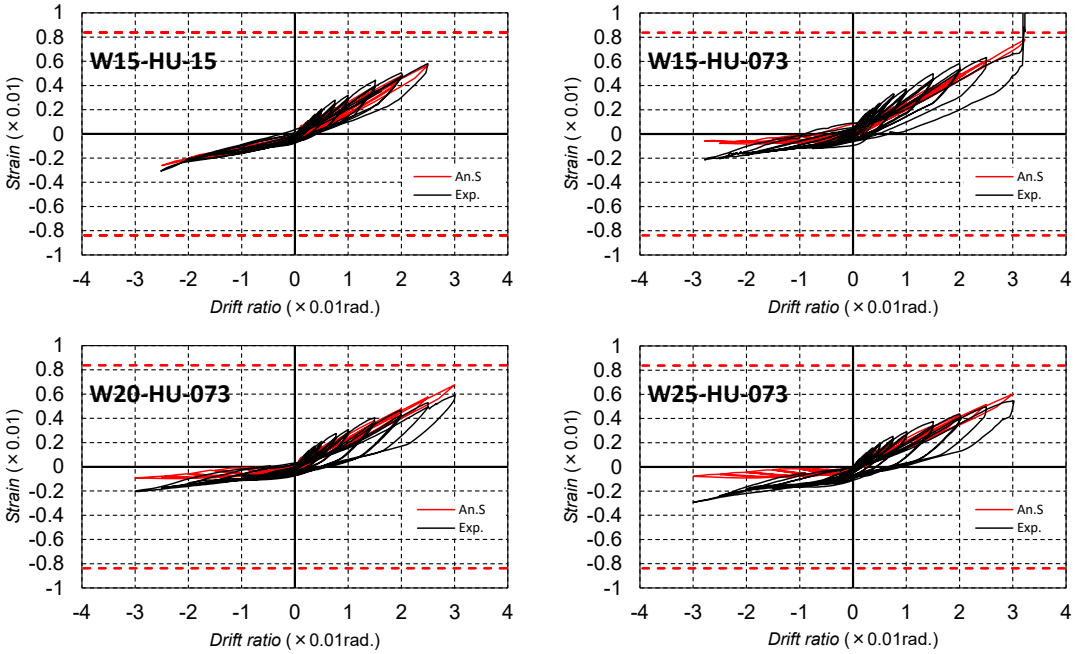

(c) Strain in concentrated rebars

Fig. 5.4-3 Continued

5.4.2 Effect of the joint between the wall toe and foundation beam

Since the proposed method could accurately evaluate the hysteresis loop of drift hardening shear walls, it is possible to analytically verify the effect of the improved joint method of precast shear walls described in Chapter Four.

As displayed in Fig. 5.4-4(a), the theoretical hysteresis loops exhibited accurate agreement with the experimental curves till drift ratio of 2.0%. From that drift ratio on, the loading curve during the test became irregular and the analytical results tend to overestimated the experimental loops. One can see from Fig. 5.4-4(b), the predicted residual drift ratio agreed very well with the measured one till drift ratio of 0.5%., but from that drift ratio on, the tested residual drift ratio increased sharply, on the other hand, the predicted remained at a very low level as what is expected for the drift hardening shear walls. These observations analytically proved that, even the damage at the wall-base joint was not confirmed directly as described in Chapter Four, the unrepairable damage around the connector resulted in the attenuation of ultimate strength for precast drift hardening shear walls, and leave relatively large residual deformation.

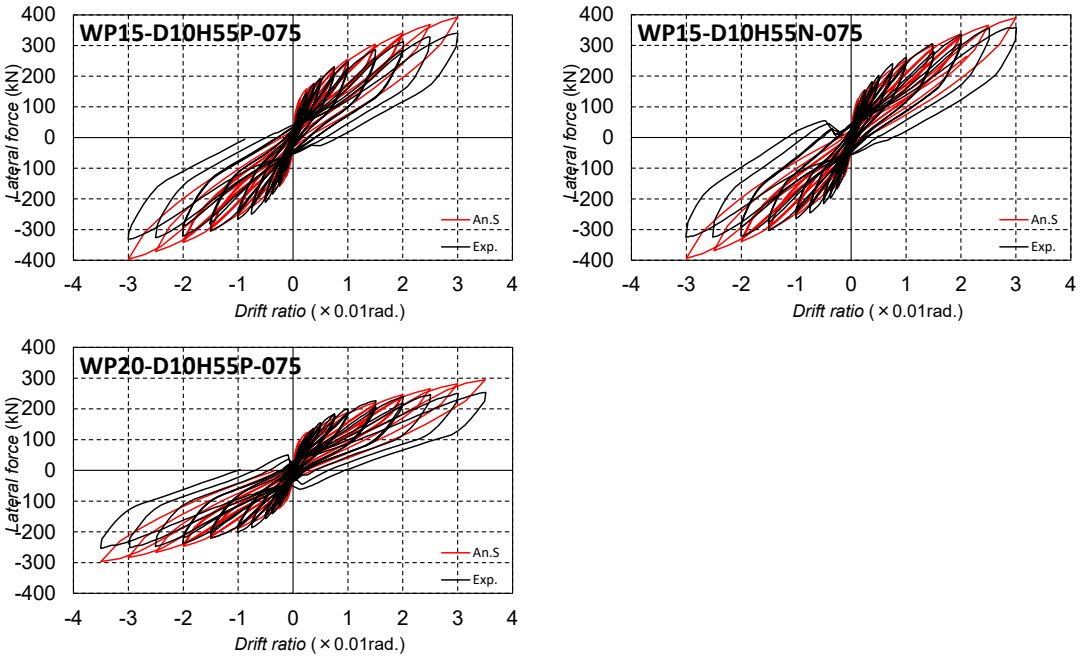

(a) *V*-*R* relationship

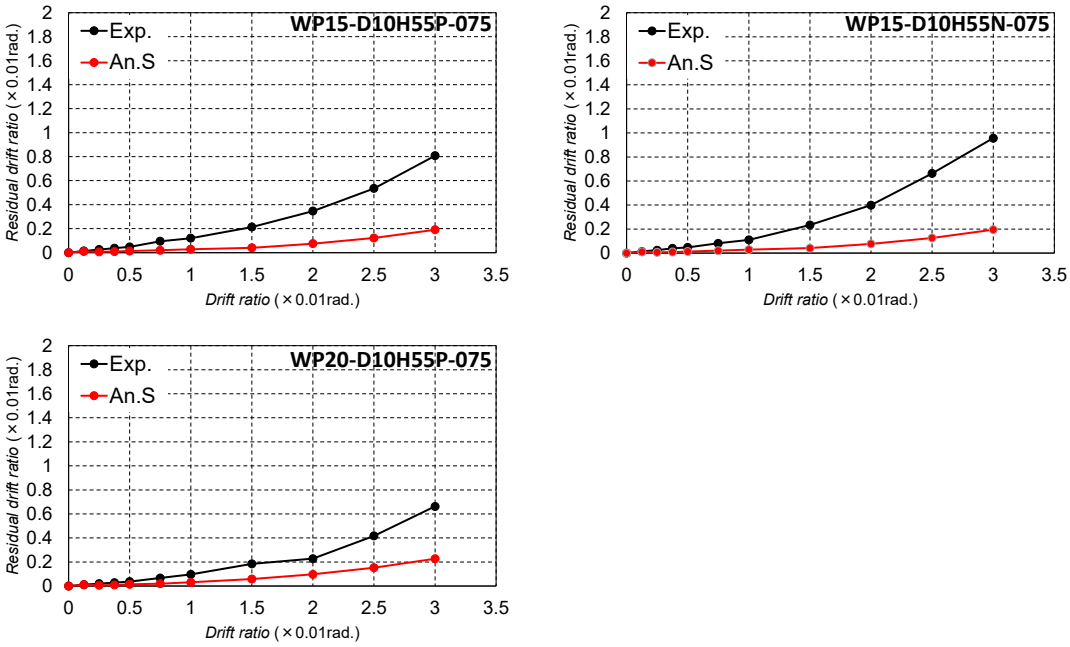

(b) Residual drift ratio

Fig. 5.4-4 Effect of the proposed joint method

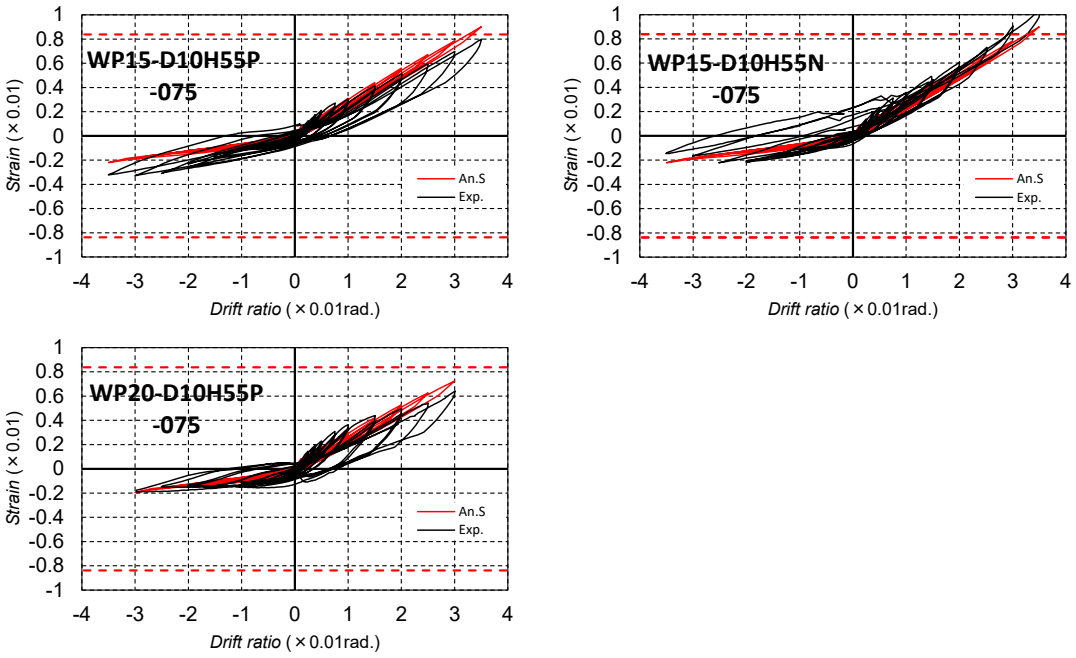

(c) Strain in concentrated rebars

Fig. 5.4-4 Continued

5.5 Conclusion

A numerical analysis method is developed to predict seismic behavior and properties of concrete walls reinforced by SBPDN rebars by modifying the method proposed by Sun et al. In addition to the effect of slippage of SBPDN rebars, the numerical method can take effects of shear deformation, plastic hinge length, and placement of distributed longitudinal bars in the wall panel. To verify validity and accuracy of the refined analytical method, the theoretical predictions by the refined method are compared with the measured results in terms of hysteresis loop, residual drift ratio, and the axial strain of concentrated rebars. Furthermore, it is also discussed whether the current code-prescribed design equations can be applied to predict the ultimate lateral capacities of the walls reinforced by SBPDN rebars.

To verify validity and accuracy of the refined analytical method, the theoretical predictions calculated by the refined method are compared with the measured results described in chapters two and four in aspects of hysteresis loop, residual drift ratio, and the axial strain of concentrated rebars. Based on the comparisons, the following conclusions can be drawn:

1) For the test walls whose DL bars were anchored into the foundation beam, theoretical hysteresis loops by the proposed analytical method exhibited very good agreement with the experimental curves with a difference of less than 10% on the conservative side. Moreover, the calculated residual drift ratios accurately predicted the experimental results up to the drift ratio of 3.0%.

2) For the specimens whose DL bars were not anchored into the foundation beam, if the four DL bars located in the boundary zones were considered to sustain axial stress induced by

moment and axial load, the analytical predictions for all these specimens exhibited very good agreement with the test curves till drift ratio of 2.5% or 3.0%, in aspects of lateral resistance and the strain in SBPDN rebars.

3) The current Japanese code-prescribed equations could predict the ultimate bending strength of ductile concrete walls reinforced by normal-strength deformed rebars, but significantly overestimated the flexure strength of the DHC walls reinforced by SBPDN rebars about 35% on average, because the SBPDN rebars did not yield until drift ratio of 3.0%. The calculated flexural strengths by NewRC block method agreed much better with the test results, but still overestimated the flexure strength by 1% - 18%, because it ignores the effect of the slippage of SBPDN rebars.

4) For the two DHC walls that failed in shear at large drift ratios, their ultimate shear strengths were underestimated by the current code-recommended equations for common concrete components, including the modified Ohno·Arakawa mean equation, method A and B prescribed in the design guidelines of AIJ.

References

[5.1] International Organization for Standardization (ISO), "ISO 3010 Bases for design of structures – seismic actions on structures", 1988.

[5.2] IS 1893-2002, "Criteria for Earthquake resistant design structures, Part 1 General provisions and buildings," Bureau of Indian Standards, New Delhi, 2002, 45 pp.

[5.3] European Committee for Standardization (CEN), "Eurocode 8 - Design of structures for earthquake resistance - Part 1: General rules, seismic actions and rules for buildings", 2003

[5.4] American Society of Civil Engineering, "ASCE 7-05 Minimum Design Loads for Buildings and Other Structures", 2006

[5.5] ICBA. et al., "Commentary on Structural Regulations of the Building Standard Law of Japan", 2015, pp.648-695, (in Japanese).

[5.6] AIJ, "Design Guidelines for Earthquake Resistant Reinforced Concrete Buildings Based on Ultimate Strength Concept", 1990, p.104, (in Japanese).

[5.7] Sun Y., Sakino K., Yoshioka T., "Flexural behavior of high-strength RC columns confined by rectilinear reinforcement, Journal of Structural and Construction Engineering", Architectural Institute of Japan, 1996, No. 486, 95-106.

[5.8] Sun Y., Fukuhara T., Kitajima H., "Analytical Study of Cyclic Response of Concrete Members Made of High-Strength Materials," Proceedings of the 8th U.S. NCEE, San

Francisco, USA, 2006; Paper No. 1581.

[5.9] Funato Y., “Seismic performance evaluation considering adhesion characteristics of RC columns using super high strength reinforcing bars with spiral grooves,” Master thesis, University of Kobe, 2012. (in Japanese).

[5.10] Sakino K. and Sun Y., “Stress-Strain Curve of Concrete Confined by Rectilinear Hoop,” J. of Struct. Constr. Eng., AIJ, No. 461, 1994, pp. 95 – 104. (in Japanese).

[5.11] Menegotto M., Pinto P.E., “Method of analysis for cyclically loaded reinforced concrete plane frames including changes in geometry and non-elastic behavior of elements under combined normal force and bending,” IABSE Symposium of Resistance and Ultimate Deformability of Structures Acted on by Well-Defined Repeated Loads, International Association of Bridge and Structural Engineering, Lisbon, Portugal, 1973; Vol. 13, pp. 15-22.

CHAPTER Six

Conclusions and future works

6.1 Conclusions

In order to promote the application of resilient or drift hardening concrete (DHC) walls reinforced by SBPDN rebars into practice, numerical and analytical works were conducted on the following aspects in this doctor dissertation; 1) to obtain and present more experimental information on seismic performance of rectangular concrete walls reinforced by SBPDN rebars, 2) to experimentally investigate the effect of shear span ratio on seismic performance of DHC walls with SBPDN rebars, 3) to verify the effectiveness of a new placement method of distributed longitudinal (DL) bars in the wall panel, 4) to propose a new type of anchorage for SBPDN rebars used in precast DHC walls and verify the effectiveness of the proposed anchorage, and 5) to propose an evaluation method for cyclic response of DHC walls by modifying the method proposed by Sun et al through taking the effects of shear deformation and placement detailing of DL bars in the wall panel into consideration.

This doctor dissertation consists of six chapters. Based on the experimental and analytical results summarized in this paper, primary finds obtained from chapter two through chapter five will be summarized below as the conclusions of this doctor dissertation.

1) For specimens whose DL bars were anchored into the adjacent beams, the specimen reinforced by (SD345 (D13) deformed bars showed excellent ductility and energy absorption capacity. The utilization of SBPDN rebars at the edge zones of wall section could assure RC walls high and stable lateral load resistance up to the drift ratio of 3.0% under axial load with axial load ratio of 0.15.

2) For specimens with axial load ratio of 0.073, regardless of their shear span ratio, SBPDN rebars could provide obvious drift hardening capability till drift ratio of 3.5%. Combination with the new arrangement of DL bars could mitigate the damage of concrete near the wall toes, and prevent the wall with shorter shear span from premature shear failure. Experimental results also implies that the adjacent members should be stiff enough to take full advantage of the new arrangement method.

3) For all the rectangular RC shear walls reinforced by SBPDN rebars, regardless of their shear span ratio, axial load ratio and the arrangement of DL bars, the residual drift ratio can be controlled as low as 0.6%., after the walls experienced large drift ratio of up to 3.0%. This residual drift ratio is only one third of that measured in the test wall reinforced with normal-strength deformed rebars SD345.

4) Comparing with the drift hardening shear walls fabricated by conventional construction method, the precast specimens exhibited nearly identical lateral resistance till the drift ratio of 2.0%. After that drift level on, the bond failure occurred between connection portion and concrete due to insufficient anchorage length of the connection portion, triggering the degradation of lateral resistance. However, the degradation is gradual, and all precast walls remained over 80% of their maximum lateral forces at the drift of 3.0%. While the bond failure between the connector and concrete caused degradation of lateral resistance at large drift, the use of SBPDN rebars could still control the residual drift ratio below 0.6% after unloading from the drift of 3.0%.

5) The bond strength between sheath ducts and concrete was evaluated on the basis of the measured strains of longitudinal rebars. The evaluated bond strength (4.6 N/mm^2) implied that to completely take the advantages of utilization of SBPDN rebars in the precast concrete walls, the embedment depths of sheath ducts should be at least 480 mm (about five times of the diameter of sheath duct) to provide sufficient bond strength for SBPDN rebars to develop strain along with drift till the yield strain.

6) If the embedment length of sheath ducts that accommodate SBPDN rebars was five times of the duct diameter, giving an embedment depth of 510 mm, both anchorage methods (by combination of the steel plate and nuts or by screwed threads of end portion) could provide sufficient bond strength to SBPDN rebars, and ensure the precast concrete walls drift-hardening capability till drift ratio of 3.0%.

7) No severe damage was observed around the anchorage portions with embedment length of 510 mm regardless of the difference of anchorage detailing. Both short walls with shear span ratio of 1.5 exhibited excellent deformability up to about 5.0% drift without obvious degradation of lateral resistance, while the lateral resistance of the test wall with shear span ratio of 2.0 at the drift of 4.0% remained almost the same value as the maximum lateral force.

8) For the test walls whose DL bars were anchored into the foundation beam, theoretical hysteresis loops by the proposed analytical method exhibited very good agreement with the experimental curves with a difference of less than 10% on the conservative side. Moreover, the calculated residual drift ratios accurately predicted the experimental results up to the drift ratio of 3.0%.

9) For the specimens whose DL bars were not anchored into the foundation beam, if the four DL bars located in the boundary zones were considered to sustain axial stress induced by moment and axial load, the analytical predictions for all these specimens exhibited very good agreement with the test curves till drift ratio of 2.5% or 3.0%, in aspects of lateral resistance and the strain in SBPDN rebars.

10) The current Japanese code-prescribed equations could predict the ultimate bending strength of ductile concrete walls reinforced by normal-strength deformed rebars, but significantly overestimated the flexure strength of the DHC walls reinforced by SBPDN rebars about 35%

on average, because the SBPDN rebars did not yield until drift ratio of 3.0%. The calculated flexural strengths by NewRC block method agreed much better with the test results, but still overestimated the flexure strength by 1% - 18%, because it ignores the effect of the slippage of SBPDN rebars.

6.2 Suggestions and future works

Due to the constraint of time, there are still several important aspects have not been covered in this dissertation. In order to promote the applications of drift hardening concrete walls, necessary further researches are listed below:

1) Investigation of the reason for the discrepancy between analytical and measured residual drifts: Although the analytical method developed in this thesis predicted tests results of the walls reinforced by SBPDN rebars very well in aspects of lateral resistance, hysteresis loop, and the steel strains, there was significant discrepancy between the calculated and measured residual drift ratios. This discrepancy became large along with drift ratio. Since the residual deformation is a fundamental index measuring the reparability of concrete structures, ductile and resilient, it is of great importance to investigate the reason for this discrepancy.

2) Development of seismic shear strength model for drift hardening concrete walls: As described in chapter five, for the DHC walls that failed in shear at large deformation, none of the current code-prescribed equations agreed well with the experimental results. While brittle shear failure must be avoided in seismic design of DHC walls, it is the development of an accurate shear strength model that is necessary for engineers to consciously avoid the design of DHC walls that may fail in shear at larger drift.

3) Effect of distributed longitudinal (DL) bars in the wall panel: For the walls whose DL bars were not anchored into wall base, it was analytically verified in chapters four that only the DL bars located at the boundary zones provided flexure resistance. This presumption needs to be confirmed by further experimental work.

List of Publications

[1] Chuxuan Wei, Yuping Sun, Takashi Takeuchi, Takao Nakagawa, “SEISMIC BEHAVIORS AND EVALUAION OF REINFORCED CONCRETE WALLS REINFORCED BY SBPDN REBARS”, Proceedings of the JCI, 2021, 43(2), pp. 175-180.

[2] Chuxuan Wei, Yuping Sun, Takashi Takeuchi, Y. Takeda: SEISMIC BEHAVIOR OF SQUARE CONCRETE BEAM-COLUMNS WITH CIRCULARLY DISTRIBUTED ULTRA-HIGH-STRENGTH REBARS, Proceedings of 17th World Conference on Earthquake Engineering, 2021, Paper No. C000411.

[3] Jiayu Che, Yuping Sun, Takashi Takeuchi, Chuxuan Wei, “Seismic performance of precast RC shear walls reinforced by SBPDN rebars”, Proceedings of the JCI, 2021, 43(2), pp. 169-174, (in Japanese).

Doctoral Dissertation, Kobe University
“Earthquake-Resisting Performance and Evaluation of Drift-hardening Concrete Walls”, 158 pages
Submitted on July, 15, 2021
The date of publication is printed in cover of repository version published in Kobe University Repository Kernel.